Flight Dynamics Modeling and Autopilot Design for Guided Projectiles via Linear Parameter-Varying Techniques

Gian Marco Vinco

To cite this version:

Gian Marco Vinco. Flight Dynamics Modeling and Autopilot Design for Guided Projectiles via Linear Parameter-Varying Techniques. Automatic. Université Grenoble Alpes [2020-..], 2024. English. NNT : 2024GRALT011 . tel-04593695

HAL Id: tel-04593695
https://theses.hal.science/tel-04593695v1

Submitted on 30 May 2024

HAL is a multi-disciplinary open access archive for the deposit and dissemination of scientific research documents, whether they are published or not. The documents may come from teaching and research institutions in France or abroad, or from public or private research centers.

L'archive ouverte pluridisciplinaire **HAL**, est destinée au dépôt et à la diffusion de documents scientifiques de niveau recherche, publiés ou non, émanant des établissements d'enseignement et de recherche français ou étrangers, des laboratoires publics ou privés.

THÈSE

Pour obtenir le grade de

DOCTEUR DE L'UNIVERSITÉ GRENOBLE ALPES

École doctorale : EEATS - Electronique, Electrotechnique, Automatique, Traitement du Signal (EEATS)
Spécialité : Automatique - Productique
Unité de recherche : Grenoble Images Parole Signal Automatique

Approches linéaires à paramètres variants pour la modélisation de la dynamique du vol et la synthèse d'autopilotes des projectiles guidés

Flight Dynamics Modeling and Autopilot Design for Guided Projectiles via Linear Parameter-Varying Techniques

Présentée par :

Gian Marco VINCO

Direction de thèse :

Olivier SENAME PROFESSEUR DES UNIVERSITES, Université Grenoble Alpes	Directeur de thèse
Guillaume STRUB Institut franco-allemand de recherches de Saint-Louis (ISL)	Co-encadrant de thèse
Spilios THEODOULIS Associate professor, Université de technologie de Delft	Co-encadrant de thèse

Rapporteurs :

Marco LOVERA
FULL PROFESSOR, École polytechnique de Milan
John ECONOMOU
FULL PROFESSOR, Université de Cranfield

Thèse soutenue publiquement le **2 février 2024**, devant le jury composé de :

John-Jairo MARTINEZ-MOLINA, PROFESSEUR DES UNIVERSITES, GRENOBLE INP	Président
Olivier SENAME, PROFESSEUR DES UNIVERSITES, GRENOBLE INP	Directeur de thèse
Marco LOVERA, FULL PROFESSOR, École polytechnique de Milan	Rapporteur
John ECONOMOU, FULL PROFESSOR, Université de Cranfield	Rapporteur
Charles POUSSOT-VASSAL, DIRECTEUR DE RECHERCHE, ONERA	Examinateur
Elmar WALLNER, SENIOR SCIENTIST, MBDA Deutschland GmbH	Examinateur

Invités :

Guillaume STRUB
CHARGE DE RECHERCHE, Institut franco-allemand de recherches de Saint-Louis
Spilios THEODOULIS
ASSOCIATE PROFESSOR, Université de technologie de Delft

Acknowledgments

This project has represented an incredible journey rich in achievements and difficulties. People who have played a significant role in the last three years of my life are too many to be mentioned, but I'll try to reach as many as I can.

There are not enough words to express my sincere gratitude to my supervisors Olivier Sename, Spilios Theodoulis, and Guillaume Strub for their guidance and support throughout the entire duration of the project. Besides the invaluable expertise and academic passion they transmitted to me as mentors, they have always encouraged and motivated me during the most challenging times of the project. Their patience and positive attitude have been the real key to facing any problems I encountered on the way. I will always be immensely grateful for the time and the kindness you have dedicated to me during these years.

An immense thanks go to my colleagues at GIPSA-lab and at ISL for all the laughs, the constructive discussions, and the coffee breaks we shared. Your support, your passion, and your energy have been an inspiring source of motivation and personal enrichment for my personal journey. I would particularly like to thank Ariel and Sofiane whom I started my Ph.D. with and whom I shared supervisors, conferences, struggles, and achievements. I have always found a good word, a cheer, and understanding from you. A chat in front of a beer might not solve LMIs (and believe me sometimes it does), but it is still refreshing.

I cannot forget my beloved flatmates Massimiliano, Nastja, Paolo, Konstantina and Benjamin. Together we shared broken washing machines, several tons of pizza and sushi, Batmaz threats, TV series, unexpected 16-km runs, ski trips, and a lot more. I have always thought that traveling was the best way to meet interesting people, but I wouldn't have expected to find someone like you guys on my way and share this much in such a short period of time.

To all the friends I met in Saint-Louis and Grenoble, for the ones back to Verona, and those spread across many other countries, thank you for sharing some of the happiest moments of these last years. I am still not sure where the next step of my journey will lead me, but I will always bring all the good memories I have with you wherever I'll be.

A special thanks go to my girlfriend Lauriane who has supported and endured me despite the stress of the last part of the project. You made everything easier and lighter, finding the right words or simply with a huge hug. Thank you for all your smiles and your sweetness.

Finally, I want to dedicate this work to my family who has been there since day one, always cheering and believing in me even when I didn't think I could do it. To all of you who were there waiting for me every time I was coming back home. Without you I would have never reached any of my achievements and, more importantly, I wouldn't be the person I am. You have always been an inexhaustible source of motivation. Thank you, I love you all.

> "*Aut viam inveniam aut faciam*"
>
> *Hannibal Barca*

> "*Weren't there times when everybody, or at least a few people, just panicked?*
> *No, when bad things happened, we just calmly laid out all the options, and* ***failure was not one of them****.*
> *We never panicked, and we never gave up on finding a solution.*"
>
> *Apollo XIII*

Contents

Résumé de Thèse

Contextualisation du Projet

Le développement des technologies sophistiquées de missiles et de munitions d'artillerie a toujours été synonyme de puissance, depuis leurs conceptions balistiques initiales non guidées. L'avènement des technologies de guidage avancées a encore renforcé leur utilisation en tant qu'armes conventionnelles, grâce à une précision accrue sur la cible. Les premières stratégies de guidage utilisaient des mesures radar ou optiques depuis le site de lancement, avec des commandes de contrôle radio ou laser transmises par un opérateur au sol. L'amélioration de la précision du guidage, notamment par l'utilisation de caméras de télévision et de faisceaux laser pour l'interception de la cible, a suscité un intérêt croissant pour le développement de munitions guidées. La conception des armes guidées repose sur trois fonctionnalités principales : le Guidage, la Navigation et le Contrôle (GNC). L'implémentation standard à double boucle GNC comprend une boucle interne rapide, qui met à jour les commandes de contrôle du pilote automatique en fonction des informations de navigation, et une boucle externe plus lente, qui ajuste les signaux de référence pour répondre aux exigences de la mission.

La dérivation d'une loi de contrôle efficace repose fortement sur l'exactitude du modèle choisi pour représenter la dynamique du système. La modélisation et la conception de contrôle ont toujours représenté des processus fastidieux à accomplir en raison de la grande non-linéarité caractérisant la dynamique de vol des missiles/projectiles et de la grande variété des paramètres opérationnels. Néanmoins, la complexité du modèle affecte la sélection de l'approche de contrôle la plus appropriée et éventuellement la charge numérique de la mise en œuvre du contrôleur. Dans ce contexte, une stratégie bien établie consiste à décomposer la tâche de contrôle globale en la conception de contrôleurs LTI locaux à chaque linéarisation locale de la dynamique non linéaire d'origine. L'ensemble résultant de contrôleurs LTI locaux peut être facilement mis en œuvre grâce à la définition d'une stratégie de planification dédiée, qui permet de sélectionner le contrôleur le plus approprié dans toutes les conditions de fonctionnement. La stratégie de planification la plus traditionnelle repose sur l'interpolation

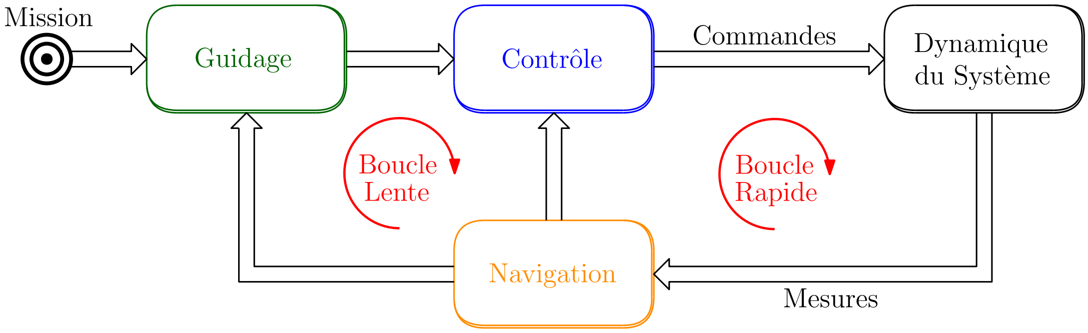

Figure 1 : Double boucle du système de guidage, navigation et contrôle (GNC).

linéaire des gains statiques des contrôleurs locaux, appelée planification de gain. Malgré une large gamme d'applications réussies, la conception de la planification de gain s'est avérée présenter des limitations de précision et de stabilité théoriques et pratiques pertinentes.

Ces dernières décennies, le cadre linéaire à paramètres variables (LPV) a émergé comme une alternative intéressante en modélisation et contrôle pour diverses applications aérospatiales. Contrairement à l'approche de linéarisation, la conception LPV vise directement la synthèse globale du contrôleur, assurant des propriétés de stabilité en boucle fermée à l'échelle globale. Les modèles LPV/quasi-LPV prennent en compte les variations temporelles d'un ensemble de paramètres sélectionnés, permettant une meilleure capture de la dynamique non linéaire du système. La synthèse du contrôleur LPV repose sur la formulation d'un problème d'optimisation dédié, réalisable soit en exploitant les caractéristiques des systèmes à affinité de paramètres, soit par une discrétisation de l'espace des paramètres à l'aide d'un processus de maillage. La première approche (polytopique) garantit une stabilité quadratique plus élevée, mais avec des performances plus conservatrices, tandis que la seconde (basée sur le maillage) offre des performances significatives avec une complexité de mise en œuvre plus élevée et des propriétés de stabilité globale réduites.

Dans ce contexte, le projet présenté propose l'analyse de la modélisation et de la conception de contrôle d'un nouveau concept de projectile guidé à longue portée (LRGP) étudié à l'Institut franco-allemand de recherche de Saint-Louis (ISL). Basé sur une architecture stabilisée par ailettes non rotatives de 155 mm, le projectile comprend quatre ailettes arrière axiales symétriques et deux canards avant pour les manœuvres de contrôle, configurés en 'X' comme illustré dans la Figure 2. L'objectif est d'améliorer la portée des obusiers standard sans recourir à des propulseurs supplémentaires ou des modifications du système de tir. La modélisation et la conception de contrôle sont étudiées dans le cadre LPV en raison de ses avantages et des applications limitées dans la littérature sur les technologies de munitions guidées.

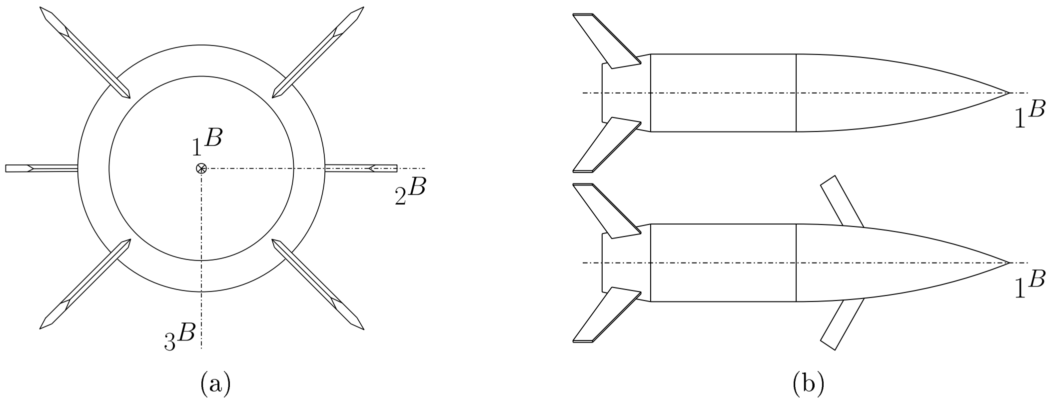

(a) (b)

Figure 2 : Concept LRGP : (a) configuration ailerons-canards en "X" ; (b) configuration du projectile balistique (en haut) et du projectile planeur (en bas).

Chapitre 1 : Développement du Modèle de Projectile

Le processus de modélisation de la dynamique du système est crucial avant la conception du contrôleur. Une identification précise du comportement du système améliore la fiabilité du modèle mathématique et l'efficacité du contrôleur. Habituellement, des dynamiques de modèle simplifiées sont dérivées pour la conception du contrôleur, ne capturant que les caractéristiques les plus pertinentes pour les performances du contrôleur. Ensuite, un modèle détaillé est utilisé pour tester la conception du contrôleur dans un scénario de simulation plus réaliste. Pour le concept LRGP, la modélisation repose sur la formulation standard des équations différentielles non linéaires décrivant la dynamique inertielle du projectile. Des simulations de dynamique des fluides numériques (CFD) ont été réalisées pour caractériser l'aérodynamique du concept LRGP, ciblant les deux principales contributions aérodynamiques du projectile. Une première campagne a examiné les coefficients aérodynamiques générés par les contributions statiques de portance et de traînée du projectile, incluant l'effet des surfaces de contrôle à déflection locale nulle. Le deuxième ensemble de données a étudié les contributions aérodynamiques supplémentaires générées par la déflection locale des surfaces de contrôle.

Afin de fournir un modèle continu décrivant l'aérodynamique du projectile dans toutes les conditions de vol, les données CFD ont été traitées par le biais d'une analyse de régression précise. Un modèle polynomial à variable unique (PR) et un modèle multivariable (MR) ont été obtenus à partir de la régression des coefficients statiques. Le modèle PR est basé sur un ensemble réduit de données CFD, ciblant certaines configurations spécifiques et conditions de vol de l'aérodynamique du projectile. Le modèle MR, quant à lui, repose sur l'ensemble complet des données CFD acquises, fournissant une description aérodynamique globale qui couvre une gamme plus étendue de conditions de vol. Une régression polynomiale a également été réalisée sur l'ensemble de données CFD des surfaces de contrôle. Dans un souci de modélisation, les contributions aérodynamiques individuelles des surfaces de contrôle ont été formulées comme des effets globaux sur le taux de rotation du corps, influençant l'orientation du projectile. La formulation du contrôle reposait sur des hypothèses de superposition linéaire concernant la réponse aérodynamique du projectile. L'intervalle de confiance du modèle aérodynamique a été estimé pour une déviation totale : $\delta \in [-20, 20]$ deg.

À partir des résultats de modélisation, plusieurs modèles ont été élaborés pour représenter différentes caractéristiques de la dynamique du projectile. En fonction du niveau de précision et de complexité, chacun de ces modèles peut être utilisé à différentes étapes de la conception et de la validation de l'autopilote. Le premier modèle visait à représenter la dynamique de tangage du projectile, en incluant la dynamique de l'angle d'attaque (AoA), $\dot{\alpha}$, du taux de tangage, $\dot{q}$, le modèle aérodynamique statique PR, ainsi que les contributions aérodynamiques des surfaces de contrôle. Ce modèle a été utilisé ultérieurement pour la modélisation LPV et la conception de l'autopilote dédié au tangage. Le deuxième modèle reposait sur une description non linéaire 6-DoF de la dynamique translationnelle et d'attitude du projectile, en incluant le modèle aérodynamique MR complet ainsi que les contributions de contrôle aérodynamique correspondantes. Ce modèle a été implémenté dans un environnement de simulateur non linéaire 6-DoF pour évaluer les performances des contrôleurs.

Chapitre 2 : Dérivation du Modèle LPV

La modélisation orientée vers le contrôle consiste en une étape intermédiaire qui permet l'application de plusieurs approches de conception de contrôle aux dynamiques non linéaires générales d'un système. Le cadre linéaire à paramètres variables (LPV) permet une représentation plus générale et complète des dynamiques temporelles du système, exploitée à travers la sélection d'un ensemble de paramètres variables, $\boldsymbol{\rho}$. Plusieurs applications aérospatiales réussies ont été proposées ces dernières années, reformulant les dynamiques non linéaires standard du véhicule en un modèle LPV/quasi-LPV précis. La conversion peut être réalisée par l'emploi de différentes approches LPV telles que la substitution de fonctions, les techniques basées sur la vitesse et la transformation d'état.

La méthode de transformation d'état a été privilégiée pour développer un modèle LPV précis de la dynamique de tangage du projectile, offrant une transformation exacte entre le système non linéaire d'origine et le modèle LPV résultant. Ainsi, aucune approximation n'a été nécessaire dans la conception, ce qui a renforcé la capacité du modèle à représenter la dynamique d'origine. Le vecteur de paramètres variables choisi est $\boldsymbol{\rho} = [\alpha, V, h]$, où V représente la vitesse de l'air du projectile et h l'altitude. Pour appliquer le processus de transformation, une approximation aérodynamique spécifique a été développée, exprimant le coefficient de contrôle aérodynamique comme une fonction linéaire de la déflection des canards, répondant ainsi aux exigences de l'approche de transformation d'état. De plus, la dynamique de l'intégrateur a été ajoutée à l'entrée du système pour compenser la configuration dépendante des paramètres d'entrée.

Le modèle quasi-LPV augmenté d'intégrateur de la dynamique de tangage du projectile, désigné par Σ_{GR}, a été utilisé pour la conception du contrôleur basé sur la grille LPV. Dans l'équation de sortie, les mesures du facteur de charge hors équilibre, $\eta_{z,\mathrm{dev}}$, ont remplacé la déflection de tangage des canards, δ_q. La matrice d'avance, $\mathcal{D}$, a été supposée nulle. L'exactitude du modèle quasi-LPV a été confirmée par simulation sur une plage de variation incluant $\alpha \in [0, 16]$ degrés, $V \in [160, 280]$ m/s, $h \in [1, 15]$ km.

Dans le but d'utiliser le modèle quasi-LPV pour la conception d'un contrôleur polytopique basé sur le LPV, une étape de modélisation supplémentaire a été nécessaire. En effet, le modèle quasi-LPV obtenu ne respectait pas la relation affine entre le modèle et les paramètres imposée par la formulation polytopique. Ainsi, une procédure d'approximation du modèle a été développée dans le but de reformuler le modèle quasi-LPV du projectile en un système polytopique. L'approximation reposait sur l'identification d'un nouvel ensemble de fonctions de planification, $\hat{\boldsymbol{\rho}}$, affines par rapport à la dynamique du système. Le processus d'approximation a abouti à la reformulation polytopique de la dynamique de tangage quasi-LPV du projectile, Σ_{PY}. Concernant l'équation de sortie, la matrice de sortie, $\mathcal{C}$, est constituée de la matrice identité, $I \in \mathbb{R}^{3\times 3}$, en supposant une architecture de rétroaction d'état. La matrice d'avance, $\mathcal{D}$, est supposée nulle. Après avoir évalué l'exactitude du processus d'approximation, le domaine d'application original du modèle quasi-LPV a été cartographié dans le nouveau polytope convexe, $\hat{\Theta}$, défini par les fonctions de planification : $\hat{\rho}_1(V, h) \in [0.4,\ 2.9] \times 10^4$, $\hat{\rho}_2(\alpha, V, h) \in [0.05,\ 0.55]$, et $\hat{\rho}_3(\alpha, V, h) \in [-1,\ 4.1]$.

Chapitre 3 : Conception de l'Autopilote LPV de Tangage

La synthèse des contrôleurs LPV repose sur la résolution de problèmes d'optimisation convexes formulés sous forme d'inégalités matricielles linéaires (LMIs). En imposant une relation affine entre le modèle et les paramètres, l'optimisation peut être résolue dans un sous-espace convexe (polytope) défini par les plages de variation du paramètre. En exploitant la variation linéaire du paramètre, la conception garantit des garanties de stabilité dans tout le polytope. Une autre approche consiste à discrétiser l'espace de variation des paramètres en un ensemble fini de conditions de conception (gridding), tout en tenant compte du taux de variation de chaque paramètre pour améliorer les performances du contrôleur. Ces approches ont été utilisées pour synthétiser un pilote automatique LPV pour la dynamique de tangage du projectile.

En ce qui concerne l'approche polytopique, les conditions du problème d'optimisation LMIs doivent être satisfaites uniquement aux sommets de l'espace convexe défini par les plages de variation des fonctions de planification. Les principaux avantages de cette approche reposent sur le nombre réduit de conditions à satisfaire simultanément et sur les garanties accrues de stabilité quadratique dans tout le domaine couvert par le polytope convexe. Le principal inconvénient réside dans le conservatisme qui affecte le processus d'optimisation, car la solution est basée sur une fonction de Lyapunov indépendante des paramètres. Afin d'améliorer les performances de l'optimisation, une analyse dédiée est développée pour optimiser la dimension du polytope, en négligeant toutes les conditions opérationnelles qui n'appartiennent pas à l'enveloppe de vol du projectile. L'analyse a permis de définir un polytope de dimensions réduites, $\hat{\Theta}_{\mathrm{R}}$, en ajustant les plages de variation des fonctions de planification comme suit : $\hat{\rho}_1 \in [0.4,\, 2] \times 10^4$, $\hat{\rho}_2 \in [0.05,\, 0.35]$, et $\hat{\rho}_3 \in [-1,\, 2]$.

La conception du contrôleur polytopique résultant était basée sur le schéma de la Figure 3, en supposant le critère d'optimisation $\mathcal{H}_\infty$. La conception vise à améliorer la robustesse du contrôleur, en tenant compte d'un ensemble de sources internes et externes de perturbation (d_i, d_o), et de la capacité à suivre un signal de guidage de référence, r, en imposant un modèle de référence, f_{ref}, et un ensemble de filtres de pondération de performance, (W_r, W_e, W_u, Wd_i, Wd_o). La dynamique des actionneurs, T_{act}, est également incluse dans la conception du contrôleur.

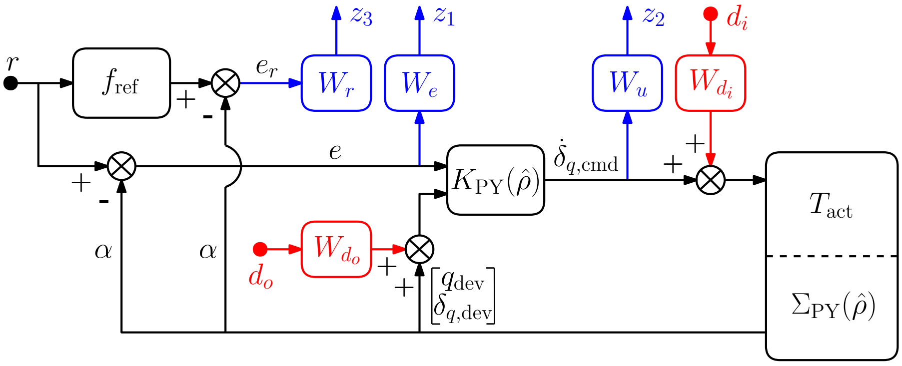

Figure 3 : Architecture du schéma de conception polytopique.

La deuxième approche repose sur la discrétisation (gridding) de l'espace de variation des variables de planification en une grille finie de conditions de vol. L'optimisation LMI définissant la synthèse du contrôleur est calculée à chacun des points de conception sélectionnés. En conséquence, la complexité computationnelle affectant l'optimisation dépend fortement de la définition de la grille. Cependant, la solution du problème LMI est basée sur des fonctions de Lyapunov dépendantes des paramètres, ce qui offre de meilleures performances d'optimisation. Pour limiter la complexité computationnelle, une analyse exhaustive de l'enveloppe de vol discrétisée a ciblé les propriétés de stabilité du système et les performances de trajectoire souhaitées. L'analyse visait à trouver une dimension de grille optimale en équilibrant la complexité computationnelle et les garanties de stabilité. De plus, la paramétrisation des fonctions de Lyapunov a été étudiée pour modéliser la dépendance des fonctions sur chaque variable de planification. Les résultats de l'analyse fournissent les plages de variations discrétisées suivantes : $\boldsymbol{\alpha}\text{grid} = [1, 5, 8, 13]$ degrés, $\boldsymbol{V}\text{grid} = [180, 200, 240, 270]$ m/s, et $\boldsymbol{h}_{\text{grid}} = [3, 6, 9, 12, 14.5]$ km, tandis que les fonctions de Lyapunov ont été formulées comme suit :

$$X(\boldsymbol{\rho}) = Y(\boldsymbol{\rho}) = X_0 + X_{\alpha,1}\sin\alpha + X_{\alpha,2}\cos\alpha + X_V V + X_h h.$$

La conception du contrôleur LPV/$\mathcal{H}_\infty$ a été basée sur le schéma de la Figure 4 et a été calculée sur l'espace de grille résultant, Ξ, composé de $n_g = 80$ points de vol. Les taux de variation de chaque variable de planification ont été définis comme suit : $\dot{\alpha}_{\text{grid}} \in [-30, 30]$ deg/s, $\dot{V}_{\text{grid}} = [-50, 50]$ m/s^2, et $\dot{h}_{\text{grid}} = [-100, 100]$ m/s.

La conception polytopique est basée sur une approximation supplémentaire de modélisation, introduisant des sources indésirables d'incertitudes. Cependant, l'approche polytopique garantit des propriétés de stabilité robustes supérieures dans tout l'espace convexe. En ce qui concerne la conception basée sur la grille, des garanties de stabilité robustes ne sont fournies qu'à proximité des points de conception. D'autre part, les performances d'optimisation attendues étaient confirmées à la fois par les résultats de γ_∞ inférieurs et par l'effort de commande réduit requis pour les actionneurs. Du point de vue de la complexité, la synthèse du contrôleur était basée sur la sélection de plusieurs paramètres de réglage (n_g, $\boldsymbol{f}_{\text{B}}$), nécessitant le développement d'une analyse dédiée chronophage. Enfin, la mise en œuvre du contrôleur basé sur la grille, K_{GR}, repose sur l'interpolation de 80 réalisations locales LTI, comparé aux 8 réalisations locales LTI requises par le contrôleur polytopique, K_{PY}.

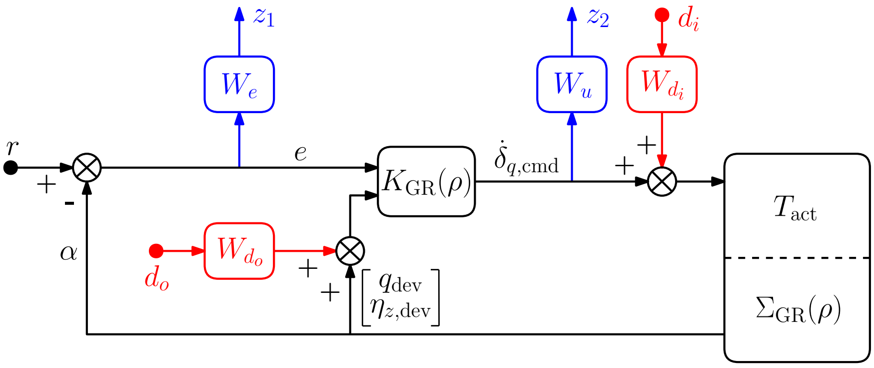

Figure 4 : Architecture du schéma de conception basé sur la grille.

Chapitre 4 : Évaluation des Performances

Les procédures standards de conception de contrôle visent la stabilité nominale (NS) et les performances (NP) du système en boucle fermée. Toutefois, les perturbations possibles peuvent dévier la dynamique du système de ses conditions nominales. La performance des contrôleurs polytopique, K_{PY}, et basé sur la grille, K_{GR}, a été examinée face à diverses perturbations et incertitudes du modèle. Une première analyse de robustesse a évalué les marges de stabilité des fonctions de transfert entrée/sortie pour chaque système.Comme les modèles quasi-LPV et polytopiques sont des systèmes à entrée unique et à sortie multiple, le calcul des marges de disque est préféré aux définitions standard des marges de gain et de phase. Les résultats montrent de larges marges de sortie pour la dynamique des première et troisième voies ($\dot{\alpha}$ et $\dot{\delta}_{q,\mathrm{dev}}$), mais des faiblesses potentielles sont apparues pour la deuxième voie ($\dot{q}$).

Les marges de stabilité fournissent des conditions nécessaires mais pas suffisantes pour évaluer la robustesse du système et peuvent conduire à une analyse très conservatrice. Ainsi, les performances des contrôleurs ont été testées plus avant à travers une analyse de sensibilité μ, visant la robustesse par rapport aux incertitudes paramétriques structurées du système. Un ensemble de paramètres a été sélectionné en fonction de l'effet de leur variation sur la stabilité de la dynamique du système. L'ensemble d'incertitudes comprend une sélection de paramètres aérodynamiques, chacun associé à une plage de tolérance estimée (exprimée en pourcentage d'incertitude). Cependant, en raison de la complexité excessive de la formulation numérique, les incertitudes paramétriques individuelles ont été modélisées comme des perturbations globales affectant chaque entrée de la représentation de l'espace d'état du système. L'analyse μ réalisée sur l'ensemble dédié d'incertitudes a révélé des propriétés de stabilité robuste et de performance robuste satisfaisantes des systèmes en boucle fermée polytopique et basé sur la grille par rapport aux incertitudes paramétriques. Le pourcentage d'incertitude du système que le contrôleur polytopique peut gérer est plus élevé par rapport au contrôleur basé sur la grille, en cohérence avec les garanties théoriques de stabilité fournies par la synthèse polytopique.

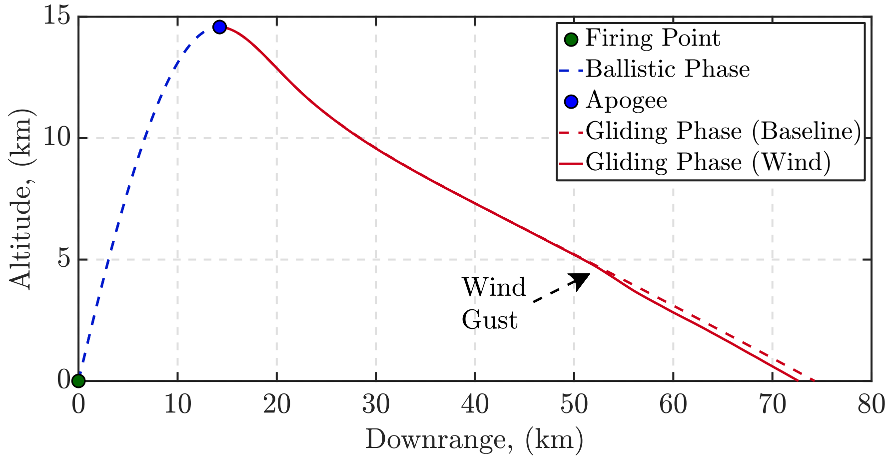

Figure 5: Comparaison des simulations : performances de la trajectoire.

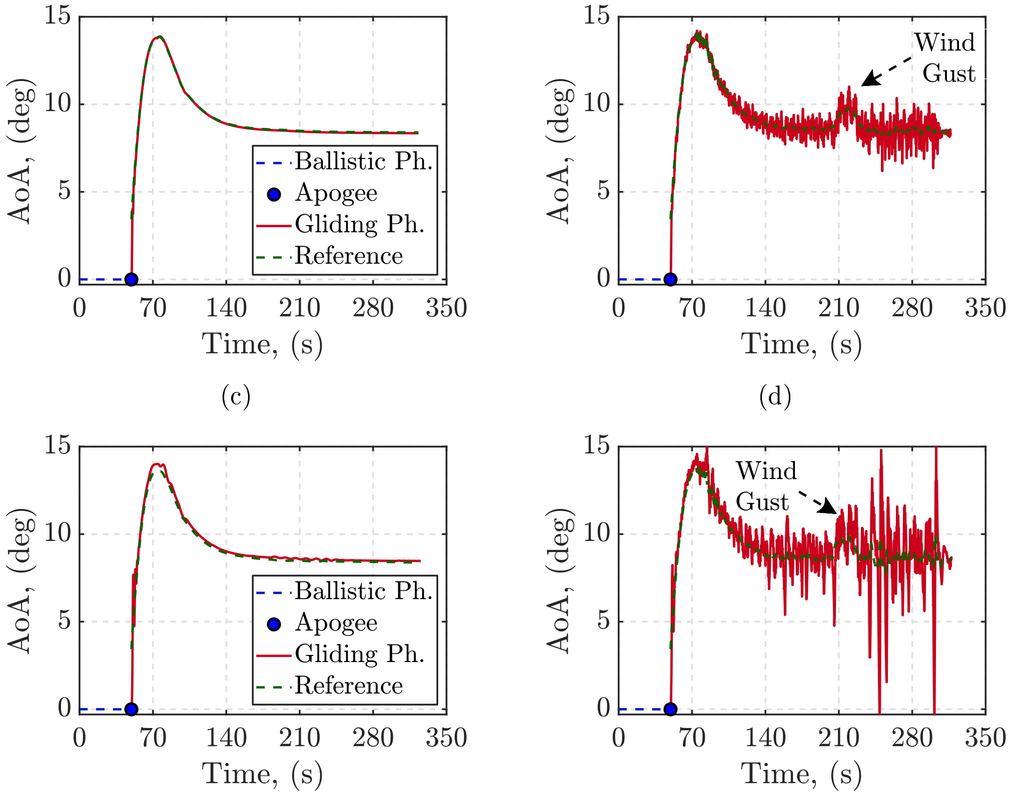

(c) (d)

(e) (f)

Figure 6: Trajectoires nominales et perturbées respectivement liées aux : (a)-(b) contrôleur polytopique ; (c)-(d) contrôleur basé sur la grille.

Enfin, les performances des contrôleurs ont été testées par rapport à l'effet des perturbations variant dans le temps. Une première série de simulations de suivi de trajectoire nominale a été réalisée en mettant en œuvre les contrôleurs dans un environnement de simulateur non linéaire 6-DoF. Les simulations ont permis d'identifier la vitesse de tir et l'angle d'élévation optimaux (939 m/s, 60 deg). Dans un deuxième temps, des perturbations dues au vent ont été incluses dans les scénarios de simulation sous forme de turbulences continues et de profils de vitesse de rafales de vent discrètes. La comparaison des trajectoires dans la Figure 5 montre comment les perturbations dues au vent affectent la capacité de portée du projectile en réduisant légèrement la distance maximale atteignable. De plus, les résultats de la Figure 6 confirment la robustesse des contrôleurs polytopique et basé sur la grille dans la gestion des oscillations de signaux importantes générées par la turbulence du vent. Malgré les oscillations, les systèmes parviennent à suivre avec succès le signal de AoA de guidage de référence sur toute la trajectoire. En ce qui concerne le contrôleur polytopique, les trajectoires des fonctions de planification perturbées se situent dans l'espace convexe utilisé lors de la synthèse du contrôleur, assurant ainsi la stabilité du système en boucle fermée même en présence de signaux de perturbation importants. Le contrôleur basé sur la grille a également réussi à préserver la stabilité du projectile sur toute la trajectoire, même si les paramètres de vol obtenus sont généralement affectés par des oscillations plus importantes autour de leurs valeurs nominales.

Conclusions et Perspectives

Cette thèse a étudié l'utilisation des techniques à paramètres linéaires variant (LPV) pour la modélisation et la conception de contrôle d'un nouveau concept de projectile guidé à longue portée (LRGP). Le développement d'une munition à portée étendue vise à combler l'écart technologique entre les projectiles balistiques/guidés lancés par canon standard et les applications de missiles à propulsion par fusée plus sophistiquées. Une contribution importante réside dans la caractérisation de la dynamique de vol/aérodynamique du nouveau concept de projectile et dans la proposition d'une procédure complète dédiée à la reformulation du modèle LPV. De plus, l'utilisation réussie de différentes approches de conception de contrôle basées sur LPV (polytopique, basée sur grille) a confirmé les avantages fournis par le cadre LPV pour ces technologies spécifiques, malgré la quantité limitée d'applications proposées dans la littérature.

Les résultats obtenus à travers les processus de modélisation LPV et de conception de contrôle suggèrent également plusieurs points d'amélioration possibles :

- **Régression Aérodynamique :** Le modèle aérodynamique pourrait être davantage développé en exploitant la dépendance des coefficients aérodynamiques par rapport à la variation de Mach.
- **Variables de Référence :** Le choix de l'angle d'attaque aérodynamique (AoA) comme variable de planification représente un choix assez inhabituel car des mesures précises nécessitent une instrumentation dédiée. La reformulation du modèle de vol du projectile en termes de dynamique d'accélération pourrait simplifier le processus de mise en œuvre.
- **Approche de Modélisation LPV :** Des techniques de modélisation alternatives pourraient être envisagées pour assouplir les contraintes imposées par l'approche de transformation d'état.
- **Définition du Polytope :** Une reformulation de la forme du polytope pourrait améliorer les performances de la conception du contrôle. Cela pourrait être réalisé en changeant de variables, en définissant le polytope autour de la trajectoire prévue du projectile.
- **Sélection de la Grille :** L'utilisation des fonctions MATLAB LPVTools pour la conception impose la définition d'une grille rectangulaire/cubique, ce qui peut entraîner l'inclusion de conditions de vol indésirables. Une reformulation appropriée du problème d'optimisation des LMI pourrait permettre de relâcher les contraintes de forme imposées par LPVTools.
- **Contrôleur Latéral :** La modélisation LPV et la conception de contrôle pourraient être étendues pour tenir compte de la dynamique de roulis et de lacet du projectile, permettant la mise en œuvre d'une stratégie de vol complète de virage sur l'aile.

List of Figures

List of Tables

Table of Acronyms

AoA	*Angle-of-Attack*
AoS	*Angle-of-Sideslip*
BTT	*Bank-To-Turn*
CCF	*Course-Corrected Fuze*
CFD	*Computational Fluid Dynamics*
CL	*Closed-Loop system*
CM	*Center of Mass*
CP	*Center of Pressure*
DCM	*Direction Cosine Matrix*
DKM	*Disk Margin*
DoF	*Degrees-of-Freedom*
GM	*Gain Margin*
GNC	*Guidance, Navigation & Control*
GPS	*Global Positioning System*
GR	*Grid-Based*
INS	*Inertial Navigation System*
ISA	*International Standard Atmosphere*
IMU	*Inertial Measurement Unit*
LDR	*Lift-to-Drag Ratio*
LF	*Load Factor*
LFT	*Linear Fractional Transformation*
LMI	*Linear Matrix Inequality*
LPV	*Linear Parameter-Varying*
LR	*Linear Regression*
LRGP	*Long Range Guided Projectiles*

LTI	*Linear Time-Invariant*
MIMO	*Multiple Inputs Multiple Outputs*
MM	*Modulus Margin*
MoI	*Moment of Inertia*
MPC	*Model Predictive Control*
MR	*Multivariable Regression*
NDI	*Nonlinear Dynamic Inversion*
NED	*North-East-Down*
NL	*Nonlinear Systems*
NP	*Nominal Performance*
NRMSE	*Normalized Root Mean Square Error*
NS	*Nominal Stability*
PGK	*Precision Guidance Kit*
PGM	*Precision Guided Munition*
PM	*Phase Margin*
PR	*Polynomial Regression*
PY	*Polytopic*
quasi-LPV	*quasi-Linear Parameter-Varying*
RMSE	*Root Mean Square Error*
RP	*Robust Performance*
RS	*Robust Stability*
SDP	*Semi-Definite Programming*
SISO	*Single Input Single Output*
SOCBT	*Secant Ogive Cylinder Boat Tail*
TA	*Taylor Approximation*
s.t.	*such that*
w.r.t.	*with respect to*

Nomenclature

General Notation

x	Scalar value
$\boldsymbol{x}$	Vector
X	Matrix
$\boldsymbol{x}^{\mathrm{T}}$(or X^{T})	Transpose of $\boldsymbol{x}$ (or X)
$\boldsymbol{x}^{-1}$(or X^{-1})	Inverse of $\boldsymbol{x}$ (or X)

Tensor Algebra Notation

$\boldsymbol{x}$	Vector (tensor form)
$\boldsymbol{X}$	Matrix (tensor form)
$[\star]^{B}$	Projection w.r.t. the coordinate system B

Control Notation

$\mathbb{R}$	Real values set
$\mathbb{C}$	Complex values set
X^{T}	Transpose of $X \in \mathbb{R}$
X^{*}	Conjugate of $X \in \mathbb{C}$
$X \succ (\succeq) 0$	Symmetric and positive (semi)definite matrix
$X \prec (\preceq) 0$	Symmetric and negative (semi)definite matrix
$(\star)^{\mathrm{T}}$	Conjugate (or transpose) element of a matrix $\in \mathbb{C}$ ($\in \mathbb{R}$)
$\mathrm{Co}(\Gamma)$	Convex hull of the set Γ
$\mathcal{A}, \mathcal{B}, \mathcal{C}, \mathcal{D}$	System state space matrices
$\mathcal{F}_l(\star, \star)$	Lower linear fractional transformation
$\mathcal{F}_u(\star, \star)$	Upper linear fractional transformation
$\bar{\sigma}(X)$	Maximum singular value of X

Introduction

Contextualization

The Advent of Guided Missiles Technologies

The development of sophisticated missiles (ballistic and cruise) and artillery munitions technologies has represented a statement of power since their early design. Ballistic missiles are generally rocket-propelled only in the initial ascending phase of their trajectory (boost), between the launch to the apogee stage. They can be considered a range and power extensions of standard cannon-launch artillery munitions in reason of the larger dimensions and the capability to deliver different payload (explosive, nuclear, chemical, and biological warhead). Cruise missiles are powered by air-breathing jet engines along the entire flight, and are characterized by a lower regime (subsonic or transonic) atmospheric flight, relying on aerodynamic lift for trajectory flight control.

With the beginning of World War II, a significant effort has been dedicated to the enhancement of missiles' accuracy and range performance. The first employment of jet-propelled missiles, such as the German Vergeltungswaffen-1 (V-1 cruise missile) ([Gil44]; [Zal11]) and Vergeltungswaffen-2 (V-2 ballistic missile) ([Dor63]; [Zal13]) in 1944–1945, with an operating range of about 300 km, initiated a new rush for the technological supremacy among the most influential nations, leading to the development of the Sovietic R-1 SS-1 *Scunner* (300 km range) in 1958, and the first multistage intercontinental ballistic missile (ICBM) R-7 *Semyorka* (8000 km range) in 1957 ([Afa98]). As a response, between 1959 and 1965, the US short-range ballistic missile (SRBM) MGM-52 *Lance* ([Gro17]), the medium-range ballistic missile (MRBM) PGM-19 *Jupiter*, and the intermediate-range ballistic missile (IRBM) PGM-17 *Thor* ([CA91]) became operational, followed by the series of ICBM missiles SM-65 *Atlas* D-E and F (12000 km range) ([Sor60]; [Genb]; [Gena]), and the SM-68 *Titan* I-II (10000 km range) ([Stu00]). Meanwhile, similar short-range weapons were tested in France (AMX 30 *Pluton* missile ([Gal76])), in the Soviet Union (SS-21 *Scarab* [PS90]), and China (SRBM SS-2, MRBM CSS-1, IRBM CSS-2, and ICBM CSS-4 *Dong Feng* series ([Pra89])).

During the Cold War, range capability represented a core deterrent of power balance, resulting in the design of increasingly sophisticated weapons, such as the series of ICBM LGM-30 *Minuteman* I, II, III between 1962-1975 ([MC65]; [Hee12]), providing a maximum operating range of 13000 km, and equipped with an inertial navigation system (INS). The limited accuracy of early guidance technologies was soon balanced through the deployment of large-scale warheads (weapons of mass destruction (WMD)), ensuring the accomplishment of extremely long-range missions. The intensification of global tension around WMD employment lead to the establishment in 1987 of the Missile Technology Control Regime (MTCR) ([Ozg94]), with the core intention of limiting the proliferation of missile technologies, especially towards nuclear weapons development. The negotiations between the US and the Soviet

Union, officially referred to as the Strategic Arms Limitation Talks (SALT I-II) ([Sma70]) held between 1969-1979, culminated in the Intermediate-Range Nuclear Forces Treaty (INF) of 1987 ([Kno93]), with the intent to limit the employment of nuclear warheads. Between 1991-1997 the Strategic Arms Reduction Treaty START I-II-III ([OPB96]) began the process of nuclear demilitarization, finalized with the Strategic Offensive Reductions Treaty (SORT) of 2002 ([WFAT03]). These international agreements have been later renovated in 2010 with the New Strategic Arms Reduction Treaty (New START), stipulated between the Russian Federation and the US. However, the interest of the most influential nations to maintain a dominant role in geopolitical warfare often resulted in the refusal of treaties concerning the limitation of weapons range and power capability. Recently in 2023, with the begin of the war between Russia and Ukraine, Russia declared the suspension of its participation in the New START ([Bug23]).

The limitation imposed by the international treaties encouraged focusing the attention on the development of shorter-range tactical missile programs. Additionally, the accuracy and precision enhancements guarantee higher on-target effectiveness in military offensive and interception missions, and consequentially significantly lower operating costs. The advent of more advanced guidance technologies boosted the employment of ballistic missiles and cannon-launched artillery munitions as conventional weapons. Early trajectory-tracking guidance strategies were accomplished through radar or optical measurements from the launch site, while radio or laser control commands were transmitted by a ground operator. Guidance accuracy improved through the employment of television cameras and laser beams for target interception. In the 1950s, INSs began to be installed on long-range ballistic missiles, and later on tactical artillery-guided munitions in the 1970s, through the development of more advanced and cheaper electronic components.

Inertial navigation relies on the employment of accurate gyroscope and accelerometer measurements to estimate the position, heading, and velocity of missiles along their trajectory. The absence of electronic emissions in INSs represented a core advantage compared to alternative technologies, being more difficult to be identified. In 1986 the *Minuteman* IIIs were replaced by the more advanced US MX *Peacekeeper* missile ([Mac87]), equipped with INSs and an exterior celestial navigation system that used the stars or satellites as a reference to estimate the missile's position. The TERrain COntour Matching navigation technique (TERCOM) ([Gol80]) was later employed on the submarine-launched cruise missile (SLCM) *Tomahawk* and on its ground-launched versions (GLCM), the BGM-109G *Gryphon* ([Kop05]), where trajectory corrections were evaluated by means of digitalized contour maps obtained from radar measurements. Modern navigation systems incorporate advanced Global Navigation Satellite Systems (GNSSs) tracking technologies as the Global Positioning System (GPS), or the Global Navigation Satellite Systems (GLONASS), to complement the performance of standard INSs. Infrared seekers, radar, and optical gyroscopes generally provide more precise information during on-target fast-homing maneuvers.

The Development of Precision Guided Munition

The first examples of precision guided munition (PGM) or 'smart munition' can be traced during World War II in the German radio-controlled gliding bomb Ruhrstahl SD1400X (*Fritz X*) ([PP97]), employed in parallel with the V-1 and V-2 missiles by the Luftwaffe to hit enemy battleships. The proven effectiveness in the battlefield, in contrast with the standard unguided weapons, encouraged the broadening of PGMs to more versatile ground launchers as tank, mortar, and howitzer (such as the U.S. M109A6/A7 *Paladin* and the French Camion Équipé d'un Système d'Artillerie (CAESAR)). In addition, the constraints imposed in the 1970s with the SALT I, and advances in microprocessors and microelectronics development increased the interest in cannon-launched ammunition characterized by appealing lower production costs and increasingly higher performance in terms of accuracy and operating range. Differently from most of the long-range ballistic missiles, guided munition trajectories lie in the lower atmosphere and rely on aerodynamic lift-based corrections imposed through the employment of aerodynamic surfaces (tail-fins/rudders, nose-mounted canards, wings-flaps, and elevators) ([CA00]; [DM08]; [SC10]; [Fre11]; [CFC12]). This solution provides with higher control authority for the autopilot design, as well as a continuous-time trajectory correction [Wr98] compared to more complicated systems relying on thrust vectoring ([JC01]; [GC02]; [BPC02]; [CWB11]), or inertial effectors ([Mur78]; [HJ89]; [FC06]; [RC08]).

The airframe stability of aerodynamic-controlled ballistic munitions is generally addressed at the design stage by selecting among two main approaches: spin-stabilization or fin-stabilization. The former architecture takes advantage of the aerodynamic forces and moments generated by the high spin rate characterizing the body roll axis, which is transmitted to the projectile at the firing stage. A relevant advantage of spin-stabilized technologies relies on the possibility of retrofitting existing unguided munitions with course-corrected fuzes (CCFs) to implement guidance and control strategies. Successful applications correspond to the U.S. ATK's M1156 Precision Guidance Kit (PGK) ([PBC07]; [Sto08]), the French Système à Précision Améliorée par CInémomètre DOppler (SPACIDO) ([Cam07]), the U.K. Smart Trajectory Artillery Round (STAR) ([GL08]; [GL09]), and the European Correction Fuze (ECF) ([Per11]). In the last decades, relevant research contributions have been carried out also at the French-German Research Institute of Saint-Louis (ISL) through the studies of Course Correction Fuze (CCFus project) projectile systems ([TW11]; [TMW11]; [TSW15]; [Sev+17]; [Tha+19]; [Tip+20]; [Pin+22]). Nevertheless, the spin-stabilized architecture presents significant drawbacks deriving from the high spin rate characterizing the projectile. Indeed, the spin generates undesired nonlinear couplings between the normal and the lateral axes dynamics ([LB79]), which can represent a non trivial challenge to face during the flight control design. Additionally, spin-stabilized projectiles generally suffer from a limited operating range, depending on the capability of the firing gun and the firing conditions.

The aerodynamics of fin-stabilized munitions is closer to standard ballistic missiles, where the employment of a non-spinning concept reduces the highly nonlinear dynamics generated by the aerodynamic coupling terms, simplifying the general flight dynamics modeling stage. However, it requires specific tail-fins configurations for stability augmentation, which can increase the design and development expenses. Several applications have been already proposed by different countries, such as the U.S. laser-guided artillery round M712 *Copperhead* ([MA77]; [NPM79]), the more recent 155 mm GPS-guided munition M982 *Excalibur* ([Wel00]), the XM395 Precision Guided Mortar Munition (PGMM) ([Mal+08]), the Italo-German long-range GPS/IR guided munitions *Vulcano* (B-C), the French semi-active laser guidance kit under the Metric Precision artillery Ammunition demonstrator (MPM) program, and the Russians 120 mm guided mortar weapon system KM-8 *GRAN* and laser-guided projectile 30F39 *Krasnopol* ([Gra05]). The autopilot design of fin-stabilized munitions can be generally performed separately for each single axis ([Bla91]), and the projectile aerodynamics is generally less affected by large and rapid variations of the flight parameters.

The continuous development in guided munitions technologies observed in the past decades has been boosting the research competition between the most influential countries worldwide. The further enhancement of the range and accuracy performance, under the minimization of the development design costs (e.g. the avoidance of any modifications of the existing firing guns), implies the investigation of innovative aerodynamic configurations and flight control strategies. A promising solution could be identified in a novel fin-stabilized architecture with a reduced number of control actuators, investigated at ISL, aiming to ameliorate the range capability through a gliding steered flight. Early studies have revealed the advantages provided by fin-stabilized design compared to spin-stabilized systems ([Cha+17]), suggesting the employment of glider-like projectile configurations in combination with Bank-To-Turn (BTT) flight strategies. Interesting properties of the analyzed concept derive from selecting a reduced set of control actuators, leading to an asymmetric canards/fins configuration ([Fre11]; [CFC12]) and a predominant statically unstable behavior. Additionally, recent research on long-range guided projectiles ([Vas+20]) underlined the impact of the canards/fins configuration, aerodynamics modeling, and guidance development on the overall range capability.

Guided Munitions Design

The Guidance, Navigation & Control Design Loop

The design of guided weapons consists of the definitions and cooperation of three different functionality: Guidance, Navigation & Control (GNC). The standard GNC double-loop implementation is represented in Figure 1. A faster inner loop updates the control commands evaluated by the autopilot based on the information provided by the navigation algorithm, while a slower outer loop updates the reference signals generated by the guidance law to accomplish the requirements of the mission.

Guidance. Consists of optimization algorithms that determine the reference signals that have to be followed by the vehicle to accomplish a predefined objective, depending on the selected mission. The guidance law relies on the information provided by the navigation system in terms of available measurements or estimated parameters, determining the current state of the vehicle. Guidance systems differ generally by the technology they rely on and the type of target they aim to. Classical approaches implement onboard guidance computers (called 'homing' guidance) to hit moving targets through proportional navigation principles ([Gue71]; [KPT13]), or active/passive homing systems employing radar and infrared seekers ([Wal02]; [VM82]). When aiming at a fixed target, no trackers are generally required and the information on the target positions is known a priori. In this scenario, navigational guidance systems provide a continuous self-evaluation and correction of the vehicle trajectory based on the known location of the target. Typical examples are the aforementioned inertial guidance (employing gyroscopes and accelerometers) ([Bra+13]), astro-inertial guidance (based on celestial navigation [AZF06]), and terrestrial guidance (as the TERCOM [Gol80]). Additionally, guidance laws can be categorized w.r.t. the specific phase of the trajectory they are engaged for (mid-course guidance, terminal guidance), characterized by different objectives (e.g. range optimization, target interception) and reference signals (e.g. accelerations, body rates).

Navigation. Implements sophisticated algorithms for an accurate estimation of the current state of the vehicle in time (in terms of position, heading, velocity). Navigation systems rely on the available sensors' measurements relative to fixed/relative reference targets or track the relative position from a priori known point. Additionally, advanced algorithms are generally developed to estimate unmeasured information, based on sensor data fusion (as in Kalman filters [Her17]). A typical technology embedded in ballistic missiles consists of inertial measurement units (IMUs) allowing for inertial dead-reckoning navigation strategies, where the position is estimated through inertial acceleration measurements ([OFS98]; [Tit+04]). More advanced navigation systems employ GNSS, radar, and infrared measurements, depending on the operational requirements of the vehicle ([Ohl+97]; [Qua+15]). Sensor data fusion algorithms represent a common strategy often used also to correct individual measurements from external noise sources.

Control. The control design accounts for the current state information provided by the navigation systems to determine the optimal control actions to be set on the available actuators thus to implement the desired guidance strategy. In early guided systems, the control actions were performed by ground operators at the launch site, and transmitted to the vehicle by means

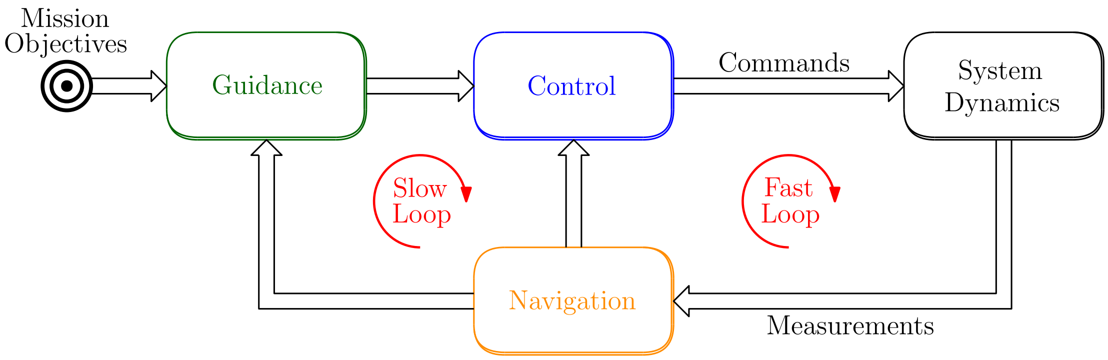

Figure 1: Guidance, Navigation, and Control (GNC) double-loop design.

of radar or laser signals. With the advent of electronic embedded systems, onboard autopilots have been designed to implement completely autonomous or semi-autonomous guided vehicles. The autopilot design relies on the development of dedicated control-oriented models of the system dynamics, characterizing the stability and performance of the system. The amount and the type of actuators installed on the system, determine the allocation strategy (static or dynamic) selected to implement the control command. This aspect strongly affects the capability of the system to perform certain maneuvers (control authority), and consequently the overall optimal control law design.

Autopilot Design Approaches: the Gain-Scheduling Control Strategy

Concerning aerospace applications, modeling and control design has always represented a tedious process to be accomplished. The high non-linearity characterizing vehicles' flight dynamics and the large variety of operational parameters to account for increase significantly the complexity of the design. Thus, an exhaustive analysis of the behavior of the system under investigation is required. Indeed, the derivation of an effective control law strongly relies on the accuracy of the model selected to represent the system dynamics. Nonetheless, the complexity of the control-oriented model affects the selection of the most appropriate control approach and eventually the numerical burden of the controller implementation. Thus, a proper trade-off between complexity and accuracy needs to be achieved. Furthermore, dealing with missile and projectile technologies implies a generally limited availability of control effectors (and related authority), combined with a larger variation of the flight parameters characterizing the typical ballistic trajectory, exploding the complexity of the overall design process.

Aiming to withstand a wide set of flight conditions, the operating domain of ballistic missiles and projectiles is composed of a selected set of parameters such as Mach number, $\mathcal{M}$, altitude, h, and angle-of-attack (AoA), among others. The resulting subspace of the flight envelope is represented as a grid of targeted operating points, as shown in Figure 2(a). Several control design approaches can be employed for autopilot synthesis at the targeted conditions. Nonlinear techniques based on feedback linearization gained popularity in the last decades in reason of the possibility to directly account for the nonlinearities of the system dynamics. Nonlinear dynamic inversion (NDI) methods have been successfully used on a wide range of missile and projectile applications ([Tip+20]; [Pin+22]; [Pin+23]; [Pfi12]) in combination with adaptive and robust approaches, depending on the addressed scenario. However, the linear time-invariant (LTI) framework still provides a broader range of design techniques and analysis tools, thanks to the intrinsic properties characterizing linear system theory. In order to exploit these properties, the nonlinear dynamics of flying vehicles is commonly linearized at targeted flight conditions (series expansion linearization), resulting in a collection of local linear representations of the original model. This method allows for employing linear control design techniques for autopilot synthesis.

In this context, a well-established strategy consists of decomposing the overall control task into the design of local LTI controllers at each local linearization of the original nonlinear dynamics. The resulting set of local LTI controllers can be easily implemented through the

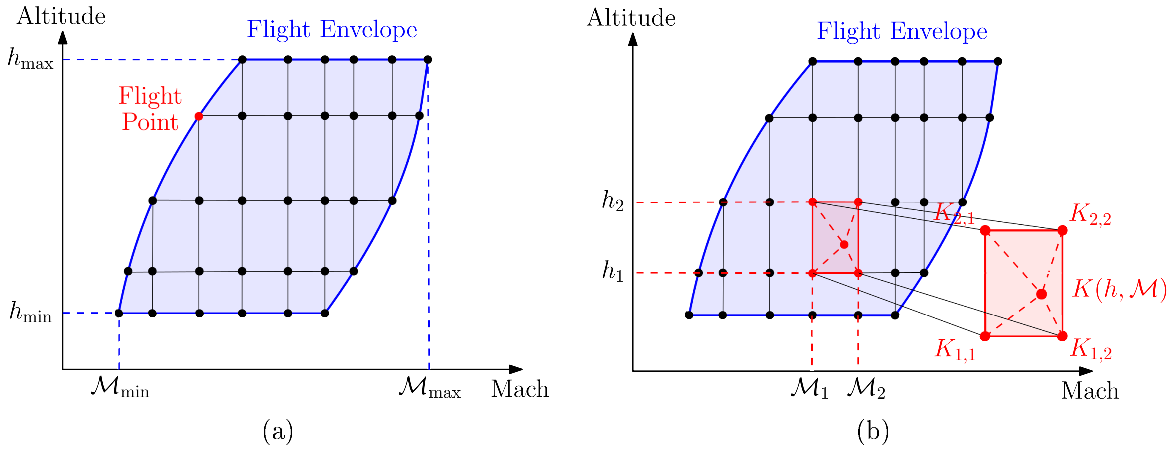

Figure 2: Gain-scheduling: (a) flight envelope parametrization; (b) controller, K, linear interpolation.

definition of a dedicated scheduling strategy, which allows selecting the most appropriate controller at any operating condition. The most traditional scheduling strategy relies on the linear interpolation of the local controllers' static gains, referred to as the gain-scheduling approach. As shown in Figure 2(b), depending on the flight parameters designated as scheduling variables, a controller, K, is obtained at any flight conditions in the operating envelope as the linear interpolation between the designed set of local LTI controllers ([HG93]; [NRR93]). A relevant advantage related to this strategy consists of the possibility of employing any control technique for the design of the local controllers. First developed in the 1960s the gain-scheduled control became a popular strategy in the 1990s ([SA90]; [Rug90]; [LL00]; [RS00]), leading to successful applications in the aerospace environment. Concerning the military sector, early examples of gain-scheduling design can be traced in the Nike Ajax missile, where the gain of the fin control system and roll autopilot were scheduled via dynamic pressure measurements, or the Talos missile ([Pad82]), implementing an altitude-based gain-scheduling system.

In the last decades, several missile/projectile technologies have relied on the gain-scheduling strategy, in reason of its high versatility to be complemented with advanced design approaches and implementation ease. Interesting $\mathcal{H}_\infty$-based applications can be found in [LSZ14]; [LSZ16], and in [BGL22]; [GB22]; [GA13] where alternative tuning approaches are proposed to optimize the control design process. Significant contributions have been investigated also at ISL through the development of gain-scheduled strategies for robust $\mathcal{H}_\infty$ autopilot design ([TD09]; [TSW15]; [TP21]; [Str+18]; [ST19]), loop-shaping techniques ([Sèv+14]; [Sè+17]), and anti-windup strategies ([Tha+20]; [Tha+23]).

Thesis Motivations

Despite a broad range of successful applications, gain-scheduling design has been proven to present important theoretical and practical limitations, which are discussed in the following:

I. **Accuracy.** From the modeling perspective, standard linearization-based gain-scheduling design is performed on a collection of LTI local linearizations of the original nonlinear system dynamics, at selected operating conditions (equilibrium points or trajectories). As a consequence, the linearized models provide only locally reliable representations of the nonlinear system, leading to the possible loss of important information regarding the system's transient behavior. Alternative approaches, implementing a velocity-based linearization, attempted to partially preserve the dynamic properties of the nonlinear system ([LL98]).

II. **Stability.** Concerning the control design, several approaches can be employed for the synthesis of local controllers based on the set of LTI linearizations of the system dynamics. However, in reason of the local validity of the LTI models, the obtained controllers ensure only local closed-loop stability guarantees in the vicinity of the selected flight points. Thus, no a priori guarantees about the stability and the performance of the local controllers' interpolation are provided at generic flight conditions across the envelope. Typical solutions to this problem rely on frozen-time theory, where the variation of the scheduling parameters across the equilibrium points is assumed 'slow enough' such that local stability properties are preserved ([KK91]; [LR90]). However, the slow-variation assumption can be extremely conservative for many application scenarios, since the guaranteed stability properties correspond to the worst-case robustness of the overall collection of LTI local systems ([SA90]; [SA92]).

In the aerospace sector, a widespread design solution consists of extending the linearization on a dense grid of conditions, and a posteriori, testing the controller robustness on a much denser grid. Nevertheless, this process requires time and high computational power since it generates a large number of local controllers to be implemented for the interpolation.

In the last decades, the linear parameter-varying (LPV) framework has attracted increasing interest in the modeling and control of a wide range of aerospace applications. Early studies in the 1990s proposed the LPV modeling approach as a perfect match for the gain-scheduling control design technique, leading to relevant contributions concerning missile ([SC93]; [CS96]; [PPV01]; [TPB00]) and aircraft ([Bal+97]; [YWA13]; [HSB14]) applications. Differently from linearization-based approaches, the LPV gain-scheduling design directly targets the synthesis of the overall controller, providing closed-loop stability properties in a global sense. Furthermore, LPV/quasi-LPV models can account for the time variations of a selected set of parameters, which results into a higher capability in capturing the nonlinear system dynamics ([MB04]; [PH11]; [PVR12]). The LPV controller synthesis is achieved through the resolution of an optimization problem formulated as a set of linear matrix inequalities (LMIs). The problem formulation can be accomplished either by exploiting the features of parameter-affine systems, or by discretizing the parameters space by means of a gridding process. The former solution (polytopic) provides higher guarantee of quadratic stability of the closed-loop system, at the expenses of more conservative performance ([ABG95]; [AGB95]). The latter (grid-based) stands as a natural extension of the standard gain-scheduling design to the LPV framework, providing significant performance together with higher implementation complexity and lower global stability properties ([WPB95]; [Wu+96]).

Several studies have also focused on the investigation of guided projectile technologies. LPV modeling has been coupled with $\mathcal{H}_\infty$ robust control design for spin-stabilized ([Sèv+14]; [The+13]; [TSW15]; [The+10]), and fin-stabilized ([Str+18]; [ST19]) projectiles' architectures. However, the LPV models were generally obtained as a family of local linearizations of the original nonlinear dynamics, while the control strategy relied on standard gain-scheduling autopilot interpolations. Only recently, an LPV approach has been developed in the framework of model predictive control (MPC) ([BG22]). The proven advantages characterizing the LPV class of systems, in contrast with the still limited amount of applications concerning guided munitions design, open several opportunities for further investigations. Additionally, the development of more sophisticated algorithms and more powerful tools for the resolution of complex LMIs optimization problems allows the design of controllers of increasing performance.

The above introduction consists of a non-exhaustive overview of the state-of-the-art concerning aerospace control technologies and LPV design applications. A dedicated discussion is provided in the introduction of each chapter of the manuscript.

LRGP Project and Thesis Objectives

The proposed thesis is part of the Long Range Guided Projectile (LRGP) *contract de subvention (CS)* begun in 2018 as a collaboration between the Direction Générale de l'Armement (DGA) and the French-German Research Institute of Saint-Louis ([Mar+18]; [Lib+19]; [Lib+20]; [Lib+21]). The core intent of the LRGP project relies on the range enhancement of standard low-cost 155 mm artillery projectiles, accounting for the minimization of the necessary time of flight. In this context, the thesis focuses on the projectile flight dynamics modeling and the LPV-based autopilot design, employed during the guided phase of the projectile trajectory to track a range extension guidance law. The main objectives of the thesis can be summarized as follows:

- Flight dynamics modeling of the new LRGP concept, including a complete aerodynamic characterization of the projectile.
- Development of a 6-DoF nonlinear simulator environment to test the performance of the projectile in multiple operating flight scenarios.
- Derivation of the LPV-based control-oriented model design of the projectile nonlinear dynamics without employing local linearization-based techniques.

- Investigation of different LPV-based robust controller design approaches for the development of a gliding phase autopilot, providing stronger guarantees of stability and performance compared to standard LTI gain-scheduling techniques.

- Implementation of a range extension guidance law based on a BTT flight strategy to improve the operating performance of the projectile.

- Assessment of the performance and the robustness of the designed autopilot in the nonlinear simulator through realistic operating scenarios.

Thesis Contributions

The project investigates the complete characterization of a new concept of guided projectiles studied at the Institute of Saint-Louis, addressing both the modeling and the control design stages. Particular focus is dedicated in the linking process among the two design stages, where the requirements of various autopilot design approaches are targeted from the system modeling perspective. The main contributions achieved during the development of the project can be summarized in the following categories:

LPV-based Flight Dynamics Modeling Contribution

I. **LRGP flight dynamics and aerodynamics modeling.** The flight dynamics model of a new concept of long range guided projectile was derived starting from the standard aerospace theoretical formulation, and implemented in a complete simulator environment. In particular, the full characterization of the projectile's aerodynamics has resulted in the proposition of a novel ad-hoc designed aerodynamic model which accurately represents the projectile's behavior across a large envelope of flight conditions.

   The complete formulation of the projectile nonlinear dynamics, including a dedicated section concerning the aerodynamics analysis and modeling process, is presented in Chapter 1.

II. **LPV modeling process of nonlinear flight dynamics.** A relevant aspect exhaustively discussed during the project consists of the non-trivial process of reformulation of the highly nonlinear projectile dynamics model as an accurate LPV system. Depending on the selected approach, multiple LPV models can be obtained from the same nonlinear system, exploiting different properties and features. Thus, a careful selection of the most appropriate varying parameters to be accounted for requires an accurate analysis of the system's behavior combined with the prior definition of the control design objectives.

   The LPV modeling design of the projectile nonlinear dynamics is discussed in Chapter 2, where the employment of the state transformation approach allows deriving a reliable LPV model of the projectile pitch channel dynamics.

LPV-based Flight Control Design Contribution

III. **Polytopic LPV $\mathcal{H}_\infty$ control design for guided projectiles.** The polytopic approach represents a well established LPV control design technique that has been employed for various applications to overcome the limitations of the standard LTI gain-scheduling design strategy. In the aerospace environment it has shown successful results in the autopilot synthesis for several applications. However, few investigations have dealt so far with trajectory tracking scenario of guided projectiles, covering a large range of flight conditions. Indeed, the conservativeness characterizing the polytopic formulation requires an accurate modeling and control design to ensure stability and satisfactory performance across the entire flight envelope targeted in the polytope definition.

The polytopic model analysis and formulation is presented in details in Chapter 2, while Chapter 3 discusses the corresponding autopilot design and robustness properties. Additionally, a robustness analysis and trajectory tracking simulations are proposed in Chapter 4 to assess the performance of the controller in the nonlinear simulator environment.

IV. **Uneven grid-based LPV $\mathcal{H}_\infty$ control design for guided projectiles.** LPV grid-based design consists of a more recent alternative solution for controller synthesis. It allows relaxing the conservativeness affecting the standard polytopic approach by gridding the parameter space. In particular, it ensures stability properties through the identification of a set of parameter-dependent Lyapunov functions. However, the dimensions of the grid represent a critical aspect concerning the computational complexity of the controller synthesis. Thus, an accurate analysis of the flight envelope is required to properly select the operating conditions to be accounted for during the control design.

In Chapter 3, a modeling procedure is developed to analyze the properties of the projectile dynamics across the gridded parameters space to reduce the complexity of the autopilot synthesis. The assessment of the controller robustness and performance is presented in Chapter 4, through the implementation of multiple simulation scenarios in the nonlinear simulator environment.

Manuscript Outline

The proposed manuscript is organized into two core parts:

- Part I: is dedicated to the complete modeling procedure of the projectile dynamics, from the nonlinear flight dynamics derivation to the control-oriented LPV model design.
    - Chapter 1: concerns the formulation of the nonlinear dynamics of a new class of guided projectiles (LRGP). A detailed aerodynamic characterization allows the derivation of a dedicated aerodynamic model for the new projectile concept. The modeling procedure is finalized through the development of a complete simulator environment.
    - Chapter 2: provides a general introduction to the LPV class of systems, including a brief overview related to the LPV modeling approaches. The nonlinear dynamics of the projectile is then converted into an accurate LPV system. The final control-oriented modeling step consists of the reformulation of the projectile LPV model as a polytopic parameter dependent system.
- Part II: deals with the LPV-based autopilot design of the guided projectile, through the comparison of two main approaches, and their final performance validation.
    - Chapter 3: details the control design based on two distinct LPV-based techniques: polytopic and grid-based. A general overview recalls the fundamental concepts concerning the LPV controller synthesis processes through the formulation of LMIs based optimization problems. For each design approach, the controller synthesis performance are improved by means of dedicated analyses that target the optimization of the related computational complexity.
    - Chapter 4: is dedicated to the main simulation results, consisting of realistic trajectory tracking scenarios. The performances of the designed LPV controllers are evaluated in the complete simulator environment addressing various sources wind disturbances. Additionally, stability margins and μ-sensitivity analyses provide a preliminary evaluation of the controllers robustness properties.

A final chapter is dedicated to the concluding remarks on the achieved results, and the proposition of possible future developments.

List of Publications

Journal Papers

Title: Linear Parameter-Varying Polytopic Modeling and Control Design for Guided Projectiles.
Authors: Vinco, G.M., Sename, O., Strub, G. and Theodoulis, S.
Journal: AIAA Journal of Guidance, Control, and Dynamics.
Status: Published, **Year:** 2024, **Volume:** 47, **Number:** 3, **Pages:** 433-447.

International Conference Papers with Proceedings

Title: Flight Dynamics Modeling and Simulator Design for a New Class of Long-Range Guided Projectiles.
Authors: Vinco, G.M., Theodoulis, S., and Sename, O.
Conference: 6th CEAS Conference on Guidance, Navigation and Control (EuroGNC 2022).
Venue: Berlin, Germany; **Date:** May 3-5, 2022.

Title: Quasi-LPV Modeling of Guided Projectile Pitch Dynamics through State Transformation Technique.
Authors: Vinco, G.M., Theodoulis, S., Sename, O., and Strub, G.
Conference: 5th IFAC Workshop on Linear Parameter Varying Systems (LPVS 2022).
Venue: Montreal, Canada; **Date:** September 27-30, 2022.

Title: Linear Parameter Varying Pitch Autopilot Design for a class of Long Range Guided Projectiles.
Authors: Vinco, G.M., Theodoulis, S., Sename, O., and Strub, G.
Conference: 2023 AIAA Science and Technology Forum and Exposition (SciTech Forum).
Venue: National Harbor, Maryland, US; **Date:** January 23-27, 2023.

Title: Uneven Grid-based Linear Parameter-Varying Controller Design for Guided Projectiles.
Authors: Vinco, G.M., Theodoulis, S., Sename, O., and Strub, G.
Conference: 22nd World Congress of the International Federation of Automatic Control (IFAC World Congress 2023).
Venue: Yokohama, Japan; **Date:** July 9-14, 2023.

International Workshops without Proceedings

Title: Flight Dynamics Modeling for Long Range Guided Projectiles (LRGP).
Authors: Vinco, G.M., Theodoulis, S., and Sename, O.
Conference: Novelties in Guidance, Navigation and Control (e-EuroGNC 2021).
Venue: Online; **Date:** October 7, 2021.

National Conferences and Workshops without Proceedings

Title: Flight Dynamics Modeling for Long Range Guided Projectiles (LRGP).
Authors: Vinco, G.M., Theodoulis, S., Sename, O.
Conference: 10th Budding Science Colloquium at ISL
Venue: Saint-Louis, France; **Date:** September 27-28, 2021.

Title: Quasi-LPV Modeling and Control of Projectile Pitch Dynamics through State Transformation Technique.
Authors: Vinco, G.M., Sename, O., Theodoulis, S., and Strub, G.
Conference: Journées de printemps de la SAGIP 2022.
Venue: Bidart, France; **Date:** May 23-25, 2022.

Title: Uneven Grid-based Linear Parameter-Varying Controller Design for Guided Projectiles.
Authors: Vinco, G.M., Theodoulis, S., Sename, O., and Strub, G.
Conference: [CT CPNL] Premier congrès annuel de la SAGIP.
Venue: Marseille, France; **Date:** June 7-9, 2023.

Title: Grid-based Linear Parameter-Varying Controller Design for Guided Projectiles.
Authors: Vinco, G.M., Strub, G., and Sename, O.
Conference: 12th Budding Science Colloquium at ISL
Venue: Saint-Louis, France; **Date:** September 27-28, 2023.

Part I

Projectile Modeling Design: From the nonlinear to the LPV-based model formulation

CHAPTER 1

Flight Dynamics Modeling

Contents

1.1 Introduction

The modeling process of system dynamics represents the most crucial stage prior to the controller design. Indeed, a proper identification and description of the system behavior improves the reliability of the mathematical model and enhances the effectiveness of the controller. However, an excessively detailed model would explode the complexity of the controller design with the risk of diminishing the achievable performance or making it unfeasible for any practical implementation. As a consequence, a compromise between accuracy and complexity is generally required. A common practice consists of the derivation of simplified model dynamics dedicated to the controller design, capturing only the most relevant features that affect the targeted controller performance. A detailed and exhaustive model of the system dynamics is eventually employed to test the controller design in a more realistic simulation scenario.

This chapter provides an overview of the complete derivation of the model dynamics for the new class of Long Range Guided Projectiles (LRGP) investigated at the Institute of Saint-Louis (ISL) ([Mar+18]; [Lib+19]; [Lib+20]; [Lib+21]). The model includes a combination of measured physical properties (such as concept dimensions, shapes, mass, and inertia) and estimated parameters (aerodynamic coefficients). The first part of the chapter is dedicated to the general formulation of the projectile flight mechanics ([Zip14]), later applied to the LRGP concept. An overview of the LRGP project highlights the main objectives to be targeted and achieved through the system modeling and the following controller design. The second part of the chapter concerns the aerodynamic characterization of the projectile's concept. An exhaustive dataset of Computational Fluid Dynamic (CFD) simulations is acquired and then analyzed by employing selected regression models. The results are used to characterize the aerodynamic terms in the general flight mechanics model of the projectile. The final nonlinear model is implemented in a simulator environment meant to test the performance of the final controller design.

The chapter is structured in the following sections:

S1.2: concerns the derivation of the projectile translational and attitude dynamics and kinematics, first expressed in the more general tensor formulation and then projected in the proper coordinate systems. A detailed introduction to the LRGP concept highlights the most relevant physical properties accounted for in the modeling process.

S1.3: discusses the complementary aerodynamic characterization through the results of an exhaustive CFD analysis, leading to the derivation of two complete aerodynamic models of increasing complexity and accuracy. The results presented in this section have been published in [Vinb].

S1.4: presents the design of the simulator environment later employed for simulation purposes, which additionally targets the dynamics of the air variables characterizing the surrounding atmosphere and affecting the projectile flight performance. The results presented in this section have been published in [Vinb].

1.2 Flight Mechanics

This section is dedicated to the derivation of the nonlinear flight mechanic model characterizing the projectile dynamics. Section 1.2.1 first recalls the fundamental principles of the tensor algebra employed for the formulation of the projectile equations of motion. The main reference frames and their associated coordinate systems are presented in Section 1.2.2, while Section 1.2.3 discusses the general derivation of the projectile nonlinear model dynamics. Finally, Section 1.2.4 introduces the fundamental features of the LRGP concept and how they characterize the general nonlinear model dynamics.

1.2.1 Tensor Algebra

The dynamics of any physical phenomena is intrinsically independent from the metric system employed to observe them. Accordingly, the derivation of the dynamic equations governing the behavior of a flying vehicle has to be expressed in a coordinate invariant form that can be adapted to any suitable metrics. This concept is formalized in the following distinction:

Definition 1.1 (Frame)
Physical entity constituted by a continuous set of a minimum of three noncollinear points having mutually time invariant distances in the 3D Euclidean space. The location and the orientation of a reference frames are defined by a base point, A, and a triad of orthonormal base vectors:

$$\boldsymbol{a}_1, \boldsymbol{a}_2, \boldsymbol{a}_3 \quad \textit{with} \quad \boldsymbol{a}_i^{\mathrm{T}} \boldsymbol{a}_j = \begin{cases} 0 & \textit{for} \quad i \neq j \\ 1 & \textit{for} \quad i = j \end{cases}; \quad i, j = 1, 2, 3.$$

Definition 1.2 (Coordinate System)
Ordered set of numbers (scalar coordinates, $]^A$) that associates a specific vector with the 3D Euclidean space, based on a orthogonal triple of directions (1^A, 2^A, 3^A). Specifically, a Cartesian coordinate system, is a a set of coordinates that satisfies the finite differences Cartesian metric:

$$\Delta s^2 = \sum_{i=1}^{3} \Delta x_i^2$$

where Δs represents a finite distance in the 3D Euclidean space and Δx_i^2 are mutually orthogonal elements.

Since a coordinate system does not refer to a specific physical quantity, several coordinate systems can be associated to the same frame. In particular, for each frame a *preferred* system of coordinates can be identified, whose directions are aligned with the base vectors of the frame, such that:

$$[\boldsymbol{a}_1]^A = \begin{bmatrix} 1 & 0 & 0 \end{bmatrix}; \qquad [\boldsymbol{a}_2]^A = \begin{bmatrix} 0 & 1 & 0 \end{bmatrix}; \qquad [\boldsymbol{a}_3]^A = \begin{bmatrix} 0 & 0 & 1 \end{bmatrix}.$$

The space-time invariance characterizing different frames and their interaction can be exploited by employing the mathematical tensors notation. Indeed, tensors are algebraic objects used to describe physical entities whose content is intrinsically independent from the coordinate system from which they are observed, as well as coordinate transformations invariant.

Definition 1.3 (Cartesian Tensors)
A ordered set of triples, $\boldsymbol{x}$, is a Cartesian vector (first-order tensor) if for any pair of allowable Cartesian coordinate systems, $]^A$, $]^B$, the following transformation holds:

$$[\boldsymbol{x}]^B = [\boldsymbol{T}]^{BA}\,[\boldsymbol{x}]^A. \tag{1.1}$$

A ordered set of 9-tuples, $\boldsymbol{X}$, is a Cartesian tensor (second-order tensor) if for any pair of allowable Cartesian coordinate systems, $]^A$, $]^B$, the following transformation holds:

$$[\boldsymbol{X}]^B = [\boldsymbol{T}]^{BA}\,[\boldsymbol{X}]^A\,[\boldsymbol{T}]^{BA,\mathrm{T}} \tag{1.2}$$

where $[\boldsymbol{T}]^{BA}$ is the associated Coordinate Transformation Matrix which maps the coordinates of a tensor from system $]^A$ to system $]^B$.

The relative location and orientation between any pair of different frames, A and B, are defined respectively as a displacement vector, $\boldsymbol{s}_{BA}$, between the base points of the two frames, and as a rotation tensor, $\boldsymbol{R}^{BA}$.

Definition 1.4 (Rotation Tensor)
Given two frames, A and B, with triad of basis vectors, ($\boldsymbol{a}_1$, $\boldsymbol{a}_2$, $\boldsymbol{a}_3$) and ($\boldsymbol{b}_1$, $\boldsymbol{b}_2$, $\boldsymbol{b}_3$) respectively, the mutual orientation of frame B w.r.t frame A is defined by the rotation tensor $\boldsymbol{R}^{BA}$ through the transformation:

$$\boldsymbol{b}_i = \boldsymbol{R}^{BA}\boldsymbol{a}_i; \qquad i = 1, 2, 3. \tag{1.3}$$

In particular, when coordinated in the preferred coordinate systems, $]^A$ and $]^B$ respectively, the following property holds:

$$\left[\boldsymbol{R}^{BA}\right]^A = \left[\boldsymbol{r}^{BA}\right]^B = [\boldsymbol{R}]^{BA,\mathrm{T}}.$$

The expression of the relative linear and angular motions between different frames implies addressing the time dependence of the displacement vector, $\boldsymbol{s}_{BA}(t)$, and the rotation tensor, $\boldsymbol{R}^{BA}(t)$, respectively. Furthermore, the time rate of change of these two quantities defines the corresponding relative linear and angular velocity, $\boldsymbol{v}_B^A$ and $\boldsymbol{\omega}^{BA}$ respectively. Under the conditions of invariant coordinate transformation expressed in Equations (1.1)-(1.2), the linear and the angular velocities inherit the properties of Cartesian tensors. Concerning the angular velocity, these conditions implies the definition of the rotational time derivative operator.

Definition 1.5 (Rotational Time Derivative)
Given a first-order tensor, $\boldsymbol{x}$, the rotational time derivative, $\mathcal{D}^A\boldsymbol{x}$, w.r.t. any arbitrary frame, A, and expressed in any allowable coordinate system, $]^B$, corresponds to:

$$\left[\mathcal{D}^A\boldsymbol{x}\right]^B = \left[\frac{\mathrm{d}\boldsymbol{x}}{\mathrm{d}t}\right]^B + [\boldsymbol{T}]^{BA}\left[\frac{\mathrm{d}\boldsymbol{T}}{\mathrm{d}t}\right]^{BA,\mathrm{T}}[\boldsymbol{x}]^B. \tag{1.4}$$

Equivalently, given a second-order tensor, $\boldsymbol{X}$*, the rotational time derivative,* $\mathcal{D}^A\boldsymbol{X}$*, w.r.t. any arbitrary frame,* A*, and expressed in any allowable coordinate system,* $]^B$*, corresponds to:*

$$[\mathcal{D}^A\boldsymbol{X}]^B = \left[\frac{\mathrm{d}\boldsymbol{X}}{\mathrm{d}t}\right]^B + [\boldsymbol{T}]^{BA}\left[\frac{\mathrm{d}\boldsymbol{T}}{\mathrm{d}t}\right]^{BA,\mathrm{T}}[\boldsymbol{X}]^B + [\boldsymbol{X}]^B\left[\frac{\mathrm{d}\boldsymbol{T}}{\mathrm{d}t}\right]^{BA}[\boldsymbol{T}]^{BA,\mathrm{T}}. \tag{1.5}$$

In reason of the coordinate invariant transformations in Equations (1.4)-(1.5)*,* $\mathcal{D}^A\boldsymbol{x}$ *and* $\mathcal{D}^A\boldsymbol{X}$ *are also tensors of first and second-order, respectively.*

Based on the above definitions, the linear velocity and linear acceleration tensors of any point B w.r.t. any point belonging to a frame A can be obtained respectively as the first and the second-order rotational time derivative of the corresponding displacement vector:

$$\boldsymbol{v}_B^A = \mathcal{D}^A\boldsymbol{s}_{BA}; \qquad \boldsymbol{a}_B^A = \mathcal{D}^A\mathcal{D}^A\boldsymbol{s}_{BA} = \mathcal{D}^A\boldsymbol{v}_B^A. \tag{1.6}$$

Equivalently, the relative rotation of a vector $\boldsymbol{b}(t)$ in frame B w.r.t. its initial position at t_0 in frame A is expressed by the rotation tensor $\boldsymbol{R}^{BA}$ as in Equation (1.3). According to Equation (1.6), the tangential velocity of the rotating vector is defined by the first-order rotational time derivative:

$$\begin{aligned}\boldsymbol{v}_B^A &= \mathcal{D}^A\boldsymbol{b}(t)\\ &= \mathcal{D}^A\boldsymbol{R}^{BA}\boldsymbol{b}(t_0)\\ &= \mathcal{D}^A\boldsymbol{R}^{BA}\boldsymbol{R}^{BA,\mathrm{T}}\boldsymbol{b}(t)\\ &= \boldsymbol{\Omega}^{BA}\boldsymbol{b}(t)\end{aligned}$$

where, the angular velocity tensor of frame B w.r.t. frame A corresponds to:

$$\boldsymbol{\Omega}^{BA} = \mathcal{D}^A\boldsymbol{R}^{BA}\boldsymbol{R}^{BA,\mathrm{T}}.$$

In particular, the angular velocity tensor, $\boldsymbol{\Omega}^{BA}$, is skew symmetric, thus for any coordinates systems, $]^C$, the following vector equivalence holds:

$$[\boldsymbol{\Omega}^{BA}]^C = \begin{bmatrix}0 & -z & y\\ z & 0 & -x\\ -y & x & 0\end{bmatrix} \iff [\boldsymbol{\omega}^{BA}]^C = \begin{bmatrix}x\\ y\\ z\end{bmatrix}.$$

The coordinate invariant formulation of the rotational time derivative is always expressed w.r.t. a selected reference frame. Thus, the last fundamental concept to be recalled concern the possibility to change the reference frame through the tensor formulation of the standard Euler transformation.

Theorem 1.1 (Generalized Euler Transformation)
Assuming any pair of arbitrary reference frames, A *and* B*, and the corresponding angular velocity tensor,* $\boldsymbol{\Omega}^{BA}$*, then the following rotational time derivative transformation holds for any vector* $\boldsymbol{x}$*:*

$$\mathcal{D}^A\boldsymbol{x} = \mathcal{D}^B\boldsymbol{x} + \boldsymbol{\Omega}^{BA}\boldsymbol{x}.$$

More detailed information concerning the properties and the proofs of the aforementioned Definitions 1.1-1.5 and Theorem 1.1 are provided in [Zip14].

1.2.2 Reference Frames and Coordinate Systems

Reference frames as in Definition 1.1 allow defying the position and the motion of a vehicle independently from a reference observer's point of view. By selecting a coordinate system to which refer all the physical measures, the previuos invariant tensor expressions can be numerically evaluated, thus enabling the implementation of software simulations. The most relevant reference frames and associated coordinate systems are presented hereafter.

Earth Frame (E). In classical physics, the position and motion of any physical object imply the designation of a common inertial reference frame. Depending on the specific application, three different inertial frames are commonly considered in the aerospace framework: Heliocentric frame (for planetary space travel), Geocentric-inertial and Earth frames (for Earth-orbiting satellites). The base points of the Geocentric-inertial and Earth frames are both located at the center of the Earth (E). However, the Geocentric-inertial frame assumes the Earth to have a fixed orientation on the ecliptic plane, while the Earth frame's base vectors ($\boldsymbol{e}_1$, $\boldsymbol{e}_2$, $\boldsymbol{e}_3$) follow the characteristic motion of rotation. As shown in Figure 1.1(a), $\boldsymbol{e}_1$ is directed to the intersection between the Greenwich meridian and the equator, while $\boldsymbol{e}_3$ is aligned with the Earth's axis of rotation, pointing to the North Pole. Despite being subjected to accelerations, the Earth frame is generally assumed inertial for any lower atmosphere flights, in reason of the negligible effect generated by the rotation (Assumption 1.1).

Body Frame (B). Under the Rigid Body Assumption 1.4, the investigated flying vehicle is commonly designated as a reference frame itself. This allows expressing its relative position and motion w.r.t. the selected inertial frame. In the body frame, the base point (B) corresponds to the vehicle's center of mass (CM), whereas the base vectors ($\boldsymbol{b}_1$, $\boldsymbol{b}_2$, $\boldsymbol{b}_3$) are aligned with the principal axes of the vehicle's inertia tensor, as shown in Figure 1.1(b): $\boldsymbol{b}_1$ generally points towards the nose of the vehicle along its longitudinal axis (rotational symmetry), $\boldsymbol{b}_2$ is parallel to the second principal moment of inertia axis, while $\boldsymbol{b}_3$ is directed downwards.

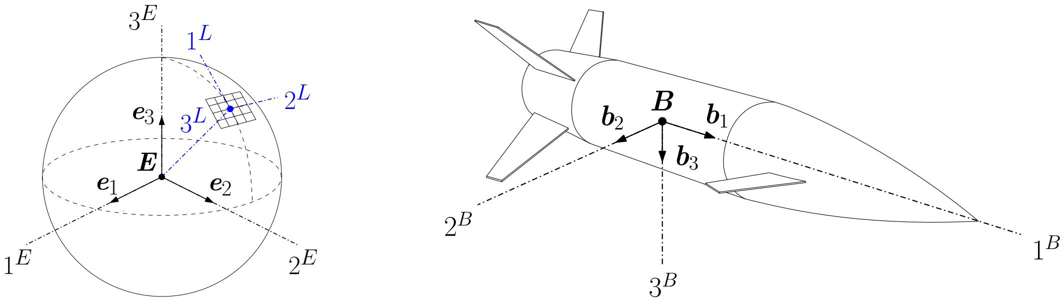

(a) (b)

Figure 1.1: Main reference frames and coordinate systems: (a) Earth frame, E, and Earth and local-level coordinates; (b) body frame, B, and body coordinates.

Air Frame (A). Assuming the air mass to behave as a compact body[1], the air itself can be considered as a physical frame. The main base vector, $\boldsymbol{a}_1$, follows the direction of the relative wind vector, $\boldsymbol{v}_B^A$, which describes the relative motion of the vehicle's CM w.r.t. the air frame. As later discussed, the air mass can be considered in motion w.r.t. the Earth frame or assumed at rest, $\boldsymbol{v}_E^A = 0$ (Zero Wind Assumption 1.3).

As previously mentioned, for atmospheric Earth-orbiting flying vehicles below the supersonic regime, the effects of the Earth's accelerations can be neglected, thus assuming the Earth as the inertial reference frame. As a consequence, the coordinate system associated with the Heliocentric frame as well as the related coordinate transformations are not considered for the purpose of this work.

Earth and Geographic Coordinate System. The preferred coordinate system associated with the Earth's frame has the three axes (1^E, 2^E, 3^E) aligned with the base vectors ($\boldsymbol{e}_1$, $\boldsymbol{e}_2$, $\boldsymbol{e}_3$), respectively, as shown in Figure 1.1(a). By subdividing the Earth's surface on a grid of vertical lines connecting the Poles (meridians) and lines parallel to the equator and concentric to the Poles (parallels), any location can be uniquely identified through the definition of its longitude, l, and latitude, λ, measures. The longitude is expressed as the angle (± 180 deg) from the Greenwich meridian in an easterly direction, while the latitude is the angle from the equator to the north (90 deg) or to the south (-90 deg). The geographic coordinate system, $]^G$, is associated with any specific pair (l, λ) and consists of an axis pointing to the north (1^G), an axis pointing to the center of the Earth (3^G), and a third axis which points east (2^G).

Local-level Coordinate System. The notion of geographic coordinates can be further generalized whenever the exact location (l, λ) of the vehicle on the Earth's surface does not relevantly affect the trajectory evaluation. This simplification implies the Flat Earth Assumption 1.2 since a geographic location is characterized by a specific surface curvature. Under this condition, any local plane tangent to the Earth's surface can be employed as a geographic coordinate system and is referred to as a local-level coordinate system, $]^L$. This system is generally associated with the launch point of the vehicle to properly express the vehicle's trajectory. Following the standard north-east-down (NED) convention, axes 1^L and 2^L lie in the tangent plane, respectively pointing north and east, while axis 3^L points downward to the center of the Earth, as shown in Figure 1.1(a).

Body Coordinate System. The body coordinate system, $]^B$, corresponds to the preferred system associated with the body frame, having the axes (1^B, 2^B, 3^B) respectively aligned with the base vectors ($\boldsymbol{b}_1$, $\boldsymbol{b}_2$, $\boldsymbol{b}_3$). The relative transformation between the body and the local-level coordinates allows defining the orientation of the vehicle across the trajectory through the Euler angles (ϕ, θ, ψ). The overall coordinate transformation is obtained through a sequential set of rotations complying with the standard aircraft intermediate coordinate systems, $]^X$ and $]^Y$. A first yaw angle rotation, ψ, about the vertical axis (3^L) defines the intermediate system

---

[1] No relative motion among the air particles.

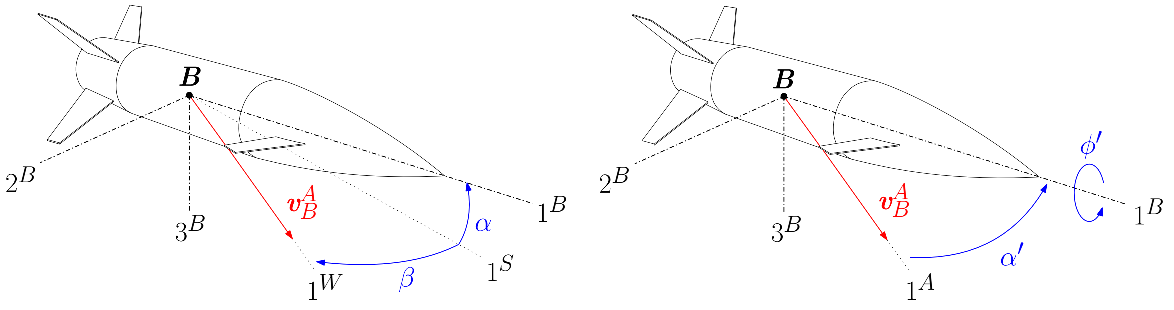

(a) (b)

Figure 1.2: Wind coordinate systems: (a) Cartesian incidence angles convention; (b) polar aeroballistic angles convention.

$]^X$, while a second pitch angle rotation, θ, about the lateral axis (2^X) leads to the intermediate system, $]^Y$. The final roll rotation, ϕ, about the longitudinal axis (1^Y) completes the sequence.

$$[\boldsymbol{T}]^{BY} = \begin{bmatrix} 1 & 0 & 0 \\ 0 & \cos\phi & \sin\phi \\ 0 & -\sin\phi & \cos\phi \end{bmatrix}; \quad [\boldsymbol{T}]^{YX} = \begin{bmatrix} \cos\theta & 0 & -\sin\theta \\ 0 & 1 & 0 \\ \sin\theta & 0 & \cos\theta \end{bmatrix}; \quad [\boldsymbol{T}]^{XL} = \begin{bmatrix} \cos\psi & \sin\psi & 0 \\ -\sin\psi & \cos\psi & 0 \\ 0 & 0 & 1 \end{bmatrix}.$$

By multiplying the set of sequential transformations in the proper order, the complete body to local-level coordinate transformation is expressed as:

$$\begin{aligned} [\boldsymbol{T}]^{BL} &= [\boldsymbol{T}]^{BY}\,[\boldsymbol{T}]^{YX}\,[\boldsymbol{T}]^{XL} \\ &= \begin{bmatrix} \cos\psi\cos\theta & \sin\psi\cos\theta & -\sin\theta \\ \cos\psi\sin\theta\sin\phi - \sin\psi\cos\phi & \sin\psi\sin\theta\sin\phi + \cos\psi\cos\phi & \cos\theta\sin\phi \\ \cos\psi\sin\theta\cos\phi + \sin\psi\sin\phi & \sin\psi\sin\theta\cos\phi - \cos\psi\sin\phi & \cos\theta\cos\phi \end{bmatrix}. \end{aligned}$$

Wind Coordinate System. The last relevant coordinate system to be defined is associated with the air frame. The axis 1^W is aligned with the relative velocity direction v_B^A, while the other two axes are defined based on the selected convention:

- **Cartesian Incidence Angles.** The body to wind coordinate transformation of any vehicle characterized by a planar symmetry relies on the definition of an intermediate stability coordinate system, $]^S$, as shown in Figure 1.2(a). The first axis, 1^S, corresponds to the projection of $\boldsymbol{v}_B^A$ in the plane (1^B, 3^B), identifying the angle-of-attack (AoA), α, as the positive rotation angle from 1^S to 1^B. Similarly, the lateral angle-of-sideslip (AoS), β, is defined as the positive rotation angle from 1^S to 1^W. The body to wind transformation matrix is expressed as follows:

$$[\boldsymbol{T}]^{WB} = \begin{bmatrix} \cos\alpha\cos\beta & \sin\beta & \sin\alpha\cos\beta \\ -\cos\alpha\sin\beta & \cos\beta & -\sin\alpha\sin\beta \\ -\sin\alpha & 0 & \cos\alpha \end{bmatrix}. \tag{1.7}$$

- **Polar Aeroballistic Angles.** Concerning rotational symmetric vehicles, a different intermediate aeroballistic coordinate system, $]^R$, is defined. This coordinate system is aligned with the load factor plane of the vehicle, where the main aerodynamic interactions are generated (Drag and Lift forces). The axis 1^R coincides with 1^B and lies in the load factor plane together with 3^R. A first aerodynamic roll angle rotation, ϕ', about the axis 1^R defines the aeroballistic to body coordinate transformation. The final aeroballistic wind coordinate system, $]^A$, is reached through the total angle-of-attack rotation, α', about the 2^A axis, defined positive from 1^B to 1^A (equal to 1^W and aligned with $\boldsymbol{v}_B^A$). The axis 3^A lies in the load factor plane, as shown in Figure 1.2(b).

$$[\boldsymbol{T}]^{AB} = \begin{bmatrix} \cos\alpha' & \sin\alpha' \sin\phi' & \sin\alpha\cos\beta \\ -\cos\alpha\sin\beta & \cos\beta & -\sin\alpha\sin\beta \\ -\sin\alpha & 0 & \cos\alpha \end{bmatrix}. \tag{1.8}$$

1.2.3 6-DoF Projectile Equations of Motion

The formulation of the projectile nonlinear dynamics relies on the standard flight mechanics theory, complying with the notation proposed in [Zip14]; [Zip19]. The equations of motion describing the translational and attitude dynamics are first derived in an invariant tensor form and then projected w.r.t. the most appropriate system of coordinates, allowing for numerical computation. The derivation is based on the following modeling assumptions:

Assumption 1.1
The Earth is assumed as the inertial reference frame (E) since the centrifugal and Coriolis accelerations are negligible when dealing with subsonic atmospheric vehicle's trajectories.

Assumption 1.2 (Flat Earth)
The Earth's surface is assumed flat, neglecting the local eccentricity of the specific geographic location where the trajectory occurs.

Assumption 1.3 (Zero Wind)
The air mass is assumed at rest (no relative motion between frames A and E, $\boldsymbol{v}_E^A = 0$).

Assumption 1.4 (Rigid Body)
The projectile is considered a rigid body with constant and uniform mass distribution.

The translational and attitude dynamics express the relative linear and angular motions between frames B and E. The equations are derived from Newton's and Euler's laws, assuming the aerodynamic forces, $\boldsymbol{f}_\mathrm{a}$, and the gravitational acceleration, $\boldsymbol{g}$, to be the only external effects contributing to the projectile dynamics. In particular, the gravity acceleration is applied on the projectile's center of mass (CM), while the aerodynamic forces are applied on the center of pressure (CP), generating relevant moment contributions, $\boldsymbol{m}_B$, w.r.t. the CM:

$$\begin{aligned} m\mathcal{D}^E\boldsymbol{v}_B^E &= \boldsymbol{f}_{\mathrm{a}} + m\boldsymbol{g}, \\ \mathcal{D}^E\boldsymbol{l}_B^{BE} &= \boldsymbol{m}_B. \end{aligned} \tag{1.9}$$

where m is the constant mass of the projectile, $\boldsymbol{v}_B^E$ represents the relative velocity of the CM w.r.t. the Earth reference frame, and $\boldsymbol{l}_B^{BE}$ is the angular momentum between the body and the Earth frames, expressed again w.r.t. the CM.

Since the translational and attitude dynamics have to be expressed in the body coordinates, the rotational time derivative operator w.r.t. the Earth frame, $\mathcal{D}^E$, is shifted to the body frame through the Euler transformation discussed in Theorem 1.1. By expanding $\boldsymbol{l}_B^{BE} = \boldsymbol{I}_B^B\boldsymbol{\omega}^{BE}$, where $\boldsymbol{I}_B^B$ is the moment of inertia (MoI) of the body referred to the CM, and $\boldsymbol{\omega}^{BE}$ represents the relative angular velocity between the body and the Earth frames, the tensor Equation (1.9) become:

$$\begin{aligned} m\mathcal{D}^B\boldsymbol{v}_B^E + m\boldsymbol{\Omega}^{BE}\boldsymbol{v}_B^E &= \boldsymbol{f}_{\mathrm{a}} + m\boldsymbol{g}, \\ \boldsymbol{I}_B^B\mathcal{D}^B\boldsymbol{\omega}^{BE} + \boldsymbol{\Omega}^{BE}\boldsymbol{I}_{\mathrm{B}}^B\boldsymbol{\omega}^{BE} &= \boldsymbol{m}_B. \end{aligned} \tag{1.10}$$

In order to enable numerical calculations, Equation (1.10) is projected in the body coordinates. The gravity contribution, simplified to a constant quantity pointing to the center of the Earth, is more appropriately expressed in the local-level coordinates as $[\boldsymbol{g}]^L = \begin{bmatrix} 0 & 0 & g \end{bmatrix}^{\mathrm{T}}$ and then coherently transformed to the body coordinate system:

$$\begin{aligned} m\left[\frac{\mathrm{d}\boldsymbol{v}_B^E}{\mathrm{d}t}\right]^B + m\left[\boldsymbol{\Omega}^{BE}\right]^B\left[\boldsymbol{v}_B^E\right]^B &= m\,[\boldsymbol{T}]^{BL}\,[\boldsymbol{g}]^L + [\boldsymbol{f}_{\mathrm{a}}]^B, \\ [\boldsymbol{I}]_B^B\left[\frac{\mathrm{d}\boldsymbol{\omega}^{BE}}{\mathrm{d}t}\right]^B + \left[\boldsymbol{\Omega}^{BE}\right]^B[\boldsymbol{I}]_B^B\left[\boldsymbol{\omega}^{BE}\right]^B &= [\boldsymbol{m}_B]^B. \end{aligned}$$

The resulting set of state variables for the translational dynamics consists of the projectile's linear velocity projections along the body coordinate (u, v, w), while the attitude dynamics is expressed in terms of the projectile's body rates, namely the roll rate, p, the pitch rate, q, and the yaw rate, r, as shown in Figure 1.3:

$$\left[\boldsymbol{v}_B^E\right]^B = \begin{bmatrix} u \\ v \\ w \end{bmatrix}; \qquad \left[\boldsymbol{\omega}^{BE}\right]^B = \begin{bmatrix} p \\ q \\ r \end{bmatrix}.$$

Moreover, the skew-symmetric form of the angular velocity tensor, $\boldsymbol{\omega}^{BE}$, and the MoI, are expressed respectively as:

$$\left[\boldsymbol{\Omega}^{BE}\right]^B = \begin{bmatrix} 0 & -r & q \\ r & 0 & -p \\ -q & p & 0 \end{bmatrix}; \qquad \left[\boldsymbol{I}_B^B\right]^B = \begin{bmatrix} I_1 & 0 & 0 \\ 0 & I_2 & 0 \\ 0 & 0 & I_3 \end{bmatrix}. \tag{1.11}$$

In particular, the content of the MoI depends on the characteristic symmetry of the investigated vehicle. Rotational symmetric bodies like projectiles are generally characterized by a diagonal MoI since the product of inertia (I_{12}, I_{13}, I_{23}) are negligible ([Zip76]).

The translational dynamics can be finally expressed explicitly in the body coordinates as:

$$\begin{aligned}
\frac{\mathrm{d}u}{\mathrm{d}t} &= rv - qw + \frac{f_{\mathrm{a}_1}}{m} - g\sin\theta, \\
\frac{\mathrm{d}v}{\mathrm{d}t} &= pw - ru + \frac{f_{\mathrm{a}_2}}{m} + g\cos\theta\sin\phi, \\
\frac{\mathrm{d}w}{\mathrm{d}t} &= qu - pv + \frac{f_{\mathrm{a}_3}}{m} + g\cos\theta\cos\phi,
\end{aligned} \tag{1.12}$$

while the attitude dynamics takes the form:

$$\begin{aligned}
\frac{\mathrm{d}p}{\mathrm{d}t} &= I_1^{-1}\left[(I_2 - I_3)\,qr + m_{B_1}\right], \\
\frac{\mathrm{d}q}{\mathrm{d}t} &= I_2^{-1}\left[(I_3 - I_1)\,pr + m_{B_2}\right], \\
\frac{\mathrm{d}r}{\mathrm{d}t} &= I_3^{-1}\left[(I_1 - I_2)\,pq + m_{B_3}\right].
\end{aligned} \tag{1.13}$$

The expressions of the aerodynamic forces (f_{a_i}), and moments (m_{B_i}), with $i = 1, 2, 3$, are coherently projected in the body coordinates. The complete characterization of the projectile's aerodynamic model is detailed later in Section 1.3.

Concerning the kinematics computation, the projectile's position, $\boldsymbol{s}_{BE}$, is expressed w.r.t. the local-level coordinates (NED). The linear velocity, $\boldsymbol{v}_B^E$, obtained through the translational dynamics in Equation (1.12) in the body coordinates, is first converted to the local coordinates:

$$\left[\boldsymbol{v}_B^E\right]^L = [\boldsymbol{T}]^{BL,\mathrm{T}} \left[\boldsymbol{v}_B^E\right]^B = \begin{bmatrix} u_L \\ v_L \\ w_L \end{bmatrix} \tag{1.14}$$

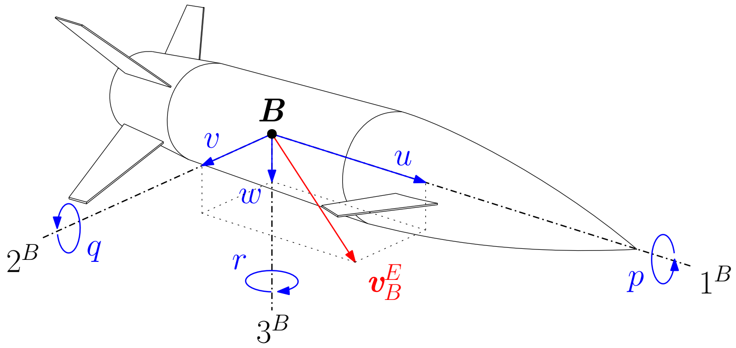

Figure 1.3: Projectile's linear and angular velocities components projected w.r.t. the body coordinates.

and then, the projectile's local position can be obtained through time integration:

$$\left[\frac{\mathrm{d}\boldsymbol{s}_{BE}}{\mathrm{d}t}\right]^{L} = \left[\boldsymbol{v}_B^E\right]^{L}. \tag{1.15}$$

In order to determine the projectile's orientation, the rotation tensor approach is preferred[2]. It is based on the formulation of the rotational time derivative of the Direction Cosine Matrix (DCM), $[\boldsymbol{T}]^{BL}$ as:

$$\left[\frac{\mathrm{d}\boldsymbol{T}}{\mathrm{d}t}\right]^{BL} = \left[\boldsymbol{\Omega}^{BE}\right]^{B,\mathrm{T}}[\boldsymbol{T}]^{BL}. \tag{1.16}$$

The resolution of the set of differential Equation (1.16) leads to the evaluation of the Euler angles (ϕ, θ, ψ), as it follows:

$$\begin{aligned}
\phi &= \arccos\left(\frac{\cos\theta\cos\phi}{\cos\theta}\right)\operatorname{sign}(\cos\theta\sin\phi),\\
\theta &= \arcsin(\sin\theta),\\
\psi &= \arccos\left(\frac{\cos\psi\cos\theta}{\cos\theta}\right)\operatorname{sign}(\sin\psi\cos\theta).
\end{aligned} \tag{1.17}$$

The last fundamental relationship to be exploited associates the aerodynamic angles (α, β, α', ϕ') to the body linear velocities (u, v, w). Indeed, the alternative formulation of the projectile's translational dynamics in terms of the aerodynamic angles is a common modeling approach for control-oriented design. Due to the Zero Wind Assumption 1.3, the simplification $\boldsymbol{v}_B^E = \boldsymbol{v}_B^A + \boldsymbol{v}_E^A = \boldsymbol{v}_B^A$ holds, thus the relative linear velocity of the body w.r.t. the air frame can be expressed in the body coordinates as $\left[\boldsymbol{v}_B^A\right]^B = \begin{bmatrix} u & v & w\end{bmatrix}^{\mathrm{T}}$. Since in the Cartesian wind coordinates the same linear velocity is projected as $\left[\boldsymbol{v}_B^A\right]^W = \begin{bmatrix} V & 0 & 0\end{bmatrix}^{\mathrm{T}}$, where V represents the airspeed, the following relation also holds:

$$\begin{bmatrix} V \\ 0 \\ 0 \end{bmatrix} = \begin{bmatrix} \cos\alpha\cos\beta & \sin\beta & \sin\alpha\cos\beta \\ -\cos\alpha\sin\beta & \cos\beta & -\sin\alpha\sin\beta \\ -\sin\alpha & 0 & \cos\alpha \end{bmatrix}\begin{bmatrix} u \\ v \\ w \end{bmatrix}; \quad \text{with} \quad V = \sqrt{u^2+v^2+w^2}. \tag{1.18}$$

The expressions of the aerodynamic angles w.r.t the linear velocity projections in the body coordinates can be derived from Equation (1.18) as:

$$\alpha = \arctan\left(\frac{w}{u}\right); \qquad \beta = \arcsin\left(\frac{v}{V}\right). \tag{1.19}$$

The same reasoning can be applied to evaluate the polar wind coordinates, leading to the following:

$$\alpha' = \arccos\left(\frac{u}{V}\right); \qquad \phi' = \arctan\left(\frac{v}{w}\right).$$

---

[2] Singularities occur in the calculation when $\theta = \pm\pi/2$.

By inverting the relation, the linear velocities can be equivalently expressed w.r.t the aerodynamic angles as:

$$u = V\cos\alpha\cos\beta; \qquad v = V\sin\beta; \qquad w = V\sin\alpha\cos\beta. \tag{1.20}$$

The derivatives of Equations (1.18)-(1.19) allow defining the desired dynamics of the air variables:

$$\frac{\mathrm{d}V}{\mathrm{d}t} = \frac{u\dot{u} + v\dot{v} + w\dot{w}}{V}; \qquad \frac{\mathrm{d}\alpha}{\mathrm{d}t} = \frac{u\dot{w} + w\dot{u}}{u^2 + w^2}; \qquad \frac{\mathrm{d}\beta}{\mathrm{d}t} = \frac{-uv\dot{u} + (u^2 + w^2)\dot{v} - vw\dot{w}}{V^2\sqrt{u^2 + w^2}}.$$

Finally, by substituting Equation (1.12) and Equation (1.20) in the previous expressions, the translational dynamics formulated in the aerodynamic variables is obtained:

$$\begin{aligned}
\frac{\mathrm{d}V}{\mathrm{d}t} &= \frac{1}{m}\left(f_{\mathrm{a}_1}\cos\alpha\cos\beta + f_{\mathrm{a}_2}\sin\beta + f_{\mathrm{a}_3}\sin\alpha\cos\beta\right) \\
&\qquad + g\left(-\sin\theta\cos\alpha\cos\beta + \cos\theta\sin\phi\sin\beta + \cos\theta\cos\phi\sin\alpha\cos\beta\right), \\
\frac{\mathrm{d}\alpha}{\mathrm{d}t} &= \frac{1}{mV\cos\beta}\left(-f_{\mathrm{a}_1}\sin\alpha + f_{\mathrm{a}_3}\cos\alpha\right) + q \\
&\qquad - (p\cos\alpha + r\sin\alpha)\tan\beta + \frac{g}{V\cos\beta}\left(\sin\theta\sin\alpha + \cos\theta\cos\phi\cos\alpha\right), \\
\frac{\mathrm{d}\beta}{\mathrm{d}t} &= \frac{1}{mV}\left(-f_{\mathrm{a}_1}\cos\alpha\sin\beta + f_{\mathrm{a}_2}\cos\beta - f_{\mathrm{a}_3}\sin\alpha\sin\beta\right) + p\sin\alpha - r\cos\alpha \\
&\qquad + \frac{g}{V}\left(\sin\theta\cos\alpha\sin\beta + \cos\theta\sin\phi\cos\beta - \cos\theta\cos\phi\sin\alpha\sin\beta\right).
\end{aligned} \tag{1.21}$$

1.2.4 The LRGP Concept

The model consists of a new concept of long range guided projectile (LRGP) investigated at the French-German Research Institute of Saint-Louis (ISL) ([Mar+18]; [Lib+19]; [Lib+20]; [Lib+21]). The interest motivating the project relies on the enhancement of the operating range capability of standard howitzer ammunition, avoiding the employment of any additional thruster propulsion or modifications of the firing system.

The projectile's design is based on a Secant Ogive Cylinder Boat Tail (SOCBT) geometry, with a full-scale 155 mm caliber and a non-rotating fin-stabilized architecture, including a set of four axial symmetrical tail-fins, and a reduced set of two front canards for control maneuvers ([Fre11]; [CFC12]). The employment of a non-spinning concept reduces the highly nonlinear dynamics generated by the aerodynamic coupling terms. Furthermore, the control canards are installed in a non-co-planar configuration ('X' configuration), as shown in Figure 1.4(a), aiming to reduce the overall canard-fin aerodynamic interaction, as well as the destabilizing effect generated by the canards aerodynamics.

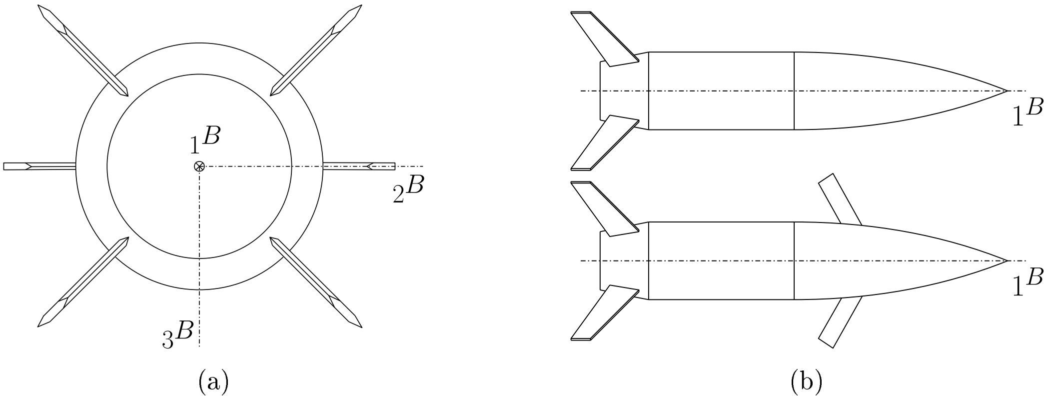

Figure 1.4: LRGP concept: (a) 'X' fins-canards configuration; (b) ballistic (top) and glider (bottom) projectile's configuration.

The proposed flight strategy consists of an initial phase of ballistic trajectory, as in Figure 1.5, where the tail-fins are unfolded from the main sabot immediately after the firing occurs, while the canards remain folded to reduce the initial aerodynamic Drag. Once the apogee of the trajectory is reached, the canards are deployed, and the guided gliding phase begins. During this phase, the optimization of the projectile's range performance relies on the engagement of an ad-hoc designed range-extension guidance law. Additionally, the employment of Bank-To-Turn (BTT) maneuvers is expected to smoothen the gliding trajectory, minimizing the lateral aerodynamic effects and optimizing the Lift contributions. In opposition to conventional Skid-To-Turn maneuvers, the BTT strategy aims to align the vertical plane of the projectile with the plane of maximum generated aerodynamic Lift through two consecutive maneuvers:

1. A banking motion about the airspeed vector that aligns the vertical plane to the plane of maximum aerodynamic Lift, minimizing the lateral displacement (ideally $\beta = 0$ deg).
2. An AoA correction to optimize the generated Lift-to-Drag Ratio (LDR).

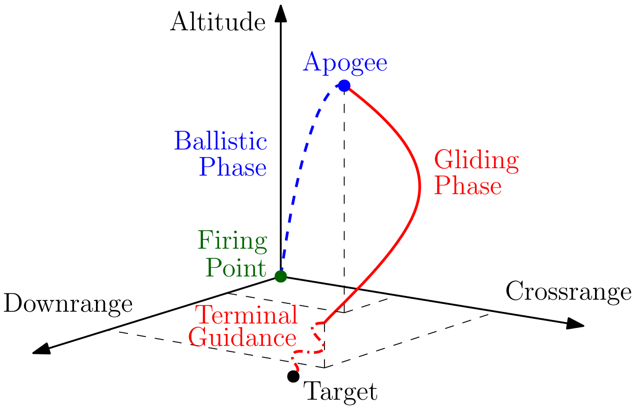

Figure 1.5: LRGP flight strategy: range-enhancement gliding trajectory.

By accounting for the specific configuration of the projectile and the flight strategy selected for the range improvement, the following assumptions can be defined to simplify the modeling and control design process:

Assumption 1.5 (Dynamic Decoupling)
The pitch and the roll-yaw channels of the projectile dynamics are assumed decoupled in reason of the limited lateral and roll effects generated by the BTT flight strategy.

Assumption 1.6 (Inertial Decoupling)
The non-co-planar configuration of the canards induces a slight geometrical asymmetry resulting in an overall second-order rotational symmetry. In this case, the inertia tensor expressed in Equation (1.11) *is characterized by the relationship:* $I_1 << I_2 < I_3$.

Based on the above considerations, for control-oriented modeling, the pitch and the roll-yaw channels can be designed separately ([Bla91]). During the control design stage, discussed in the next chapters, particular attention is dedicated to the pitch channel dynamics, being the main target of the range optimization process.

1.2.4.1 Pitch Channel Dynamics

The pitch channel dynamics is obtained by constraining the projectile's trajectory in the vertical (pitch) plane. In this context, the translational dynamics expressed w.r.t. the aerodynamic variables provides a more convenient model formulation in view of the control design. Thus, the AoA dynamics (short-period mode) in Equation (1.21) is coupled with the pitch rate dynamics (long-period mode) in Equation (1.13), neglecting the lateral contributions ($\beta \approx 0$ deg), and the roll-yaw coupling terms ($p, r \approx 0$ deg/s):

$$\begin{aligned} \frac{\mathrm{d}\alpha}{\mathrm{d}t} &= \frac{1}{mV}\left(-f_{\mathrm{a}_1}\sin\alpha + f_{\mathrm{a}_3}\cos\alpha\right) + q + \frac{g}{V}\left(\sin\theta\sin\alpha + \cos\theta\cos\phi\cos\alpha\right), \\ \frac{\mathrm{d}q}{\mathrm{d}t} &= \frac{m_{B_2}}{I_2}. \end{aligned} \tag{1.22}$$

By including the airspeed dynamics, $\dot{V}$, in the model above, the complete formulation of the projectile longitudinal dynamics could be employed for the control design (also addressing the phugoid oscillation). However, the absence of any direct control authority on the longitudinal motion and the targeted control design approach makes this formulation unfeasible for the purposes of this study, as it will be explained in the next chapter. As a final remark, load factor measurements (LF), η_z, can be employed at the control design stage. They are generally modeled as:

$$\eta_z = \frac{f_{\mathrm{a}3}}{mg}. \tag{1.23}$$

1.3 Projectile Aerodynamic Characterization

The complete derivation of the projectile flight dynamics implies an appropriate aerodynamic characterization. The mutual interaction between the projectile and the airflow is affected by several factors, such as the flow regime (Mach number, Reynolds number), the flight trajectory (incidence angles, body rates), the control actions (control surface deflections), and the projectile's geometry. The interaction generates a set of aerodynamic forces and corresponding moments ($\boldsymbol{f}_{\mathrm{a}}$, $\boldsymbol{m}_B$), applied in the center of pressure (CP) of the body. Whenever a projectile is characterized by a CP located ahead of the CM, the contributions of the aerodynamic moments result in a destabilizing effect, deviating the system away from the desired trajectory. Nevertheless, unstable systems are also characterized by a more reactive aerodynamic response, providing generally higher maneuverability ([CFC12]). Thus, at the design stage, a compromise has to be reached between the required stability and performance properties.

1.3.1 Aerodynamics Formulation

The fundamental aerodynamic forces are generated in the load factor plane of any flying vehicle by the interaction with the airflow, in terms of Drag, D, and Lift, L, contributions ([McC99]). As shown in Equations (1.12)-(1.13), the aerodynamic forces and moments derived from the projections of Drag and Lift in the projectile's body coordinates are expressed as:

$$[\boldsymbol{f}_{\mathrm{a}}]^B = \begin{bmatrix} f_{\mathrm{a}_1} \\ f_{\mathrm{a}_2} \\ f_{\mathrm{a}_3} \end{bmatrix} = \bar{q}S \begin{bmatrix} C_X \\ C_Y \\ C_Z \end{bmatrix}; \qquad [\boldsymbol{m}_B]^B = \begin{bmatrix} m_{B_1} \\ m_{B_2} \\ m_{B_3} \end{bmatrix} = \bar{q}Sd \begin{bmatrix} C_l \\ C_m \\ C_n \end{bmatrix}. \tag{1.24}$$

Specifically, S represents the body reference surface, d is the caliber, $\bar{q} = \frac{1}{2}\rho V^2$ is the dynamic pressure, and $\mathcal{M} = \frac{V}{a}$ is the Mach number. These quantities are defined as functions of the airspeed, V, and of the altitude-dependent air density, $\rho(h)$, and speed of sound, $a(h)$.

The projectile's aerodynamic characterization process relies on the derivation of the aerodynamic coefficients, C_i, with $i = X, Y, Z, l, m, n$. These non-dimensional coefficients are obtained either from real wind tunnel aerodynamic measurements, normalized by the vehicle's dimensions, or from sophisticated Computational Fluid Dynamic (CFD) software simulations. Due to the high technical costs implied by the development of real wind tunnel tests, CFD simulations are generally preferred for early modeling stages of the design optimization process, especially if several flight regimes are investigated (subsonic, and transonic flow). Each of the coefficients depends on a large number of flight parameters, as $\mathcal{M}$, the incidence angles, α and β (or α' and ϕ'), the body rates, p, q, and r, and the control deflections, accounted for in the measurements procedure.

Concerning the control deflections, the LRGP concept is equipped with two front canards (right and left), providing two independent local control deflections (δ_{r}, δ_{l}), as shown in Figure 1.6. However, for control-oriented modeling, the control actions are conventionally expressed in terms of roll, pitch, and yaw contributions (δ_p, δ_q, δ_r), respectively. This virtual set of control

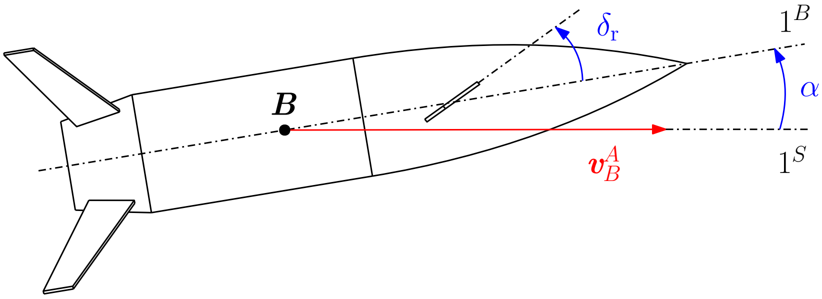

Figure 1.6: Canards local control deflection.

deflections is implemented through the selection of a dedicated control allocation logic. The availability of two horizontal front canards, aligned with the intent of improving the range capability of the projectile, suggested the employment of a BTT control strategy, leading to the definition of the static allocation matrix, $\boldsymbol{T}_{\mathrm{CA}}$:

$$\begin{bmatrix} \delta_p \\ \delta_q \\ \delta_r \end{bmatrix} = \begin{bmatrix} -\frac{1}{2} & +\frac{1}{2} \\ +\frac{1}{2} & +\frac{1}{2} \\ 0 & 0 \end{bmatrix} \begin{bmatrix} \delta_{\mathrm{r}} \\ \delta_{\mathrm{l}} \end{bmatrix} = [\boldsymbol{T}_{\mathrm{CA}}] \begin{bmatrix} \delta_{\mathrm{r}} \\ \delta_{\mathrm{l}} \end{bmatrix}. \tag{1.25}$$

1.3.2 Computational Fluid Dynamics Data

The design of the LRGP concept is based on a multi-objective aerodynamic optimization targeting both the range capability and the required time of flight to reach the target. The complete analysis is detailed in [BLM22]. The optimization aims to define fundamental geometrical features of the concept (fins and canards airfoil profile, canards sweep angle), having a relevant impact on the aerodynamic performance. Operational parameters such as the initial firing elevation angle of the gun, θ_{e}, the operating AoA range, and Mach regime are also considered. In reason of the extremely large computational complexity and the related processing time required to compute the aerodynamic optimization, a superposition hypothesis is proposed ([BLM22]).

Assumption 1.7 (Aerodynamic Superposition)
The aerodynamic control contributions, C_δ, provided by the local deflections of the control surfaces, δ, can be superposed to the general static effect, C_{S}, generated by the variation of the AoA on the overall projectile's body (including the control surfaces).

$$C = C_{\mathrm{S}}\Big|_{\delta=0}(\alpha, \mathcal{M}) + C_\delta\Big|_{\alpha=0}(\delta, \mathcal{M}). \tag{1.26}$$

The aerodynamic coefficients are then parameterized through the superposition of several mutually independent contributions as it follows:

$$\begin{aligned}
C_X(\mathcal{M},\alpha,\beta,\delta_{\text{eff}}) &= C_{X_{\text{S}}}(\mathcal{M},\alpha,\beta) + C_{X_{\delta_{\text{eff}}}}(\mathcal{M},\delta_{\text{eff}}),\\
C_Y(\mathcal{M},\alpha,\beta) &= C_{Y_{\text{S}}}(\mathcal{M},\alpha,\beta) + \left(\frac{d}{2V}\right)C_{Y_r}(\mathcal{M})\,r,\\
C_Z(\mathcal{M},\alpha,\beta,\delta_q) &= C_{Z_{\text{S}}}(\mathcal{M},\alpha,\beta) + \left(\frac{d}{2V}\right)C_{Z_q}(\mathcal{M})\,q + C_{Z_{\delta_q}}(\mathcal{M},\delta_q),\\
C_l(\mathcal{M},\alpha,\beta,\delta_p) &= C_{l_{\text{S}}}(\mathcal{M},\alpha,\beta) + \left(\frac{d}{2V}\right)C_{l_p}(\mathcal{M})\,p + C_{l_{\delta_p}}(\mathcal{M},\delta_p),\\
C_m(\mathcal{M},\alpha,\beta,\delta_q) &= C_{m_{\text{S}}}(\mathcal{M},\alpha,\beta) + \left(\frac{d}{2V}\right)C_{m_q}(\mathcal{M})\,q + C_{m_{\delta_q}}(\mathcal{M},\delta_q),\\
C_n(\mathcal{M},\alpha,\beta) &= C_{n_{\text{S}}}(\mathcal{M},\alpha,\beta) + \left(\frac{d}{2V}\right)C_{n_r}(\mathcal{M})\,r,
\end{aligned} \tag{1.27}$$

where $C_{i_{\text{S}}}$ represent the static aerodynamic contributions related to the projectile's body interaction with the airflow, C_{i_j} correspond to the dynamic damping effects, and $C_{i_{\delta_j}}$ are the additional aerodynamic contributions provided by the control surfaces deflections, with $i = X, Y, Z, l, m, n$ and $j = p, q, r$. In particular, the longitudinal control deflection is expressed as the combined nonlinear contributions of roll and pitch, $\delta_{\text{eff}} = \sqrt{\delta_p^2 + \delta_q^2}$.

As stated in Assumption 1.7, the superposition hypothesis relies on the idea that in the linear region of the canards' response (away from stall conditions), the aerodynamic contributions generated by the local control deflections (δ_{r}, δ_{l}) can be independently estimated and a posteriori added to the overall body contributions, which depend on the incidence angles (α', ϕ', α, β). This allows for significantly reducing the computational complexity of the aerodynamic optimization by performing two independent campaigns of CFD simulations to characterize the projectile aerodynamics and define the geometrical properties of the concept.

1.3.2.1 Static Coefficients: ($C_{X_{\text{S}}}$, $C_{Y_{\text{S}}}$, $C_{Z_{\text{S}}}$, $C_{l_{\text{S}}}$, $C_{m_{\text{S}}}$, $C_{n_{\text{S}}}$)

The first CFD simulation campaign targets the static aerodynamic characterization of the full projectile's body by estimating the aerodynamic forces and moments coefficients: $C_{X_{\text{S}}}$, $C_{Y_{\text{S}}}$, $C_{Z_{\text{S}}}$, $C_{l_{\text{S}}}$, $C_{m_{\text{S}}}$, $C_{n_{\text{S}}}$. Two different datasets were acquired, one characterizing the ballistic configuration employed during the ascending phase of the trajectory, and one concerning the gliding configuration, including the static effect of the control surfaces at zero local deflections ($\delta_{\text{r}}, \delta_{\text{l}} = 0$ deg). Both the configurations are shown in Figure 1.4(b).

	$\mathcal{M}$	α' (deg)	ϕ' (deg)	$\delta_{\text{r}}, \delta_{\text{l}}$ (deg)
min	0.3	0	0	0
max	1	16	90	0

Table 1.1: Static coefficients CFD acquisition ranges.

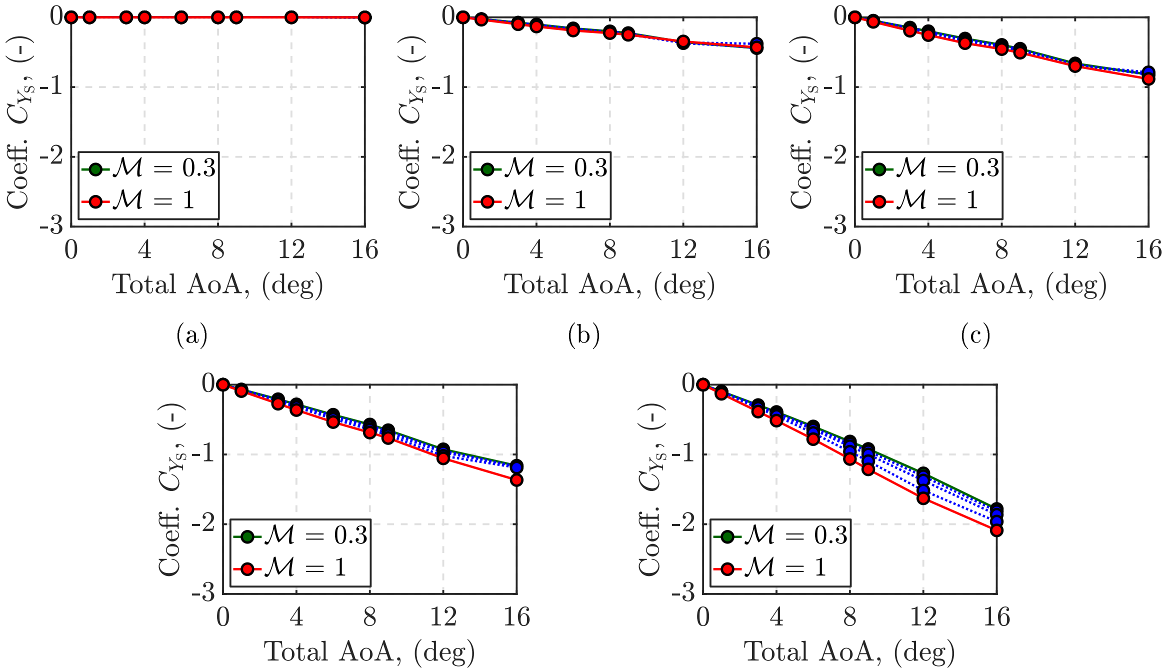

(a) (b) (c)

(d) (e)

Figure 1.7: CFD static lateral coefficient dataset, C_{Y_S}: (a) $\phi' = 0$ deg; (b) $\phi' = 15$ deg; (c) $\phi' = 30$ deg; (d) $\phi' = 45$ deg; (e) $\phi' = 90$ deg.

The data were acquired as a function of $\mathcal{M}$ in the subsonic/transonic regime, and of the polar angles α' and ϕ', more suitable for the CFD software environment, assuming the variation ranges in Table 1.1.

Thus, for any pair ($\mathcal{M}$, ϕ'), the coefficients were investigated across the variation of α'. A sample of the acquisition results is presented in Figure 1.7, concerning the lateral coefficient C_{Y_S} in the gliding configuration.[3] The complete dataset of aerodynamic measurements is provided in Appendix A.1. For modeling coherence, the coefficients have been converted a posteriori as a function of the Cartesian incidence angles (α, β) based on the transformations:

$$\alpha = \arctan\left(\tan\alpha' \cos\phi'\right); \qquad \beta = \arcsin\left(\sin\alpha' \sin\phi'\right). \tag{1.28}$$

At higher values of ϕ' correspond an increasing dependence of the coefficients w.r.t. β and vice versa, defining the following limit aerodynamic configurations:

Conf$_1$: for $\phi' = 0°$ → $\alpha' = \alpha$, the aerodynamic coefficients depend only on α.

Conf$_2$: for $\phi' = 90°$ → $\alpha' = \beta$, the aerodynamic coefficients depend only on β.

---

[3] The coefficients' values have been normalized in reason of confidentiality.

1.3.2.2 Stability and Control Considerations

The aerodynamic stability of any vehicle is a fundamental aspect to be extensively investigated from the design stage. Indeed, a higher instability increases the complexity of the autopilot design. On the other hand, highly unstable vehicles are characterized by a responsive dynamics, capable to perform sharper and more aggressive maneuvers. Concerning the LRGP concept, an exhaustive aerodynamics analysis has been developed to find a proper compromise between stability and operating range performance.

The former property is generally analyzed through the variation of the relative position between the CP and the CM, $X_{\mathrm{CP,CM}}$, or equivalently through the value of the pitching moment coefficient, C_{m_S}. Indeed, negative $X_{\mathrm{CP,CM}}$ values correspond to the generation of a negative stabilizing C_{m_S}, which tends to maintain the direction of the projectile aligned with the relative velocity $\boldsymbol{v}_B^A$, minimizing the AoA. The canards installed in the front part of the projectile produce an aerodynamic Lift contribution that moves the overall CP of the projectile ahead. Thus, a design compromise has to be achieved between the improvement in the range performance and the unwanted destabilizing effect generated by the canards. The results presented in Figure 1.8 show the variation of the coefficient C_{m_S} as a function of the AoA and the Mach number.[4] The LRGP concept is characterized by a predominantly unstable behavior, since the coefficient C_{m_S} is positive across most of the flight domain.

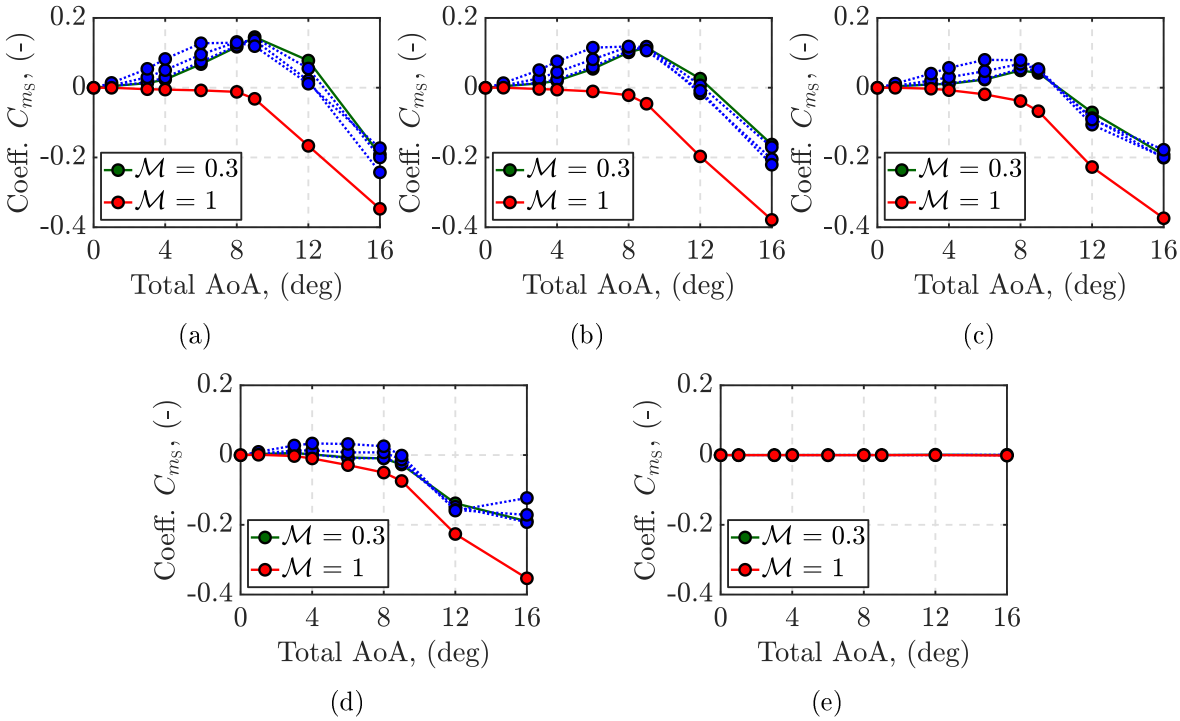

(a) (b) (c)

(d) (e)

Figure 1.8: CFD static pitching moment coefficient dataset, C_{m_S}: (a) $\phi' = 0$ deg; (b) $\phi' = 15$ deg; (c) $\phi' = 30$ deg; (d) $\phi' = 45$ deg; (e) $\phi' = 90$ deg.

---

[4] The coefficients' values have been normalized in reason of confidentiality.

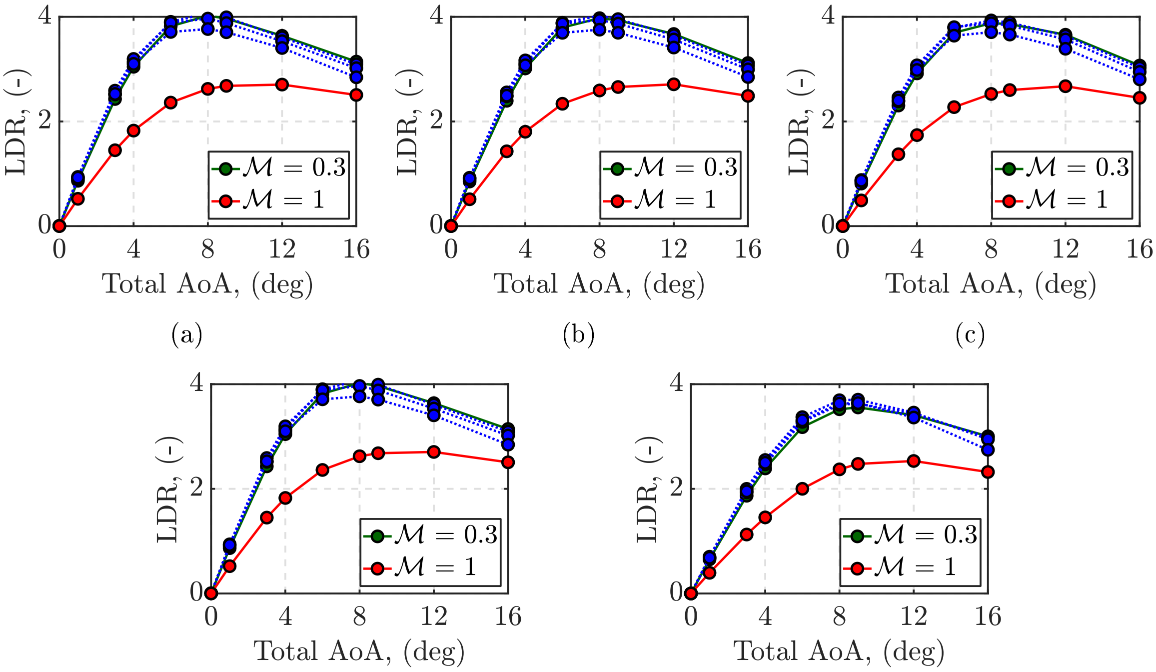

(a) (b) (c)

(d) (e)

Figure 1.9: CFD Lift-to-Drag Ratio dataset, LDR: (a) $\phi' = 0$ deg; (b) $\phi' = 15$ deg; (c) $\phi' = 30$ deg; (d) $\phi' = 45$ deg; (e) $\phi' = 90$ deg.

The aerodynamic stability tends to improve at higher values of AoA (> 10 deg), and towards the transonic regime ($\mathcal{M} \approx 1$). Additionally, the pitching moment contribution decreases significantly as the aerodynamic roll angle increases. The range efficiency is estimated through the variation of the Lift-to-Drag Ratio index, LDR $= C_L/C_D$. At the concept design stage, this index suggests the optimal aerodynamic configuration to be selected in terms of canards/fins sweep angles, cant angles, and geometrical dimensions.

The variation of the LDR w.r.t. the aerodynamic variables, such as AoA, AoS, roll angle, and Mach, is also employed during the definition of the guidance law to find the flight conditions that optimize the projectile performance. The results of the analysis shown in Figure 1.9, reveal an optimal LDR index for a total AoA $\in [5, 10]$ deg, with a peak around 8 deg. The LDR decreases dramatically during the transition from subsonic to transonic regime, in reason of the lower Lift contribution generated by the turbulent airflow.

1.3.2.3 Control Coefficients ($C_{X_{\delta_{\text{eff}}}}$, $C_{Z_{\delta_q}}$, $C_{l_{\delta_p}}$, $C_{m_{\delta_q}}$)

The second CFD simulation campaign focused on the analysis of the aerodynamic control coefficients ($C_{X_{\delta_{\text{eff}}}}$, $C_{Z_{\delta_q}}$, $C_{l_{\delta_p}}$, $C_{m_{\delta_q}}$) generated by the canards' local deflections, δ_{r} and δ_{l}. The data were acquired only w.r.t. the local right canard deflection, δ_{r}, assuming the variation ranges in Table 1.2. The aerodynamic coefficients related to the left canard deflection, δ_{l}, can be easily obtained by means of symmetrical considerations.

	$\mathcal{M}$	α' (deg)	ϕ' (deg)	$\delta_\mathrm{r}, \delta_\mathrm{l}$ (deg)
min	0.3	0	0	0
max	1	0	0	36

Table 1.2: Control coefficients CFD acquisition ranges.

During the acquisition, the angles ϕ' and α' were set to zero, and the residual static contributions generated by the projectile's body were subtracted in post-processing as:

$$\begin{pmatrix} C_{X_{\delta_\mathrm{r}}} \\ C_{Z_{\delta_\mathrm{r}}} \\ C_{l_{\delta_\mathrm{r}}} \\ C_{m_{\delta_\mathrm{r}}} \end{pmatrix} = \begin{pmatrix} C_{X_{\delta_\mathrm{r}}} \\ C_{Z_{\delta_\mathrm{r}}} \\ C_{l_{\delta_\mathrm{r}}} \\ C_{m_{\delta_\mathrm{r}}} \end{pmatrix} (\delta_\mathrm{r}, \mathcal{M}) - \begin{pmatrix} C_{X_{\delta_\mathrm{r}}} \\ C_{Z_{\delta_\mathrm{r}}} \\ C_{l_{\delta_\mathrm{r}}} \\ C_{m_{\delta_\mathrm{r}}} \end{pmatrix} (\delta_\mathrm{r} = 0, \mathcal{M}).$$

The results of the acquisitions for each control coefficient are presented in Figure 1.10.[5] The specific canards configuration does not provide any control authority on the yaw plane, thus the lateral contributions $C_{Y_{\delta_\mathrm{r}}}$ and $C_{n_{\delta_\mathrm{r}}}$ are not considered. The modeling procedure employed to convert the measured coefficients, ($C_{X_{\delta_\mathrm{r}}}$, $C_{Z_{\delta_\mathrm{r}}}$, $C_{l_{\delta_\mathrm{r}}}$, $C_{m_{\delta_\mathrm{r}}}$), into the corresponding virtual counterparts, ($C_{X_{\delta_\mathrm{eff}}}$, $C_{Z_{\delta_q}}$, $C_{l_{\delta_p}}$, $C_{m_{\delta_q}}$), is discussed in detail in Section 1.3.3.4.

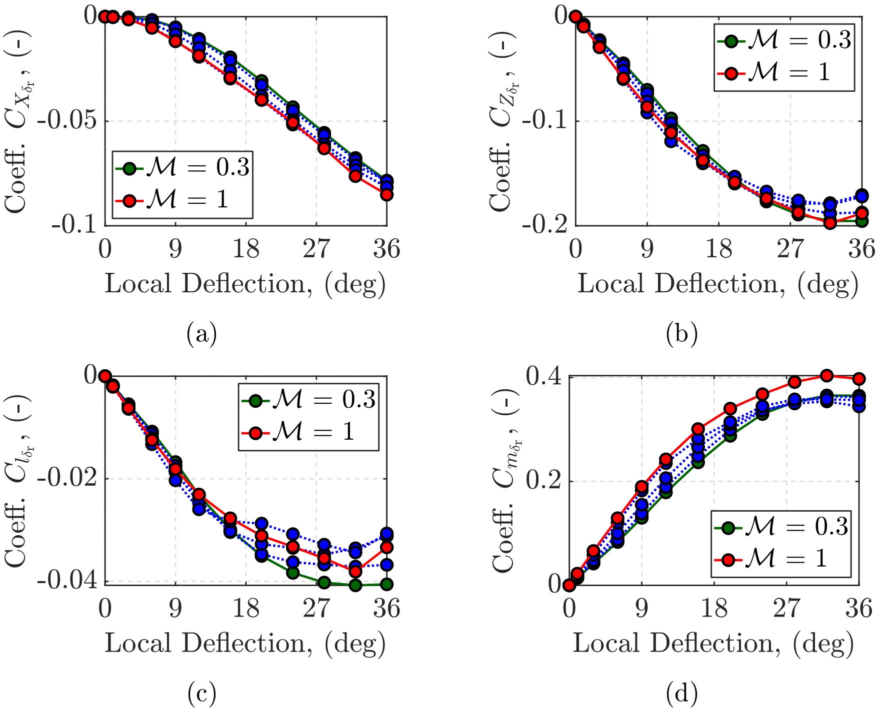

Figure 1.10: CFD control coefficient dataset: (a) longitudinal force, $C_{X_{\delta_\mathrm{r}}}$; (b) vertical force, $C_{Z_{\delta_\mathrm{r}}}$; (c) rolling moment, $C_{l_{\delta_\mathrm{r}}}$; (d) pitching moment, $C_{m_{\delta_\mathrm{r}}}$.

---

[5] The coefficients' values have been normalized to a range [0,1] in reason of confidentiality.

1.3.3 Aerodynamics Modeling

The results of the CFD acquisitions can be implemented in simulation either by direct interpolation of the obtained tables of measurements or through Taylor expansion by decomposing each coefficient in a set of derivative components ([Zip14]; [McC99]). The former approach is preferred during the initial ballistic ascending phase of the projectile's trajectory, while for control-oriented modeling, a continuous regression model is generally derived to characterize the aerodynamics of the guided phase.

In reason of the Aerodynamic Superposition Assumption 1.7, the static and control CFD datasets are analyzed separately:

- **Static:** two different regression models are proposed. A first model accounts only for the decoupled dynamics (pitch - roll/yaw), where the aerodynamics is either dependent on the variation of α (Conf$_1$) or β (Conf$_2$). This formulation is coherent with the dynamics developed for control design purposes in Equations (1.22)-(1.23). The second model accounts for the simultaneous variation of α and β induced by $\phi' \in (0, 90)$ deg. The regression is based on a multivariable approach and the resulting model is employed in the 6-DoF simulator environment to validate the controller design. The two regression analyses are discussed in Sections 1.3.3.1 and 1.3.3.2, respectively.
- **Control:** the CFD data acquired in terms of individual local canard variations (δ_r) are first modeled through a single variable regression analysis. Complying with the general aerodynamic parametrization in Equation (1.27), the resulting regression models are reformulated w.r.t. the virtual deflections set (δ_eff, δ_p, δ_q). The overall control modeling procedure is presented in Section 1.3.3.4.

1.3.3.1 Polynomial Regression (Static) Model

The first regression analysis relies on a reduced set of the static aerodynamic CFD coefficients, corresponding to the data related to the extreme configurations: Conf$_1$ and Conf$_2$. In the former scenario, the aerodynamic coefficients are measured across the variation of α, ideally without any contribution deriving from β. The latter configuration addresses the opposite scenario, since the aerodynamics of the projectile strictly depends on the variation of β. The dependence of the coefficients on the $\mathcal{M}$ variation is not explicitly modeled by the regression analysis. Thus, the regression is performed for all the considered Mach conditions, and the results are tabulated for directed online interpolation during the simulations.

These assumptions allow the employment of a polynomial regression approach based on least-squares optimization ([Ost12]). Several polynomial models of increasing order have been investigated for each of the aerodynamic coefficients, aiming to find the best compromise between regression accuracy and model complexity. In particular, for the pitch plane coefficients (C_{Z_S}, C_{m_S}), only the α dependence is investigated in reason of the dynamics decoupling. Similarly, for the yaw plane coefficients (C_{Y_S}, C_{n_S}), only the β dependence is considered. The only exceptions occur for the longitudinal coefficient, C_{X_S}, since the variations of α and β generate the same contribution due to the projectile's axial symmetry, and for the roll coefficient, C_{l_S}, which is negligible in reason of the fin-stabilized configuration of the projectile. The regression models are parameterized as follows:

$$\begin{aligned}
C_{X_\mathrm{S}}(\mathcal{M},\alpha) &= C_{X_{\alpha 0}}(\mathcal{M}) + \sum_{i=2}^{N} C_{X_{\alpha i}}(\mathcal{M}) \sin^i\alpha, \\
C_{Y_\mathrm{S}}(\mathcal{M},\beta) &= \sum_{j=1}^{M} C_{Y_{\beta j}}(\mathcal{M}) \sin^j\beta, \\
C_{Z_\mathrm{S}}(\mathcal{M},\alpha) &= \sum_{j=1}^{M} C_{Z_{\alpha j}}(\mathcal{M}) \sin^j\alpha, \\
C_{m_\mathrm{S}}(\mathcal{M},\alpha) &= \sum_{j=1}^{M} C_{m_{\alpha j}}(\mathcal{M}) \sin^j\alpha, \\
C_{n_\mathrm{S}}(\mathcal{M},\beta) &= \sum_{j=1}^{M} C_{n_{\beta j}}(\mathcal{M}) \sin^j\beta.
\end{aligned} \tag{1.29}$$

where $i = 2, 4, \ldots, N$ is an even polynomial order sequence, while $j = 1, 3, \ldots, M$ is an odd polynomial order sequence.

The accuracy of the data regressions is assessed at each $\mathcal{M}$ condition by evaluating the statistical indexes: Root Mean Square Error (RMSE) and Coefficient of Determination (R^2). In particular, the RMSE values have been normalized by the difference between the maximum and the minimum values of the CFD data (Min-Max), providing an estimation of the relative regression error (NRMSE). The R^2 and NRMSE results obtained during the regression of the relevant α coefficient derivatives are displayed in Figure 1.11, while the β coefficient derivatives are presented in Figure 1.12. The model selection criteria consist of a correlation index $\mathrm{R}^2 > 0.9$ and a relative regression error NRMSE$< 10\%$.

Based on the statistical results, the following *Polynomial Regression* (PR) aerodynamic model was selected as a compromise between accuracy and model complexity:

$$\begin{aligned}
C_{X_\mathrm{S}}(\mathcal{M},\alpha) &= C_{X_{\alpha 0}}(\mathcal{M}) + C_{X_{\alpha 2}}(\mathcal{M}) \sin^2\alpha + C_{X_{\alpha 4}}(\mathcal{M}) \sin^4\alpha, \\
C_{Y_\mathrm{S}}(\mathcal{M},\beta) &= C_{Y_{\beta 1}}(\mathcal{M}) \sin\beta, \\
C_{Z_\mathrm{S}}(\mathcal{M},\alpha) &= C_{Z_{\alpha 1}}(\mathcal{M}) \sin\alpha, \\
C_{m_\mathrm{S}}(\mathcal{M},\alpha) &= C_{m_{\alpha 1}}(\mathcal{M}) \sin\alpha + C_{m_{\alpha 3}}(\mathcal{M}) \sin^3\alpha + C_{m_{\alpha 5}}(\mathcal{M}) \sin^5\alpha, \\
C_{n_\mathrm{S}}(\mathcal{M},\beta) &= C_{n_{\beta 1}}(\mathcal{M}) \sin\beta.
\end{aligned} \tag{1.30}$$

The main justification behind the choice of sinusoidal regression polynomials relies on the complexity of modeling the projectile aerodynamics across the transonic regime ($\mathcal{M} > 0.7$), characterized by a highly nonlinear variation.

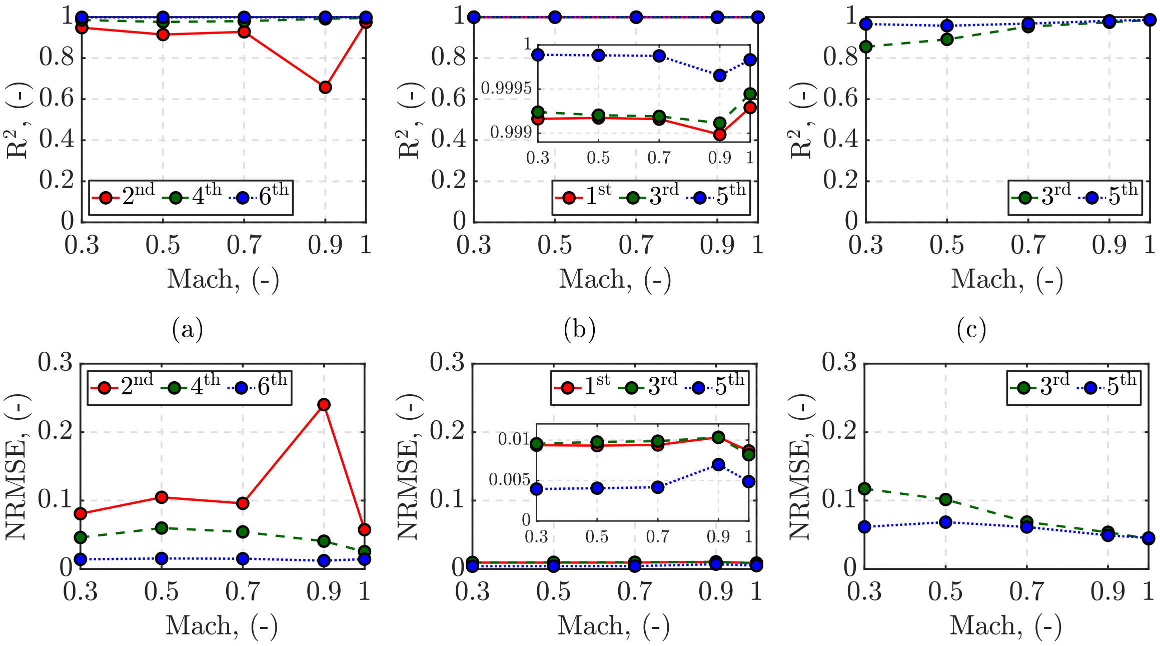

(a) (b) (c)

(d) (e) (f)

Figure 1.11: R^2 and NRMSE regression results: (a)-(d) longitudinal force coefficient, C_{X_S}; (b)-(e) vertical force coefficient, C_{Z_S}; (c)-(f) pitching moment coefficient, C_{m_S}.

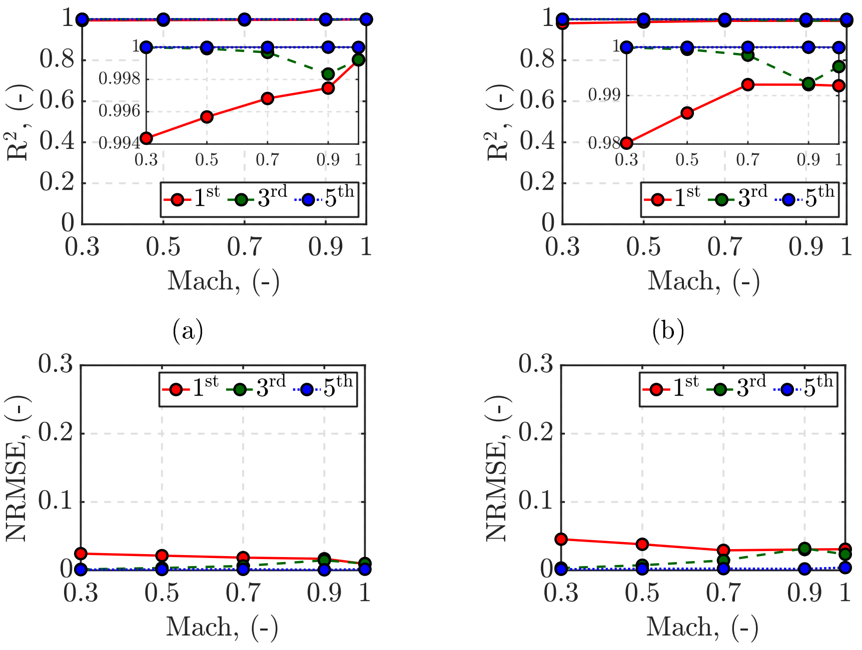

(a) (b)

(c) (d)

Figure 1.12: R^2 and NRMSE regression results: (a)-(c) lateral force coefficient, C_{Y_S}; (b)-(d) yawing moment coefficient, C_{n_S}.

1.3.3.2 Multivariable Regression (Static) Model

The second regression analysis relies on the entire available CFD static aerodynamic dataset, also addressing the coupling effects generated by the simultaneous variation of the incidence angles, α and β (equivalently, $\phi' \in [0, 90]$ deg). Since the analysis involves several variables, different sets of multivariable models have been selected for the data regression. As assumed in the previous analysis, the dependence on $\mathcal{M}$ is not exploited in the model to avoid an excessively complicated formulation. Each of the coefficients has been investigated considering several models. However, only the most relevant ones are discussed hereafter.

Model$_1$: this model is obtained from the theoretical flight mechanics and aerodynamics formulation proposed in [McC99]. The aerodynamic forces and moments are expressed in the tensor form in terms of Drag and Lift contributions, generated in the projectile's load factor plane, and then projected in the aeroballistic wind coordinate system. By employing the coordinate transformation in Equation (1.7), the resulting forces and moments are expressed w.r.t. the body coordinates as a function of the Cartesian incidence angles (α, β). These final Cartesian projections are employed as regression models. The full derivation of these models is detailed in Appendix A.2. As a result, the first multivariable regression model corresponds to the following:

$$\begin{aligned}
C_{X_\mathrm{S}}(\mathcal{M},\alpha,\beta) &= C_{X_0}(\mathcal{M}) + C_{X_2}(\mathcal{M})\cos\alpha\cos\beta + C_{X_4}(\mathcal{M})\cos^2\!\alpha\cos^2\!\beta,\\
C_{Y_\mathrm{S}}(\mathcal{M},\alpha,\beta) &= C_{Y_1}(\mathcal{M})\sin\beta + C_{Y_3}(\mathcal{M})\cos\alpha\sin\beta\cos\beta,\\
C_{Z_\mathrm{S}}(\mathcal{M},\alpha,\beta) &= C_{Z_2}(\mathcal{M})\sin\alpha\cos\beta,\\
C_{m_\mathrm{S}}(\mathcal{M},\alpha,\beta) &= C_{m_2}(\mathcal{M})\sin\alpha\cos\beta + C_{m_4}(\mathcal{M})\sin\alpha\cos\alpha\cos^2\!\beta,\\
C_{n_\mathrm{S}}(\mathcal{M},\alpha,\beta) &= C_{n_1}(\mathcal{M})\sin\beta + C_{n_3}(\mathcal{M})\cos\alpha\sin\beta\cos\beta.
\end{aligned} \tag{1.31}$$

Model$_2$: it models the relevance of the mutually independent variation of each incidence angle by means of uncorrelated regression coefficients, corresponding to either α or β coefficient derivatives. Thus, no bilinear terms are included in the model in comparison to Model$_1$. The order of the selected multivariable polynomial regression models is consistent with (or lower than) the corresponding Model$_1$ counterparts:

$$\begin{aligned}
C_{X_\mathrm{S}}(\mathcal{M},\alpha,\beta) &= C_{X_{\alpha 0}}(\mathcal{M}) + C_{X_{\alpha 2}}(\mathcal{M})\sin^2\!\alpha\\
&\qquad + C_{X_{\beta 2}}(\mathcal{M})\sin^2\!\beta + C_{X_{\alpha 4}}(\mathcal{M})\sin^4\!\alpha + C_{X_{\beta 4}}(\mathcal{M})\sin^4\!\beta,\\
C_{Y_\mathrm{S}}(\mathcal{M},\alpha,\beta) &= C_{Y_{\alpha 1}}(\mathcal{M})\sin\alpha + C_{Y_{\beta 1}}(\mathcal{M})\sin\beta,\\
C_{Z_\mathrm{S}}(\mathcal{M},\alpha,\beta) &= C_{Z_{\alpha 1}}(\mathcal{M})\sin\alpha + C_{Z_{\beta 1}}(\mathcal{M})\sin\beta,\\
C_{m_\mathrm{S}}(\mathcal{M},\alpha,\beta) &= C_{m_{\alpha 1}}(\mathcal{M})\sin\alpha + C_{m_{\beta 1}}(\mathcal{M})\sin\beta + C_{m_{\alpha 3}}(\mathcal{M})\sin^3\!\alpha\\
&\qquad + C_{m_{\beta 3}}(\mathcal{M})\sin^3\!\beta + C_{m_{\alpha 5}}(\mathcal{M})\sin^5\!\alpha + C_{m_{\beta 5}}(\mathcal{M})\sin^5\!\beta,\\
C_{n_\mathrm{S}}(\mathcal{M},\alpha,\beta) &= C_{n_{\alpha 1}}(\mathcal{M})\sin\alpha + C_{n_{\beta 1}}(\mathcal{M})\sin\beta.
\end{aligned} \tag{1.32}$$

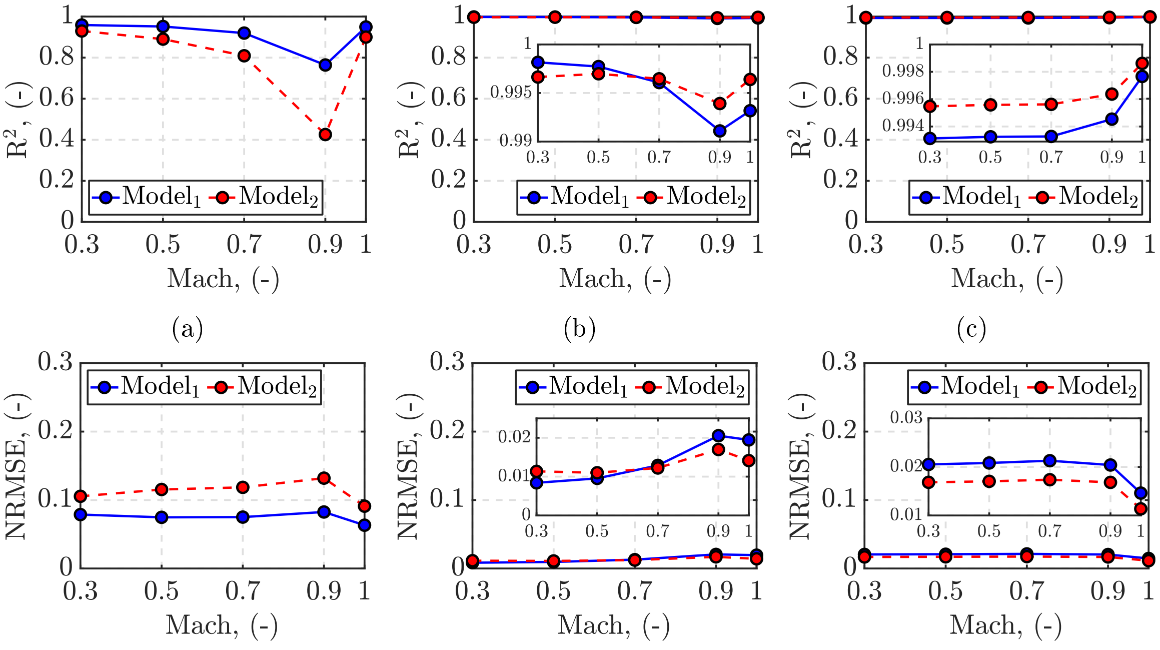

(a) (b) (c)

(d) (e) (f)

Figure 1.13: R^2 and NRMSE regression results: (a)-(d) longitudinal force coefficient, C_{X_S}; (b)-(e) lateral force coefficient, C_{Y_S}; (c)-(f) vertical force coefficient, C_{Z_S}.

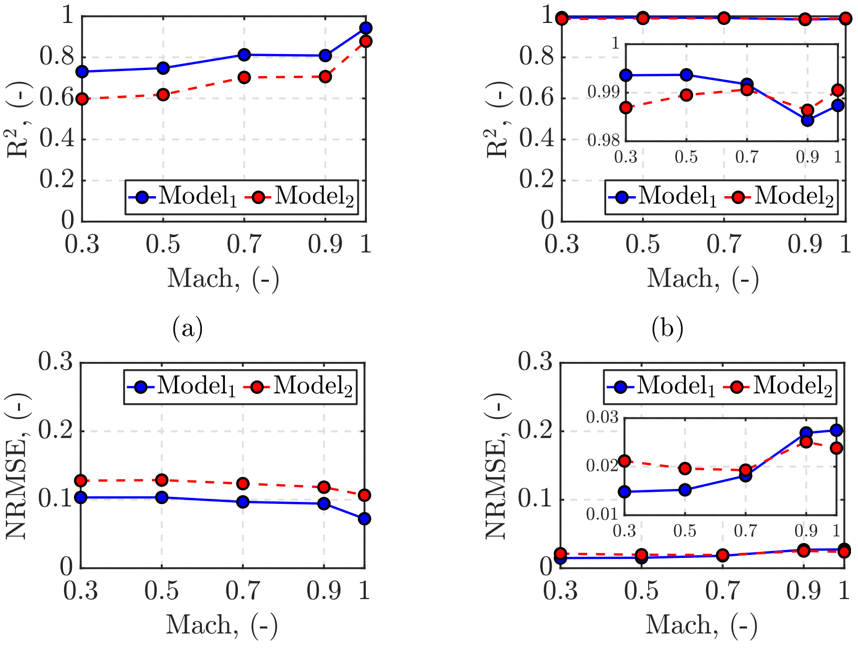

(a) (b)

(c) (d)

Figure 1.14: R^2 and NRMSE regression results: (a)-(c) pitching moment coefficient, C_{m_S}; (b)-(d) yawing moment coefficient, C_{n_S}.

As for the *Polynomial Regression*, the accuracy of the investigated models is assessed through the statistical indexes (NRMSE, R^2). The results in Figures 1.13-1.14 show how the Model_1 regression provides a more generally accurate description of the projectile aerodynamics w.r.t. the full CFD dataset. Additionally, in the limit configurations (Conf_1, Conf_2) the Model_1 better approximates the results obtained with the dedicated PR model. In particular, in the Conf_1 scenario ($\beta = 0$) the lateral coefficients (C_{Y_S} ,C_{n_S}) should have ideally zero impact on the projectile aerodynamics because of the Dynamic Decoupling Assumption 1.5. Similarly, Conf_2 ($\alpha = 0$) implies ideally zero pitch contributions (C_{Z_S} ,C_{m_S}).

These conditions are clearly respected by the multivariable model Model_1, while a parasitic contribution would appear in simulation if the Model_2 model were to be employed. As a consequence the Model_1 in Equation (1.31) is selected and referred to as *Multivariable Regression* model (MR) for the rest of the dissertation. As a general consideration, the pitching moment, C_{m_S}, turned out to be the toughest coefficient to be properly modeled because of the highly nonlinear influence deriving from both the α and the β variations. Once again, the rolling moment coefficient, C_{l_S}, has not been included in the model in reason of the negligible magnitude observed in the acquired data.

1.3.3.3 Regression Approaches Comparison

The previous sections have dealt with the derivation of the aerodynamic regression models (PR and MR) selected to fit the CFD dataset describing the projectile aerodynamics. The *Polynomial Regression* model in Equation (1.30) relies only on a reduced set of the available data, corresponding to the limit configurations, Conf_1 and Conf_2. Despite the lack of accuracy guarantees at more general flight conditions, this model complies with the Decoupling Assumptions 1.5-1.6. Thus, it will be employed at the control design stage for the decoupled channels autopilot. Differently, the *Multivariable Regression* model in Equation (1.31) accounts for all the acquired CFD data, providing a more global description of the projectile aerodynamics across a wider flight envelope. As a consequence, this model is more suitable for simulation purposes and will be implemented in the complete simulator environment.

Since the PR and MR models were derived from different CFD datasets, their accuracy cannot be directly compared at different flight conditions through the statistical results obtained in Section 1.3.3.1 and Section 1.3.3.2. To deal with this issue, a dedicated accuracy analysis has been developed between the two models, targeting the full range of $\mathcal{M}$, ϕ', and α' investigated during the CFD campaigns. The value of each aerodynamic coefficient is interpolated first directly on the CFD surfaces as a ground truth reference. Then, the same interpolation is performed on the modeled surfaces obtained through the two regression approaches (PR, MR). The interpolation error corresponds to the RMSE of the difference between the results provided by the CFD coefficient interpolations, $C_{j,\mathrm{CFD}}$, and the selected model ones, $C_{j,\mathrm{PR}}$ or $C_{j,\mathrm{PR}}$, for $j = X, Y, Z, l, m, n$. The RMSE is evaluated along the α' variation by selecting iteratively a specific pair of ($\mathcal{M}$, ϕ'). These settings allow observing the accuracy of the models as a function of the increasing roll configuration and consequently of the different (α, β) combinations, as well as of $\mathcal{M}$.

The complete analysis algorithm is presented hereafter.

Algorithm 1 Interpolation Accuracy Analysis

```
For any $j = X, Y, Z, l, m, n$:
    For any $(\mathcal{M}, \phi', \alpha')$ combination:
        1. Select the flight condition: $(\mathcal{M}, \phi', \alpha')$.
        2. Convert the incidence angles, based on Equation (1.28):
               $$(\alpha, \beta) = f(\phi', \alpha').$$
        3. Interpolate on the CFD surfaces:
               $$C_{j,\text{CFD}} = \text{interp}(\mathcal{M}, \phi', \alpha').$$
        3. Interpolate on the PR and MR models:
               $$C_{j,\text{PR}} = \text{interp}(\mathcal{M}, \alpha, \beta); \qquad C_{j,\text{MR}} = \text{interp}(\mathcal{M}, \alpha, \beta).$$
        4. Evaluate the interpolation NRMSE of the PR model as:
               $$\text{NRMSE}_{j,\text{PR}}(\mathcal{M}, \phi') = \frac{\text{RMSE}_{j,\text{PR}}(\mathcal{M}, \phi')}{C_{j,\text{CFD,Min-Max}}(\mathcal{M}, \phi')},$$
           with
               $$\text{RMSE}_{j,\text{PR}}(\mathcal{M}, \phi') = \sqrt{\frac{\sum_{i=1}^{n} \left(C_{j,\text{PR}}(\mathcal{M}, \alpha_i, \beta_i) - C_{j,\text{CFD}}(\mathcal{M}, \phi', \alpha_i')\right)^2}{n}},$$
               $$C_{j,\text{CFD,Min-Max}}(\mathcal{M}, \phi') = \max_{\alpha'} \left(C_{j,\text{CFD}}(\mathcal{M}, \phi', \alpha')\right) - \min_{\alpha'} \left(C_{j,\text{CFD}}(\mathcal{M}, \phi', \alpha')\right),$$
           where $n$ is the dimension of the investigated $\alpha'$ range.
        5. Repeat (4.) to evaluate the NRMSE of the MR model.
    end.
end.
```

Samples of the results obtained from the analysis are displayed in Figure 1.15 and Figure 1.16, concerning the interpolation error of the vertical and lateral force coefficients, respectively, as a function of the roll configuration. As expected, at the limit configurations, Conf_1 ($\phi' = 0$ deg) and Conf_2 ($\phi' = 90$ deg), the PR model better approximates the aerodynamics of the projectile, as shown in Figure 1.15(a) (Conf_1) and Figure 1.16(c) (Conf_2). Nevertheless, as soon as the aerodynamic roll is increased, the PR model does not compare any longer with the global MR. Indeed, the effect provided by mutual $\alpha - \beta$ variations is not addressed by the PR model. The complete set of interpolation errors is provided in Appendix A.3.

The results of the analysis confirm the reliability of the two aerodynamic models when

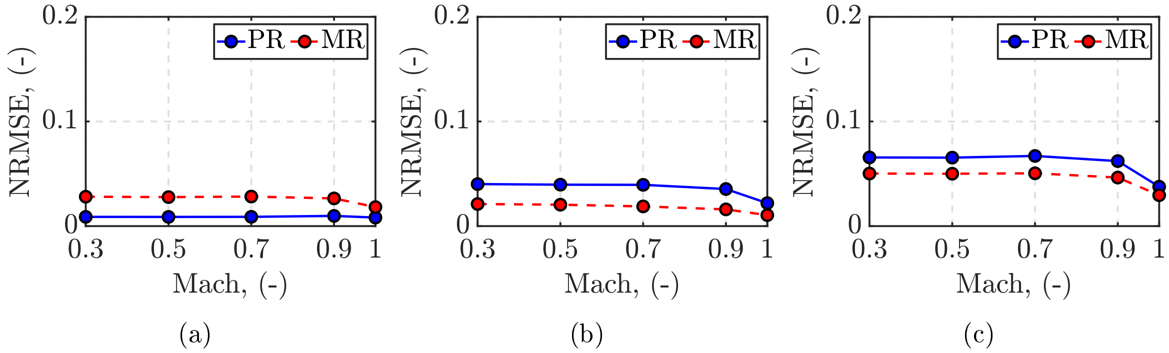

(a) (b) (c)

Figure 1.15: C_{Z_S} interpolation NRMSE comparison at different flight conditions: (a) $\phi' = 0$ deg; (b) $\phi' = 30$ deg; (c) $\phi' = 45$ deg.

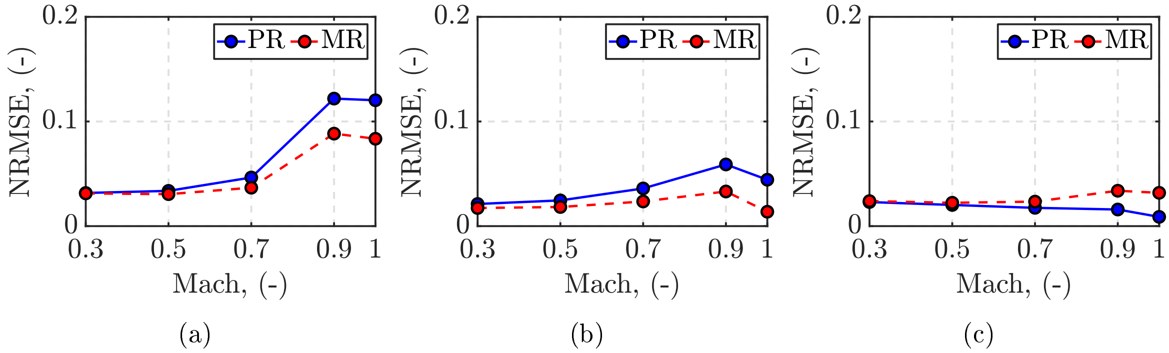

(a) (b) (c)

Figure 1.16: C_{Y_S} interpolation NRMSE comparison at different flight conditions: (a) $\phi' = 15$ deg; (b) $\phi' = 45$ deg; (c) $\phi' = 90$ deg.

employed in different configuration scenarios. Even in the worst-case interpolation scenarios for both models, the regression error is always maintained $< 20\%$. In particular, the uncertainties deriving from the limited regression accuracy of PR will be taken into account at the control design stage to ensure the robustness and reliability of the design. Coherently, the uncertainties affecting the MR model, employed in the simulator environment, will serve to test the capability of the controller to handle any source of uncertainties or disturbances.

1.3.3.4 Canards Aerodynamic (Control) Model

The second campaign of CFD simulations discussed in Section 1.3.2.3 was dedicated to the aerodynamic characterization of the right canard local deflection, δ_r. The corresponding left canards coefficients were inferred from the symmetrical properties of the projectile's concept. A polynomial regression approach is employed in the data fitting analysis for the coefficients $C_{X_{\delta_r}}$, $C_{Z_{\delta_r}}$, $C_{l_{\delta_r}}$ and $C_{m_{\delta_r}}$. The same regression model parameterization presented in Equation (1.29) is considered (increasing polynomial orders), accounting for the δ_r variation. The accuracy of the regression analysis is assessed through the standard statistical indexes. The overall results are presented in Figure 1.17 and Figure 1.18, in terms of R^2 and NRMSE.

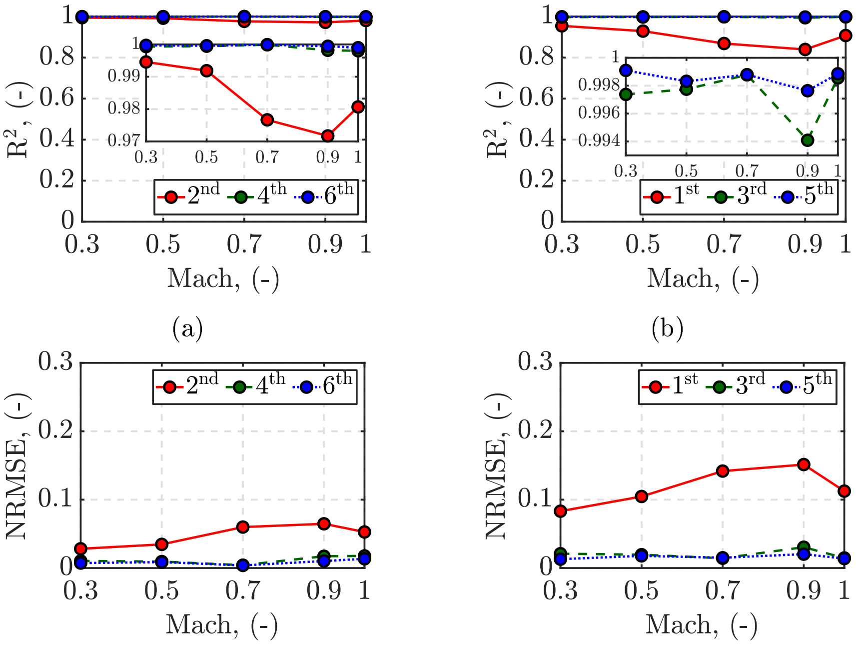

(a) (b)

(c) (d)

Figure 1.17: R^2 and NRMSE regression results: (a)-(c) longitudinal force control coefficient, $C_{X_{\delta_r}}$; (b)-(d) vertical force control coefficient, $C_{Z_{\delta_r}}$.

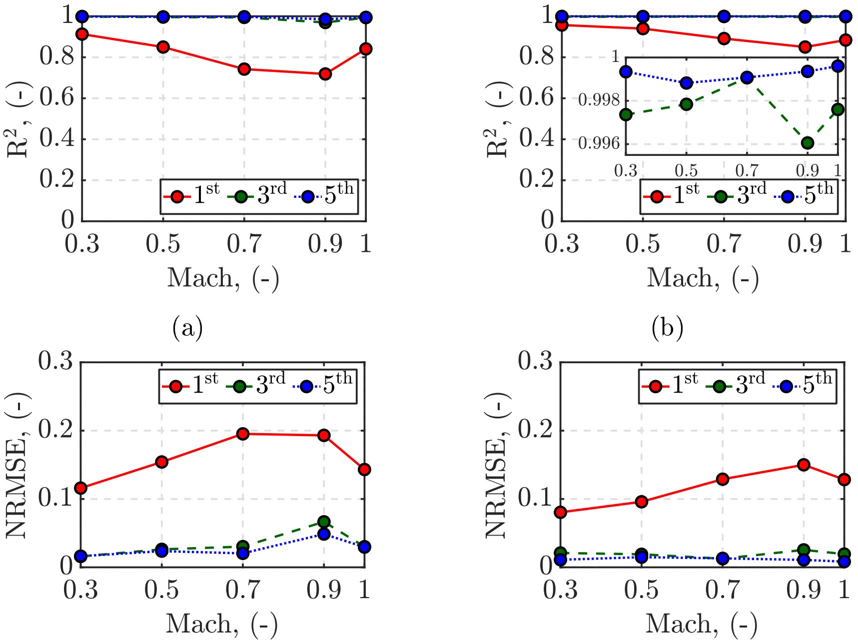

(a) (b)

(c) (d)

Figure 1.18: R^2 and NRMSE regression results: (a)-(c) rolling moment control coefficient, $C_{l_{\delta_r}}$; (b)-(d) pitching moment control coefficient, $C_{m_{\delta_r}}$.

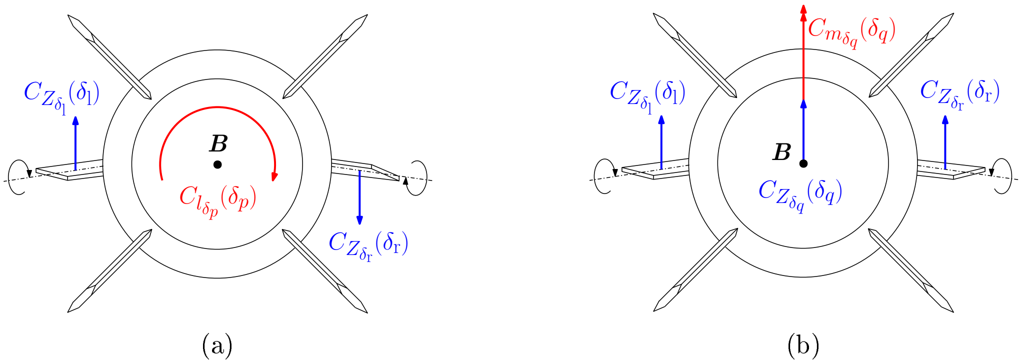

Figure 1.19: Virtual control deflections: (a) roll coefficients; (b) pitch coefficients.

Based on the regression results, the following model is selected to express the right (and left) canard control aerodynamic coefficients:

$$\begin{aligned}
C_{X_{\delta_{\rm r}}}(\mathcal{M},\delta_{\rm r}) &= C_{X_{\delta_{\rm r}0}}(\mathcal{M}) + C_{X_{\delta_{\rm r}2}}(\mathcal{M})\sin^2\delta_{\rm r},\\
C_{Z_{\delta_{\rm r}}}(\mathcal{M},\delta_{\rm r}) &= C_{Z_{\delta_{\rm r}1}}(\mathcal{M})\sin\delta_{\rm r} + C_{Z_{\delta_{\rm r}3}}(\mathcal{M})\sin^3\delta_{\rm r},\\
C_{l_{\delta_{\rm r}}}(\mathcal{M},\delta_{\rm r}) &= C_{l_{\delta_{\rm r}1}}(\mathcal{M})\sin\delta_{\rm r} + C_{l_{\delta_{\rm r}3}}(\mathcal{M})\sin^3\delta_{\rm r},\\
C_{m_{\delta_{\rm r}}}(\mathcal{M},\delta_{\rm r}) &= C_{m_{\delta_{\rm r}1}}(\mathcal{M})\sin\delta_{\rm r} + C_{m_{\delta_{\rm r}3}}(\mathcal{M})\sin^3\delta_{\rm r}.
\end{aligned} \tag{1.33}$$

The overall control contributions generated by the canard deflections can be computed by superposition, assuming the aerodynamic response of the canards to be in a linear domain:

$$\begin{aligned}
C_{X_\delta}(\mathcal{M},\delta) &= C_{X_{\delta_{\rm r}}}(\mathcal{M},\delta_{\rm r}) + C_{X_{\delta_{\rm l}}}(\mathcal{M},\delta_{\rm l}),\\
C_{Z_\delta}(\mathcal{M},\delta) &= C_{Z_{\delta_{\rm r}}}(\mathcal{M},\delta_{\rm r}) + C_{Z_{\delta_{\rm l}}}(\mathcal{M},\delta_{\rm l}),\\
C_{l_\delta}(\mathcal{M},\delta) &= C_{l_{\delta_{\rm r}}}(\mathcal{M},\delta_{\rm r}) + C_{l_{\delta_{\rm l}}}(\mathcal{M},\delta_{\rm l}),\\
C_{m_\delta}(\mathcal{M},\delta) &= C_{m_{\delta_{\rm r}}}(\mathcal{M},\delta_{\rm r}) + C_{m_{\delta_{\rm l}}}(\mathcal{M},\delta_{\rm l}).
\end{aligned} \tag{1.34}$$

The control allocator in Equation (1.25) converts the individual deflections of the canards into a combined set of virtual contributions, δ_p and δ_q, which is more convenient for control design. Coherently, the aerodynamic model has to address the virtual set of coefficients, ($C_{X_{\delta_{\rm eff}}}$, $C_{Z_{\delta_q}}$, $C_{l_{\delta_p}}$, $C_{m_{\delta_q}}$) in Figure 1.19, instead of the global contributions in Equation (1.34). Since no CFD measurements of the virtual deflections are available, and according to the superposition hypothesis, the aerodynamic virtual coefficients can be approximated as the direct interpolation of the virtual deflections (δ_p, δ_q) on the available regression surfaces in Equation (1.33). The approximated interpolation is expressed as follows:

$$\begin{aligned}
C_{Z_{\delta_q}}(\mathcal{M},\delta_q) &\simeq C_{Z_{\delta_{\rm r}}}\left(\mathcal{M},\frac{\delta_{\rm r}+\delta_{\rm l}}{2}\right) \simeq \frac{C_{Z_{\delta_{\rm r}}}(\mathcal{M},\delta_{\rm r}) + C_{Z_{\delta_{\rm l}}}(\mathcal{M},\delta_{\rm l})}{2},\\
C_{l_{\delta_p}}(\mathcal{M},\delta_p) &\simeq C_{l_{\delta_{\rm r}}}\left(\mathcal{M},\frac{\delta_{\rm l}-\delta_{\rm r}}{2}\right) \simeq \frac{C_{l_{\delta_{\rm l}}}(\mathcal{M},\delta_{\rm l}) - C_{l_{\delta_{\rm r}}}(\mathcal{M},\delta_{\rm r})}{2},\\
C_{m_{\delta_q}}(\mathcal{M},\delta_q) &\simeq C_{m_{\delta_{\rm r}}}\left(\mathcal{M},\frac{\delta_{\rm r}+\delta_{\rm l}}{2}\right) \simeq \frac{C_{m_{\delta_{\rm r}}}(\mathcal{M},\delta_{\rm r}) + C_{m_{\delta_{\rm l}}}(\mathcal{M},\delta_{\rm l})}{2}.
\end{aligned} \tag{1.35}$$

Concerning the longitudinal control coefficient, the highly nonlinear behavior characterizing the CFD acquisitions in Figure 1.10(a) at lower deflection angles implies the definition of a nonlinear interpolation, based on the roll and pitch contribution, $\delta_{\text{eff}} = \sqrt{\delta_p^2 + \delta_q^2}$:

$$C_{X_{\delta_{\text{eff}}}}(\mathcal{M}, \delta_{\text{eff}}) \simeq C_{X_{\delta_{\text{r}}}}\left(\mathcal{M}, \sqrt{\delta_p^2 + \delta_q^2}\right) \simeq \frac{C_{X_{\delta_{\text{r}}}}(\mathcal{M}, \delta_{\text{r}}) + C_{X_{\delta_{\text{l}}}}(\mathcal{M}, \delta_{\text{l}})}{2}. \tag{1.36}$$

The approximations accuracy relies on the assumption of a linear aerodynamic response of the canards. To analyze the range of validity of Equations (1.35)-(1.36), an interpolation analysis targets the entire deflection ranges, $\delta_{\text{r}}, \delta_{\text{l}} \in [-36, 36]$ deg, and Mach values investigated during the CFD simulations. The analysis is based on the Algorithm 2, where a linearity error, e_{N}, is evaluated at each flight condition as the difference between the global coefficients in Equation (1.34), interpolated on the CFD surfaces, and the approximated virtual ones in Equations (1.35)-(1.36), interpolated on the regression models. The results are normalized by the corresponding average value of the CFD surface interpolated at the same Mach conditions.

The results in Figures 1.20-1.23 show the influence of the Mach variation on the linearity error of the coefficients $C_{X_{\delta_{\text{eff}}}}$, $C_{Z_{\delta_q}}$, $C_{l_{\delta_p}}$, $C_{m_{\delta_q}}$, respectively. The error is represented in terms of level contours of increasing values. As expected, the deflection range corresponding to a linearity error $e_{\text{l}} \leq 10\%$ is generally wider at a lower Mach value, $\mathcal{M} < 0.7$, while it tends to increase when approaching the transonic flight regime. The only exception is represented by the longitudinal coefficient in Figure 1.20, which shows low error at any conditions due to the nonlinear nature of the interpolation selected in Equation (1.36). Finally, the order of complexity of the polynomial regression models in Equation (1.33) also affects the accuracy of the interpolation since the regression process is an additional source of model uncertainties. Higher-order models would provide lower interpolation error, but they would explode the complexity at the control design stage.

As a global result, the linear approximations formulated in Equations (1.35)-(1.36) provide reliable modeling properties for canard deflections $|\delta_{\text{r}}|, |\delta_{\text{l}}| < 20$ deg, preventing possible stall conditions characterizing the CFD curves in Figure 1.10.

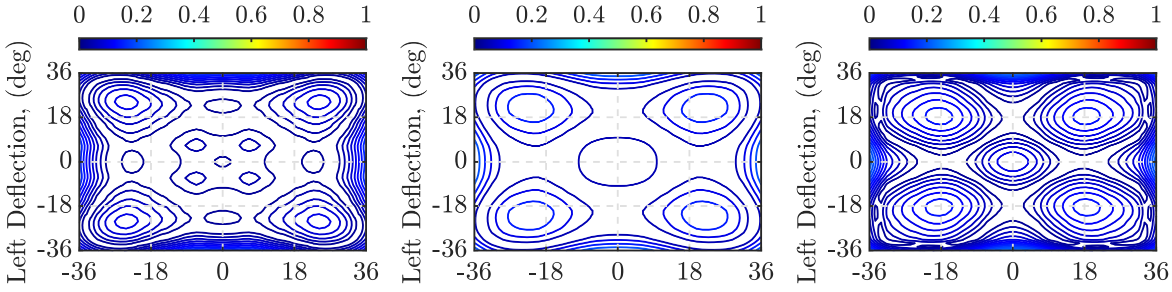

(a) (b) (c)

Figure 1.20: $C_{X_{\delta_{\text{eff}}}}$ coefficient linearity error surfaces at different flight regimes: (a) $\mathcal{M} = 0.3$; (b) $\mathcal{M} = 0.7$; (c) $\mathcal{M} = 1$.

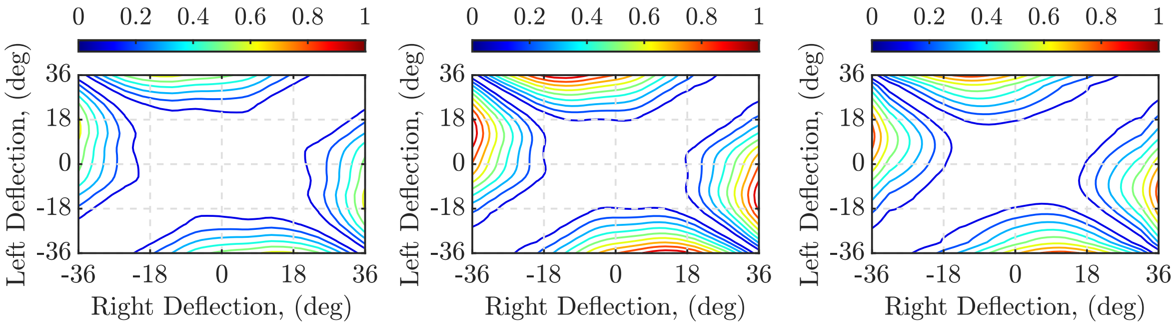

(a) (b) (c)

Figure 1.21: $C_{Z_{\delta_q}}$ coefficient linearity error surfaces at different flight regimes: (a) $\mathcal{M} = 0.3$; (b) $\mathcal{M} = 0.7$; (c) $\mathcal{M} = 1$.

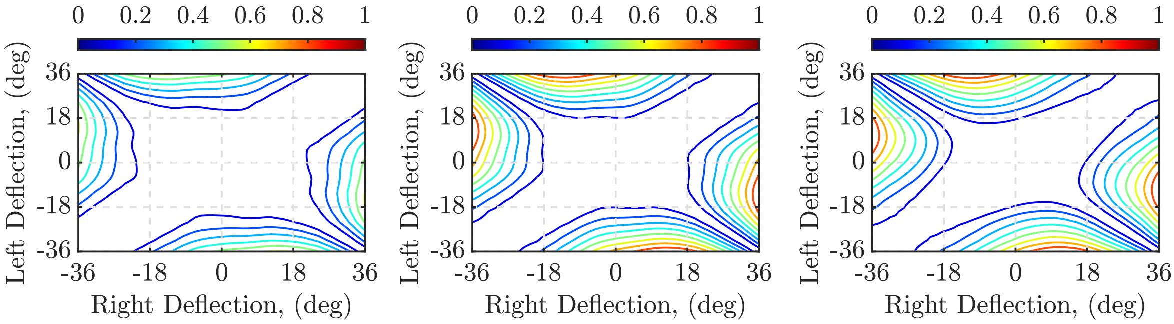

(a) (b) (c)

Figure 1.22: $C_{l_{\delta_p}}$ coefficient linearity error surfaces at different flight regimes: (a) $\mathcal{M} = 0.3$; (b) $\mathcal{M} = 0.7$; (c) $\mathcal{M} = 1$.

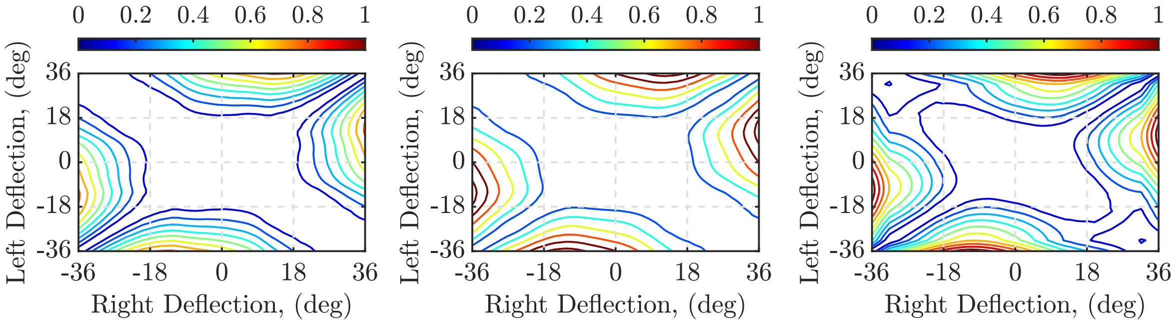

(a) (b) (c)

Figure 1.23: $C_{m_{\delta_q}}$ coefficient linearity error surfaces at different flight regimes: (a) $\mathcal{M} = 0.3$; (b) $\mathcal{M} = 0.7$; (c) $\mathcal{M} = 1$.

Algorithm 2 Linearity Error Analysis

```
For any $j = X, Z, l, m$:
    For any $\mathcal{M}$:
        For any $(\delta_{\mathrm{r}}, \delta_{\mathrm{l}})$ combination:
            1. Select the flight condition: $(\mathcal{M}, \delta_{\mathrm{r}}, \delta_{\mathrm{l}})$.
            2. Convert the deflection angles, based on the allocation logic in Equation (1.25):
                   $(\delta_{\mathrm{eff}}, \delta_q, \delta_q) = f(\delta_{\mathrm{r}}, \delta_{\mathrm{l}})$.
            3. Interpolate $\delta_{\mathrm{r}}$ and $\delta_{\mathrm{l}}$ on the CFD surfaces:
                   $C_{j_{\delta_{\mathrm{r}}},\mathrm{CFD}} = \mathrm{interp}(\mathcal{M}, \delta_{\mathrm{r}}); \qquad C_{j_{\delta_{\mathrm{l}}},\mathrm{CFD}} = \mathrm{interp}(\mathcal{M}, \delta_{\mathrm{l}}),$
               and evaluated the global coefficients as in Equation (1.34):
                   $C_{j_\delta,\mathrm{CFD}}(\mathcal{M}, \delta_{\mathrm{r}}, \delta_{\mathrm{l}}) = C_{j_{\delta_{\mathrm{l}}},\mathrm{CFD}} + C_{j_{\delta_{\mathrm{r}}},\mathrm{CFD}}; \qquad \text{if } j = X, Z, m.$
                   $C_{j_\delta,\mathrm{CFD}}(\mathcal{M}, \delta_{\mathrm{r}}, \delta_{\mathrm{l}}) = C_{j_{\delta_{\mathrm{l}}},\mathrm{CFD}} - C_{j_{\delta_{\mathrm{r}}},\mathrm{CFD}}; \qquad \text{if } j = l.$
            4. Interpolate $\delta_{\mathrm{eff}}$, $\delta_q$ or $\delta_p$ on the regression models in Equation (1.33):
                   $C_{j_{\delta_{\mathrm{eff}}}} = \mathrm{interp}(\mathcal{M}, \delta_{\mathrm{eff}}); \qquad \text{if } j = X.$
                   $C_{j_{\delta_q}} = \mathrm{interp}(\mathcal{M}, \delta_q); \qquad \text{if } j = Z, m.$
                   $C_{j_{\delta_p}} = \mathrm{interp}(\mathcal{M}, \delta_p); \qquad \text{if } j = l.$
            5. Evaluate the normalized linearity error as:
                   $e_{j,\mathrm{N}}(\mathcal{M}, \delta_{\mathrm{r}}, \delta_{\mathrm{l}}) = \dfrac{e_j(\mathcal{M}, \delta_{\mathrm{r}}, \delta_{\mathrm{l}})}{\bar{C}_{j,\mathrm{CFD}}(\mathcal{M})},$
               with
                   $e_j(\mathcal{M}, \delta_{\mathrm{r}}, \delta_{\mathrm{l}}) = C_{j_{\delta_h}}(\mathcal{M}, \delta_i) - C_{j_\delta,\mathrm{CFD}}(\mathcal{M}, \delta_{\mathrm{r}}, \delta_{\mathrm{l}}); \qquad \text{for } h = \mathrm{eff}, q, p.$
                   $\bar{C}_{j,\mathrm{CFD}}(\mathcal{M}) = \dfrac{\sum_{i=1}^{n} \sum_{k=1}^{n} C_{j,\mathrm{CFD}}(\mathcal{M}, \delta_{\mathrm{r},i}, \delta_{\mathrm{l},k})}{n^2},$
               where $n$ is the dimension of the investigated $\delta_{\mathrm{r}}$, $\delta_{\mathrm{l}}$ range.
        end.
    end.
end.
```

1.4 6-DoF Simulator Environment

The results obtained in the previous sections are implemented in a complete nonlinear flight simulator environment, meant to be later employed in the validation phase of the autopilot design. The simulator is designed in the MATLAB/Simulink environment, by means of the dedicated System Modeling Ammunition Research Toolbox (SMART) library developed at ISL and presented in Section 1.4.1. The complete architecture of the simulator is discussed in Section 1.4.2, while ballistic simulations are employed in Section 1.4.3 to validate the overall environment design.

1.4.1 The SMART Toolbox

The System Modeling Ammunition Research Toolbox (SMART) Simulink library consists of a project proposed and developed in the past fifteen years at the French-German Research Institute of Saint-Louis. The core idea was to provide a standardized and common software environment to perform the guidance, navigation, and control design of several models of aircraft, missiles, and projectiles. The first version of the environment was initially coded in FORTRAN and consisted of an exterior ballistic 6-DoF simulator, which did not include any control design features. Later in 2004, the Computer Aided Design of Aerospace Concepts (CADAC) presented in [Zip14] was employed as a reference model for the development of the Simulink environment, extending the modeling features to the rolling and the non-spinning dynamic frames of the vehicle's airframe ([Wer07]). In 2013 a complete version of the simulation environment allowed selecting among several projectile/missile dynamic models and integrating guidance, navigation, and control features in the same simulation. The library consists of generalized Simulink blocks whose parameters can be tuned to implement both vehicle dynamics and atmosphere models, as well as different control architectures, guidance strategies, and navigation algorithms ([GWT13]). The library finally addressed as SMART, has been further developed in the last few years by including spinning projectile models.

1.4.2 Nonlinear Simulator

The nonlinear simulator intends to provide an accurate representation of the flight conditions in which the controller is supposed to operate. Thus, it targets the flight dynamics of the projectile, as well as the dynamics of the environment including the atmosphere properties, unwanted wind disturbances, and the gravitational effect. The scheme in Figure 1.24 exhibits the complete architecture of the simulation environment developed in Simulink, addressing each aspect of the standard GNC loop.

Guidance. The guidance Simulink block allows implementing different flight strategies depending on the objectives that are selected for a specific simulation. As introduced in Section 1.2.4, the LRGP project aims to improve the operating range of standard guided ammunition.

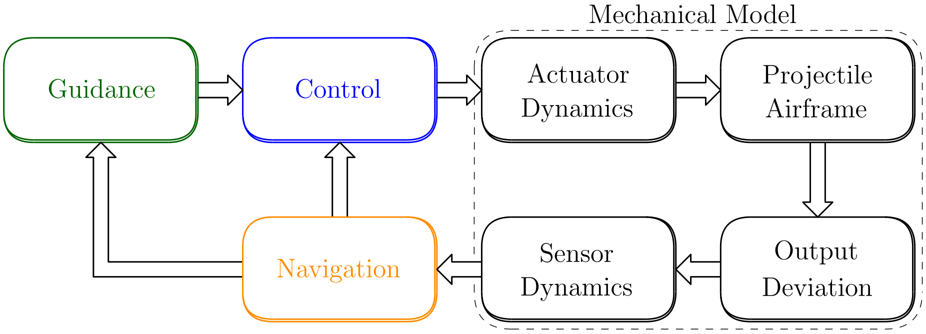

Figure 1.24: Nonlinear simulator: complete software environment.

Coherently with the purposes of the project, the guidance block implements online the LDR optimization law proposed in [KCL82]. The algorithm provides a trade-off between highly complicated head-on approaches and sub-optimal architectures based on a set of open-loop offline evaluations of a standard pitch-attitude dynamics. Assuming quasi-steady state glide equilibrium conditions with approximately constant dynamic pressure for the 2-DoF pitch-attitude dynamics, and assuming that an optimal Lift-to-Drag Ratio, $\mathrm{LDR}_{\mathrm{max}}$, exists at each flight condition, the corresponding equilibrium flight-path angle, γ_{eq}, can be expressed as:

$$\gamma_{\mathrm{eq}} = -\frac{1}{\mathrm{LDR}_{\mathrm{max}}|1 + \beta_{\mathrm{atm}}(\frac{V^2}{2g})|} \tag{1.37}$$

where $\beta_{\mathrm{atm}} = 1.389 \cdot 10^{-4}$ 1/m represents the exponent of the atmosphere density, modeled as $\rho_{\mathrm{atm}} = \rho_{\mathrm{atm},0} e^{-\beta_{\mathrm{atm}} h}$ with $\rho_{\mathrm{atm},0} = 1.227$ kg/m^3. A reference AoA command, α_{ref}, can be derived from the combination:

$$\alpha_{\mathrm{ref}} = \alpha_{\mathrm{LDR,max}} + k_\gamma(\gamma_{\mathrm{eq}} - \gamma) \tag{1.38}$$

where $\alpha_{\mathrm{LDR,max}}$ consists of the optimal AoA, obtained by trimming the pitch-attitude dynamics at each $\mathrm{LDR}_{\mathrm{max}}$ condition, and γ is the actual flight-path angle measured along the trajectory. The coefficient k_γ allows adjusting the relevance of the flight-path angle correction with respect to the trimmed $\alpha_{\mathrm{LDR,max}}$, aiming to find an optimal trad-off and to avoid excessively sharp variations of the resulting reference signal. For the present study, $k_\gamma = 0.35$ has been selected, and a dataset of ($\mathrm{LDR}_{\mathrm{max}}$, $\alpha_{\mathrm{LDR,max}}$) has been provided through dedicated CFD campaigns on the complete projectile dynamics to increase the accuracy.

Navigation. The navigation block allows the implementation of any kind of estimation algorithm or measurement processing to determine the current state of the system. During the controller design, perfect navigation conditions (accurate and undelayed) are assumed. However, at the validation stage, sensor noise (measurement noise) should be taken into account for a more realistic simulation scenario.

Control. The control block includes the designed autopilot to be tested in simulation. This represents the core objective of the present work, and it will be treated in detail in Chapter 3 and Chapter 4, where different LPV-based controller design approaches and architectures will be proposed and eventually compared.

Actuator and Sensor Dynamics. The impact of the actuators and the sensor dynamics is also accounted for, aiming to improve the accuracy of the simulator. In particular, the actuators are modeled as second-order systems characterized by the following transfer function:

$$T_{\text{act}} = \frac{\omega_\delta}{s^2 + 2\omega_\delta \xi_\delta s + \omega_\delta^2} \tag{1.39}$$

where $\omega_\delta = 150$ rad/s is the actuator bandwidth, and $\xi_\delta = 0.707$ represents the damping ratio. Additionally, angular position and angular rate saturation are also addressed, respectively as the ranges $[-40, 40]$ deg, and $[-100, 100]$ deg/s.

Projectile Airframe. The airframe block contains a complete description of the flight mechanics, the environment, and the generation of the aerodynamic contributions, as presented in Figure 1.25. In particular, the *Environment Model* provides a general representation of the atmosphere following the International Standard Atmosphere (ISA) 1975, ISO 2533 ([Atm]). In addition, it includes continuous and discrete models of the wind contributions (turbulence, gusts), employed as sources of disturbance to assess the robustness of the controller in more realistic scenarios. Further details will be provided in Chapter 4.

Concerning the *Aerodynamic Model*, the *Multivariable Regression* static model (Model_1 in Equation (1.31)), and the control contributions described in Equations (1.33)-(1.36) are employed in the simulator environment. Based on a significant CFD dataset, this model allows accounting for all the possible flight configurations that the projectile might experience during the trajectory. The *Flight Mechanics* block implements the 6-DoF model of the projectile, including the dynamic and kinematic equations of motion discussed in Equations (1.12)-(1.13), and Equations (1.14)-(1.17) respectively. Finally, the control allocator converts the individual right and left canards' deflections into combined pitch and roll contributions, as previously expressed in Equation (1.25).

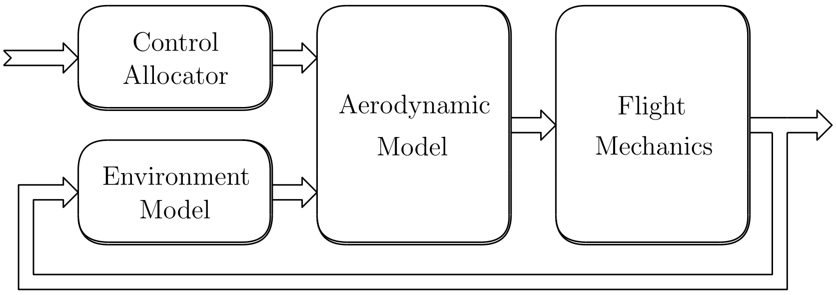

Figure 1.25: Nonlinear simulator: projectile airframe architecture.

1.4.3 Model Validating Simulations

The validation of the nonlinear simulator environment relies on open-loop ballistic simulations, targeting each phase of the projectile trajectory:

I. Ballistic ascending phase (from the firing point to the apogee).

II. Ballistic gliding phase (from the apogee to the target).

In particular, during phase I, the projectile is in the ballistic configuration shown in Figure 1.4(b), having the control surfaces folded inside the sabot. Thus, the projectile aerodynamics is based on the online interpolation of the static coefficient surfaces acquired through the first CFD campaign. The firing stage consists of an initial elevation angle $\theta_\mathrm{e} = 60$ deg at zone 6, equivalent to an initial longitudinal velocity of approximately $u_0 = 939$ m/s. The projectile is supposed to be ideally fired with almost no spin, in reason of the fin-stabilized architecture. Any residual spinning motion is expected to be damped during the ascending phase by the opposing Drag generated by the fins.

Concerning the ballistic gliding phase II, Figure 1.26 highlights the comparison between a gliding phase characterized by a ballistic configuration where the canards are not deployed at the apogee of the trajectory (dashed blue), and a gliding phase assuming a glider configuration in Figure 1.4(b) with the canards fully deployed and maintained at zero local deflection angles, δ_r,$\delta_\mathrm{l} = 0$ deg (solid red). The former trajectory depends on the aerodynamic CFD dataset interpolation employed for the ballistic ascending phase. Differently, the glider-based trajectory relies on the *Multivariable Regression* model described in the *Projectile Airframe* paragraph. Since no guidance references are provided and zero control actions are applied on the projectile across the trajectory, the terminal guidance phase is not considered for the simulation. Similarly, the lateral dynamics of the projectile is also neglected due to the absence of lateral steering maneuvers and wind contributions.

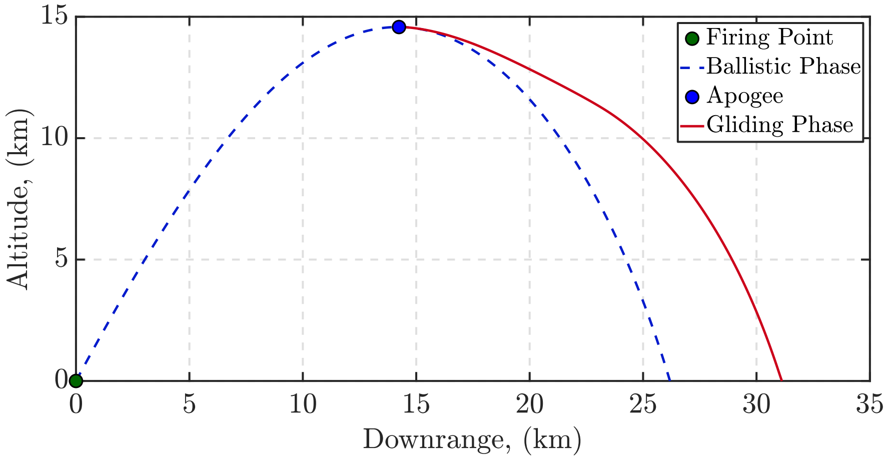

Figure 1.26: Ballistic simulations: trajectory performance comparison.

The trajectory results in Figure 1.26 show the range enhancement provided by the additional lifting contribution of the control surfaces, even in the absence of direct control commands. However, the canard contributions generate a relevant destabilizing effect on the projectile aerodynamics, since the overall CP, where the aerodynamic forces are ideally applied, is pushed ahead of the projectile CM. This destabilizing effect is consistent with the CFD data acquired during the aerodynamic characterization of the projectile, and it is highlighted by the oscillation affecting the results in Figures 1.27(a)(c)(d)(e).

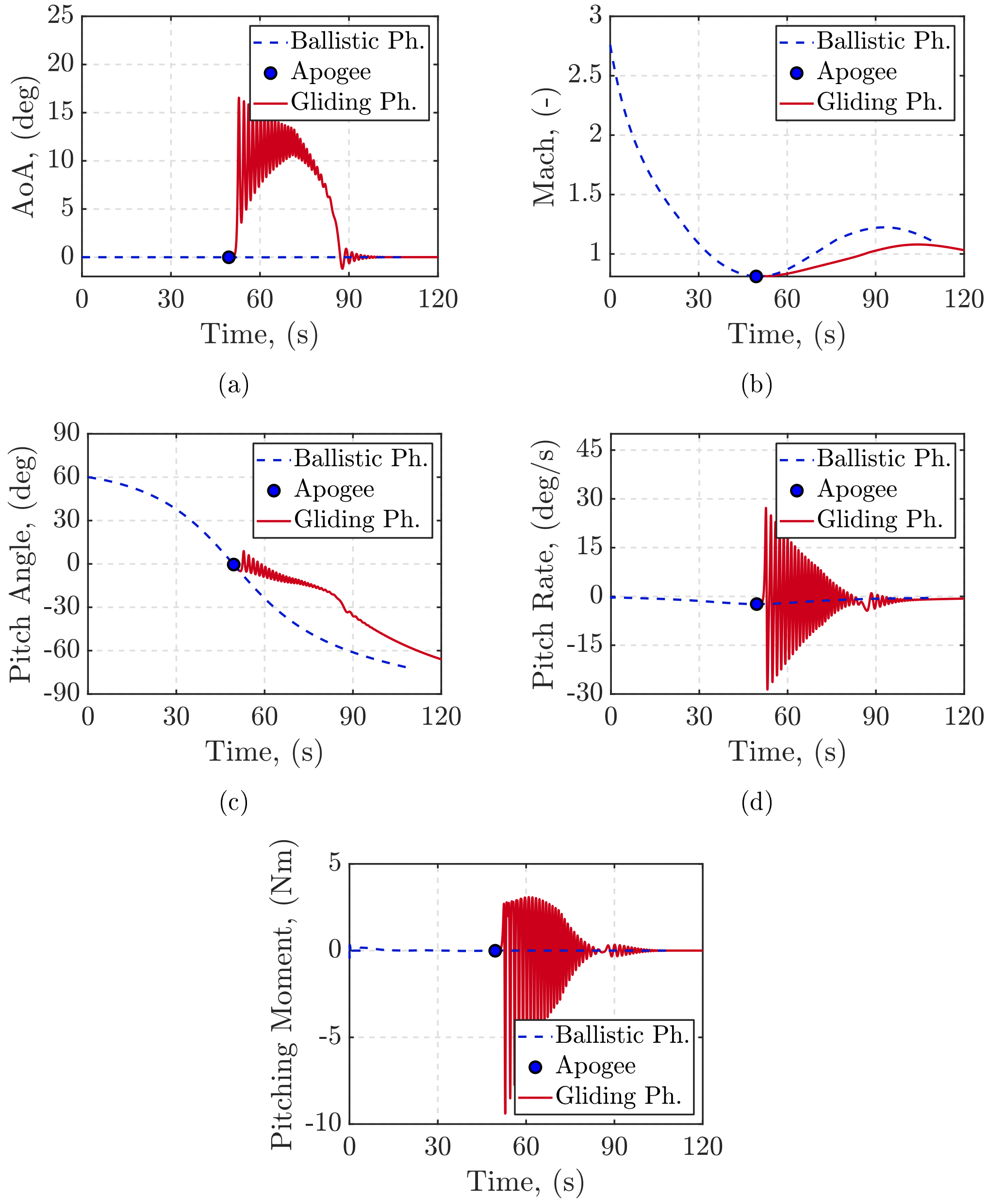

(a) (b) (c) (d) (e)

Figure 1.27: Ballistic simulations: (a) AoA trajectories; (b) Mach trajectories; (c) pitch angle trajectories; (d) pitch rate trajectories; (e) pitching moment trajectories.

In particular, the aerodynamic instability is numerically quantified by the positive values of the pitching moment in Figure 1.27(e), which induce a divergent increase of the projectile's AoA, until a new equilibrium condition is found across the trajectory ($t = 90$ s). These observation are coherent with the aerodynamic analysis previously discussed in Section 1.3.2.2. These preliminary open-loop results serve as validation, not only for the accuracy of the aerodynamic model developed through the regression analysis, but for the overall simulator environment architecture. Indeed, the simulator will be later employed for the assessment of the autopilot design performance.

1.5 Concluding Remarks

In this chapter, the nonlinear flight dynamics model of a new class of long-range guided projectiles (LRGP) has been derived. The modeling process relies on the standard formulation of the nonlinear differential equations describing the projectile inertial dynamics. An overview of the fundamental reference frames and coordinate systems was provided at the beginning of the chapter. The core part was dedicated to an exhaustive analysis developed to characterize the aerodynamics of the LRGP concept. The definition of a dedicated acquisition framework allowed reducing the computational complexity related to the estimation of a large set of CFD data. The CFD analysis targeted the two main aerodynamic contributions of the projectile. A first acquisition campaign analyzed the aerodynamic coefficients generated by the static Lift and Drag contributions of the projectile's body, including the effect of the control surfaces at zero local deflection. The second acquisition dataset investigated the additional aerodynamic contributions generated by the local deflection of the control surfaces.

In order to provide a continuous model that describes the projectile aerodynamics at any flight conditions, the CFD data have been processed through an accurate regression analysis. A polynomial single variable model (PR), and a multivariable model (MR) were obtained from the regression of the static coefficients. The former PR model is based on a reduced set of CFD data, targeting the most critical conditions of the projectile aerodynamics. The latter MR model relies on the entire CFD acquisition dataset, providing a global aerodynamic description that targets a wider range of flight conditions. A polynomial regression has been performed also on the control surfaces CFD dataset. For control-oriented modeling purposes, the individual aerodynamic contributions of the control surfaces are formulated as global body rate effects that influence the projectile's orientation. The overall control formulation relies on linear superposition assumptions concerning the aerodynamic response of the projectile. The range of confidence of the aerodynamic model was estimated around a total deflection equal to $\delta \in [-20, 20]$ deg.

Based on the results of the flight dynamics and aerodynamics modeling processes, different models have been developed to represents specific features of the projectile dynamics. Depending on the level of accuracy and complexity, each model can be employed in different stages of the autopilot design and validation.

Projectile Pitch Channel Nonlinear Model. The first model targets the projectile pitch channel dynamics defined in Equations (1.22)-(1.23), including the dynamics of the AoA and the pitch rate, the PR static aerodynamic model in Equation (1.30), and the aerodynamic contributions of the control surfaces derived in Equations (1.33)-(1.36), as:

$$\begin{aligned}
\frac{\mathrm{d}\alpha}{\mathrm{d}t} &= \frac{\bar{q}S}{mV}\left[-\left(C_{X_\mathrm{S}} + C_{X_{\delta_\mathrm{eff}}}\right)\sin\alpha + \left(C_{Z_\mathrm{S}} + \left(\frac{d}{2V}\right)C_{Z_q}q + C_{Z_{\delta_q}}\right)\cos\alpha\right] \\
&\qquad + q + \frac{g}{V}\left(\sin\theta\sin\alpha + \cos\theta\cos\phi\cos\alpha\right), \\
\frac{\mathrm{d}q}{\mathrm{d}t} &= \frac{\bar{q}Sd}{I_2}\left(C_{m_\mathrm{S}} + \left(\frac{d}{2V}\right)C_{m_q}q + C_{m_{\delta_q}}\right), \\
\eta_z &= \frac{\bar{q}S}{mg}\left(C_{Z_\mathrm{S}} + \left(\frac{d}{2V}\right)C_{Z_q}q + C_{Z_{\delta_q}}\right),
\end{aligned} \tag{1.40}$$

where the PR static aerodynamic model is expressed as:

$$\begin{aligned}
C_{X_\mathrm{S}} &= C_{X_{\alpha 0}}(\mathcal{M}) + C_{X_{\alpha 2}}(\mathcal{M})\sin^2\alpha + C_{X_{\alpha 4}}(\mathcal{M})\sin^4\alpha, \\
C_{Z_\mathrm{S}} &= C_{Z_{\alpha 1}}(\mathcal{M})\sin\alpha, \\
C_{m_\mathrm{S}} &= C_{m_{\alpha 1}}(\mathcal{M})\sin\alpha + C_{m_{\alpha 3}}(\mathcal{M})\sin^3\alpha + C_{m_{\alpha 5}}(\mathcal{M})\sin^5\alpha,
\end{aligned} \tag{1.41}$$

and the control contributions are formulated as:

$$\begin{aligned}
C_{X_{\delta_\mathrm{eff}}} &= C_{X_{\delta_\mathrm{eff}0}}(\mathcal{M}) + C_{X_{\delta_\mathrm{eff}2}}(\mathcal{M})\sin^2\delta_\mathrm{eff}, \\
C_{Z_{\delta_q}} &= C_{Z_{\delta_q 1}}(\mathcal{M})\sin\delta_q + C_{Z_{\delta_q 3}}(\mathcal{M})\sin^3\delta_q, \\
C_{m_{\delta_q}} &= C_{m_{\delta_q 1}}(\mathcal{M})\sin\delta_q + C_{m_{\delta_q 3}}(\mathcal{M})\sin^3\delta_q.
\end{aligned} \tag{1.42}$$

This model will be employed for the LPV modeling and control design of a dedicated pitch autopilot, respectively in Chapter 2 and Chapter 3.

Projectile 6-DoF Nonlinear Model. A full nonlinear description of the projectile dynamics and aerodynamics is derived through the employment of the translational and attitude dynamics in Equation (1.12) and Equation (1.13) respectively, the complete MR aerodynamic model in Equation (1.31), and the corresponding aerodynamic control contributions, formulated as:

$$\begin{aligned}
\frac{\mathrm{d}u}{\mathrm{d}t} &= rv - qw + \frac{\bar{q}S}{m}\left(C_{X_\mathrm{S}} + C_{X_{\delta_\mathrm{eff}}}\right) - g\sin\theta, \\
\frac{\mathrm{d}v}{\mathrm{d}t} &= pw - ru + \frac{\bar{q}S}{m}\left(C_{Y_\mathrm{S}} + \left(\frac{d}{2V}\right)C_{Y_r}r\right) + g\cos\theta\sin\phi, \\
\frac{\mathrm{d}w}{\mathrm{d}t} &= qu - pv + \frac{\bar{q}S}{m}\left(C_{Z_\mathrm{S}} + \left(\frac{d}{2V}\right)C_{Z_q}q + C_{Z_{\delta_q}}\right) + g\cos\theta\cos\phi,
\end{aligned} \tag{1.43}$$

and:

$$
\begin{aligned}
\frac{\mathrm{d}p}{\mathrm{d}t} &= I_1^{-1}\left[(I_2 - I_3)\,qr + \bar{q}Sd\left(\left(\frac{d}{2V}\right)C_{l_p}p + C_{l_{\delta_p}}\right)\right],\\
\frac{\mathrm{d}q}{\mathrm{d}t} &= I_2^{-1}\left[(I_3 - I_1)\,pr + \bar{q}Sd\left(C_{m_\mathrm{S}} + \left(\frac{d}{2V}\right)C_{m_q}q + C_{m_{\delta_q}}\right)\right],\\
\frac{\mathrm{d}r}{\mathrm{d}t} &= I_3^{-1}\left[(I_1 - I_2)\,pq + \bar{q}Sd\left(C_{n_\mathrm{S}} + \left(\frac{d}{2V}\right)C_{n_r}r\right)\right],
\end{aligned}
\tag{1.44}
$$

where the MR static aerodynamic model is expressed as:

$$
\begin{aligned}
C_{X_\mathrm{S}} &= C_{X_0}(\mathcal{M}) + C_{X_2}(\mathcal{M})\cos\alpha\cos\beta + C_{X_4}(\mathcal{M})\cos^2\!\alpha\cos^2\!\beta,\\
C_{Y_\mathrm{S}} &= C_{Y_1}(\mathcal{M})\sin\beta + C_{Y_3}(\mathcal{M})\sin\beta\cos\beta\cos\alpha,\\
C_{Z_\mathrm{S}} &= C_{Z_2}(\mathcal{M})\sin\alpha\cos\beta,\\
C_{m_\mathrm{S}} &= C_{m_2}(\mathcal{M})\sin\alpha\cos\beta + C_{m_4}(\mathcal{M})\sin\alpha\cos\alpha\cos^2\!\beta,\\
C_{n_\mathrm{S}} &= C_{n_1}(\mathcal{M})\sin\beta + C_{n_3}(\mathcal{M})\sin\beta\cos\beta\cos\alpha.
\end{aligned}
\tag{1.45}
$$

while the control contributions are:

$$
\begin{aligned}
C_{X_{\delta_\mathrm{eff}}} &= C_{X_{\delta_\mathrm{eff}0}}(\mathcal{M}) + C_{X_{\delta_\mathrm{eff}2}}(\mathcal{M})\sin^2\delta_\mathrm{eff},\\
C_{Z_{\delta_q}} &= C_{Z_{\delta_q1}}(\mathcal{M})\sin\delta_q + C_{Z_{\delta_q3}}(\mathcal{M})\sin^3\delta_q,\\
C_{l_{\delta_p}} &= C_{l_{\delta_p1}}(\mathcal{M})\sin\delta_p + C_{l_{\delta_p3}}(\mathcal{M})\sin^3\delta_p,\\
C_{m_{\delta_q}} &= C_{m_{\delta_q1}}(\mathcal{M})\sin\delta_q + C_{m_{\delta_q3}}(\mathcal{M})\sin^3\delta_q.
\end{aligned}
\tag{1.46}
$$

This model will be implemented in the nonlinear simulator environment in Chapter 4 to test the performance of the designed controllers in realistic trajectory-tracking simulation scenarios.

In the last section, the complete nonlinear flight dynamics model of the LRGP concept has been tested in simulation to assess the coherency with the aerodynamic dataset and the preliminary open-loop properties of the system dynamics. A first open-loop simulations comparison shows already the advantages provided by the deployment of the control surfaces, in terms of operating range capability. However, the improved range performance comes at the price of a higher unstable behavior. The simulations are performed in a nonlinear simulator, fully developed through a proprietary MATLAB/Simulink environment (SMART toolbox). A core aspect of the nonlinear simulator consists of the ease of integrating any guidance and navigation functionality to assess the performance of the later-designed autopilot.

Chapter 2

LPV Control-Oriented Modeling

Contents

2.1 Introduction

Control-oriented modeling consists of the intermediate step which allows the application of several control design approaches to the general nonlinear dynamics of a system. In the aerospace environment, a standard technique corresponds to the trimming and linearization process of a system flight envelope. The nonlinear dynamics of the vehicle is trimmed at selected flight conditions, aiming to identify the control input required to maintain the system at each desired steady-state point. The nonlinear dynamics is then linearized at the same flight points, assuming the identified trimming conditions. As a result, a collection of local linearizations of the system nonlinear dynamics is obtained and employed for the application of linear control design techniques ([The+10], [PPV01]). Despite its feasibility, the main drawbacks of this method consist of the inability to fully capture the system dynamics away from the design points. As a consequence, important nonlinearities and coupling terms that can affect the system behavior might be potentially neglected.

The linear parameter-varying (LPV) framework represents an interesting modeling alternative. Indeed, it allows for a more general and complete time-dependent representation of the system dynamics. Several successful aerospace applications have been proposed in the last years, relying on different LPV approaches such as function substitution ([Pfi12]; [MB04]), velocity-based techniques ([LL98]), and state transformation ([SC93]; [CS96]). In this chapter, the state transformation method is investigated to develop an accurate LPV model of the projectile pitch channel dynamics. The state transformation provides an exact transformation between the original nonlinear system and the obtained LPV model. Thus, no approximations are involved in the design, increasing the model capability to represent the original dynamics. The performance of the obtained LPV model is validated in simulation and compared with the original nonlinear dynamics. Finally, the LPV modeling process is completed through the control-oriented reformulation of the LPV system in a polytopic form, characterized by an affine model-parameter relation. The general LPV and the polytopic representations of the system dynamics are employed later, in the second part of the manuscript, for the corresponding control design approaches.

The chapter is structured in the following sections:

S2.2: provides a general introduction to the LPV class of systems, recalling the fundamental concepts related to the systems classification and the main parameter-varying formulations. An overview is dedicated to the different modeling approaches that allow reformulating the nonlinear dynamics of a system as an LPV model.

S2.3: presents the state transformation approach employed for the LPV modeling of the guided projectile nonlinear dynamics. The accuracy of the modeling process is verified in simulation, highlighting the advantages and drawbacks of the approach. Some relevant remarks are discussed in view of the later control design. The results presented in this section have been published in [Vina].

S2.4: discusses the modeling procedure developed to formulate the obtained LPV model of the projectile dynamics as a polytopic system. The procedure relies on a model approximation aimed at identifying a new set of scheduling functions, that respect the affine conditions required by the polytopic formulation. The ultimate objective consists of the identification of the convex space of model validity, defined by the new set of scheduling functions. The results presented in this section have been published in [Vina].

2.2 LPV Framework

Linear Parameter-Varying (LPV) refers to a class of systems whose state space representation is defined as a continuous function of a time-varying vector of scheduling parameters, denoted as $\boldsymbol{\rho}(t)^1$. In particular, the scheduling parameters are assumed to be measurable in real-time. A more detailed definition is provided in [SGB13] and [MS12].

In the following sections, some relevant definitions concerning the LPV class of systems are recalled together with an overview of the different LPV model formulations and the related properties. Particular attention is dedicated to the modeling approaches that allow the reformulation of the general nonlinear dynamics of a system into an accurate LPV model. Indeed, depending on the selected method, multiple LPV models can be derived from the same nonlinear dynamics, requiring a careful and detailed analysis.

2.2.1 LPV/quasi-LPV Systems

In this section, some key definitions concerning the mathematical representation of dynamical systems are recalled to introduce the LPV/quasi-LPV formulations. As summarized in Figure 2.1, LPV systems are a subclass of the more general nonlinear systems (NL). The time dependence characterizing the dynamics of LPV systems is expressed through the variation of a set of selected scheduling parameters. Furthermore, the linear time-invariant (LTI) class of systems can be interpreted as a local realization of LPV systems, evaluated at 'frozen' values of the scheduling parameters.

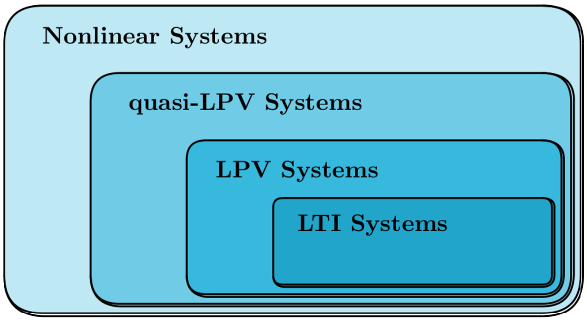

Figure 2.1: Classification diagram of dynamical systems.

Definition 2.1 (Nonlinear Systems (NL))
Given the set of nonlinear ordinary differential equations (ODEs), $\boldsymbol{f}(\boldsymbol{x}(t),\boldsymbol{u}(t)) \in \mathbb{R}^{n_x}$*, and* $\boldsymbol{g}(\boldsymbol{x}(t),\boldsymbol{u}(t)) \in \mathbb{R}^{n_y}$*, the nonlinear dynamics of a system,* Σ_{NL}*, can be expressed as:*

$$\Sigma_{\mathrm{NL}} : \begin{cases} \dot{\boldsymbol{x}}(t) = \boldsymbol{f}(\boldsymbol{x}(t),\boldsymbol{u}(t)) \\ \boldsymbol{y}(t) = \boldsymbol{g}(\boldsymbol{x}(t),\boldsymbol{u}(t)) \end{cases} \tag{2.1}$$

---

[1] The scheduling vector $\boldsymbol{\rho}(t)$ used in this chapter is different from the air density, $\rho(h)$, previously defined.

where $\boldsymbol{x} \in \mathbb{R}^{n_x}$ *represents the state vector of the system,* $\boldsymbol{u} \in \mathbb{R}^{n_u}$ *corresponds to the vector of exogenous input, and* $\boldsymbol{y} \in \mathbb{R}^{n_y}$ *is the measured output vector of the system.*

Definition 2.2 (Linear Parameter-Varying (LPV)/quasi-LPV Systems)
Given the vector of time-varying parameters, $\boldsymbol{\rho}(t) \in \mathbb{R}^{n_\rho}$*, and the set of parameter-varying matrices* $\mathcal{A}(\boldsymbol{\rho}(t)) \in \mathbb{R}^{n_x \times n_x}$*,* $\mathcal{B}(\boldsymbol{\rho}(t)) \in \mathbb{R}^{n_x \times n_u}$*,* $\mathcal{C}(\boldsymbol{\rho}(t)) \in \mathbb{R}^{n_y \times n_x}$*, and* $\mathcal{D}(\boldsymbol{\rho}(t)) \in \mathbb{R}^{n_y \times n_u}$*, the linear parameter-varying system,* Σ_{LPV}*, can be expressed as:*

$$\Sigma_{\mathrm{LPV}}: \begin{cases} \dot{\boldsymbol{x}}(t) = \mathcal{A}(\boldsymbol{\rho}(t))\boldsymbol{x}(t) + \mathcal{B}(\boldsymbol{\rho}(t))\boldsymbol{u}(t) \\ \boldsymbol{y}(t) = \mathcal{C}(\boldsymbol{\rho}(t))\boldsymbol{x}(t) + \mathcal{D}(\boldsymbol{\rho}(t))\boldsymbol{u}(t) \end{cases} \tag{2.2}$$

where $\boldsymbol{x} \in \mathbb{R}^{n_x}$ *represents the state vector of the system,* $\boldsymbol{u} \in \mathbb{R}^{n_u}$ *corresponds to the vector of exogenous input, and* $\boldsymbol{y} \in \mathbb{R}^{n_y}$ *is the measured output vector of the system.*
In particular, when the vector of scheduling parameters, $\boldsymbol{\rho}(t)$*, includes part or the full state vector,* $\boldsymbol{x}(t)$*, the system is defined as quasi-LPV. In this case, the state vector of the system can be partitioned in a scheduling part,* $\boldsymbol{z} \in \mathbb{R}^{n_z}$*, and a non-scheduling part,* $\boldsymbol{w} \in \mathbb{R}^{n_w}$*:*

$$\Sigma_{\text{q-LPV}}: \begin{cases} \dot{\boldsymbol{z}}(t) = \mathcal{A}_{11}(\boldsymbol{\rho}(t))\boldsymbol{z}(t) + \mathcal{A}_{12}(\boldsymbol{\rho}(t))\boldsymbol{w}(t) + \mathcal{B}_1(\boldsymbol{\rho}(t))\boldsymbol{u}(t) \\ \dot{\boldsymbol{w}}(t) = \mathcal{A}_{21}(\boldsymbol{\rho}(t))\boldsymbol{z}(t) + \mathcal{A}_{22}(\boldsymbol{\rho}(t))\boldsymbol{w}(t) + \mathcal{B}_2(\boldsymbol{\rho}(t))\boldsymbol{u}(t) \\ \boldsymbol{y}(t) = \mathcal{C}_1(\boldsymbol{\rho}(t))\boldsymbol{z}(t) + \mathcal{C}_2(\boldsymbol{\rho}(t))\boldsymbol{w}(t) + \mathcal{D}(\boldsymbol{\rho}(t))\boldsymbol{u}(t) \end{cases} \tag{2.3}$$

The vector of scheduling parameters is coherently divided in an endogenous subset, $\boldsymbol{z}(t)$*, and in an exogenous subset,* $\boldsymbol{\Omega}(t) \in \mathbb{R}^{n_\Omega}$*, as:* $\boldsymbol{\rho}(t) = [\boldsymbol{z}(t), \boldsymbol{\Omega}(t)]^{\mathrm{T}}$*.*

Definition 2.3 (Linear Time-Invariant (LTI) Systems)
Given the set of time-invariant matrices $\mathcal{A} \in \mathbb{R}^{n_x \times n_x}$*,* $\mathcal{B} \in \mathbb{R}^{n_x \times n_u}$*,* $\mathcal{C} \in \mathbb{R}^{n_y \times n_x}$*, and* $\mathcal{D} \in \mathbb{R}^{n_y \times n_u}$*, the linear time-invariant system,* Σ_{LTI}*, can be expressed as:*

$$\Sigma_{\mathrm{LTI}}: \begin{cases} \dot{\boldsymbol{x}}(t) = \mathcal{A}\boldsymbol{x}(t) + \mathcal{B}\boldsymbol{u}(t) \\ \boldsymbol{y}(t) = \mathcal{C}\boldsymbol{x}(t) + \mathcal{D}\boldsymbol{u}(t) \end{cases}$$

where $\boldsymbol{x} \in \mathbb{R}^{n_x}$ *represents the state vector of the system,* $\boldsymbol{u} \in \mathbb{R}^{n_u}$ *corresponds to the vector of exogenous input, and* $\boldsymbol{y} \in \mathbb{R}^{n_y}$ *is the measured output vector of the system.*

Depending on the specific dependence of the model on the varying parameters vector, LPV systems can be classified in three fundamental frameworks:

I. Polytopic systems: characterized by an affine model-parameter relation. This formulation provides higher stability guarantees due to the convexity of the parameters space. However, it can result conservative and restrictive for highly nonlinear system dynamics.

II. Parameter-dependent systems: based on a more general model-parameter relation, suitable for a larger class of nonlinear systems.

III. Linear Fractional Transformation (LFT) systems: allows splitting the constant part ('nominal') of the system dynamics, from the parameter-varying one, modeled as the uncertain system dynamics. The interest relies on the possibility of individually modeling and analyzing the two contributions ([Pac+91]; [CL08]; [PH11]; [PVR12]; [Mar+15]).

In the following, the LPV formulations I and II are employed for the modeling and control design of the guided projectile.

2.2.1.1 Polytopic Formulation

The polytopic formulation is restricted to a class of LPV systems characterized by an affine dependence on the selected set of time-varying scheduling variables, $\boldsymbol{\rho}(t)$, ([AGB95]; [AG95]; [MS12]). As seen later for control-oriented modeling, the system must be input and output parameter-independent. The latter restriction can be generally relaxed by pre-filtering the input and the output at the modeling stage, as discussed in [AGB95].

Definition 2.4 (Affine LPV Systems)
The LPV model in Equation (2.2) *represents an affine system in the set of scheduling parameters,* $\boldsymbol{\rho}(t)$*, if the matrices of the system,* $\mathcal{A}(\boldsymbol{\rho})$*,* $\mathcal{B}(\boldsymbol{\rho})$*,* $\mathcal{C}(\boldsymbol{\rho})$*, and* $\mathcal{D}(\boldsymbol{\rho})$*, comply with the following parameterization:*

$$\left[\begin{array}{c|c} \mathcal{A}(\boldsymbol{\rho}) & \mathcal{B}(\boldsymbol{\rho}) \\ \hline \mathcal{C}(\boldsymbol{\rho}) & \mathcal{D}(\boldsymbol{\rho}) \end{array}\right] = \left[\begin{array}{c|c} \mathcal{A}_0 & \mathcal{B}_0 \\ \hline \mathcal{C}_0 & \mathcal{D}_0 \end{array}\right] + \sum_{j=1}^{n_\rho} \rho_j \left[\begin{array}{c|c} \mathcal{A}_j & \mathcal{B}_j \\ \hline \mathcal{C}_j & \mathcal{D}_j \end{array}\right]$$

where $\mathcal{A}_0$*,* $\mathcal{A}_j$*,* $\mathcal{B}_0$*,* $\mathcal{B}_j$*,* $\mathcal{C}_0$*,* $\mathcal{C}_j$*,* $\mathcal{D}_0$*,* $\mathcal{D}_j$ *are constant LTI matrices.*

The LPV model in Equation (2.2), can be formulated as a polytopic system if the affine condition in Definition 2.4 is respected, and if the time-varying parameters in the scheduling set are bounded and measurable in real-time ([AGB95]).

Assumption 2.1
Given a set of time-varying parameters, $\boldsymbol{\rho}(t) \in \mathbb{R}^{n_\rho}$*, each element of the set,* ρ_j*, is measurable in real-time and bounded between a maximum and a minimum value:*

$$\underline{\rho_j} \leq \rho_j \leq \overline{\rho_j}$$

where $j \in [1, n_\rho]$*, and* $\overline{\rho_j}$*,* $\underline{\rho_j}$ *indicate the upper and lower bound, respectively, of the* j^{th} *scheduling variable.*

Therefore, the variation of the scheduling vector, $\boldsymbol{\rho}(t)$, lies in a polytope, Θ, defined by the convex hull of n_Θ vertices, $\boldsymbol{\theta}_i$, as shown in Figure 2.2. The vertices of the polytope correspond to the overall set of possible combinations of the scheduling variables' boundary values:

$$\Theta := \mathrm{Co}\Big\{\boldsymbol{\theta}_1, \boldsymbol{\theta}_2, \ldots, \boldsymbol{\theta}_{n_\Theta}\Big\}.$$

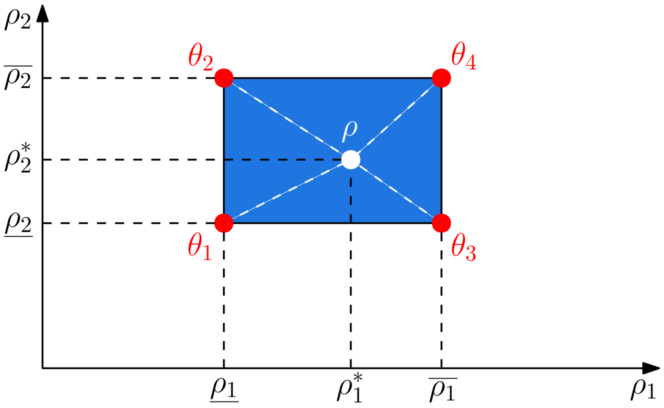

Figure 2.2: 2D polytope representation.

Then, each vertex is expressed as $\boldsymbol{\theta}_i = \left[\nu_{i,1}, \ldots, \nu_{i,n_\rho}\right]$, where $\nu_{i,j}$ is the j^{th} scheduling variable that equals either $\overline{\rho_j}$ or $\underline{\rho_j}$. The LPV system is obtained as the convex interpolation, μ_θ, of the corresponding set of LTI system realizations, evaluated at each vertex of the polytope:

$$\left[\begin{array}{c|c}\mathcal{A}(\boldsymbol{\rho}) & \mathcal{B}(\boldsymbol{\rho})\\ \hline \mathcal{C}(\boldsymbol{\rho}) & \mathcal{D}(\boldsymbol{\rho})\end{array}\right] = \sum_{i=1}^{n_\Theta} \mu_{\theta_i}(\boldsymbol{\rho}) \left[\begin{array}{c|c}\mathcal{A}(\boldsymbol{\theta}_i) & \mathcal{B}(\boldsymbol{\theta}_i)\\ \hline \mathcal{C}(\boldsymbol{\theta}_i) & \mathcal{D}(\boldsymbol{\theta}_i)\end{array}\right]; \quad \text{with:} \quad \boldsymbol{\rho} = \sum_{i=1}^{n_\Theta} \mu_{\theta_i}\boldsymbol{\theta}_i. \tag{2.4}$$

By defining the polytope as a general cuboid of $n_\Theta = 2^{n_\rho}$ vertices as in [Dub18][2], the interpolation function, μ_θ, evolves across the unitary polytope:

$$\Gamma := \left\{ \underset{i}{\mathrm{col}}(\mu_{\theta_i}(\boldsymbol{\rho})) : \sum_{i=1}^{2^{n_\rho}} \mu_{\theta_i}(\boldsymbol{\rho}) = 1,\ \mu_{\theta_i}(\boldsymbol{\rho}) \geq 0 \right\}$$

and is computed in real-time at each vertex as a function of the parameters vector as follows:

$$\mu_{\theta_i}(\boldsymbol{\rho}) = \frac{\prod\limits_{j=1}^{n_\rho} \left|\rho_j - C^c\left(\boldsymbol{\theta}_i\right)_j\right|}{\prod\limits_{j=1}^{n_\rho}\left(\overline{\rho_j} - \underline{\rho_j}\right)} > 0\ ; \qquad C^c\left(\boldsymbol{\theta}_i\right)_j = \begin{cases}\overline{\rho_j} & \text{if } \boldsymbol{\theta}_i = \underline{\rho_j}\\ \underline{\rho_j} & \text{otherwise}\end{cases} \tag{2.5}$$

where $C^c\left(\boldsymbol{\theta}_i\right)_j$ indicates the j^{th} element of the vector $C^c(\boldsymbol{\theta}_i)$.

2.2.1.2 Parameter-Dependent Formulation

The parameter-dependent LPV formulation does not impose any specific model-parameter relation, thus it can be applied to any kind of system. However, differently from the polytopic formulation, the space of variation of the scheduling parameters is not guaranteed to be convex.

---

[2] Alternative definitions of the convex subset are investigated in [Jin+18]; [Kap+22]; [ZZW14]; [Cor+20]; [PDP05]; [Pan+21]; [HW15]; [KW08], aiming to reduced the polytope's dimensions and the resulting conservativeness affecting the control design.

Definition 2.5 (Parameter-Dependent Systems)
An LPV model as in Equation 2.2, whose generic model-parameter relation is expressed through a set of scalar differentiable basis functions $\{a_j : \mathbb{R}^{n_\rho} \to \mathbb{R}\}_{j=1}^{N}$, *can be parameterized as the following parameter-dependent system:*

$$\left[\begin{array}{c|c} \mathcal{A}(\boldsymbol{\rho}) & \mathcal{B}(\boldsymbol{\rho}) \\ \hline \mathcal{C}(\boldsymbol{\rho}) & \mathcal{D}(\boldsymbol{\rho}) \end{array}\right] = \left[\begin{array}{c|c} \mathcal{A}_0 & \mathcal{B}_0 \\ \hline \mathcal{C}_0 & \mathcal{D}_0 \end{array}\right] + \sum_{j=1}^{N} a_j(\boldsymbol{\rho}) \left[\begin{array}{c|c} \mathcal{A}_j & \mathcal{B}_j \\ \hline \mathcal{C}_j & \mathcal{D}_j \end{array}\right]$$

where $\mathcal{A}_0$, $\mathcal{A}_j$, $\mathcal{B}_0$, $\mathcal{B}_j$, $\mathcal{C}_0$, $\mathcal{C}_j$, $\mathcal{D}_0$, $\mathcal{D}_j$ *are constant LTI matrices.*

The formulation presented in Definition 2.5 consists of a generalization of the affine parameterization introduced in Definition 2.4. Indeed, the model formulated in Definition 2.5 is affine in any function, $a_j(\boldsymbol{\rho})$, of the scheduling vector, $\boldsymbol{\rho}(t)$. Thus, a generalized polytopic model could be also derived by exploiting the affine model dependence on $a_j(\boldsymbol{\rho})$.

2.2.2 LPV Modeling of Nonlinear Systems

The LPV formulation of general nonlinear system dynamics is a nontrivial and tedious process. Depending on the selected approach and the considered vector of scheduling variables, different LPV/quasi-LPV models can be derived from the same nonlinear system. Thus, in most of the scenarios, ad-hoc modeling procedures have to be developed depending on the system under analysis, without clear guidelines on the optimal approach to employ, if any. Early LPV modeling approaches consisted of an extension of the standard LTI gain-scheduling framework. Linearization-based LPV techniques approximate the nonlinear dynamics through the derivation of a family of local linearization of the system, at selected operating points. In the last decades, several methods have been investigated, trying to propose a generalized procedure to convert the nonlinear dynamics of a system into an accurate LPV model, exploiting the dynamic dependence on the scheduling variables. A brief non-exhaustive overview of the most relevant approaches is provided in the following.

2.2.2.1 Linearization-Based Techniques

As aforementioned, linearization-based approaches have been early developed to couple LPV control design with standard gain-scheduling strategies. Since the equilibrium points employed for the local linearization of the nonlinear dynamics can result in stable or unstable conditions, the approach is coherently developed as equilibrium-based or off-equilibrium-based.

Equilibrium-Based. The modeling process involves a standard first-order Jacobian linearization of the nonlinear dynamics across a set of $j = 1, \dots, N$ equilibrium (trim) points. Assuming the nonlinear dynamics in Definition 2.1, the set of local linearizations is expressed at each equilibrium condition, $(\bar{\boldsymbol{x}}, \bar{\boldsymbol{u}})$, at 'frozen' parameter values, $\bar{\boldsymbol{\rho}}$, as:

$$\mathcal{A}_j = \frac{\partial \boldsymbol{f}}{\partial \boldsymbol{x}}\bigg|_{\bar{\boldsymbol{\rho}}_j}(\bar{\boldsymbol{x}}_j, \bar{\boldsymbol{u}}_j); \qquad \mathcal{B}_j = \frac{\partial \boldsymbol{f}}{\partial \boldsymbol{u}}\bigg|_{\bar{\boldsymbol{\rho}}_j}(\bar{\boldsymbol{x}}_j, \bar{\boldsymbol{u}}_j); \qquad \mathcal{C}_j = \frac{\partial \boldsymbol{g}}{\partial \boldsymbol{x}}\bigg|_{\bar{\boldsymbol{\rho}}_j}(\bar{\boldsymbol{x}}_j, \bar{\boldsymbol{u}}_j); \qquad \mathcal{D}_j = \frac{\partial \boldsymbol{g}}{\partial \boldsymbol{u}}\bigg|_{\bar{\boldsymbol{\rho}}_j}(\bar{\boldsymbol{x}}_j, \bar{\boldsymbol{u}}_j).$$

The corresponding first-order Taylor series expansion allows approximating the input/output nonlinear dynamics around each equilibrium point. The overall linearization-based LPV model relies on the interpolation of the obtained local LTI realization of the nonlinear dynamics. Several applications of this method have been proposed in the aerospace environment ([The+10]; [PH10]; [Sèv+14]; [Str+15]; [Tha+20]). However, the linearization process often generates a loss of transient properties of the modeled system. A slow variation of the scheduling parameters often must be assumed to increase the accuracy of the LPV model. Additionally, an explicit solution of the equilibrium conditions is not always feasible.

Off-Equilibrium-Based. The derivation of linearization-based off-equilibrium LPV models relies on the same approach described in the previous section. When a nonequilibrium point is selected for the linearization, additional terms appear in the partial derivatives of the linearized matrices. These terms are generally neglected and addressed as disturbances to be compensated during the control design. Even though the off-equilibrium dynamics preserves more information concerning the transient properties of the nonlinear system, this approach is affected by the same issues discussed previously.

2.2.2.2 Substitution-Based Techniques

This class of modeling approaches relies on the reformulation of the system nonlinear dynamics in Definition 2.1, without employing any linearization process. The substitution process can target both the state and the input variables of the nonlinear system, generating different techniques. A detailed classification can be found in [Tót10]. The state transformation approach is discussed in the next section.

Linear Differential Inclusion. The LPV model is obtained by means of mathematical manipulations, which aim at embedding the nonlinearities of the system as new scheduling parameters of the corresponding LPV model. The approach is based on the Differential Inclusion theorem, stating that given the nonlinear dynamics in Equation (2.1), if for each state, $\boldsymbol{x}(t)$, and input $\boldsymbol{u}(t)$, there exists a matrix, $\mathcal{F}(\boldsymbol{x}(t), \boldsymbol{u}(t)) \in \mathbb{R}^{(n_x+n_y)\times(n_x+n_u)}$, such that:

$$\begin{bmatrix} \boldsymbol{f}(\boldsymbol{x}(t), \boldsymbol{u}(t)) \\ \boldsymbol{g}(\boldsymbol{x}(t), \boldsymbol{u}(t)) \end{bmatrix} = \mathcal{F}(\boldsymbol{x}(t), \boldsymbol{u}(t)) \begin{bmatrix} \boldsymbol{x}(t) \\ \boldsymbol{u}(t) \end{bmatrix}, \tag{2.6}$$

the solution of the nonlinear system in Definition 2.1 are also solution of the system in Equation (2.6) ([Boy+94]). The selection of the 'virtual' scheduling parameters relies on an ad-hoc analysis of the system under investigation. Thus, several different LPV/quasi-LPV models can be derived from a common nonlinear system. Additionally, the selection of a virtual set of scheduling variables often results in the loss of physical intuition in the system dynamics. Thus, the solution of the obtained LPV system might diverge from the desired one at certain operating conditions, depending on the scheduling variables definition.

Velocity-Based Techniques. This approach aims to generalize the local domain of validity of standard linearization-based models to the entire subspace of admissible solutions of the nonlinear system ([LL98]). By differentiating the nonlinear dynamics in Definition 2.1, the nonlinear system can be reformulated as:

$$\begin{cases} \dot{\boldsymbol{x}}(t) = \boldsymbol{\xi} \\ \dot{\boldsymbol{\xi}}(t) = \frac{\partial \boldsymbol{f}(\boldsymbol{x},\boldsymbol{u})}{\partial \boldsymbol{x}}\boldsymbol{\xi} + \frac{\partial \boldsymbol{f}(\boldsymbol{x},\boldsymbol{u})}{\partial \boldsymbol{u}}\dot{\boldsymbol{u}} \\ \dot{\boldsymbol{y}}(t) = \frac{\partial \boldsymbol{g}(\boldsymbol{x},\boldsymbol{u})}{\partial \boldsymbol{x}}\boldsymbol{\xi} + \frac{\partial \boldsymbol{g}(\boldsymbol{x},\boldsymbol{u})}{\partial \boldsymbol{u}}\dot{\boldsymbol{u}} \end{cases} \tag{2.7}$$

The corresponding quasi-LPV model can be obtained by simply defining the scheduling signal, $\boldsymbol{\rho} = \mathrm{Col}(\boldsymbol{x}, \boldsymbol{u})$, and by substituting:

$$\tilde{\boldsymbol{x}} = \dot{\boldsymbol{x}}; \qquad \tilde{\boldsymbol{u}} = \dot{\boldsymbol{u}}; \qquad \tilde{\boldsymbol{y}} = \dot{\boldsymbol{y}}.$$

In particular, for a set of appropriate initial conditions, the solutions of the nonlinear dynamics in Definition 2.1, and the velocity-based quasi-LPV representation in Equation (2.7) are equivalent. However, the employment of differentiated expressions as scheduling variables might alter the behavior of the LPV model. From the implementation perspective, measurements in terms of $\dot{\boldsymbol{u}}$ and $\dot{\boldsymbol{y}}$ are not always available.

Function Substitution. Restricted to the output nonlinear system parameterization, later detailed in Definition 2.6, this modeling approach relies on the reformulation of the state, $(\boldsymbol{z}(t),\boldsymbol{w}(t))$, and input, $\boldsymbol{u}(t)$, vectors of the nonlinear system around a selected equilibrium point, $(\bar{\boldsymbol{z}}, \bar{\boldsymbol{w}}, \bar{\boldsymbol{u}})$, as:

$$\tilde{\boldsymbol{z}} = \boldsymbol{z} - \bar{\boldsymbol{z}}; \qquad \tilde{\boldsymbol{w}} = \boldsymbol{w} - \bar{\boldsymbol{w}}; \qquad \tilde{\boldsymbol{u}} = \boldsymbol{u} - \bar{\boldsymbol{u}}.$$

The resulting nonlinear model is expressed w.r.t. the new set of variables by collecting the nonlinearities in the function $\boldsymbol{f}(\boldsymbol{z})$, as:

$$\begin{bmatrix} \dot{\tilde{\boldsymbol{z}}} \\ \dot{\tilde{\boldsymbol{w}}} \end{bmatrix} = \mathcal{A}(\boldsymbol{z}) \begin{bmatrix} \tilde{\boldsymbol{z}} \\ \tilde{\boldsymbol{w}} \end{bmatrix} + \mathcal{B}(\boldsymbol{z})\tilde{\boldsymbol{u}} + \boldsymbol{f}(\boldsymbol{z}); \qquad \text{with: } \tilde{\boldsymbol{f}}(\boldsymbol{z}) = \mathcal{A}(\boldsymbol{z}) \begin{bmatrix} \bar{\boldsymbol{z}} \\ \bar{\boldsymbol{w}} \end{bmatrix} + \mathcal{B}(\boldsymbol{z})\bar{\boldsymbol{u}} + \boldsymbol{f}(\boldsymbol{z}).$$

The objective is to find a matrix $\Gamma(\boldsymbol{\rho})$, with $\boldsymbol{\rho}(t) = \boldsymbol{z}(t)$, shuch that the nonlinear function $\tilde{\boldsymbol{f}}(\boldsymbol{z})$ can be properly approximated for every trajectory of $\boldsymbol{z}(t)$ as:

$$\tilde{\boldsymbol{f}}(\boldsymbol{z}) \approx \Gamma(\boldsymbol{\rho})\tilde{\boldsymbol{z}} \tag{2.8}$$

The estimation of $\Gamma(\boldsymbol{\rho})$ relies on the resolution of an optimization problem based on linear programming that aims at minimizing the approximation error in Equation (2.8) ([TPB00]; [SBK02]; [MB04]; [Pfi12]). The main drawback of this approach consists of the strong dependence on the selected equilibrium conditions.

2.3 The State Transformation Approach

The state transformation approach consists of the reformulation of a plant nonlinear dynamics through an alternative selection of the state variables. The new set of parameters, defined through the change of variables, is supposed to hide the nonlinear terms affecting the plant dynamics. Different from standard linearization-based gain-scheduling techniques ([The+10]; [PPV01]), the transformation does not rely on a local linearization process. Thus, the validity of the obtained LPV model is not limited to the selection of a set of design points. This approach was first introduced in the 1990s ([SA92]; [LL00]; [RS00]) as an alternative technique to generate families of LTI models of a general nonlinear system. The first examples of successful applications employed the state transformation for standard gain-scheduling control design of guided missiles ([SC93]; [CS96]). Later, the state transformation has been extended also to aircraft modeling applications ([MB04]).

2.3.1 General Formulation

The state transformation modeling approach is suitable for a restricted class of systems, defined as *Output Nonlinear* or *Output Dependent.*

Definition 2.6 (Output Nonlinear Systems)
The nonlinear system in Equation (2.1) *is called output nonlinear (or output dependent) if the nonlinear terms depend only on the scheduling part of the state vector,* $\boldsymbol{z}(t) \in \mathbb{R}^{n_z}$*. As in the quasi-LPV system definition in Equation* (2.3)*, the state vector,* $\boldsymbol{x}(t) \in \mathbb{R}^{n_x}$*, is partitioned in a scheduling vector,* $\boldsymbol{z}(t)$*, assumed known in real-time, and in a non-scheduling vector,* $\boldsymbol{w}(t) \in \mathbb{R}^{n_w}$*. Thus, the nonlinear system can be reformulated as follows:*

$$\begin{aligned} \begin{bmatrix} \dot{\boldsymbol{z}} \\ \dot{\boldsymbol{w}} \end{bmatrix} &= \begin{bmatrix} \boldsymbol{f}_1(\boldsymbol{z}) \\ \boldsymbol{f}_2(\boldsymbol{z}) \end{bmatrix} + \begin{bmatrix} \mathcal{A}_{11}(\boldsymbol{z}) & \mathcal{A}_{12}(\boldsymbol{z}) \\ \mathcal{A}_{21}(\boldsymbol{z}) & \mathcal{A}_{22}(\boldsymbol{z}) \end{bmatrix} \begin{bmatrix} \boldsymbol{z} \\ \boldsymbol{w} \end{bmatrix} + \begin{bmatrix} \mathcal{B}_1(\boldsymbol{z}) \\ \mathcal{B}_2(\boldsymbol{z}) \end{bmatrix} \boldsymbol{u}, \\ \boldsymbol{y} &= \boldsymbol{z}, \end{aligned} \tag{2.9}$$

where the functions $\boldsymbol{f}_1(\boldsymbol{z})$ *and* $\boldsymbol{f}_2(\boldsymbol{z})$ *include all the nonlinearities of the system that depend on the scheduling state.*
The formulation in Equation (2.9) *can be generalized by accounting for additional exogenous scheduling parameters,* $\boldsymbol{\Omega}(t) \in \mathbb{R}^{n_\Omega}$*, as:*

$$\begin{aligned} \begin{bmatrix} \dot{\boldsymbol{z}} \\ \dot{\boldsymbol{w}} \end{bmatrix} &= \begin{bmatrix} \boldsymbol{f}_1(\boldsymbol{\rho}) \\ \boldsymbol{f}_2(\boldsymbol{\rho}) \end{bmatrix} + \begin{bmatrix} \mathcal{A}_{11}(\boldsymbol{\rho}) & \mathcal{A}_{12}(\boldsymbol{\rho}) \\ \mathcal{A}_{21}(\boldsymbol{\rho}) & \mathcal{A}_{22}(\boldsymbol{\rho}) \end{bmatrix} \begin{bmatrix} \boldsymbol{z} \\ \boldsymbol{w} \end{bmatrix} + \begin{bmatrix} \mathcal{B}_1(\boldsymbol{\rho}) \\ \mathcal{B}_2(\boldsymbol{\rho}) \end{bmatrix} \boldsymbol{u}, \\ \boldsymbol{y} &= \boldsymbol{z}, \end{aligned} \tag{2.10}$$

where the generalized scheduling vector, $\boldsymbol{\rho}(t) = [\boldsymbol{z}(t)\,, \boldsymbol{\Omega}(t)]^{\mathrm{T}}$*, includes both the endogenous and the exogenous parameters.*

Additionally, to reformulate the generalized output nonlinear model in Equation (2.10) as a quasi-LPV system through the state transformation approach, the following conditions have to be satisfied.

Assumption 2.2
The non-scheduling state variables and the control inputs of the output nonlinear model in Equation (2.10) *have to be linear w.r.t. the system. Nonlinearities w.r.t. the scheduling state variables,* $\boldsymbol{z}(t)$, *are allowed and collected in the functions* $\boldsymbol{f}_1(\boldsymbol{\rho})$ *and* $\boldsymbol{f}_2(\boldsymbol{\rho})$.

Assumption 2.3
The dimension of the scheduling state vector, $\boldsymbol{z}(t)$, *matches the dimension of the control input vector,* $\boldsymbol{u}(t)$:

$$n_z = n_u$$

Assumption 2.4
For all values of the scheduling parameters, $\boldsymbol{\rho}(t) \in \mathbb{R}^{n_\rho}$, *there exists a set of continuously differentiable functions,* $(\boldsymbol{w}_{\text{eq}}(\boldsymbol{\rho}), \boldsymbol{u}_{\text{eq}}(\boldsymbol{\rho}))$, *such that the output nonlinear system in Equation* (2.10) *is in steady-state conditions:*

$$\begin{bmatrix} 0 \\ 0 \end{bmatrix} = \begin{bmatrix} \boldsymbol{f}_1(\boldsymbol{\rho}) \\ \boldsymbol{f}_2(\boldsymbol{\rho}) \end{bmatrix} + \begin{bmatrix} \mathcal{A}_{11}(\boldsymbol{\rho}) & \mathcal{A}_{12}(\boldsymbol{\rho}) \\ \mathcal{A}_{21}(\boldsymbol{\rho}) & \mathcal{A}_{22}(\boldsymbol{\rho}) \end{bmatrix} \begin{bmatrix} \boldsymbol{z} \\ \boldsymbol{w}_{\text{eq}}(\boldsymbol{\rho}) \end{bmatrix} + \begin{bmatrix} \mathcal{B}_1(\boldsymbol{\rho}) \\ \mathcal{B}_2(\boldsymbol{\rho}) \end{bmatrix} \boldsymbol{u}_{\text{eq}}(\boldsymbol{\rho}). \tag{2.11}$$

Remark 2.1
Since no a priori guarantees are provided concerning the existence of the trimming functions, an analysis of the feasible trim map is required before developing the state transformation.

The state transformation is achieved by defining the trimming functions $(\boldsymbol{w}_{\text{eq}}(\boldsymbol{\rho}), \boldsymbol{u}_{\text{eq}}(\boldsymbol{\rho}))$, as in Equation (2.11), across the feasible trim map. Then, by subtracting the steady-state dynamics in Equation (2.11) from the nonlinear system in Equation (2.10), the following expression is obtained:

$$\begin{bmatrix} \dot{\boldsymbol{z}} \\ \dot{\boldsymbol{w}} \end{bmatrix} = \begin{bmatrix} 0 & \mathcal{A}_{12}(\boldsymbol{\rho}) \\ 0 & \mathcal{A}_{22}(\boldsymbol{\rho}) \end{bmatrix} \begin{bmatrix} \boldsymbol{z} \\ \boldsymbol{w}_{\text{dev}} \end{bmatrix} + \begin{bmatrix} \mathcal{B}_1(\boldsymbol{\rho}) \\ \mathcal{B}_2(\boldsymbol{\rho}) \end{bmatrix} \boldsymbol{u}_{\text{dev}} \tag{2.12}$$

where the new off-equilibrium values of the non-scheduling state, $\boldsymbol{w}_{\text{dev}}$, and input, $\boldsymbol{u}_{\text{dev}}$, are defined by the transformation as:

$$\boldsymbol{w}_{\text{dev}} = \boldsymbol{w} - \boldsymbol{w}_{\text{eq}}(\boldsymbol{\rho}); \qquad \boldsymbol{u}_{\text{dev}} = \boldsymbol{u} - \boldsymbol{u}_{\text{eq}}(\boldsymbol{\rho}). \tag{2.13}$$

In order to account for the dynamics of the off-equilibrium non-scheduling state, the partial derivatives of the corresponding trimming function, $\boldsymbol{w}_{\text{eq}}(\boldsymbol{\rho})$, are performed w.r.t. the scheduling variables (endogenous and exogenous):

$$\dot{\boldsymbol{w}}_{\text{dev}} := \dot{\boldsymbol{w}} - \dot{\boldsymbol{w}}_{\text{eq}}(\boldsymbol{\rho}) \tag{2.14}$$

with:

$$\begin{aligned}\dot{\boldsymbol{w}}_{\mathrm{eq}} &= \frac{\mathrm{d}\boldsymbol{w}_{\mathrm{eq}}}{\mathrm{d}t} \\ &= \frac{\partial \boldsymbol{w}_{\mathrm{eq}}}{\partial \boldsymbol{z}}\dot{\boldsymbol{z}} + \frac{\partial \boldsymbol{w}_{\mathrm{eq}}}{\partial \boldsymbol{\Omega}}\dot{\boldsymbol{\Omega}}.\end{aligned} \tag{2.15}$$

By substituting the scheduling state dynamics, $\dot{\boldsymbol{z}}$, of Equation (2.12) into the equilibrium dynamics expressed in Equation (2.15), the off-equilibrium state dynamics in Equation (2.14) becomes:

$$\dot{\boldsymbol{w}}_{\mathrm{dev}} = (\mathcal{A}_{22} - \frac{\partial \boldsymbol{w}_{\mathrm{eq}}}{\partial \boldsymbol{z}}\mathcal{A}_{12})\boldsymbol{w}_{\mathrm{dev}} + (\mathcal{B}_2 - \frac{\partial \boldsymbol{w}_{\mathrm{eq}}}{\partial \boldsymbol{z}}\mathcal{B}_1)\boldsymbol{u}_{\mathrm{dev}} - \frac{\partial \boldsymbol{w}_{\mathrm{eq}}}{\partial \boldsymbol{\Omega}}\dot{\boldsymbol{\Omega}}. \tag{2.16}$$

The resulting quasi-LPV formulation of the output nonlinear system in Equation (2.10) corresponds to:

$$\begin{bmatrix}\dot{\boldsymbol{z}} \\ \dot{\boldsymbol{w}}_{\mathrm{dev}}\end{bmatrix} = \begin{bmatrix}0 & \mathcal{A}_{12}(\boldsymbol{\rho}) \\ 0 & \tilde{\mathcal{A}}_{22}(\boldsymbol{\rho})\end{bmatrix}\begin{bmatrix}\boldsymbol{z} \\ \boldsymbol{w}_{\mathrm{dev}}\end{bmatrix} + \begin{bmatrix}\mathcal{B}_1(\boldsymbol{\rho}) \\ \tilde{\mathcal{B}}_2(\boldsymbol{\rho})\end{bmatrix}\boldsymbol{u}_{\mathrm{dev}} + \begin{bmatrix}0 \\ \boldsymbol{\mathcal{E}}(\boldsymbol{\rho})\end{bmatrix}\dot{\boldsymbol{\Omega}} \tag{2.17}$$

where:

$$\begin{aligned}\tilde{\mathcal{A}}_{22}(\boldsymbol{\rho}) &:= \mathcal{A}_{22}(\boldsymbol{\rho}) - \frac{\partial \boldsymbol{w}_{\mathrm{eq}}}{\partial \boldsymbol{z}}\mathcal{A}_{12}(\boldsymbol{\rho}), \\ \tilde{\mathcal{B}}_2(\boldsymbol{\rho}) &:= \mathcal{B}_2(\boldsymbol{\rho}) - \frac{\partial \boldsymbol{w}_{\mathrm{eq}}}{\partial \boldsymbol{z}}\mathcal{B}_1(\boldsymbol{\rho}), \\ \boldsymbol{\mathcal{E}}(\boldsymbol{\rho}) &:= -\frac{\partial \boldsymbol{w}_{\mathrm{eq}}}{\partial \boldsymbol{\Omega}}.\end{aligned} \tag{2.18}$$

The additional input, $\dot{\boldsymbol{\Omega}}$, accounts for the dynamics of the exogenous scheduling variables. These perturbation terms can be assumed arbitrarily small through Taylor expansion theory, providing that the magnitude of $\boldsymbol{w}_{\mathrm{dev}}$ and $\boldsymbol{u}_{\mathrm{dev}}$ is sufficiently contained ([Bal02]; [LL00]). They are generally neglected and treated as external disturbances to be compensated through the design of a controller with reliable disturbance rejection properties.

A final observation concerns the off-equilibrium input, $\boldsymbol{u}_{\mathrm{dev}}$. The reformulated input of the quasi-LPV system in Equations (2.17)-(2.18) strictly depends on the equilibrium conditions, continuously updated online. The resulting inner feedback loop that updates $\boldsymbol{u}_{\mathrm{eq}}$, can affect the robustness of the outer closed-loop, destabilizing the system. A straightforward solution consists of restricting the feasible trim map to those flight points with zero trimmed input, $\boldsymbol{u}_{\mathrm{eq}} = 0$. However, this approach would impose strong limitations on the domain of validity of the model. For control-oriented modeling, when the controller output is the only input to the system and the controller to be designed includes integral action, the integrator dynamics can be formally augmented at the input of the system ([SC93]; [CS96]), by defining:

$$\boldsymbol{u} = \int \boldsymbol{\sigma}.$$

In this way, the new input is uniformly zero at every equilibrium point, and the feedback loop does not affect the system anymore. Additionally, the integration redefines the input matrix, $\mathcal{B}$, of the quasi-LPV system in a parameter-independent form expressed by the identity matrix, $I \in \mathbb{R}^{n_u}$. The latter observation represents a fundamental requirement for the employment of certain LPV control design techniques, as later detailed.

By applying the same algebraic manipulations in Equations (2.14)-(2.16) to the off-equilibrium input, $\boldsymbol{u}_{\text{dev}}$, the final integrator-augmented quasi-LPV is expressed as:

$$\begin{bmatrix} \dot{\boldsymbol{z}} \\ \dot{\boldsymbol{w}}_{\text{dev}} \\ \dot{\boldsymbol{u}}_{\text{dev}} \end{bmatrix} = \begin{bmatrix} 0 & \mathcal{A}_{12}(\boldsymbol{\rho}) & \mathcal{B}_1(\boldsymbol{\rho}) \\ 0 & \tilde{\mathcal{A}}_{22}(\boldsymbol{\rho}) & \tilde{\mathcal{B}}_2(\boldsymbol{\rho}) \\ 0 & \tilde{\mathcal{A}}_{32}(\boldsymbol{\rho}) & \tilde{\mathcal{B}}_3(\boldsymbol{\rho}) \end{bmatrix} \begin{bmatrix} \boldsymbol{z} \\ \boldsymbol{w}_{\text{dev}} \\ \boldsymbol{u}_{\text{dev}} \end{bmatrix} + \begin{bmatrix} 0 \\ 0 \\ I \end{bmatrix} \boldsymbol{\sigma},$$

with:

$$\tilde{\mathcal{A}}_{32}(\boldsymbol{\rho}) := -\frac{\partial \boldsymbol{u}_{\text{eq}}}{\partial \boldsymbol{z}} \mathcal{A}_{12}(\boldsymbol{\rho}); \qquad \tilde{\mathcal{B}}_3(\boldsymbol{\rho}) := -\frac{\partial \boldsymbol{u}_{\text{eq}}}{\partial \boldsymbol{z}} \mathcal{B}_1(\boldsymbol{\rho}).$$

As previously claimed, the state transformation approach corresponds to an exact transformation between the original nonlinear system and the obtained quasi-LPV model, avoiding any forms of approximation. Additionally, due to the integration of the control input, the accuracy of the quasi-LPV model does not depend on the specific operating point, and the terms $\dot{\boldsymbol{w}}_{\text{eq}} = \frac{\partial \boldsymbol{w}_{\text{eq}}}{\partial \boldsymbol{z}} \dot{\boldsymbol{z}}$ and $\dot{\boldsymbol{u}}_{\text{eq}} = \frac{\partial \boldsymbol{u}_{\text{eq}}}{\partial \boldsymbol{z}} \dot{\boldsymbol{z}}$, allow accounting for any off-equilibrium operating conditions.

2.3.2 The quasi-LPV Projectile Pitch Channel Modeling

Despite the restrictions discussed in the previous section, the state transformation is generally suitable for aerospace applications. Indeed, flight dynamics models often can be formulated in the output nonlinear fashion displayed in Equation (2.10), by accounting for mild simplifications. In this section, the state transformation is employed to formulate the projectile nonlinear pitch channel dynamics in Equations (1.40)-(1.42), at the end of Chapter 2, as an accurate quasi-LPV system. However, the pitch channel dynamics does not respect the criteria imposed by Assumption 2.2 for the output linear reformulation. Indeed, the aerodynamic longitudinal and vertical forces, (f_{a_1} and f_{a_3}, respectively), and the pitching moment coefficient, (m_{B_2}), are non-affine in the virtual control inputs, δ_{eff} and δ_q, as shown below.

$$\begin{aligned} \frac{\mathrm{d}\alpha}{\mathrm{d}t} &= \frac{1}{mV}\left(-f_{\text{a}_1}\sin\alpha + f_{\text{a}_3}\cos\alpha\right) + q + \frac{g}{V}\left(\sin\theta\sin\alpha + \cos\theta\cos\phi\cos\alpha\right), \\ \frac{\mathrm{d}q}{\mathrm{d}t} &= \frac{m_{B_2}}{I_2}, \end{aligned} \tag{2.19}$$

where:

$$\begin{aligned}
f_{\mathrm{a}_1} &= \bar{q}S\Big(C_{X_{\alpha 0}}(\mathcal{M}) + C_{X_{\alpha 2}}(\mathcal{M})\sin^2\alpha + C_{X_{\alpha 4}}(\mathcal{M})\sin^4\alpha \\
&\qquad\qquad + C_{X_{\delta_{\mathrm{eff}}0}}(\mathcal{M}) + C_{X_{\delta_{\mathrm{eff}}2}}(\mathcal{M})\sin^2\delta_{\mathrm{eff}}\Big), \\
f_{\mathrm{a}_3} &= \bar{q}S\Big(C_{Z_{\alpha 1}}(\mathcal{M})\sin\alpha + \left(\frac{d}{2V}\right)C_{Z_q}(\mathcal{M}) + C_{Z_{\delta_q 1}}(\mathcal{M})\sin\delta_q + C_{Z_{\delta_q 3}}(\mathcal{M})\sin^3\delta_q\Big), \qquad (2.20) \\
m_{B_2} &= \bar{q}Sd\Big(C_{m_{\alpha 1}}(\mathcal{M})\sin\alpha + C_{m_{\alpha 3}}(\mathcal{M})\sin^3\alpha + C_{m_{\alpha 5}}(\mathcal{M})\sin^5\alpha + \left(\frac{d}{2V}\right)C_{m_q}(\mathcal{M}) \\
&\qquad\qquad + C_{m_{\delta_q 1}}(\mathcal{M})\sin\delta_q + C_{m_{\delta_q 3}}(\mathcal{M})\sin^3\delta_q\Big).
\end{aligned}$$

As a consequence, prior to the output nonlinear model reformulation, the aerodynamic control contributions have to be adjusted to respect the conditions in Assumption 2.2.

2.3.2.1 Aerodynamic Approximation

The regression models of the aerodynamic control coefficients, $C_{X_{\delta_{\mathrm{eff}}}}$, $C_{Z_{\delta_q}}$, and $C_{m_{\delta_q}}$ have been derived in Section 1.3.3.4, as a function of the Mach number, and respectively, of the longitudinal deflection, δ_{eff}, and the virtual pitch deflection, δ_q. These models correspond to the following polynomial expressions, up to the second and third order:

$$\begin{aligned}
C_{X_{\delta_{\mathrm{eff}}}}(\mathcal{M},\delta_{\mathrm{eff}}) &= C_{X_{\delta_{\mathrm{eff}}0}}(\mathcal{M}) + C_{X_{\delta_{\mathrm{eff}}2}}(\mathcal{M})\sin^2\delta_{\mathrm{eff}}, \\
C_{Z_{\delta_q}}(\mathcal{M},\delta_q) &= C_{Z_{\delta_q 1}}(\mathcal{M})\sin\delta_q + C_{Z_{\delta_q 3}}(\mathcal{M})\sin^3\delta_q, \qquad (2.21) \\
C_{m_{\delta_q}}(\mathcal{M},\delta_q) &= C_{m_{\delta_q 1}}(\mathcal{M})\sin\delta_q + C_{m_{\delta_q 3}}(\mathcal{M})\sin^3\delta_q.
\end{aligned}$$

For control-oriented modeling, the longitudinal control contribution is neglected in reason of the limited effect generated on the projectile dynamics. Indeed, the values of the regression coefficients, $C_{X_{\delta_{\mathrm{eff},0}}}(\mathcal{M})$ and $C_{X_{\delta_{\mathrm{eff},2}}}(\mathcal{M})$, are one order of magnitude smaller than the rest of the control coefficients. The longitudinal effect consists of the additional drag contribution generated by the increasing deflection angle of the canards. Since, it does not provide a direct degree of control on the projectile dynamics, $C_{X_{\delta_{\mathrm{eff}}}} = 0$ is assumed.

The vertical force and pitching moment control contributions have been investigated more in detail. The CFD acquisition curves in Figure 1.10 of Section 1.3.2.3 show an approximately linear behavior across a canards' local deflection range equal to $\delta_{\mathrm{r}}, \delta_{\mathrm{l}} \in [-20, 20]$ deg, at any Mach conditions. The transition from linear to full stall regime occurs for $\delta_{\mathrm{r}}, \delta_{\mathrm{l}} \in (20, 30]$ deg (the same behavior was observed for negative deflection angles). In order to obtain a linear model of the aerodynamic control contributions, two different approaches are investigated.

- **Taylor Approximation (TA):** it relies on a standard first-order Taylor series approximation of the polynomial models in Equation (2.21), assuming the small angle approximation. The resulting linearized regression models are the following:

$$\tilde{C}_{Z_{\delta_q}}(\mathcal{M}, \delta_q) = C_{Z_{\delta_q 1}}(\mathcal{M})\, \delta_q; \qquad \tilde{C}_{m_{\delta_q}}(\mathcal{M}, \delta_q) = C_{m_{\delta_q 1}}(\mathcal{M})\, \delta_q. \tag{2.22}$$

- **Linear Regression (LR):** a new linear regression analysis is performed, only accounting for the CFD data that belong to the range of linear response of the canards. Thus, assuming the quasi-linear canard deflections range $\delta_\mathrm{r}, \delta_\mathrm{l} \approx \delta_q \in [-20, 20]$, and the approximated interpolation in Equation (1.35), the following linear regression models are selected:

$$\tilde{C}_{Z_{\delta_q}}(\mathcal{M}, \delta_q) = C_{Z_{\delta_q \mathrm{A}}}(\mathcal{M})\, \delta_q; \qquad \tilde{C}_{m_{\delta_q}}(\mathcal{M}, \delta_q) = C_{m_{\delta_q \mathrm{A}}}(\mathcal{M})\, \delta_q.$$

The accuracy of the two approaches is compared through the evaluation of the approximation error, first w.r.t. the nonlinear regression models in Equation (2.21), and then w.r.t. the original CFD data. In the former scenario, the error, e_PR, is evaluated as the difference between each model (TA, LR) and the polynomial regression models at any Mach conditions. The error is normalized by the mean value of the nonlinear regression models across the variation of the canards' pitch deflection, as below:

$$e_{k,\mathrm{PR}}(\delta_q, \mathcal{M}) = \left| \frac{\tilde{C}_{k_{\delta_q}}(\delta_q, \mathcal{M}) - C_{k_{\delta_q}}(\delta_q, \mathcal{M})}{\bar{C}_{k_{\delta_q}}(\mathcal{M})} \right|; \qquad \bar{C}_{k_{\delta_q}}(\mathcal{M}) = \frac{\sum_{i=1}^{n_{\delta_q}} C_{k_{\delta_q i}}(\delta_q, \mathcal{M})}{n_{\delta_q}}; \tag{2.23}$$
$$\text{with:} \qquad k = [Z, m]; \qquad \mathcal{M} \in [0.3, 1]; \qquad \delta_q \in [0, 20]\text{deg}.$$

The same evaluation is performed for the approximation error related to the CFD data, e_CFD, by simply substituting the polynomial regression coefficients in Equation (2.23) with the corresponding CFD data.

The results related to the vertical force control coefficients are shown in Figure 2.3. In particular, Figures 2.3(a)-(b) compare the approximation error, e_PR, respectively obtained employing the TA and the LR approaches. Similarly, Figures 2.3(c)-(d) provide the same information in terms of e_CFD. In both cases, the approximation error affecting the TA approach tends to increase nonlinearly w.r.t. δ_q, while the corresponding LR errors show peaks of amplitude at half of the range, $\delta_q \approx 10$ deg. Even though the TA approach presents higher peak error values compared to the LR ones, it is still more suitable for the aerodynamic approximation. Indeed, the TA errors, e_PR and e_CFD, never exceed the 5% and the 10%, respectively, for pitch deflections $|\delta_q| < 10$ deg. Differently, the LR approach is affected by 10%, and 20% of corresponding error values, in the same deflection range.

Remark 2.2
As discussed in Section 1.3.3.4, the canards control contributions modeling relies on the aerodynamic superposition Assumption 1.7, and the approximated interpolation in Equation (1.35)*. The former assumes the linear superposition between the static and the control aerodynamic contributions, individually estimated as a function of the projectile AoA, the former, and the*

canards' local deflections, the latter. On the other side, the approximated interpolation analysis identified the linear range of canard response limited to $|\delta_r|, |\delta_l| < 20$ *deg. Thus, by combining these results, the aerodynamic superposition assumption is reliable in a limited range of total canard deflections,* $|\alpha_{\text{CAN}}| = |\alpha + \delta_{\text{r,l}}| \approx |\alpha + \delta_q| < 20$ *deg.*

The considerations expressed in Remark 2.2 suggest that the canards' local deflections values, $(\delta_{\text{r}}, \delta_{\text{l}})$, and consequently their virtual combinations, (δ_p, δ_q), must always remain far below the boundaries of the linear range, $[-20, 20]$ deg. Indeed, the amplitude of the AoA during a gliding trajectory is never null. Thus, the most significant deflection range concerning the accuracy of the aerodynamic approximations results to be $\delta_q \in [-10, 10]$ deg, rather than at higher values. The approximation errors related to the pitching moment coefficient in Figure 2.4 present the same trend as the vertical force ones. As a consequence, the Taylor approximation models in Equation (2.22) are selected as the most accurate linearization approach for the aerodynamic control contributions. The approximated control coefficients are finally linear w.r.t. the pitch channel dynamics in Equations (2.19)-(2.20), allowing the employment of the state transformation approach. The discussed aerodynamic approximations are accounted for as sources of uncertainties to be handled at the control design stage.

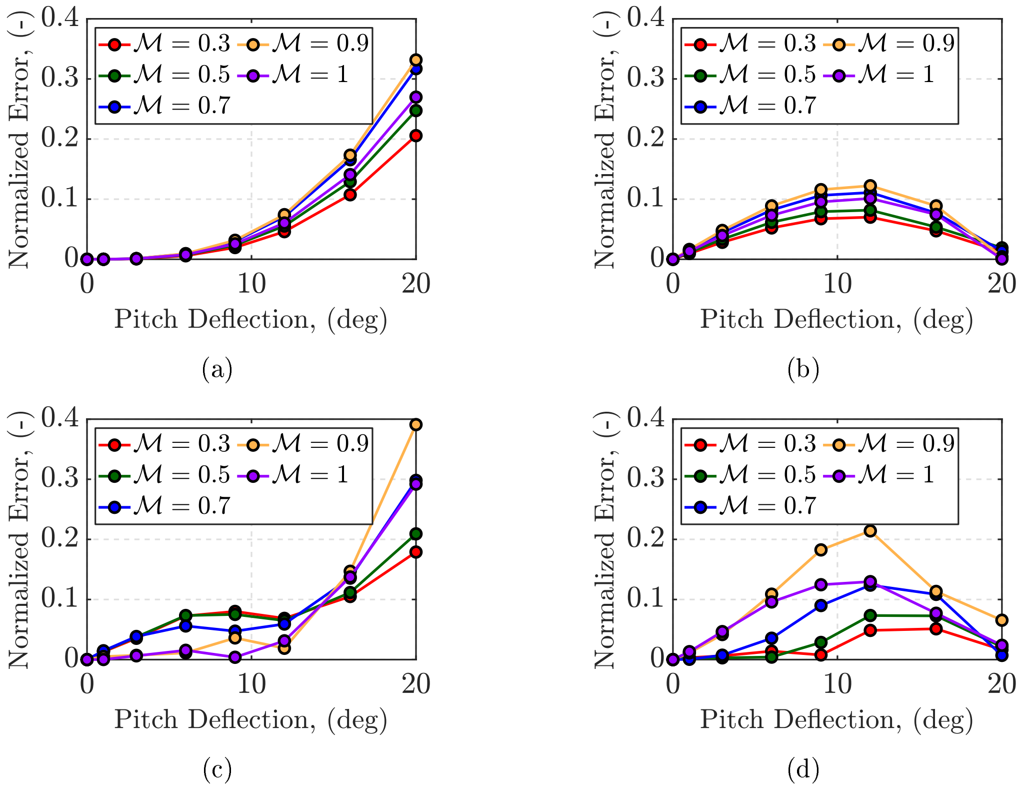

(a)

(b)

(c)

(d)

Figure 2.3: $C_{Z_{\delta_q}}$ approximation errors: (a) e_{PR} related to the TA approach; (b) e_{PR} related to the LR approach; (c) e_{CFD} related to the TA approach; (d) e_{CFD} related to the LR approach.

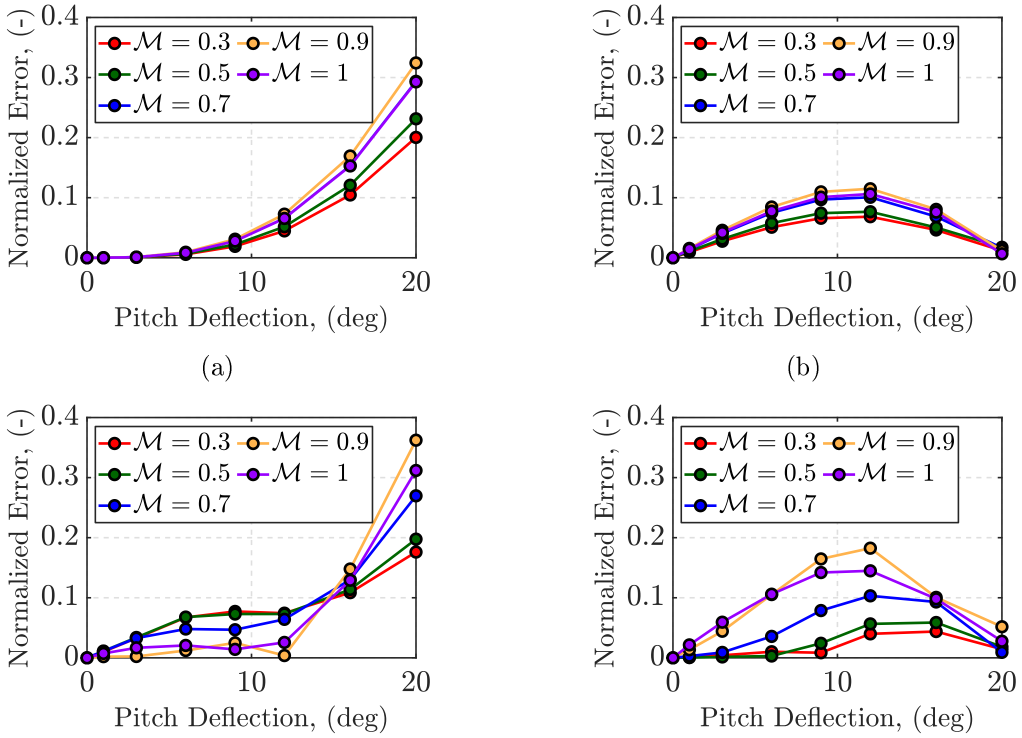

(a) (b) (c) (d)

Figure 2.4: $C_{m_{\delta_q}}$ approximation errors: (a) e_{PR} related to the TA approach; (b) e_{PR} related to the LR approach; (c) e_{CFD} related to the TA approach; (d) e_{CFD} related to the LR approach.

2.3.2.2 Integrator-Augmented Model

The aerodynamic approximations in Equation (2.22) allow reformulating the nonlinear pitch channel dynamics in Equations (2.19)-(2.20) as the output nonlinear system in Equation (2.10). The vector of scheduling variables, $\boldsymbol{\rho}(t)$, selected to accomplish the state transformation, includes the endogenous variable, $z = \alpha(t)$, and the exogenous variables, $\boldsymbol{\Omega} = [V(t), h(t)]^{\mathrm{T}}$.

$$\boldsymbol{\rho}(t) = [z, \boldsymbol{\Omega}]^{\mathrm{T}} = [\alpha(t), V(t), h(t)]^{\mathrm{T}}$$

The scheduling variables have been selected in reason of their relevant impact on the dynamics and the stability of the projectile. The nonlinear terms affecting the pitch channel dynamics are all functions of α. Thus, it has to be addressed as an endogenous parameter. Additionally, to account for the large variation of V, and h, during the standard ballistic trajectory of the projectile, these parameters must be considered in the LPV modeling process.

Assumption 2.5

As already mentioned in Assumption 2.1, the vector of scheduling variables, $\boldsymbol{\rho}(t)$, is assumed to be known and available in real-time. Thus, the selected scheduling flight parameters $(\alpha(t), V(t), h(t))$ are assumed to be either measured or estimated online, by means of navigation algorithms.

Remark 2.3
The airspeed dynamics, $\dot{V}$, could have been included in the pitch channel model, addressing the long-period longitudinal dynamics (phugoid) of the projectile. However, the requirements imposed by Assumption 2.3, prevent the selection of V as an endogenous scheduling variable. Indeed, since the set of available control inputs is limited to the virtual pitch deflection, δ_q, the scheduling state vector can include only one parameter, thus $z(t) = \alpha(t)$. This aspect is coherent with the absence of relevant control authority on the projectile longitudinal velocity, since no thruster vectoring is employed for control purposes.

As a final comment, the pitch and the roll angles, θ and ϕ, respectively, represent the only parameters not accounted for in the scheduling vector. Due to the Dynamic Decoupling Assumption 1.5, the variation of the roll angle does not provide a significant contribution to the pitch channel dynamics. Thus, a nominal value, $\bar{\phi} = 0$ deg, is assumed for the roll angle. The variation of the pitch angle has an impact on the projectile dynamics. However, the inclusion of an additional scheduling variable might over-complicate the synthesis of the controller, which could become unfeasible. Additionally, the dynamics of the AoA partially accounts for the attitude of the projectile. Thus, a nominal value is also selected for θ. The selection has been performed iteratively. An initial value, $\bar{\theta} = 0$ deg, was selected for simplicity during the first control design stage. The resulting closed-loop trajectory simulations showed how the pitch angle tends to stabilize around a nominal value, $\bar{\theta} = -2$ deg, during the gliding phase. As a consequence, the new value has been updated to improve the accuracy of the LPV model and the performance of the control design.

According to these last observations, the projectile nonlinear pitch channel dynamics in Equations (2.19)-(2.20) can be finally expressed as the following output nonlinear system:

$$\begin{bmatrix}\dot{\alpha}\\ \dot{q}\end{bmatrix} = \begin{bmatrix}f_1(\boldsymbol{\rho})\\ f_2(\boldsymbol{\rho})\end{bmatrix} + \begin{bmatrix}0 & \mathcal{A}_{12}(\boldsymbol{\rho})\\ 0 & \mathcal{A}_{22}(\boldsymbol{\rho})\end{bmatrix}\begin{bmatrix}\alpha\\ q\end{bmatrix} + \begin{bmatrix}\mathcal{B}_1(\boldsymbol{\rho})\\ \mathcal{B}_2(\boldsymbol{\rho})\end{bmatrix}\delta_q; \qquad \boldsymbol{\rho}(t) = [\alpha(t), V(t), h(t)] \tag{2.24}$$

where:

$$\begin{aligned} \mathcal{A}_{12}(\boldsymbol{\rho}) &= 1 + \frac{\bar{q}S\cos\alpha}{mV}\left(\frac{d}{2V}\right)C_{Z_q}; & \mathcal{B}_1(\boldsymbol{\rho}) &= \frac{\bar{q}S\cos\alpha}{mV}C_{Z_{\delta_q 1}};\\ \mathcal{A}_{22}(\boldsymbol{\rho}) &= \frac{\bar{q}Sd}{I_2}\left(\frac{d}{2V}\right)C_{m_q}; & \mathcal{B}_2(\boldsymbol{\rho}) &= \frac{\bar{q}Sd}{I_2}C_{m_{\delta_q 1}}; \end{aligned} \tag{2.25}$$

and:

$$\begin{aligned} f_1(\boldsymbol{\rho}) &= -\frac{\bar{q}S\sin\alpha}{mV}\left(C_{X_{\alpha 0}}(\mathcal{M}) + C_{X_{\alpha 2}}(\mathcal{M})\sin^2\alpha + C_{X_{\alpha 4}}(\mathcal{M})\sin^4\alpha\right)\\ &\qquad + \frac{\bar{q}S\sin\alpha\cos\alpha}{mV}C_{Z_{\alpha 1}}(\mathcal{M}) + \frac{g}{V}\left(\sin\alpha\sin\bar{\theta} + \cos\alpha\cos\bar{\theta}\right);\\ f_2(\boldsymbol{\rho}) &= \frac{\bar{q}Sd}{I_2}\left(C_{m_{\alpha 1}}(\mathcal{M})\sin\alpha + C_{m_{\alpha 3}}(\mathcal{M})\sin^3\alpha + C_{m_{\alpha 5}}(\mathcal{M})\sin^5\alpha\right). \end{aligned} \tag{2.26}$$

After satisfying Assumptions 2.2-2.3, the state transformation approach implies verifying the existence of the trim functions, $(q_{\text{eq}},\, \delta_{q,\text{eq}})$, as well as the feasible trim map, as discussed in Assumption 2.4 and Remark 2.1, respectively. By zeroing the dynamics in Equations (2.24)-(2.26), the trimming functions can be evaluated w.r.t. the variation of $\boldsymbol{\rho}(t)$, as it follows:

$$\begin{cases} f_1(\boldsymbol{\rho}) + \mathcal{A}_{12}(\boldsymbol{\rho})q_{\text{eq}} + \mathcal{B}_1(\boldsymbol{\rho})\delta_{q,\text{eq}} = 0 \\ f_2(\boldsymbol{\rho}) + \mathcal{A}_{22}(\boldsymbol{\rho})q_{\text{eq}} + \mathcal{B}_2(\boldsymbol{\rho})\delta_{q,\text{eq}} = 0 \end{cases} \tag{2.27}$$

The resolution of the above system of equations leads to the definition of trimming functions, parameterized as:

$$q_{\text{eq}}(\boldsymbol{\rho}) = \frac{\mathcal{B}_1(\boldsymbol{\rho})f_2(\boldsymbol{\rho}) - \mathcal{B}_2(\boldsymbol{\rho})f_1(\boldsymbol{\rho})}{\mathcal{A}_{12}(\boldsymbol{\rho})\mathcal{B}_2(\boldsymbol{\rho}) - \mathcal{A}_{22}(\boldsymbol{\rho})\mathcal{B}_1(\boldsymbol{\rho})}; \qquad \delta_{q,\text{eq}}(\boldsymbol{\rho}) = -\frac{\mathcal{A}_{12}(\boldsymbol{\rho})f_2(\boldsymbol{\rho}) - \mathcal{A}_{22}(\boldsymbol{\rho})f_1(\boldsymbol{\rho})}{\mathcal{A}_{12}(\boldsymbol{\rho})\mathcal{B}_2(\boldsymbol{\rho}) - \mathcal{A}_{22}(\boldsymbol{\rho})\mathcal{B}_1(\boldsymbol{\rho})}. \tag{2.28}$$

As a first step, the existence of the trimming functions is investigated across the entire parameters range of variation. The existence conditions analysis is detailed in the Appendix B, while a graphical representation of the functions continuity is shown in Figure 2.5 and Figure 2.6. The curves in Figure 2.5 represent the continuous variation of the trimming functions evaluated across the ranges of $(\alpha,\, \mathcal{M})$, that are selected consistently with the domain of validity of the aerodynamic coefficients. The Mach number is used here as a reference parameter instead of the airspeed, for a direct interpretation of the flight regime under analysis. Similarly,

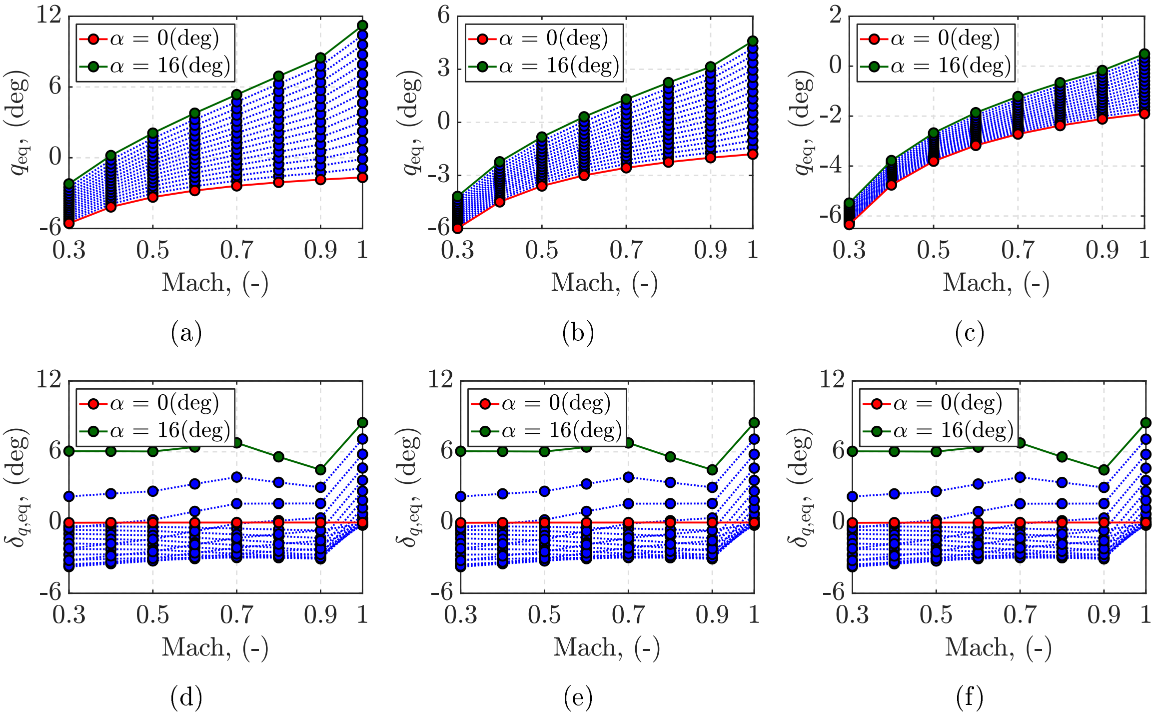

(a) (b) (c)

(d) (e) (f)

Figure 2.5: Trimming functions analysis: (a)-(b)-(c) pitch rate curves at $h = [1, 7, 15]$ km, respectively; (d)-(e)-(f) pitch deflection curves at $h = [1, 7, 15]$ km, respectively.

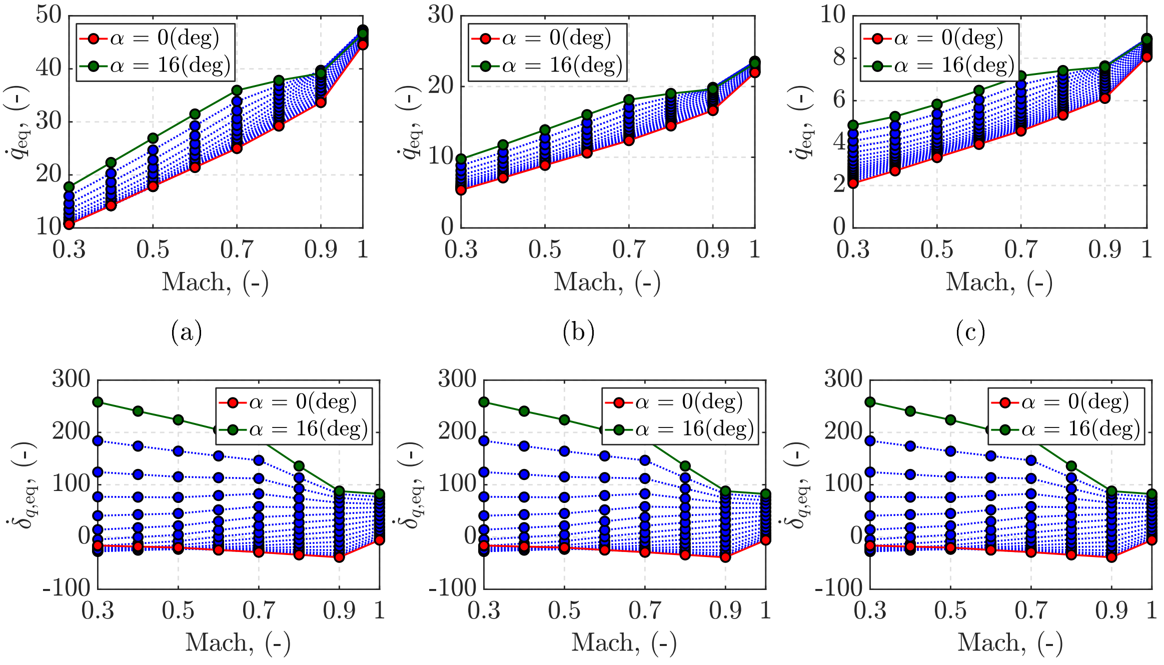

(a) (b) (c)

(d) (e) (f)

Figure 2.6: Trimming functions partial derivatives analysis: (a)-(b)-(c) pitch rate curves at $h = [1, 7, 15]$ km, respectively; (d)-(e)-(f) pitch deflection curves at $h = [1, 7, 15]$ km, respectively.

the analyzed altitude range targets the gliding phase of the projectile trajectory, equal to $h \in [1, 15]$ km. The existence and the continuity of the partial derivatives, $(\frac{\partial q_{\text{eq}}(\boldsymbol{\rho})}{\partial \alpha}, \frac{\partial \delta_{q,\text{eq}}(\boldsymbol{\rho})}{\partial \alpha})$, are assessed across the same $\boldsymbol{\rho}(t)$ domain through the curves in Figure 2.6. As a consequence, Assumption 2.4 is satisfied.

The last step consists of the identification of the feasible trim map, where the trimming functions assume reasonable values. Indeed, at highly unstable conditions, the control effort required to trim the projectile dynamics might exceed the linear range of deflection of the control canards. As shown in the results of Figures 2.5(d)-(e)-(f), the trimmed input curves, $\delta_{q,\text{eq}}$, lie in the identified canards linear deflection range, $\delta_q \in [-20, 20]$ deg, at any (α, $\mathcal{M}$, h) conditions. In particular, the trimming functions are highly affected by the variations of α and $\mathcal{M}$, while the influence of h on $\delta_{q,\text{eq}}$, and $\frac{\partial \delta_{q,\text{eq}}}{\partial \alpha}$ results to be negligible. A sudden increase in the values of the trimmed input is observed during the transient regime, at $\mathcal{M} > 0.9$, in reason of the higher instability of the projectile. The analysis of the feasible trim map satisfies the requirements raised in Remark 2.1.

According to the previous results, the projectile output nonlinear pitch channel dynamics in Equations (2.24)-(2.26) can be finally converted into a quasi-LPV model. However, the state transformation relies on the reformulation of the non-scheduling state and input as off-equilibrium variables, q_{dev} and $\delta_{q,\text{dev}}$, respectively. As previously discussed, the resulting critical dependence of the off-equilibrium input to the trimming condition, $\delta_{q,\text{eq}}$, can be avoided either by restricting the trim map to the flight conditions where $\delta_{q,\text{eq}} = 0$ deg, or by augmenting integrator dynamics at the input of the system. As shown in Figure 2.5, the flight points that respect the trimming condition belong to a very limited envelope, unfeasible for control design purposes. Thus, integrator dynamics is augmented to the projectile output nonlinear model, defining the new input, σ, as:

$$\delta_q = \int \sigma.$$

The resulting integrator-augmented quasi-LPV model, describing the projectile pitch channel dynamics, is expressed as:

$$\begin{bmatrix} \dot{\alpha} \\ \dot{q}_{\text{dev}} \\ \dot{\delta}_{q,\text{dev}} \end{bmatrix} = \begin{bmatrix} 0 & \mathcal{A}_{12}(\boldsymbol{\rho}) & \mathcal{B}_1(\boldsymbol{\rho}) \\ 0 & \tilde{\mathcal{A}}_{22}(\boldsymbol{\rho}) & \tilde{\mathcal{B}}_2(\boldsymbol{\rho}) \\ 0 & \tilde{\mathcal{A}}_{32}(\boldsymbol{\rho}) & \tilde{\mathcal{B}}_3(\boldsymbol{\rho}) \end{bmatrix} \begin{bmatrix} \alpha \\ q_{\text{dev}} \\ \delta_{q,\text{dev}} \end{bmatrix} + \begin{bmatrix} 0 \\ 0 \\ 1 \end{bmatrix} \sigma \tag{2.29}$$

with:

$$\begin{aligned} \tilde{\mathcal{A}}_{22}(\boldsymbol{\rho}) &:= \mathcal{A}_{22}(\boldsymbol{\rho}) - \frac{\partial q_{\text{eq}}}{\partial \alpha}\mathcal{A}_{12}(\boldsymbol{\rho}); & \tilde{\mathcal{B}}_2(\boldsymbol{\rho}) &:= \mathcal{B}_2(\boldsymbol{\rho}) - \frac{\partial q_{\text{eq}}}{\partial \alpha}\mathcal{B}_1(\boldsymbol{\rho}); \\ \tilde{\mathcal{A}}_{32}(\boldsymbol{\rho}) &:= -\frac{\partial \delta_{q,\text{eq}}}{\partial \alpha}\mathcal{A}_{12}(\boldsymbol{\rho}); & \tilde{\mathcal{B}}_3(\boldsymbol{\rho}) &:= -\frac{\partial \delta_{q,\text{eq}}}{\partial \alpha}\mathcal{B}_1(\boldsymbol{\rho}). \end{aligned} \tag{2.30}$$

The new state vector includes the AoA, and the off-equilibrium values of the pitch rate, q_{dev}, and the virtual pitch deflection, $\delta_{q,\text{dev}}$.

Concerning the output measurements, a dynamic output feedback control approach will be employed, assuming to have full access to the state vector of the system (state feedback). In this scenario, the output matrix, $\mathcal{C}$, corresponds to the identity $I \in \mathbb{R}^{3\times3}$. Alternatively, the vertical load factor measurements (LF), η_z, expressed in Equation (1.23), can substitute the virtual pitch deflection ones, leading to a standard dynamic output feedback configuration. In order to comply with the formulation of the quasi-LPV model, the off-equilibrium expression of the vertical LF is computed as:

$$\begin{aligned} \eta_{z,\text{dev}} &= \eta_z - \eta_{z,\text{eq}}(\boldsymbol{\rho}) \\ &= \frac{\bar{q}S}{mg}\left[\left(\frac{d}{2V}\right)C_{Z_q}q_{\text{dev}} + C_{Z_{\delta_q 1}}\delta_{q,\text{dev}}\right] \end{aligned} \tag{2.31}$$

where the trimmed load factor, $\eta_{z,\text{eq}}$, is simply obtained by substituting q_{eq} and $\delta_{q,\text{eq}}$ in the general formulation in Equation (1.23), as:

$$\begin{aligned} \eta_{z,\text{eq}}(\boldsymbol{\rho}) &= \frac{Z\left(q_{\text{eq}}, \delta_{q,\text{eq}}\right)}{mg} \\ &= \frac{\bar{q}S}{mg}\left[C_{Z_{\text{S}}}(\mathcal{M}, \alpha) + \left(\frac{d}{2V}\right)C_{Z_q}(\mathcal{M})\, q_{\text{eq}} + C_{Z_{\delta_q 1}}(\mathcal{M}, \delta_q)\, \delta_{q,\text{eq}}\right]. \end{aligned} \tag{2.32}$$

As a consequence, the output equations in the output feedback configuration are expressed as:

$$\begin{bmatrix} \alpha \\ q_{\text{dev}} \\ \eta_{z,\text{dev}} \end{bmatrix} = \begin{bmatrix} 1 & 0 & 0 \\ 0 & 1 & 0 \\ 0 & \tilde{\mathcal{C}}_{32}(\boldsymbol{\rho}) & \tilde{\mathcal{C}}_{33}(\boldsymbol{\rho}) \end{bmatrix} \begin{bmatrix} \alpha \\ q_{\text{dev}} \\ \delta_{q,\text{dev}} \end{bmatrix} \tag{2.33}$$

where:

$$\tilde{\mathcal{C}}_{32}(\boldsymbol{\rho}) = \frac{\bar{q}S}{mg}\left(\frac{d}{2V}\right)C_{Z_q}; \qquad \tilde{\mathcal{C}}_{33}(\boldsymbol{\rho}) = \frac{\bar{q}S}{mg}C_{Z_{\delta_q 1}}. \tag{2.34}$$

For both the state and the output feedback configurations, the input feedforward matrix, $\mathcal{D}$, is assumed zero.

2.3.3 Model Matching Simulations

The accuracy of the obtained quasi-LPV model is assessed through a set of open-loop simulations. In reason of the instability characterizing the projectile dynamics, the simulations are performed across a reduced stable domain of the flight envelope. Step deflection commands, δ_q, are employed to perturb the quasi-LPV model from a selected steady-state equilibrium condition. The performance of the quasi-LPV model (q-LPV), which accounts for the aerodynamic approximation in Equation (2.22), is compared with the full nonlinear pitch channel dynamics (NL) in Equations (2.19)-(2.20). The simulator scheme is shown in Figure 2.7. An integrator is added at the input of the nonlinear system to compensate for the dynamics augmentation introduced in the quasi-LPV model during the state transformation. Additionally, the off-equilibrium state, $q_{\text{dev}}(t)$, and input, $\delta_{q,\text{dev}}(t)$, of the nonlinear model are obtained in post-processing by applying the transformation in Equation (2.13) to the evaluated state, $q(t)$, and input, $\delta_q(t)$. This process is performed in the *Output Deviation* block of the scheme in Figure 2.7, allowing for a better comparison of the systems' responses.

The scheduling parameters considered during the simulations are $\boldsymbol{\rho}_{\text{sim}} = [\alpha, V]$, while the altitude, h, is assumed as constant. Indeed, the trim map analysis in Figure 2.5 did not show a significant dependence of the trimming functions on the altitude conditions. At

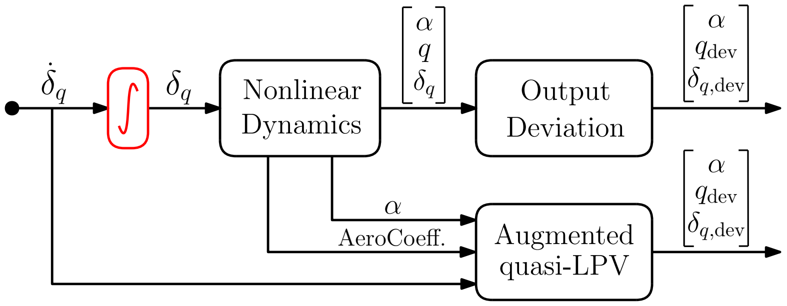

Figure 2.7: Simulation scheme: quasi-LPV model assessment.

each selected initial flight point, $\boldsymbol{\rho}_{\text{sim}}$, the corresponding trimming functions, $q_{\text{eq}}(\boldsymbol{\rho}_{\text{sim}})$ and $\delta_{q,\text{eq}}(\boldsymbol{\rho}_{\text{sim}})$, define the equilibrium conditions of the projectile. The selection criteria for the initial $\boldsymbol{\rho}_{\text{sim}}$ rely on the minimization of the trimmed input deflection. Indeed, the requirement of a limited equilibrium deflection, $\delta_{q,\text{eq}}$, allows the employment of a larger step perturbation command, without exceeding the validity range of the aerodynamic model defined in Remark 2.2. The results observed through the trim map of Figure 2.5 suggest the selection of the initial conditions in Table 2.1, corresponding to a gliding phase flight point at $\mathcal{M} = 0.7$.

Table 2.1: Trim point conditions.

$\boldsymbol{\alpha}$**(deg)**	$\boldsymbol{V}$**(m/s)**	$\boldsymbol{h}$**(km)**	$\boldsymbol{q}_{\mathbf{eq}}$**(deg/s)**	$\boldsymbol{\delta}_{\boldsymbol{q},\mathbf{eq}}$**(deg)**
13	220	7	0.47	-0.08

The simulations are performed assuming a set of sequential commands corresponding to a first pitch deflection, $\delta_{q_1} = 5$ deg at $t_1 = 5\,\text{s}$, and a second deflection of $\delta_{q_2} = -3$ deg at $t_2 = 30\,\text{s}$. Since the input deflections are integrated for both the quasi-LPV and the nonlinear model, two pulses are actually implemented as perturbations, simulating the corresponding canards deflection rates $(\dot{\delta}_{q_1},\ \dot{\delta}_{q_2})$. Once integrated, the pulses provide the desired control

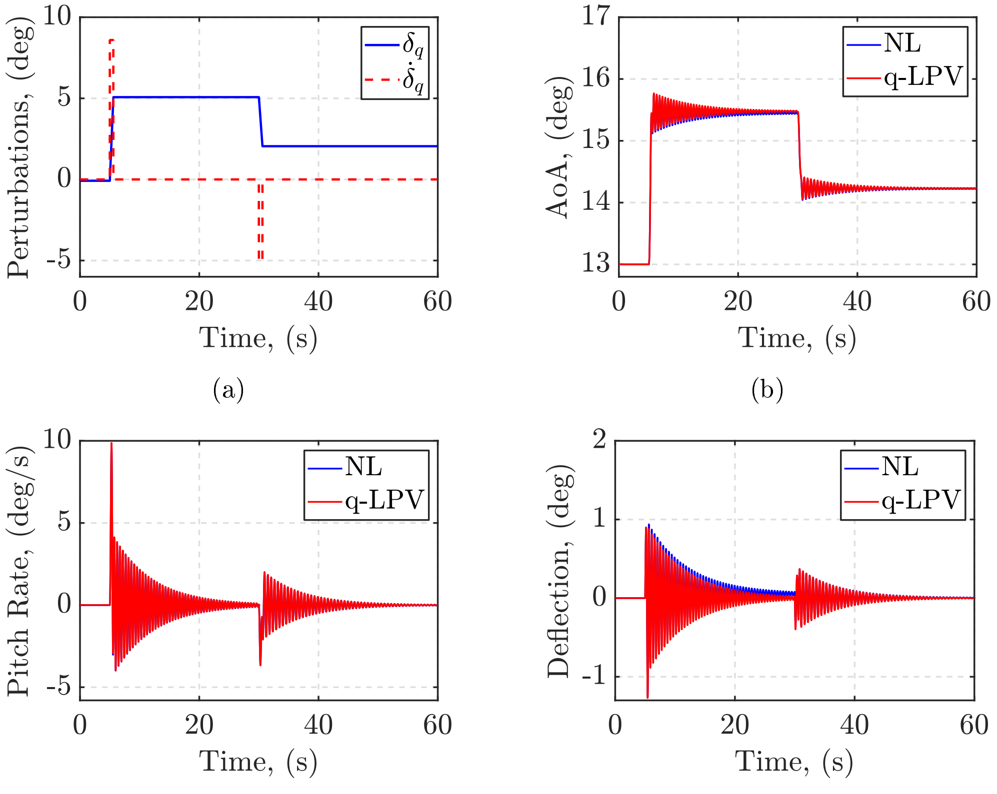

(a) (b)

(c) (d)

Figure 2.8: Simulation curves comparison: (a) input perturbations; (b) angle-of-attack; (c) off-equilibrium pitch rate; (d) off-equilibrium pitch deflections.

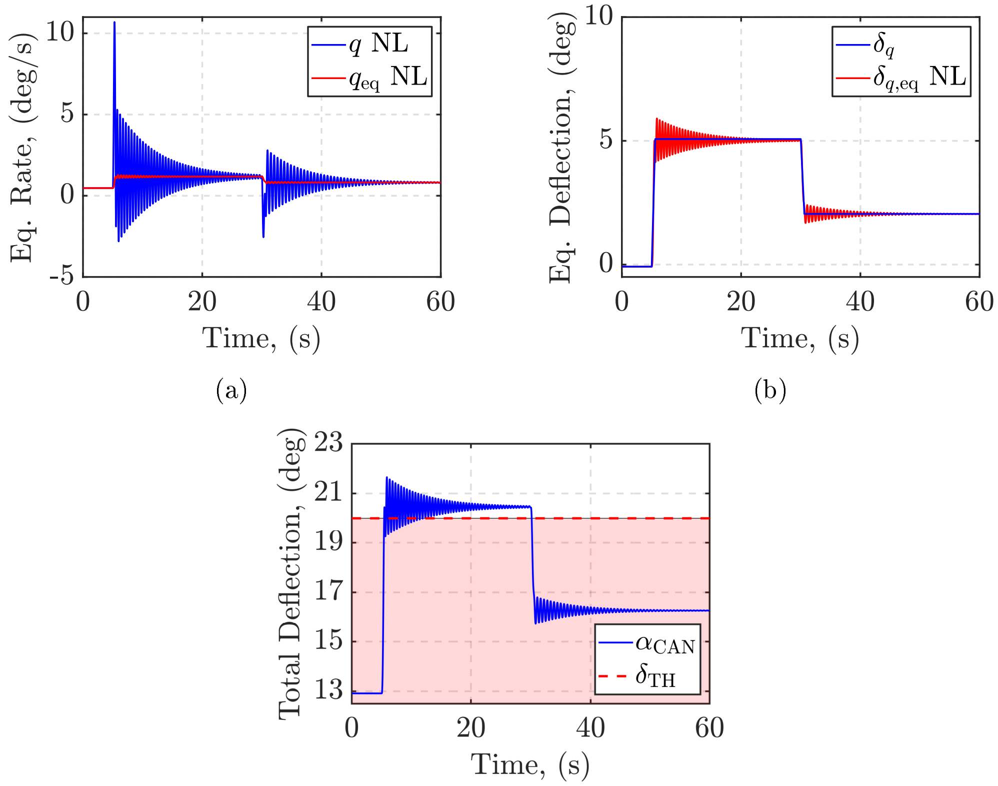

(a)

(b)

(c)

Figure 2.9: Simulation curves comparison: (a) equilibrium pitch rate; (b) equilibrium pitch deflection; (c) total canards deflection.

deflection steps (δ_{q_1}, δ_{q_2}), as shown in Figure 2.8(a). Aiming for a more realistic simulation scenario, the AoA and the aerodynamic coefficients generated by the nonlinear system are assumed to be measured and fed as scheduling variables to the quasi-LPV model. This configuration is coherent with the real-time availability of the scheduling variables imposed by the general definition of LPV systems, and stated in Assumption 2.5. In particular, the aerodynamic coefficients are interpolated online at each (α, $\mathcal{M}$) conditions, based on the approximated linear regression models.

The results in Figures 2.8(b)-(c)-(d) show the comparison between the open-loop time responses of the two systems, related to the state variables, $\alpha(t)$ and $q_{\text{dev}}(t)$, and to the input, $\delta_{q,\text{dev}}(t)$, respectively. The curves describing the quasi-LPV (q-LPV) and the nonlinear model (NL) are almost perfectly overlapped, confirming the accuracy of the state transformation modeling process. At higher AoA, a slight mismatch is observed between the off-equilibrium input curves in Figure 2.8(d), which attenuates a lower AoA. Consistently, the AoA results in Figure 2.8(b) are more accurate at lower steady-state values. The reason behind this behavior can be found in Figure 2.9(c), where the total canard deflection, $\alpha_{\text{CAN}} = \alpha + \delta_q$, is presented. When the first deflection step is commanded, the projectile AoA surpasses the linear deflection range assumed through the aerodynamic approximations, and represented by the deflection threshold, δ_{TH}. At those conditions, the reliability of both the quasi-LPV model, and aerodynamic superposition assumption begins to decrease. As soon as the second deflection command reduces the projectile AoA, the model matching is reestablished.

The curves in Figures 2.9(a)-(b) show the accuracy of the trimming functions, $q_{\mathrm{eq}}(t)$ and $\delta_{q,\mathrm{eq}}(t)$, respectively in compensating for the corresponding signals. The initial large oscillation and the slow damping of the system responses are caused by the limited stability of the projectile dynamics.

The results in Table 2.2 consist of the standard RMSE, evaluated as the difference between the value of each state variable obtained through the NL model and through the quasi-LPV model, and normalized by the Min-Max range of the same variable generated by the NL model. The Min-Max range has been preferred to the standard mean value since both the off-equilibrium pitch rate and pitch deflection converge to zero. The NRMSE results confirm the high capability of the quasi-LPV model to represent the nonlinear dynamics of the projectile.

Table 2.2: Model matching NRMSE evaluation.

	$\boldsymbol{\alpha}$**(deg)**	$\boldsymbol{q}_{\mathbf{dev}}$**(deg/s)**	$\boldsymbol{\delta}_{\boldsymbol{q},\mathbf{dev}}$**(deg)**
NRMSE	0.008	0.001	0.017

2.4 Polytopic Modeling Process

The state transformation process developed in the previous section allowed converting the projectile nonlinear pitch channel dynamics into the integrator-augmented quasi-LPV system in Equations (2.29)-(2.30). The quasi-LPV model is based on the general parameter-dependent formulation discussed in Section 2.2.1.2 since the scheduling variables, $\boldsymbol{\rho}(t) = [\alpha(t), V(t), h(t)]$, enter nonlinearly the model dynamics. Indeed, the entries of the state matrix, $\mathcal{A}$, in Equation (2.25) show an explicit nonlinear dependence on $\alpha(t)$ and $V(t)$, and an implicit nonlinear dependence on $h(t)$, through the definition of the dynamic pressure, $\bar{q}(h)$. As a consequence, the quasi-LPV model in Equations (2.29)-(2.30) is not suitable for a polytopic control-oriented modeling formulation.

As will be detailed in the following chapter, the LPV polytopic design provides higher theoretical guarantees of dynamics stability, compared to alternative controller synthesis, at the expense of more conservative performance. In order to assess the advantages of this design method, the state matrix of the projectile quasi-LPV model has to be reformulated in a way to satisfy the affine model-parameter relation expressed in Definition 2.4. Concerning the controller design, input/output parameter independence represents an additional requirement to ensure the affine formulation. This aspect is clarified through the resolution of the polytopic controller synthesis problem, detailed in the next chapter. As discussed in Section 2.3.1, the input matrix has been redefined as a constant parameter-independent matrix, $\mathcal{B} = [0, 0, 1]^{\mathrm{T}} \in \mathbb{R}^{3\times 1}$, through the inclusion of an integrator during the state transformation process. Furthermore, by assuming the state feedback control architecture introduced at the end of Section 2.3.2.2, the output matrix, $\mathcal{C} = I \in \mathbb{R}^{3\times 3}$, becomes also constant parameter-independent. Thus, the polytopic input/output parameter-independence requirement have been already satisfied.

In the following section, a polytopic model approximation procedure is developed to reformulate the state matrix of the projectile quasi-LPV model, $\mathcal{A}$, into a polytopic form, $\tilde{\mathcal{A}}$. The procedure relies on the identification of a new set of scheduling functions, $\hat{\boldsymbol{\rho}}(t)$, such that the resulting state matrix, $\tilde{\mathcal{A}}$, is affine in $\hat{\boldsymbol{\rho}}(t)$ as in Definition 2.4. The procedure is presented through the scheme in Figure 2.10, and consists of the following sequential steps:

- **I. Parameters Identification:** identify a new set $\hat{\boldsymbol{\rho}}(t)$ characterized by the least necessary number of scheduling functions, $n_{\hat{\rho}}$. Indeed, the computational complexity of the later controller synthesis tends to rapidly increase with $n_{\hat{\rho}}$, as $\mathcal{O}(2^{n_{\hat{\rho}}})$. The selection of the new set of scheduling functions relies on an extensive model-parameter dependence analysis.
- **II. Polytope Mapping:** map the convex space described by the variation ranges of the original scheduling vector, $\boldsymbol{\rho}(t)$, into a new space defined by the set $\hat{\boldsymbol{\rho}}(t)$, identified in step **I**. The intention is to redefine the domain of validity of the approximated polytopic model across the variation of the new scheduling functions, $\hat{\boldsymbol{\rho}}(t)$.

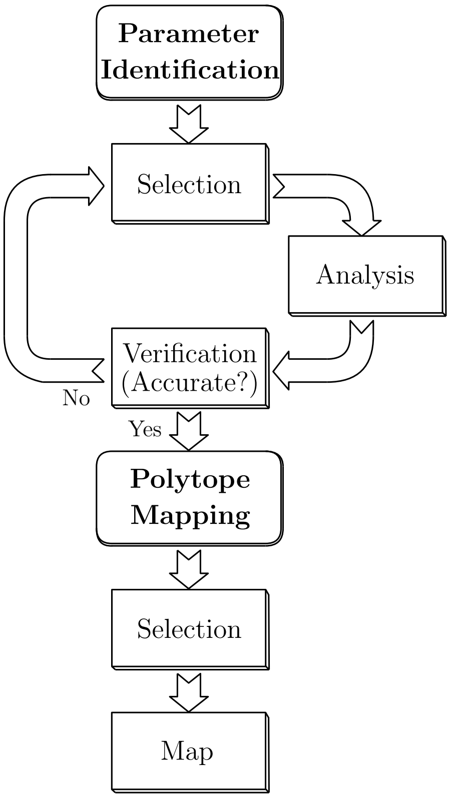

Figure 2.10: Polytopic model approximation scheme.

2.4.1 Parameter Identification

The state matrix, $\mathcal{A}$, is first parameterized in the least possible number of scheduling functions, $\tilde{\boldsymbol{\rho}}(t)$, selected based on the following criteria:

- Favor the selection of nonlinear terms that appear repeatedly in the state matrix.
- The functions must be affine with the system to comply with the polytopic formulation.
- Neglect the effect of the parameters with limited relevance on the system dynamics.

Then, the identified scheduling functions are extensively studied to assess their relevance in the characterization of the system dynamics. Based on the results, each function is either included in the final scheduling vector, $\hat{\boldsymbol{\rho}}(t)$, or neglected. The resulting approximated polytopic model, $\tilde{\mathcal{A}}(\hat{\boldsymbol{\rho}})$, is compared to the original one, $\mathcal{A}(\boldsymbol{\rho})$, to assess the accuracy of the analysis. In the following, the procedure is subdivided into three main phases: **Selection**, **Analysis**, and **Verification**.

2.4.1.1 Selection

The nonlinear terms characterizing the state matrix of the projectile quasi-LPV model in Equations (2.29)-(2.30) are selected in accordance with the above criteria, and accounted for as possible candidates for the new scheduling vector, $\tilde{\boldsymbol{\rho}}(t)$:

$$\begin{aligned} &\tilde{\rho}_1 := \frac{\bar{q}S\cos\alpha}{mV}\left(\frac{d}{2V}\right)C_{Z_q}; && \tilde{\rho}_3 := \frac{\partial q_{\text{eq}}}{\partial\alpha}; && \tilde{\rho}_5 := \frac{\bar{q}Sd}{I_2}\left(\frac{d}{2V}\right)C_{m_q}; \\ &\tilde{\rho}_2 := \frac{\bar{q}S\cos\alpha}{mV}C_{Z_{\delta_q 1}}; && \tilde{\rho}_4 := \frac{\partial \delta_{q,\text{eq}}}{\partial\alpha}; && \tilde{\rho}_6 := \frac{\bar{q}Sd}{I_2}C_{m_{\delta_q 1}}. \end{aligned} \tag{2.35}$$

As a consequence, the state matrix can be expressed as a function of the new set, $\tilde{\boldsymbol{\rho}}(t)$, as:

$$A(\tilde{\boldsymbol{\rho}}) = \begin{bmatrix} 0 & (1+\tilde{\rho}_1) & \tilde{\rho}_2 \\ 0 & \tilde{\rho}_5 - \tilde{\rho}_3(1+\tilde{\rho}_1) & \tilde{\rho}_6 - \tilde{\rho}_3\tilde{\rho}_2 \\ 0 & -\tilde{\rho}_4(1+\tilde{\rho}_1) & -\tilde{\rho}_4\tilde{\rho}_2 \end{bmatrix}. \tag{2.36}$$

The reformulated state matrix, $A(\tilde{\boldsymbol{\rho}})$, is still non-affine in the original set of scheduling variables, $\boldsymbol{\rho}(t)$, but it is affine in the new set, $\tilde{\boldsymbol{\rho}}(t)$, as desired. However, this formulation relies on a large set of scheduling functions, $n_{\tilde{\rho}} = 6$, unfeasible for controller design purposes. Thus, the next phase aims to analyze and neglect the scheduling functions that do not significantly affect the dynamics of the system.

Remark 2.4
The selection of a different parameterization of the state matrix, $\mathcal{A}$, would result in a different set of scheduling functions. The ***Selection*** *phase requires extensive insight and knowledge of the system dynamics under investigation.*

2.4.1.2 Analysis

In order to reduce the dimension of the new scheduling vector, $n_{\tilde{\rho}}$, the variation of each identified scheduling function is analyzed w.r.t. the original set of parameters, $\boldsymbol{\rho}(t)$. Indeed, $\boldsymbol{\rho}(t)$ represents the envelope of all the flight conditions characterizing the projectile's trajectory as a convex subspace (polytope). Any trial scheduling function in $\tilde{\boldsymbol{\rho}}(t)$, which is highly varying inside the original polytope, must be maintained, while the functions with limited effect on the system dynamics might be approximated or completely neglected.

The evaluation is based on the flight envelope defined by: $\alpha \in$ [0, 16] deg, $V \in$ [160, 280] m/s, and $h \in$ [1, 15] km. Since the design aims at improving the range capability of the projectile, only positive values of AoA are considered. Similarly, $h = 15$ km corresponds to the maximum apogee conditions estimated for the range optimization, while $h = 1$ km is assumed as the altitude level where the transition from the gliding phase to the terminal guidance occurs. Finally, the airspeed range covers the most relevant corresponding flight regime, $\mathcal{M} \in [0.3, 1]$.

Function: $\tilde{\boldsymbol{\rho}}_1$. The scheduling function $\tilde{\rho}_1$ is the first investigated. The results in Figure 2.11 show the variation of $\tilde{\rho}_1$ as a function of the airspeed and the altitude in the selected ranges. In particular, the variation of $\tilde{\rho}_1$ is computed at increasing values of altitude with an increment of $\Delta h = 1$ km (blue curves). In reason of the low order of magnitude, the variation of $\tilde{\rho}_1$ has a negligible impact on the system dynamics at any (V, h) flight conditions. The results concerning the variation of $\tilde{\rho}_1$ as a function α provide the same conclusion, thus only two flight scenarios are proposed, one targeting an unstable flight condition, $\alpha = 4$ deg in Figure 2.11(a), and one related to a stable condition, $\alpha = 12$ deg in Figure 2.11(b). As a consequence, the following approximation holds:

$$\tilde{\rho}_1 \approx 0 \mid A_{12}(\tilde{\boldsymbol{\rho}}) = (1 + \tilde{\rho}_1) \approx 1.$$

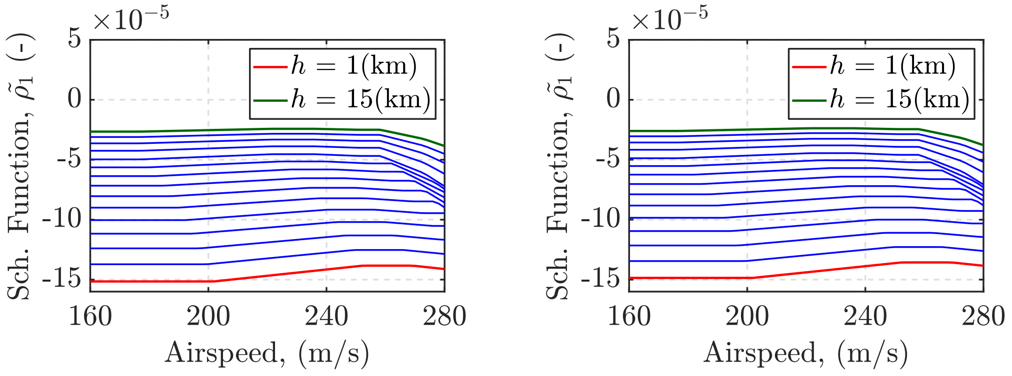

(a) (b)

Figure 2.11: Approximation analysis: (a) $\tilde{\rho}_1$ at $\alpha = 4$ deg; (b) $\tilde{\rho}_1$ at $\alpha = 12$ deg.

Functions: $\tilde{\rho}_2$, $\tilde{\rho}_5$, and $\tilde{\rho}_6$. As observed in Equation (2.35), the functions $\tilde{\rho}_2$, $\tilde{\rho}_5$, and $\tilde{\rho}_6$ have a common affine dependence on the dynamic pressure value, $\bar{q}$. The formulation of $\bar{q}$ itself includes the variations of two of the original scheduling variables: V and h. Thus, the three scheduling functions can be approximated uniquely as a linear function of the dynamic pressure. All the remaining parameters affecting $\tilde{\rho}_2$, $\tilde{\rho}_5$, and $\tilde{\rho}_6$ are frozen to a nominal average value, $(\bar{V}, \bar{C}_{Z_{\delta_{q1}}}, \bar{C}_{m_q}, \bar{C}_{m_{\delta_{q1}}})$, in their range of variations, leading to the approximations:

$$\bar{\rho}_2(\bar{q}) = \frac{\bar{q}S}{m\bar{V}}\bar{C}_{Z_{\delta_{q1}}} \approx \tilde{\rho}_2; \qquad \bar{\rho}_5(\bar{q}) = \frac{\bar{q}Sd}{I_2}\left(\frac{d}{2\bar{V}}\right)\bar{C}_{m_q} \approx \tilde{\rho}_5; \qquad \bar{\rho}_6(\bar{q}) = \frac{\bar{q}Sd}{I_2}\bar{C}_{m_{\delta_{q1}}} \approx \tilde{\rho}_6. \tag{2.37}$$

Concerning the approximations, the aerodynamic coefficients have been acquired as a function of the Mach value, hence of V and h, but their variations are very limited, thus negligible. Similarly, the impact of the AoA variation on $\tilde{\rho}_2$ is assumed negligible for the present analysis. The nominal value selected for the airspeed corresponds to $\bar{V} = 220$ m/s, representing the average airspeed condition experienced by the projectile during the gliding phase of the trajectory.

The accuracy of these approximations is verified at each flight condition (V, h) as the RMSE between the original and the approximated function, evaluated in the full range of

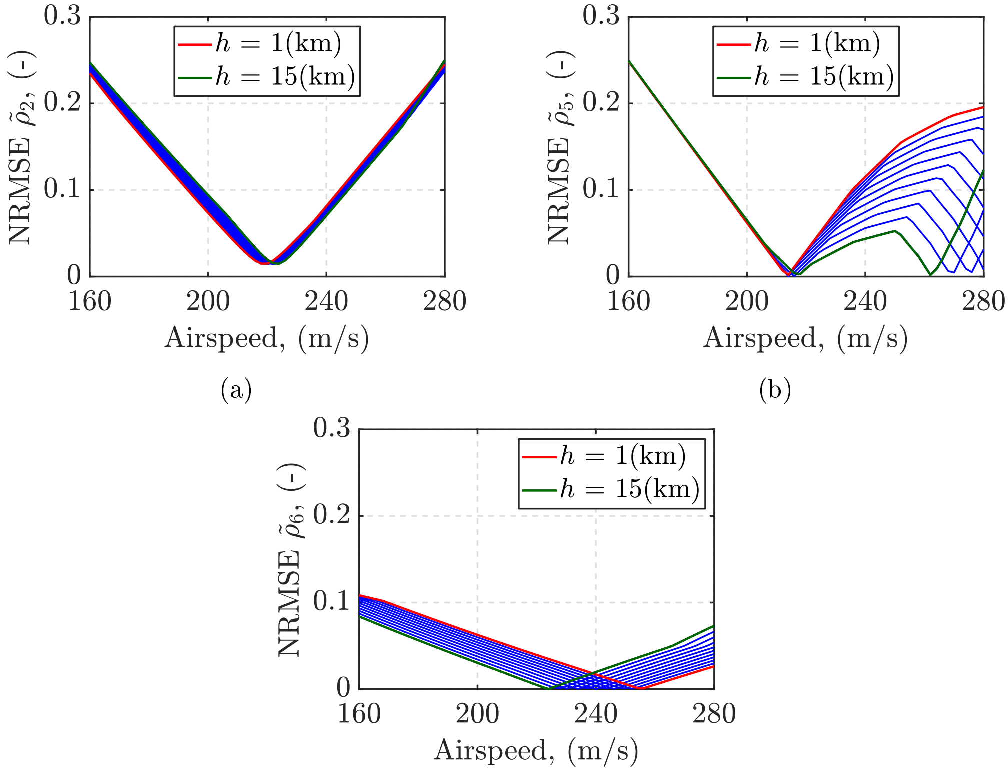

(a) (b)

(c)

Figure 2.12: Approximation analysis: (a) NRMSE of $\tilde{\rho}_2$; (b) NRMSE of $\tilde{\rho}_5$; (c) NRMSE of $\tilde{\rho}_6$.

$\alpha = [0, \dots, 16] \in \mathbb{R}^N$, and normalized by the mean value of the original scheduling function at the same flight point:

$$\text{NRMSE}_j(V,h) := \frac{\sqrt{\frac{\sum_{i=1}^{N}(\tilde{\rho}_j(\alpha_i,V,h)-\bar{\rho}_j(\alpha_i,V,h))^2}{N}}}{\frac{\sum_{i=1}^{N}\tilde{\rho}_j(\alpha_i,V,h)}{N}}; \qquad j \in [2,5,6].$$

The results related to the function $\tilde{\rho}_2$ are shown in Figure 2.12(a). The approximation error is minimal at the airspeed conditions around the selected nominal value, $\bar{V}$. However, it does not exceed 15% in the main range of variation occurring during the gliding phase, regardless of the (α, h) values. Similarly, the accuracy of $\tilde{\rho}_5$ is lower at lower airspeed values ($\leq$ 15%) and improves at higher conditions ($\leq$ 10%). Indeed, conditions of $V \geq 240$ m/s never occur at low altitude levels, during the characteristic gliding trajectory of the projectile. Thus, the upper curves on the right half of Figure 2.12(b) are not relevant to the analysis.

Finally, the approximation of $\tilde{\rho}_6$ provides extremely accurate results, as observed in Figure 2.12(c). Indeed, this function is not dependent on the inverse of V as the previous, but only on the dynamic pressure. All the previous results are summarized in Table 2.3.

Table 2.3: NRMSE of the functions approximation.

Functions	**NRMSE max**	**NRMSE min**	**ref. error %**
$\tilde{\boldsymbol{\rho}}_2$	0.25	0.01	15
$\tilde{\boldsymbol{\rho}}_5$	0.25	0	10
$\tilde{\boldsymbol{\rho}}_6$	0.11	0	5

Based on the analysis, the approximations in Equation (2.37) hold, and the variation of three scheduling functions, ($\tilde{\rho}_2$, $\tilde{\rho}_5$, $\tilde{\rho}_6$), can be represented in terms of the dynamic pressure variation only. By including $\bar{q}$ instead of ($\tilde{\rho}_2$, $\tilde{\rho}_5$, $\tilde{\rho}_6$) in the new scheduling vector, the corresponding dimension, $n_{\tilde{\rho}}$, reduces significantly.

Functions: $\tilde{\boldsymbol{\rho}}_3$, and $\tilde{\boldsymbol{\rho}}_4$. Concerning the remaining functions, $\tilde{\rho}_3$ and $\tilde{\rho}_4$, the curves in Figures 2.13(a)-(b) and Figures 2.13(c)-(d), respectively, reveal the highly nonlinear behavior characterizing the derivatives of the equilibrium functions, $\frac{\partial q_{\text{eq}}}{\partial \alpha}$ and $\frac{\partial \delta_{q,\text{eq}}}{\partial \alpha}$. Additionally, their complex symbolic expressions prevent any possible parameterization as linear functions of the dynamic pressure, or of any of the original set of scheduling variables.

As a consequence, they are directly assumed as new scheduling functions leading to the definition of the final scheduling vector, $\hat{\boldsymbol{\rho}} = [\hat{\rho}_1,\ \hat{\rho}_2,\ \hat{\rho}_3]$, with:

$$\hat{\rho}_1 := \bar{q}; \qquad \hat{\rho}_2 := \frac{\partial q_{\text{eq}}}{\partial \alpha}; \qquad \hat{\rho}_3 := \frac{\partial \delta_{q,\text{eq}}}{\partial \alpha}. \tag{2.38}$$

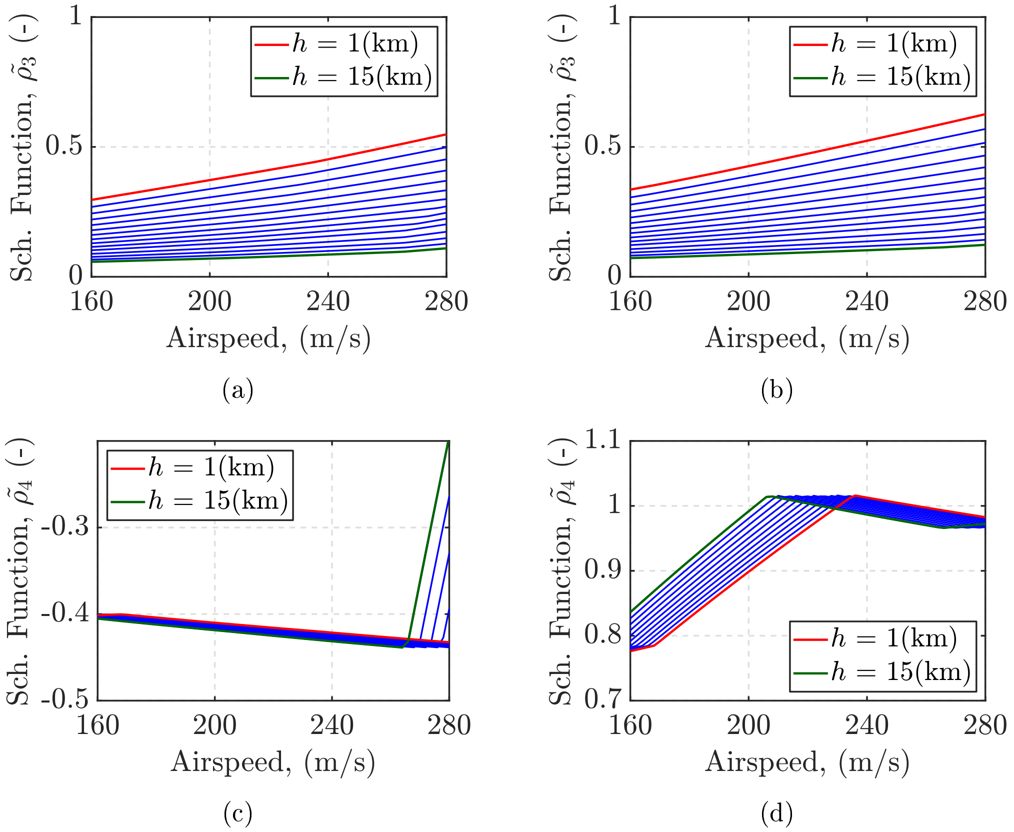

(a) (b) (c) (d)

Figure 2.13: Approximation analysis: (a)-(b) $\tilde{\rho}_3$ variation at $\alpha = 4$ deg, and $\alpha = 12$ deg, respectively; (c)-(d) $\tilde{\rho}_4$ variation at $\alpha = 4$ deg, and $\alpha = 12$ deg, respectively.

Consistently, the state matrix in Equation (2.36) can be reformulated in a parameter-affine form as:

$$\tilde{A}(\hat{\boldsymbol{\rho}}) = \begin{bmatrix} 0 & 1 & \bar{A}_{13}(\hat{\rho}_1) \\ 0 & \bar{A}_{22}(\hat{\rho}_1) - \hat{\rho}_2 & \bar{A}_{23}(\hat{\rho}_1) \\ 0 & -\hat{\rho}_3 & -\hat{\rho}_3 \bar{A}_{13}(\hat{\rho}_1) \end{bmatrix}, \tag{2.39}$$

where $\bar{A}_{13} = \bar{\rho}_2$, and $\bar{A}_{22} = \bar{\rho}_5$ are the approximated forms of $\tilde{\rho}_2$, and $\tilde{\rho}_5$, respectively discussed in Equation (2.37), accounting for the selected parameters' nominal values. The final approximation targets the matrix entry $\bar{A}_{23}$. Since the approximated product, $\hat{\rho}_2 \bar{A}_{13}$, results in some order of magnitude lower than the nominal entry $\hat{\rho}_6$, $\bar{A}_{23}$ can be approximated as:

$$\begin{aligned} \bar{A}_{23} &\coloneqq \bar{\rho}_6 - \hat{\rho}_2 \bar{A}_{13} \\ &\approx \bar{\rho}_6 = \frac{\bar{q}Sd}{I_2} \bar{C}_{m_{\delta_q 1}}. \end{aligned}$$

2.4.1.3 Verification

In order to assess the accuracy of the overall approximation procedure, Figures 2.14(a)-(b) show a comparison between the dynamics of the original model (Full) in Equation (2.36), and

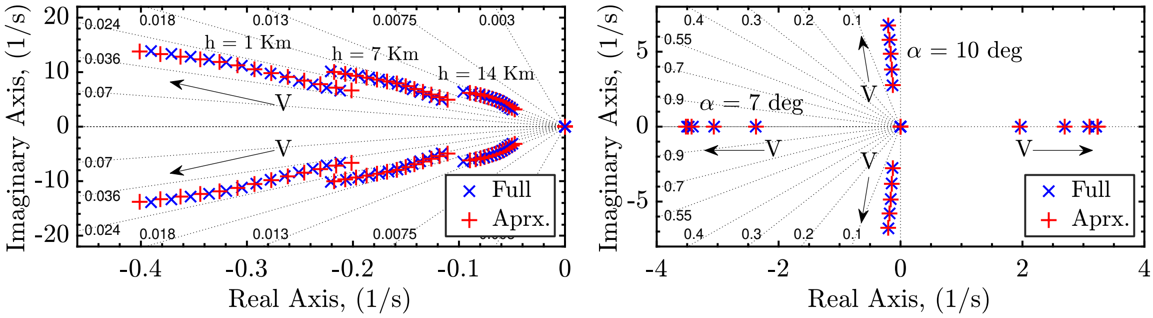

(a) (b)

Figure 2.14: Pole-zero maps: (a) (V, h) variation at $\alpha = 12$ deg; (b) stable/unstable α conditions.

the approximated model (Aprx.) in Equation (2.39). Specifically, Figure 2.14(a) corresponds to the pole-zero maps of the two models, evaluated at stable flight conditions, assuming $\alpha = 12$ deg, and increasing values of V and h. Similarly, Figure 2.14(b) compares the pole-zero maps at a stable, $\alpha = 10$ deg, and at an unstable, $\alpha = 7$ deg, configuration, for increasing values of V, and at a constant altitude level, $h = 7$ km. Different axes scales are selected to improve the readability of the presented results.

A slight difference between the original and the approximated poles is observed, especially for higher values of V and lower values of h. However, the effects of the approximations do not generate relevant modifications in the system dynamics, confirming the accuracy of the modeling procedure. These new sources of uncertainties will be taken into account at the control design stage, which is discussed in the next chapter.

2.4.2 Polytope Mapping

The second step of the polytopic model approximation procedure in Figure 2.10 focuses on the identification of the convex polytope, $\hat{\Theta}$, defined by the new set of scheduling functions, $\hat{\boldsymbol{\rho}} = [\hat{\rho}_1(V,h),\, \hat{\rho}_2(\alpha,V,h),\, \hat{\rho}_3(\alpha,V,h)]$. The identification relies on a precise conversion process, where the original flight envelope described by the scheduling variable ranges: $\alpha \in [0,\ 16]$ deg, $V \in [160,\ 280]$ m/s, and $h \in [1,\ 15]$ km, is mapped into the corresponding convex domain defined by the new set of scheduling functions ranges:

$$\hat{\rho}_j \in \left[\overline{\hat{\rho}_j}, \underline{\hat{\rho}_j}\right]; \qquad j = 1, 2, 3.$$

where $\overline{\hat{\rho}_j}$, $\underline{\hat{\rho}_j}$ are the upper and lower bounds of each scheduling function, respectively, defining the vertices of the new polytope. The following procedure allows estimating the range of variation of each new scheduling function, $\hat{\rho}_j$, across the entire set of flight conditions described by α, V, and h. It consists of two sequential phases: **Selection**, and **Map**.

2.4.2.1 Selection

Since the scheduling functions in $\hat{\boldsymbol{\rho}}$ are highly nonlinear w.r.t. the original scheduling variables, $(\alpha,\ V,\ h)$, the flight envelope is sampled into a fine 3D grid of flight points. However, the scheduling functions are evaluated only on a subset of the overall grid. The selection criteria rely on the identification of those flight points that respect the physical constraints affecting the variables across a standard projectile gliding phase trajectory. In particular, Figure 2.15(a) shows the specific relation characterizing the variables h/V during a gliding trajectory scenario. The trajectory has been obtained by performing closed-loop guidance simulations based on a simplified planar point-mass model of the projectile dynamics, and assuming the Lift-to-Drag Ratio optimization guidance law discussed in Section 1.4.2 of Chapter 1.

The figure shows how certain $(h,\ V)$ conditions are inconsistent with the targeted projectile trajectory, thus they must be neglected in the mapping process. As a first polytope identification step, a cluster of n_c flight conditions (red points) is selected only around the reference gliding trajectory. The selection of the n_c points relies on an iterative process where a progressively finer grid of conditions, $(\alpha,\ V,\ h)$, has been employed for a more accurate estimation of the boundaries of each new scheduling function, $(\hat{\rho}_1,\ \hat{\rho}_2,\ \hat{\rho}_3)$, during the following **Map** phase. The final 3D design grid additionally accounts for the variation of the AoA, as shown in Figure 2.15(b).

Remark 2.5

The polytope identification process intrinsically depends on the selection of the investigated flight envelope. Since the later polytopic controller synthesis is generally affected by computation conservatism, the optimization of the polytope's dimension represents a crucial aspect of the design. Depending on the objectives of the control design, different ad-hoc selection criteria can be employed. In the presented scenario, the aim is to enhance the range capability of the projectile, thus a nominal gliding trajectory has been assumed as reference criteria.

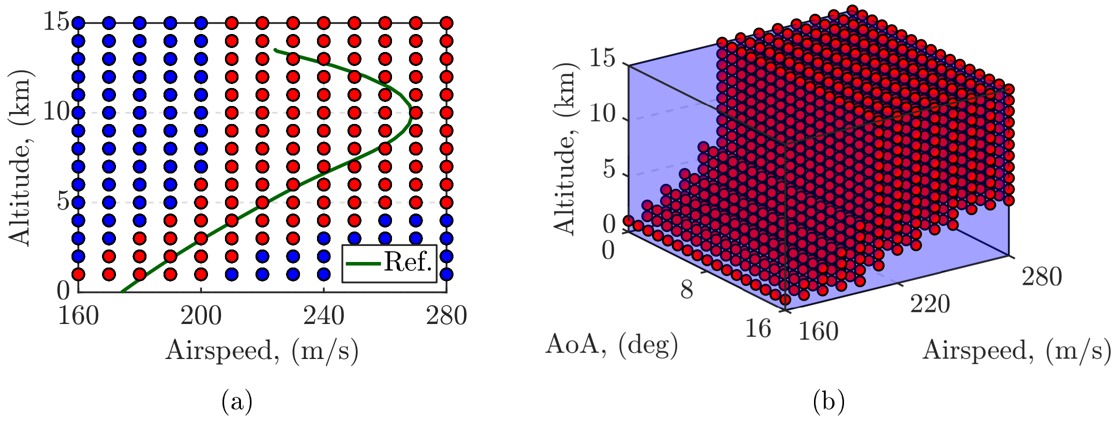

Figure 2.15: Flight points selection: (a) $V-h$ trajectory constraints; (b) $(\alpha,\ V,\ h)$ 3D subspace.

2.4.2.2 Map

The scheduling functions in the new set, $\hat{\boldsymbol{\rho}}$, are evaluated across the selected n_c flight points, generating a new 3D convex subspace, $\hat{\Theta}$, as presented in Figure 2.16(d). The vertices of the new polytope, $\hat{\boldsymbol{\theta}}_i \in \hat{\Theta}$ with $i = 1, \ldots, 8$, are defined by the boundary values of each scheduling function, represented in Figures 2.16(a)-(c) as: $\hat{\rho}_1 \in [0.4,\ 2.9] \times 10^4$, $\hat{\rho}_2 \in [0.05,\ 0.55]$, and $\hat{\rho}_3 \in [-1,\ 4.1]$.

The new polytope is still affected by a certain level of conservatism since the selection of the grid points was based on an approximated reference trajectory. As discussed in Remark 2.5, the minimization of the modeling conservatism is a fundamental requirement at the control design stage. Thus, in Chapter 3, the polytope's dimension will be further investigated and optimized, based on the additional knowledge acquired progressively during the controller synthesis.

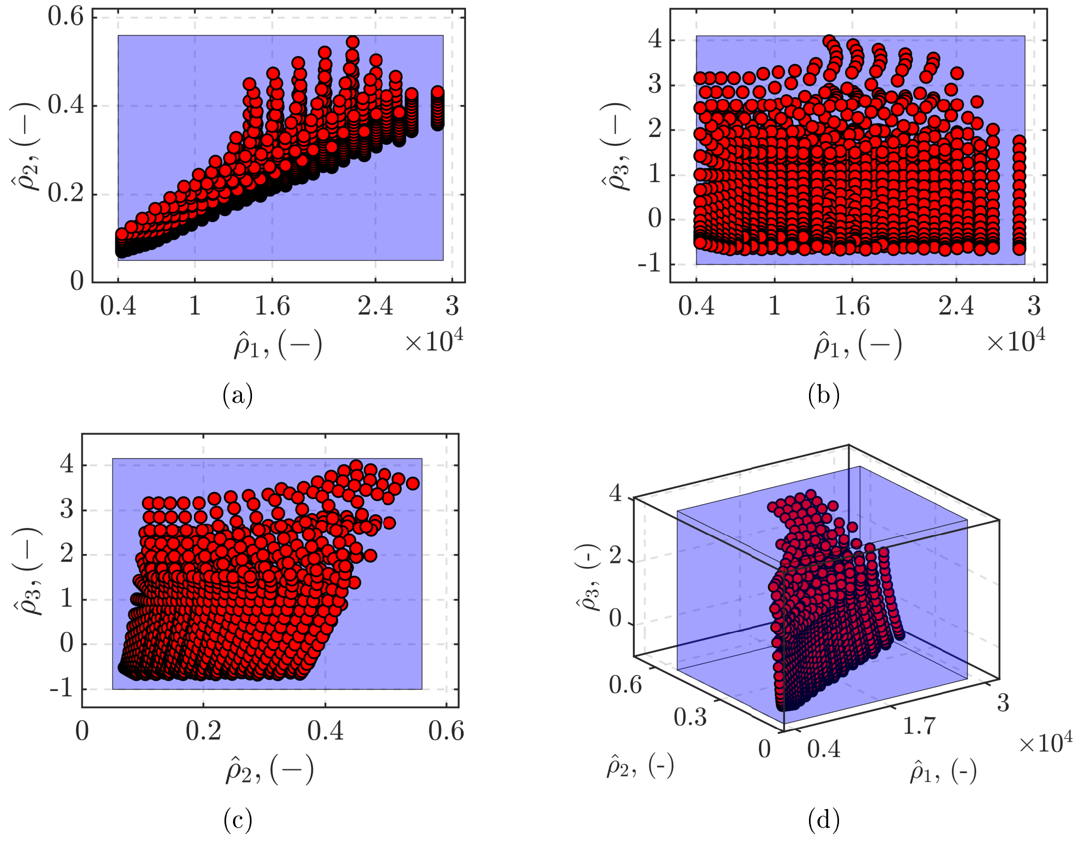

Figure 2.16: Polytope identification: (a) $\hat{\rho}_1$-$\hat{\rho}_2$ subspace; (b) $\hat{\rho}_1$-$\hat{\rho}_3$ subspace; (c) $\hat{\rho}_2$-$\hat{\rho}_3$ subspace; (d) ($\hat{\rho}_1$, $\hat{\rho}_2$, $\hat{\rho}_3$) 3D polytope.

2.5 Concluding Remarks

In this chapter, the projectile nonlinear pitch channel dynamics has been modeled as an accurate quasi-LPV model. The conversion relies on the state transformation approach that allows the formulation of the quasi-LPV model as an exact transformation of the original nonlinear dynamics. The state transformation is restricted to a limited class of output nonlinear systems, characterized by a linear model-input relation. In order to apply the transformation process to the projectile pitch channel dynamics, a dedicated aerodynamic approximation has been developed. The approximation aims at expressing the aerodynamic control coefficients as a linear function of the canards deflection input, thus satisfying the requirements of the state transformation approach. Additionally, integrator dynamics has been augmented at the input of the system, $\delta_q = \int \sigma$, to compensate for the input-parameter dependence configuration.

Projectile Pitch Channel quasi-LPV Model. The resulting integrator-augmented quasi-LPV model of the projectile pitch channel dynamics in Equations (2.29)-(2.30) and Equations (2.33)-(2.34) is expressed w.r.t. the off-equilibrium state vector, (α, q_{dev}, $\delta_{q,\text{dev}}$). Since it will be employed for the LPV grid-based controller design, from now it will be referred to as Σ_{GR}:

$$\Sigma_{\text{GR}}: \begin{bmatrix} \dot{\alpha} \\ \dot{q}_{\text{dev}} \\ \dot{\delta}_{q,\text{dev}} \end{bmatrix} = \begin{bmatrix} 0 & \mathcal{A}_{12}(\boldsymbol{\rho}) & \mathcal{B}_1(\boldsymbol{\rho}) \\ 0 & \tilde{\mathcal{A}}_{22}(\boldsymbol{\rho}) & \tilde{\mathcal{B}}_2(\boldsymbol{\rho}) \\ 0 & \tilde{\mathcal{A}}_{32}(\boldsymbol{\rho}) & \tilde{\mathcal{B}}_3(\boldsymbol{\rho}) \end{bmatrix} \begin{bmatrix} \alpha \\ q_{\text{dev}} \\ \delta_{q,\text{dev}} \end{bmatrix} + \begin{bmatrix} 0 \\ 0 \\ 1 \end{bmatrix} \sigma; \qquad \boldsymbol{\rho}(t) = [\alpha(t), V(t), h(t)]. \tag{2.40}$$

with:

$$\mathcal{A}_{12}(\boldsymbol{\rho}) = 1 + \frac{\bar{q}S\cos\alpha}{mV}\left(\frac{d}{2V}\right)C_{Z_q}; \qquad \mathcal{B}_1(\boldsymbol{\rho}) = \frac{\bar{q}S\cos\alpha}{mV}C_{Z_{\delta_q 1}};$$

$$\mathcal{A}_{22}(\boldsymbol{\rho}) = \frac{\bar{q}Sd}{I_2}\left(\frac{d}{2V}\right)C_{m_q}; \qquad \mathcal{B}_2(\boldsymbol{\rho}) = \frac{\bar{q}Sd}{I_2}C_{m_{\delta_q 1}};$$

$$\tilde{\mathcal{A}}_{22}(\boldsymbol{\rho}) := \mathcal{A}_{22}(\boldsymbol{\rho}) - \frac{\partial q_{\text{eq}}}{\partial \alpha}\mathcal{A}_{12}(\boldsymbol{\rho}); \qquad \tilde{\mathcal{B}}_2(\boldsymbol{\rho}) := \mathcal{B}_2(\boldsymbol{\rho}) - \frac{\partial q_{\text{eq}}}{\partial \alpha}\mathcal{B}_1(\boldsymbol{\rho});$$

$$\tilde{\mathcal{A}}_{32}(\boldsymbol{\rho}) := -\frac{\partial \delta_{q,\text{eq}}}{\partial \alpha}\mathcal{A}_{12}(\boldsymbol{\rho}); \qquad \tilde{\mathcal{B}}_3(\boldsymbol{\rho}) := -\frac{\partial \delta_{q,\text{eq}}}{\partial \alpha}\mathcal{B}_1(\boldsymbol{\rho}).$$

Concerning the output equation, off-equilibrium LF measurements, $\eta_{z,\text{dev}}$, are employed to substitute the canards pitch deflection, assuming the following dynamic output feedback configuration, as:

$$\begin{bmatrix} \alpha \\ q_{\text{dev}} \\ \eta_{z,\text{dev}} \end{bmatrix} = \begin{bmatrix} 1 & 0 & 0 \\ 0 & 1 & 0 \\ 0 & \tilde{\mathcal{C}}_{32}(\boldsymbol{\rho}) & \tilde{\mathcal{C}}_{33}(\boldsymbol{\rho}) \end{bmatrix} \begin{bmatrix} \alpha \\ q_{\text{dev}} \\ \delta_{q,\text{dev}} \end{bmatrix} \tag{2.41}$$

where:

$$\tilde{\mathcal{C}}_{32}(\boldsymbol{\rho}) = \frac{\bar{q}S}{mg}\left(\frac{d}{2V}\right)C_{Z_q}; \qquad \tilde{\mathcal{C}}_{33}(\boldsymbol{\rho}) = \frac{\bar{q}S}{mg}C_{Z_{\delta_q 1}}.$$

The feedforward matrix, $\mathcal{D}$, is assumed zero.

The accuracy of the quasi-LPV model has been validated in simulation across a flight envelope described by the variation ranges: $\alpha \in [0, 16]$ deg, $V \in [160, 280]$ m/s, $h \in [1, 15]$ km.

Aiming to employ the quasi-LPV model for the design of an LPV-based polytopic controller, a further modeling step has been necessary. Indeed, the obtained quasi-LPV model does not respect the affine model-parameter relation imposed by the polytopic formulation. Thus, a model approximation procedure has been developed, with the purpose to reformulate the projectile quasi-LPV model into a polytopic system. The approximation relies on the identification of a new set of scheduling functions, $\hat{\boldsymbol{\rho}}$ in Equation (2.38), affine w.r.t. the system dynamics.

Projectile Pitch Channel quasi-LPV/Polytopic Model. The approximation process results in the polytopic reformulation of the projectile quasi-LPV pitch channel dynamics, Σ_{PY}, defined in Equation (2.39) as follows:

$$\Sigma_{\mathrm{PY}}: \begin{bmatrix} \dot{\alpha} \\ \dot{q}_{\mathrm{dev}} \\ \dot{\delta}_{q,\mathrm{dev}} \end{bmatrix} = \begin{bmatrix} 0 & 1 & \bar{A}_{13}(\hat{\rho}_1) \\ 0 & \bar{A}_{22}(\hat{\rho}_1) - \hat{\rho}_2 & \bar{A}_{23}(\hat{\rho}_1) \\ 0 & -\hat{\rho}_3 & -\hat{\rho}_3 \bar{A}_{13}(\hat{\rho}_1) \end{bmatrix} \begin{bmatrix} \alpha \\ q_{\mathrm{dev}} \\ \delta_{q,\mathrm{dev}} \end{bmatrix} + \begin{bmatrix} 0 \\ 0 \\ 1 \end{bmatrix} \sigma \tag{2.42}$$

where:

$$\hat{\rho}_1 := \bar{q}; \qquad \hat{\rho}_2 := \frac{\partial q_{\mathrm{eq}}}{\partial \alpha}; \qquad \hat{\rho}_3 := \frac{\partial \delta_{q,\mathrm{eq}}}{\partial \alpha}$$

and:

$$\bar{A}_{13}(\hat{\rho}_1) = \frac{\bar{q}S}{m\bar{V}} \bar{C}_{Z_{\delta_q 1}}; \qquad \bar{A}_{22}(\hat{\rho}_1) = \frac{\bar{q}Sd}{I_2}\left(\frac{d}{2\bar{V}}\right) \bar{C}_{m_q}; \qquad \bar{A}_{23}(\hat{\rho}_1) = \frac{\bar{q}Sd}{I_2} \bar{C}_{m_{\delta_q 1}}.$$

Concerning the output equation, the output matrix, $\mathcal{C}$, consists of the identity matrix, $I \in \mathbb{R}^{3\times 3}$, assuming a state feedback architecture. The feedforward matrix, $\mathcal{D}$, is assumed zero.

After assessing the accuracy of the approximation process, the original domain of validity of the quasi-LPV model has been mapped into the new convex polytope, $\hat{\Theta}$, defined by the scheduling functions: $\hat{\rho}_1(V, h) \in [0.4,\ 2.9] \times 10^4$, $\hat{\rho}_2(\alpha, V, h) \in [0.05,\ 0.55]$, and $\hat{\rho}_3(\alpha, V, h) \in [-1,\ 4.1]$. In the next chapter, the projectile quasi-LPV model, and the corresponding polytopic approximation, will be used respectively for the design of grid-based and polytopic LPV autopilot. The performance of the two design approaches will be deeply investigated and compared.

Part II

Projectile Autopilot Design: LPV-based robust controller design approaches for guided munitions

Chapter 3

LPV Controller Design

Contents

3.1 Introduction

The synthesis of LPV controllers relies on the resolution of convex optimization problems, formulated as linear matrix inequalities (LMIs). Different from standard LTI gain-scheduling strategies, the design guarantees relevant stability properties not only in the vicinity of a selected set of operating conditions but also across the transient phase. Indeed, the gain-scheduling design is often based on the online interpolation of a set of independently designed LTI local controllers. As a consequence, no guarantees are provided concerning the performance of the interpolated controller, especially in the case of sharp variations in the operating conditions. By limiting the admissible variation range of each operating parameter ('slow variation' assumption as discussed in [SA92]), stability performance can be recovered in the transition between two steady-state conditions, at the expense of significant restrictions on the range of applications ([RS00]).

In the LPV framework, higher stability guarantees and performance can be obtained depending on the formulation of the LMIs optimization problem. Due to the continuous variation of the parameters, the optimization problem results in an unfeasible infinite number of conditions. Through the imposition of an affine model-parameter relation, the optimization can be solved across a convex (polytope) subspace defined by the ranges of variation of the parameters. By exploiting the linear variation of the parameters, the design ensures stability guarantees across the polytope. Alternatively, the continuous space of variation of the parameters can be discretized into a finite set of design conditions (gridding). By additionally accounting for the rate of variation of each parameter, the optimization problem can be further constrained, improving the performance of the resulting controller.

In this chapter, the aforementioned approaches are employed for the synthesis of a robust LPV autopilot for the projectile pitch channel dynamics, based on the $\mathcal{H}_\infty$ criterion. The former polytopic approach ensures broader stability guarantees at the expense of a more conservative optimization performance ([AGB95]; [SGC97]). The conservatism of the approach is targeted through the optimization of the polytope's dimensions and the consistency of the operating conditions belonging to the convex subset ([Jin+18]; [Kap+22]; [ZZW14]; [Cor+20]; [PDP05]; [Pan+21]; [HW15]; [KW08]). Conversely, the grid-based formulation, improves the optimization performance of the controller synthesis, even though the stability guarantees in the transient between different design points are weaker than the polytopic case ([WPB95]; [Wu+96]). However, by simultaneously satisfying the LMIs at all the grid conditions through a parameter-dependent solution, the likelihood of reliable performance related to the controller interpolation is much higher than in the standard LTI gain-scheduling approach.

The chapter is structured in the following sections:

S3.2: recalls the fundamental concepts related to the stability properties of different classes of LPV systems. The LPV-based controller synthesis is formulated as an LMIs optimization problem that aims at minimizing the induced L_2-norm of the system. The conditions related to the resolution of the LMIs optimization through the polytopic and grid-based approaches are finally detailed.

S3.3: focuses on the design of an LPV autopilot for the projectile pitch channel dynamics, based on the polytopic approach. The control scheme is first introduced by addressing the core objectives of the design. The conservatism affecting the controller synthesis is addressed by analyzing the variation of the scheduling functions across the selected convex space. The results of the design are finally investigated in the frequency domain. The results presented in this section have been published in [Vin+23a]; [Vin+23b].

S3.4: discusses the resolution of the LPV controller synthesis, by gridding the scheduling variables space. An output feedback configuration is employed for the design of the grid-based autopilot for the projectile pitch channel dynamics. The gridding process is extensively investigated in order to optimize the performance of the controller synthesis. As for the polytopic case, the results of the design are analyzed in the frequency domain. The results presented in this section have been published in [Vin+23c].

3.2 Fundamentals on LPV Control Design

This section provides a brief and non-exhaustive overview concerning the different notions of stability properties for LPV systems and the conditions that have been developed to assess the degree of stability of a generic LPV system. Finally, the synthesis of LPV-based controllers is formulated in terms of feasible optimization problems. Further information can be found in [Boy+94]; [Bri14]; [MS12]; [SGB13].

3.2.1 Linear Matrix Inequalities

The resolution of linear matrix inequalities (LMIs) systems represents a fundamental tool in the formulation of convex optimization problems, such as the synthesis of LPV controllers.

Definition 3.1 (Linear Matrix Inequalities (LMIs))
A linear matrix inequality consists of a compact formulation to express an algebraic convex constraint on a generic vector $\boldsymbol{x} \in \mathbb{R}^N$*, as:*

$$\mathcal{L}(\boldsymbol{x}) \coloneqq \mathcal{L}_0 + \sum_{i=1}^{N} \mathcal{L}_i x_i \succeq 0 \tag{3.1}$$

where $\mathcal{L}_0 = \mathcal{L}_0^{\mathrm{T}}$*, and* $\mathcal{L}_i = \mathcal{L}_i^{\mathrm{T}} \in \mathbb{R}^{N \times N}$ *are known matrices. The constraint can impose a symmetric and positive semi-definite matrix condition,* $\mathcal{L} \succeq 0$*, or a positive definite matrix condition,* $\mathcal{L} \succ 0$*. In the latter case, it is referred to as 'strict' LMI.*
The solution of an LMIs problem consists of finding a convex set, $\mathbb{L}$*, defined by all the possible vectors,* $\boldsymbol{x}$*, that satisfy the constraint in Equation* (3.1)*:*

$$\mathbb{L} = \{\boldsymbol{x} \in \mathbb{R}^N | \mathcal{L}(\boldsymbol{x}) \succeq 0 \text{ (or } \succ 0)\}.$$

In control applications, LMIs as in Definition 3.1 are employed to target the location of the eigenvalues of $\mathcal{L}$, imposing either positive $\mathcal{L} \succ 0$, or negative values, $\mathcal{L} \prec 0$. In particular, multiple LMIs constraints can be formulated as a single condition, as follows:

$$\mathcal{L}(\boldsymbol{x}) = \begin{pmatrix} \mathcal{L}^1(\boldsymbol{x}) & 0 & \cdots & 0 \\ 0 & \mathcal{L}^2(\boldsymbol{x}) & \cdots & 0 \\ \vdots & \vdots & \ddots & \vdots \\ 0 & 0 & \dots & \mathcal{L}^k(\boldsymbol{x}) \end{pmatrix} \tag{3.2}$$

The solution of the system in Equation (3.2) is given by the union of the eigenvalues of the individual matrices, $\mathcal{L}^j(\boldsymbol{x})$ with $j = 1, \dots, k$. Since it consists of the intersection of multiple convex sets, the solution of the system in Equation (3.2) defines also a convex set.

Systems of inequalities defined as in Equation (3.2) represent a standard formulation for convex control design optimization problems. Depending on the constraints imposed through the definition of the LMIs, optimization problems can be classified as in the following.

Definition 3.2 (Semi-Definite Programming LMIs Problem (SDP))
A semi-definite LMIs optimization programming problem is formally defined as:

$$\begin{aligned} &\min \boldsymbol{c}^{\mathrm{T}}\boldsymbol{x} \\ &\quad \text{s.t. } \boldsymbol{x} \in \mathbb{R}^N \\ &\qquad \mathcal{L}(\boldsymbol{x}) \succ 0 \end{aligned}$$

where $\boldsymbol{c} \in \mathbb{R}^N$.

Definition 3.3 (Semi-Infinite LMIs Problem)
A semi-infinite LMIs optimization problem is formally defined as:

$$\begin{aligned} &\min \boldsymbol{c}^{\mathrm{T}}\boldsymbol{x} \\ &\quad \text{s.t. } \boldsymbol{x} \in \mathbb{R}^N \\ &\mathcal{L}(\boldsymbol{x}, \boldsymbol{\rho}) \coloneqq \mathcal{L}_0(\boldsymbol{\rho}) + \sum_{i=1}^{N} \mathcal{L}_i(\boldsymbol{\rho}) x_i \succeq 0; \qquad \textit{with} \quad \boldsymbol{\rho} \in \mathbb{U}_\rho \end{aligned}$$

where $\boldsymbol{c} \in \mathbb{R}^N$*, and* $\mathbb{U}_\rho \in \mathbb{R}^{n_\rho}$ *is a compact set.*

Definition 3.4 (Infinite-Dimensional LMIs Problem)
An infinite-dimensional LMIs optimization problem is formally defined as:

$$\begin{aligned} &\min \boldsymbol{c}^{\mathrm{T}}\boldsymbol{x}(\boldsymbol{\rho}) \\ &\quad \text{s.t. } \boldsymbol{x} : \mathbb{U}_\rho \to \mathbb{R}^N \\ &\mathcal{L}(\boldsymbol{x}(\boldsymbol{\rho}), \boldsymbol{\rho}) \coloneqq \mathcal{L}_0(\boldsymbol{\rho}) + \sum_{i=1}^{N} \mathcal{L}_i(\boldsymbol{\rho}) x_i(\boldsymbol{\rho}) \succeq 0; \qquad \textit{with} \quad \boldsymbol{\rho} \in \mathbb{U}_\rho \end{aligned}$$

where $\boldsymbol{c} \in \mathbb{R}^N$*,* $\mathbb{U}_\rho \in \mathbb{R}^{n_\rho}$ *is a compact set, and* $\boldsymbol{x} : \mathbb{U}_\rho \to \mathbb{R}^N$ *is a parameter-dependent function.*

Several optimization tools have been developed in the past years to solve SDP LMIs problems in Definition 3.2, such as Yalmip ([Lof04]) and CVX ([GB08]), equipped with sophisticated solver algorithms (e.g. SDPT3, Mosek, and SeDuMi). Differently, in semi-infinite and infinite-dimensional LMIs problems, the constraints are parameter-dependent, meaning that the corresponding LMIs have to be satisfied for an infinite number of conditions, defined by the continuous variation of the parameters, $\boldsymbol{\rho} \in \mathbb{U}_\rho$. As detailed in the next section, semi-infinite LMIs optimization problems can be converted into solvable SDP problems by means of standard matrix relaxation techniques. Instead, the solution of an infinite-dimensional LMIs problem requires a first reformulation as a semi-infinite problem by converting the infinite parameter-dependent decision variables, $\boldsymbol{x}(\boldsymbol{\rho})$, into a finite set. Then, the resulting semi-infinite problem is addressed through relaxation techniques, as previously mentioned.

3.2.2 Stability of LPV Systems

This section recalls the basic concepts concerning the stability conditions of different classes of LPV systems. The stability of LPV systems is achieved through the imposition of a set of constraints on the eigenvalues of the system state matrix, in the form of LMIs conditions. In particular, it relies on the extension to the LPV framework of the well-established Lyapunov definition of system equilibrium properties, and the corresponding Lyapunov's Stability Theorem of dynamical systems, discussed in [Lya92]; [Kha02].

Lyapunov Stability. Without loss of generality, from the general formulation in Equation (2.2) assume the autonomous LPV continuous dynamics, given by:

$$\begin{aligned} \dot{\boldsymbol{x}}(t) &= \mathcal{A}(\boldsymbol{\rho}(t))\boldsymbol{x}(t); \qquad \text{with: } \boldsymbol{x}(t) \in \mathbb{R}^{n_x};\ \boldsymbol{\rho}(t) \in \mathbb{R}^{n_\rho};\ t \geq 0 \\ \boldsymbol{x}(0) &= \boldsymbol{x}_0. \end{aligned} \tag{3.3}$$

From Lyapunov theory, the stability of the parameter-varying system in Equation (3.3) relies on the identification of a Lyapunov function:

$$V(\boldsymbol{x}) := \boldsymbol{x}^{\mathrm{T}} P \boldsymbol{x}; \qquad \text{with: } P \in \mathbb{R}^{n_x \times n_x} \succ 0$$

such that the derivative, $\dot{V}(\boldsymbol{x}, \boldsymbol{\rho})$, satisfies the following Lyapunov condition:

$$\dot{V}(\boldsymbol{x}, \boldsymbol{\rho}) := \boldsymbol{x}(t)^{\mathrm{T}} \left(\mathcal{A}(\boldsymbol{\rho})^{\mathrm{T}} P + P\mathcal{A}(\boldsymbol{\rho})\right) \boldsymbol{x}(t) \prec 0 \tag{3.4}$$

for all the parameters' trajectories, $\boldsymbol{\rho} \in \mathbb{R}^{n_\rho}$.

In particular, depending on the parameterization of the selected Lyapunov function, the conditions expressed in Equation (3.4) can be reformulated providing different guarantees of stability ([Bri14]).

Definition 3.5 (Quadratic Stability)
The system in Equation (3.3) *is said to be quadratically stable if there exists a parameter-independent Lyapunov function,* $V(\boldsymbol{x}) = \boldsymbol{x}^{\mathrm{T}} P \boldsymbol{x} \succ 0$ *for every* $\boldsymbol{x} \neq 0$*, and* $V(0) = 0$*, that satisfies the Lyapunov condition in Equation* (3.4)*, reformulated as:*

$$\mathcal{A}(\boldsymbol{\rho})^{\mathrm{T}} P + P\mathcal{A}(\boldsymbol{\rho}) \prec 0$$

for every $\boldsymbol{x} \neq 0$*, and such that* $\dot{V}(0, \boldsymbol{\rho}) = 0$ *for every* $\boldsymbol{\rho} \in \mathbb{R}^{n_\rho}$*.*

Definition 3.6 (Robust Stability)
The system in Equation (3.3) *is said to be robustly stable if there exists a parameter-dependent Lyapunov function,* $V(\boldsymbol{x}, \boldsymbol{\rho}) = \boldsymbol{x}^{\mathrm{T}} P(\boldsymbol{\rho}) \boldsymbol{x} \succ 0$ *for every* $\boldsymbol{x} \neq 0$*, and* $V(0) = 0$*, that satisfies the Lyapunov condition in Equation* (3.4)*, reformulated as:*

$$\mathcal{A}(\boldsymbol{\rho})^{\mathrm{T}} P(\boldsymbol{\rho}) + P(\boldsymbol{\rho})\mathcal{A}(\boldsymbol{\rho}) + \sum_{i=1}^{n_\rho} \dot{\rho}_i \frac{\partial P(\boldsymbol{\rho})}{\partial \rho_i} \prec 0$$

for every $\boldsymbol{x} \neq 0$*, and such that* $\dot{V}(0, \boldsymbol{\rho}) = 0$ *for every* $\boldsymbol{\rho} \in \mathbb{R}^{n_\rho}$*.*

Remark 3.1

The definition of quadratic stability does not account for bounded rates of variation of the parameters, $\dot{\boldsymbol{\rho}}$*, possibly resulting in a very conservative condition to be satisfied. Indeed, it represents a sufficient but not necessary condition for asymptotic stability ([Bri14]). Differently, robust stability distinguishes between slow and fast-varying parameters, providing less conservatism in the formulation of the constraints, but also lower global guarantees of stability. In reason of these definitions, quadratic stability implies robust stability, but not vice versa. Indeed, the derivative of the Lyapunov function is not guaranteed to be negative definite for all* $(\boldsymbol{\rho}, \dot{\boldsymbol{\rho}})$ *conditions because of the additional terms:*

$$\sum_{i=1}^{n_\rho} \dot{\rho}_i \frac{\partial P(\boldsymbol{\rho})}{\partial \rho_i}.$$

The assessment of quadratic and robust stability of LPV systems relies on the formulation of the semi-infinite and infinite-dimensional LMIs problems, introduced in Definition 3.3 and Definition 3.4, respectively. In the following, the robust stability of a generic LPV system is addressed through the projection of the infinite-dimensional LMIs decision variables into a set of finite-dimensional basis functions. The resulting semi-infinite problem is solved through the relaxation of the LMIs conditions by gridding the parameters' space. Concerning the feasibility of the quadratic stability conditions, the reformulation of the LPV system in Equation (3.3) as a polytopic model allows exploiting the advantages of the affine-parameter dependence in the resolution of convex optimization problems. The alternative gridding approach is not detailed in the presence work for brevity.

3.2.2.1 Robust Stability via Gridding Approach

The resolution of the infinite-dimensional LMIs problem that guarantees robust stability in the sense of Definition 3.6 can be achieved through the projection of the parameter-dependent matrix, $P(\boldsymbol{\rho}) = P(\boldsymbol{\rho})^{\mathrm{T}} \succ 0$, on a set of scalar basis functions, $f_i(\boldsymbol{\rho})$ with $i = 1, \ldots, n_{\mathrm{B}}$. Based on the selection of $f_i(\boldsymbol{\rho})$, the parameter-dependent matrix can be parameterized as:

$$P(\boldsymbol{\rho}) = \sum_{i=1}^{n_{\mathrm{B}}} P_i f_i(\boldsymbol{\rho})$$

where the new set of decision variables, corresponding to the matrices $P_i = P_i^{\mathrm{T}}$, has a finite dimension. As a consequence, the robust stability condition in Definition 3.6 can be expressed as in the following theorem.

Theorem 3.1

The LPV system formulated in Equation (3.3) *is robustly stable if there exist matrices* $P_i = P_i^{\mathrm{T}}$

such that the following LMIs:

$$\mathcal{A}(\boldsymbol{\rho})^{\mathrm{T}}\left(\sum_{i=1}^{n_{\mathrm{B}}} P_i f_i(\boldsymbol{\rho})\right)+\left(\sum_{i=1}^{n_{\mathrm{B}}} P_i f_i(\boldsymbol{\rho})\right)\mathcal{A}(\boldsymbol{\rho})+\sum_{i=1}^{n_\rho}\nu_i\left(\sum_{i=1}^{n_{\mathrm{B}}} P_i\frac{\partial f_i(\boldsymbol{\rho})}{\partial \rho_i}\right)\prec 0$$
$$\sum_{i=1}^{n_{\mathrm{B}}} P_i f_i(\boldsymbol{\rho})\succ 0$$

hold for all $\boldsymbol{\rho}\in\mathbb{U}_\rho$, where $\mathbb{U}_\rho\in\mathbb{R}^{n_\rho}$ is a compact set, and all the vertices of the polytope, $\nu=\operatorname*{col}_{i=1}^{n_\rho}(\nu_i)$, where the parameters' derivative, $\dot{\boldsymbol{\rho}}$, evolves.

Remark 3.2
The selection of the set of basis functions, $f_i(\boldsymbol{\rho})$, is not restricted to any specific parameter dependence. Thus, the projection approach can be applied to all classes of LPV systems. However, the higher the number of selected functions, n_{B}, the higher the computational complexity affecting the resolution of the LMIs problem. Additionally, no standard criteria are provided for the selection of the basis functions. Generally, it relies on the mimic principle, where the functions are chosen in a way to replicate the same model-parameter dependence presented by the LPV system ([AA98]).

Through the reformulation discussed in Theorem 3.1, the infinite-dimensional robust stability LMIs problem has been converted into a semi-infinite problem. The last conversion step consists of the relaxation of the infinite number of parameter-varying LMIs to be solved. A standard solution relies on the discretization of the continuous space of variation of the parameters into a finite grid of n_{g} selected values, $\boldsymbol{\rho}\in\bar{\mathbb{U}}_\rho:=\{\boldsymbol{\rho}^1,\ldots,\boldsymbol{\rho}^{n_{\mathrm{g}}}\}$. Thus, the semi-infinite LMIs condition in Theorem 3.1 can be reformulated as:

Proposition 3.1
The LPV system in Equation (3.3) *is robustly stable if there exists matrices $P_i=P_i^{\mathrm{T}}$ such that the LMIs:*

$$\mathcal{A}(\boldsymbol{\rho})^{\mathrm{T}}\left(\sum_{i=1}^{n_{\mathrm{B}}} P_i f_i(\boldsymbol{\rho})\right)+\left(\sum_{i=1}^{n_{\mathrm{B}}} P_i f_i(\boldsymbol{\rho})\right)\mathcal{A}(\boldsymbol{\rho})+\sum_{i=1}^{n_\rho}\nu_i\left(\sum_{i=1}^{n_{\mathrm{B}}} P_i\frac{\partial f_i(\boldsymbol{\rho})}{\partial \rho_i}\right)\prec 0$$
$$\sum_{i=1}^{n_{\mathrm{B}}} P_i f_i(\boldsymbol{\rho})\succ 0$$

hold for all the n_{g} values of $\boldsymbol{\rho}\in\bar{\mathbb{U}}_\rho$, where $\bar{\mathbb{U}}_\rho:=\{\boldsymbol{\rho}^1,\ldots,\boldsymbol{\rho}^{n_{\mathrm{g}}}\}$, and all the vertices of the polytope, $\nu=\operatorname*{col}_{i=1}^{n_\rho}(\nu_i)$, where the parameters' derivative, $\dot{\boldsymbol{\rho}}$, evolves.

Remark 3.3
The resolution of the LMIs optimization through grid-based relaxation consists of an approximation of the LMIs problem in Theorem 3.1. A major drawback related to this technique relies on the lack of guidelines for the optimal selection of the grid points during the discretization. Indeed, the selection of an optimal grid that ensures capturing the most significant and criti-

cal parameters' values, implies the prior knowledge of the feasible/unfeasible conditions of the optimization problem itself, generating a paradox.

A relevant consequence inferred from Remark 3.3 concerns the lack of guarantees about the system dynamics variation between the grid points. The selection of a denser and unevenly discretized grid can increase the likelihood of imposing stable conditions in the transient dynamics between known points. However, the computational complexity related to the resolution of the LMIs problem tends to increase with the number of grid points as $\mathcal{O}({n_\mathrm{g}}^{n_\rho})$. Thus, depending on the application, ad-hoc solutions might be necessary for an accurate identification of the critical areas of the parameters' space.

3.2.2.2 Quadratic Stability via Polytopic Formulation

An alternative solution for the conversion of a semi-infinite LMIs problem into a solvable SDP one consists of the reformulation of the LPV system as a polytopic model.

The polytopic formulation presented in Section 2.2.1.1 relies on the affine model-parameter dependence assumption expressed in Definition 2.4. Without loss of generality, assume the LPV autonomous system in Equation (3.3), expressed in the polytopic formulation presented in Equation (2.4), and accounting for $n_\Theta = 2^{n_\rho}$, as:

$$\begin{aligned} \dot{\boldsymbol{x}}(t) &= \sum_{i=1}^{2^{n_\rho}} \mu_{\theta_i}(t)\mathcal{A}_i\boldsymbol{x}(t); \qquad \text{with:} \quad \boldsymbol{\rho} = \sum_{i=1}^{2^{n_\rho}} \mu_{\theta_i}\boldsymbol{\theta}_i \\ \boldsymbol{x}(0) &= \boldsymbol{x}_0 \end{aligned} \tag{3.5}$$

where the scheduling parameters, $\boldsymbol{\rho}(t) \in \mathbb{R}^{n_\rho}$, belong to the polytope, Θ, defined by the convex hull of the finite set of vertices, $\mathcal{V} = [\boldsymbol{\theta}_i, \dots, \boldsymbol{\theta}_{2^{n_\rho}}]$. The interpolation variables, μ_{θ_i}, define the corresponding unitary polytope:

$$\Gamma := \left\{ \operatorname*{col}_i(\mu_{\theta_i}(t)) : \sum_{i=1}^{2^{n_\rho}} \mu_{\theta_i}(t) = 1, \ \mu_{\theta_i}(t) \geq 0 \right\}$$

Based on this assumption, the convexity of the polytope can be exploited by observing that, if the LMIs condition in Equation (3.4) holds for all of the vertices, $\boldsymbol{\theta}_i \in \mathcal{V}$, such that:

$$\mathcal{A}_i^\mathrm{T} P + P\mathcal{A}_i \prec 0$$

the corresponding sum of negative-definite matrices:

$$\sum_{i=1}^{2^{n_\rho}} \mu_{\theta_i} \left[\mathcal{A}_i^\mathrm{T} P + P\mathcal{A}_i\right]$$

is also negative-definite for all $\mu_{\theta_i} \in \Gamma$. Then, the quadratic stability condition presented in Definition 3.5 can be equivalently formulated as in the following.

Theorem 3.2
The LPV polytopic system in Equation (3.5) *is quadratically stable in the sense of Definition 3.5, if and only if there exists a matrix* $P = P^{\mathrm{T}} \succ 0$ *such that the LMI:*

$$\mathcal{A}_i^{\mathrm{T}} P + P\mathcal{A}_i \prec 0$$

holds for all $i = 1, \dots, 2^{n_\rho}$.

The polytopic formulation allows converting the semi-infinite LMIs problem in Definition 3.5 into the equivalent finite number of 2^{n_ρ} conditions in Theorem 3.2, feasible for semi-definite programming computation.

Remark 3.4
Despite the feasibility of Theorem 3.2, the number of LMI conditions to be satisfied grows exponentially w.r.t. the number of scheduling variables, as $\mathcal{O}(2^{n_\rho})$. *Thus, the higher the dimension of* $\boldsymbol{\rho}(t)$, *the higher the computational complexity related to the stability assessment.*

As mentioned in Remark 3.4, quadratic stability tends to result in a generally conservative condition. Indeed, a common constant Lyapunov matrix, P, has to satisfy contemporary the LMIs at each vertex of the convex space of the parameters' variations. Additionally, the rates of variation of the scheduling parameters are not accounted for in the formulation. The robust stability condition introduced in Theorem 3.1 relies on parameter-varying Lyapunov matrices that can more optimally target the stability of the system at each parameter condition. The definition of robust stability for polytopic systems is not immediate since it requires the additional definition of the convex set of variation of the parameters' derivative, $\dot{\boldsymbol{\rho}}$. A standard solution, which is not detailed here, is based on the employment of slack-variables, introduced in [DOBG99]; [DOGH99] for discrete-time systems and then extended to the continuous case, as in [ATB01].

3.2.3 LPV Control Synthesis Problem

The criteria defined in the previous section, in the form of LMIs optimization problems, can be used to formulate the synthesis of a controller that guarantees certain stability and performance properties of the resulting closed-loop system. In particular, control systems can be classified based on the purpose they are designed to achieve, as:

- **Regulator:** targets the attenuation of external and internal disturbance signals that may affect the input or the output of the system.
- **Servo:** aims to follow a selected external reference signal, which guarantees the accomplishments of specific objectives.

For control-oriented purposes, the LPV state space representation introduced in Definition 2.2 of the previous chapter can be generalized, thus emphasizing the objectives targeted through the control design, and distinguishing between the different inputs the model is subjected to. Indeed, the dynamics of any closed-loop system is generally affected by additional sources of internal and external disturbances, that can significantly deteriorate the performance of the controller, if not properly compensated. Model uncertainties, deriving from approximation processes or an inaccurate estimation of specific parameters, are typical examples of internal sources of disturbance. Instead, external disturbances are generally associated with the operating conditions of the system. In terms of aerospace applications, launch conditions and undesired wind contributions are generally accounted for as major sources of external disturbances. As a consequence, a more detailed state space representation of a general LPV model is employed for the formulation of the control synthesis problem.

Definition 3.7 (Generalized LPV System)
Given the vector of time-varying parameters, $\boldsymbol{\rho}(t) \in \mathbb{U}_\rho$*, where* $\mathbb{U}_\rho \in \mathbb{R}^{n_\rho}$ *is a compact set, and* $|\dot{\boldsymbol{\rho}}(t)| < \{\nu_i\}_{i=1}^{n_\rho}$ *evolves in a convex polytope of bounded ranges, and given the set of parameter-varying matrices* $\mathcal{A}(\boldsymbol{\rho}) \in \mathbb{R}^{n_{x\mathrm{P}} \times n_{x\mathrm{P}}}$, $\mathcal{B}_1(\boldsymbol{\rho}) \in \mathbb{R}^{n_{x\mathrm{P}} \times n_w}$, $\mathcal{B}_2(\boldsymbol{\rho}) \in \mathbb{R}^{n_{x\mathrm{P}} \times n_u}$, $\mathcal{C}_1(\boldsymbol{\rho}) \in \mathbb{R}^{n_z \times n_{x\mathrm{P}}}$, $\mathcal{C}_2(\boldsymbol{\rho}) \in \mathbb{R}^{n_y \times n_{x\mathrm{P}}}$, $\mathcal{D}_{11}(\boldsymbol{\rho}) \in \mathbb{R}^{n_z \times n_w}$, $\mathcal{D}_{12}(\boldsymbol{\rho}) \in \mathbb{R}^{n_z \times n_u}$, $\mathcal{D}_{21}(\boldsymbol{\rho}) \in \mathbb{R}^{n_y \times n_w}$, *and* $\mathcal{D}_{22}(\boldsymbol{\rho}) \in \mathbb{R}^{n_y \times n_u}$*, the generalized LPV system,* Σ_P*, is formulated as:*

$$\Sigma_\mathrm{P} : \begin{bmatrix} \dot{\boldsymbol{x}}_\mathrm{P}(t) \\ \hline \boldsymbol{z}(t) \\ \boldsymbol{y}(t) \end{bmatrix} = \left[\begin{array}{c|cc} \mathcal{A}(\boldsymbol{\rho}) & \mathcal{B}_1(\boldsymbol{\rho}) & \mathcal{B}_2(\boldsymbol{\rho}) \\ \hline \mathcal{C}_1(\boldsymbol{\rho}) & \mathcal{D}_{11}(\boldsymbol{\rho}) & \mathcal{D}_{12}(\boldsymbol{\rho}) \\ \mathcal{C}_2(\boldsymbol{\rho}) & \mathcal{D}_{21}(\boldsymbol{\rho}) & \mathcal{D}_{22}(\boldsymbol{\rho}) \end{array}\right] \begin{bmatrix} \boldsymbol{x}_\mathrm{P}(t) \\ \hline \boldsymbol{w}(t) \\ \boldsymbol{u}(t) \end{bmatrix}$$

where $\boldsymbol{x}_\mathrm{P}(t) \in \mathbb{R}^{n_{x\mathrm{P}}}$ *represents the state vector of the system,* $\boldsymbol{w}(t) \in \mathbb{R}^{n_w}$ *corresponds to the vector of exogenous inputs,* $\boldsymbol{u}(t) \in \mathbb{R}^{n_u}$ *stands for the vector of control inputs,* $\boldsymbol{z}(t) \in \mathbb{R}^{n_z}$ *includes the controlled outputs signals, targeting the design objectives, and* $\boldsymbol{y}(t) \in \mathbb{R}^{n_y}$ *is the vector of measured outputs.*

Remark 3.5
The definition of the exogenous input vector, $\boldsymbol{w}(t)$*, and of the controlled output vector,* $\boldsymbol{z}(t)$*, is not related to the state vector partition in the scheduling and non-scheduling subsets introduced in the quasi-LPV system Definition 2.2 of Chapter 2. Coherently, the partitions of the matrices* $\mathcal{A}$, $\mathcal{B}$, $\mathcal{C}$, *and* $\mathcal{D}$ *are not the same as the ones in Definition 2.2.*

The employment of design methods in the robust control framework guarantees the capability ('robustness') of the resulting closed-loop system to handle any deviations from its ideal nominal operating conditions. The stability and performance objectives of the control design are distinguished into nominal, NS/NP (not accounting for disturbances), and robust, RS/RP (accounting for a certain level of disturbances). In this framework, a standard design approach consists of the $\mathcal{H}_\infty$ synthesis.

3.2.3.1 $\mathcal{H}_\infty$ Design Criterion

The effect of the input disturbances on the system dynamics can be quantified in terms of the amplification observed in the output signal energy, induced by the energy associated with the disturbance signal. This amplification is defined through the evaluation of the system induced L_2-norm ([BP94]).

Definition 3.8 (Induced L_2-norm ([Boy+94]))
Given the generalized system, Σ_{P}, in Definition 3.7, the corresponding induced L_2-norm is evaluated as:

$$\sup_{\|\boldsymbol{w}\|_2 \neq 0} \frac{\|\boldsymbol{z}\|_2}{\|\boldsymbol{w}\|_2}$$

where the L_2-norm, $\|\boldsymbol{z}\|_2^2 = \int_0^\infty (\boldsymbol{z}^{\mathrm{T}}\boldsymbol{z})\mathrm{d}t$ and $\|\boldsymbol{w}\|_2^2 = \int_0^\infty (\boldsymbol{w}^{\mathrm{T}}\boldsymbol{w})\mathrm{d}t$ represents the energy associated with the controlled output and exogenous input signals, respectively.

Remark 3.6
The concept of $\mathcal{H}_\infty$-norm is defined only when dealing with LTI systems, while the L_2-norm is generally employed in the case of LPV systems. However, for LTI systems, the L_2 gain equals the $\mathcal{H}_\infty$-norm. Since LTI systems can be interpreted as 'frozen' realizations of a generic LPV system, the $\mathcal{H}_\infty$ criterion can be imposed through the minimization of the L_2-norm of the closed-loop system.

The control design based on the $\mathcal{H}_\infty$ criterion in Definition 3.8 aims at finding a controller that stabilizes the system by minimizing the sensitivity to any source of input disturbances, $\boldsymbol{w}$. In particular, the design targets the nominal stability and the nominal performance of the closed-loop system, Σ_{CL}, consisting of the interconnection between the generalized plant, Σ_{P}, and the LPV controller, $K(\boldsymbol{\rho})$. The properties of Σ_{CL} are shaped in the frequency domain through a set of weighting filters. By imposing conditions on the operating bandwidth and responsiveness of the system, it is possible to enhance the robustness of Σ_{CL} w.r.t. certain types of disturbances.

Definition 3.9 (Induced L_2-norm ($\mathcal{H}_\infty$) Control Problem)
Given an LPV closed-loop system, Σ_{CL}, resulting from the interconnection between a generalized LPV system, Σ_{P}, as in Definition 3.7, and an LPV controller, $K(\boldsymbol{\rho})$, as:

$$\Sigma_{\mathrm{CL}} : \begin{cases} \dot{\boldsymbol{x}}_{\mathrm{CL}}(t) = \mathcal{A}_{\mathrm{CL}}(\boldsymbol{\rho}(t))\boldsymbol{x}_{\mathrm{CL}}(t) + \mathcal{B}_{\mathrm{CL}}(\boldsymbol{\rho}(t))\boldsymbol{w}(t) \\ \boldsymbol{z}(t) \quad = \mathcal{C}_{\mathrm{CL}}(\boldsymbol{\rho}(t))\boldsymbol{x}_{\mathrm{CL}}(t) + \mathcal{D}_{\mathrm{CL}}(\boldsymbol{\rho}(t))\boldsymbol{w}(t) \end{cases} \tag{3.6}$$

where $\boldsymbol{x}_{\mathrm{CL}} = \left[\boldsymbol{x}_{\mathrm{P}}^{\mathrm{T}}, \boldsymbol{x}_{K}^{\mathrm{T}}\right]^{\mathrm{T}}$ is the state vector of the closed-loop system, which includes both the generalized LPV system and the controller state variables, $\boldsymbol{x}_{\mathrm{P}}$ and $\boldsymbol{x}_K$, respectively.

An $\mathcal{H}_\infty$ control problem consists of finding a controller, $K(\boldsymbol{\rho})$, that guarantees the LPV closed-loop system in Equation (3.6) to be robustly (or quadratically) stable, by minimizing the closed-loop system induced L_2-norm, computed as is Definition 3.8, as:

$$\min_{k(\boldsymbol{\rho}),\gamma_\infty} \text{ s.t. } \frac{\|\boldsymbol{z}\|_2}{\|\boldsymbol{w}\|_2} \leq \gamma_\infty$$

3.2.3.2 Grid-based Control Problem Formulation

Without loss of generality, consider a simplified parameterization of the generalized LPV plant described in Definition 3.7:

$$\Sigma_{\mathrm{P}}:\left[\begin{array}{c}\dot{\boldsymbol{x}}_{\mathrm{P}}(t)\\ \hline \begin{bmatrix}\boldsymbol{z}_1(t)\\ \boldsymbol{z}_2(t)\end{bmatrix}\\ \boldsymbol{y}(t)\end{array}\right]=\left[\begin{array}{c|cc}A(\boldsymbol{\rho}) & [B_{11}(\boldsymbol{\rho}) \;\; B_{12}(\boldsymbol{\rho})] & B_2(\boldsymbol{\rho})\\ \hline \begin{bmatrix}\mathcal{C}_{11}(\boldsymbol{\rho})\\ \mathcal{C}_{12}(\boldsymbol{\rho})\end{bmatrix} & \begin{bmatrix}0 & 0\\ 0 & 0\end{bmatrix} & \begin{bmatrix}0\\ I_{n_{w_2}}\end{bmatrix}\\ C_2(\boldsymbol{\rho}) & \begin{bmatrix}0 & I_{n_{z_2}}\end{bmatrix} & 0\end{array}\right]\left[\begin{array}{c}\boldsymbol{x}_{\mathrm{P}}(t)\\ \hline \begin{bmatrix}\boldsymbol{w}_1(t)\\ \boldsymbol{w}_2(t)\end{bmatrix}\\ \boldsymbol{u}(t)\end{array}\right] \tag{3.7}$$

where the partitions $\boldsymbol{z}(t)=[\boldsymbol{z}_1(t),\boldsymbol{z}_2(t)]^{\mathrm{T}}\in\mathbb{R}^{n_z}$, $\boldsymbol{w}(t)=[\boldsymbol{w}_1(t),\boldsymbol{w}_2(t)]^{\mathrm{T}}\in\mathbb{R}^{n_w}$, $B_1(\boldsymbol{\rho})=[B_{11}(\boldsymbol{\rho}),B_{12}(\boldsymbol{\rho})]\in\mathbb{R}^{n_{x\mathrm{P}}\times n_w}$, and $C_1(\boldsymbol{\rho})=[C_{11}(\boldsymbol{\rho}),C_{12}(\boldsymbol{\rho})]^{\mathrm{T}}\in\mathbb{R}^{n_z\times n_{x\mathrm{P}}}$ hold, and assume $D_{11}(\boldsymbol{\rho})=0_{n_z\times n_w}$, $D_{22}(\boldsymbol{\rho})=0_{n_y\times n_u}$, $D_{12}(\boldsymbol{\rho})\in\mathbb{R}^{n_z\times n_u}$ is full column rank, and $D_{21}(\boldsymbol{\rho})\in\mathbb{R}^{n_y\times n_w}$ is full row rank for all $\boldsymbol{\rho}(t)\in\mathbb{U}_\rho$.

The following theorem provides the conditions to ensure the generalized LPV system in Equation (3.7) to be robustly stable in the sense of Definition 3.6, guaranteeing the induced L_2-norm performance of the resulting closed-loop system, through the resolution of the optimization problem in Definition 3.9.

Theorem 3.3 ([Wu+96])
Given a compact set $\mathbb{U}_\rho\subset\mathbb{R}^{n_\rho}$, non-negative numbers $\{\nu_i\}_{i=1}^{n_\rho}$, performance level γ, and the open-loop LPV system in Equation (3.7), the LPV synthesis γ-performance/ν-variation problem is solvable if and only if there exist continuously differentialble functions $X:\mathbb{R}^{n_\rho}\to\mathbb{R}^{n_{x\mathrm{P}}\times n_{x\mathrm{P}}}$ and $Y:\mathbb{R}^{n_\rho}\to\mathbb{R}^{n_{x\mathrm{P}}\times n_{x\mathrm{P}}}$, such that for all $\boldsymbol{\rho}\in\mathbb{U}_\rho$, $X(\boldsymbol{\rho})$, $Y(\boldsymbol{\rho})>0$, and:

$$\begin{bmatrix} Y(\boldsymbol{\rho})\hat{\mathcal{A}}^{\mathrm{T}}(\boldsymbol{\rho})+\hat{\mathcal{A}}(\boldsymbol{\rho})Y(\boldsymbol{\rho})-\sum_{i=1}^{n_\rho}\pm\left(\nu_i\dfrac{\partial Y(\boldsymbol{\rho})}{\partial\rho_i}\right)-\gamma\mathcal{B}_2(\boldsymbol{\rho})\mathcal{B}_2^{\mathrm{T}}(\boldsymbol{\rho}) & (\star)^{\mathrm{T}} & (\star)^{\mathrm{T}}\\ \mathcal{C}_{11}(\boldsymbol{\rho})Y(\boldsymbol{\rho}) & -\gamma I_{n_{z1}} & 0\\ \mathcal{B}_1^{\mathrm{T}}(\boldsymbol{\rho}) & 0 & -\gamma I_{n_w}\end{bmatrix}\prec 0$$

$$\begin{bmatrix} \tilde{\mathcal{A}}^{\mathrm{T}}(\boldsymbol{\rho})X(\boldsymbol{\rho})+X(\boldsymbol{\rho})\tilde{\mathcal{A}}(\boldsymbol{\rho})-\sum_{i=1}^{n_\rho}\pm\left(\nu_i\dfrac{\partial X(\boldsymbol{\rho})}{\partial\rho_i}\right)-\gamma\mathcal{C}_2(\boldsymbol{\rho})\mathcal{C}_2^{\mathrm{T}}(\boldsymbol{\rho}) & (\star)^{\mathrm{T}} & (\star)^{\mathrm{T}}\\ \mathcal{B}_{11}^{\mathrm{T}}(\boldsymbol{\rho})X(\boldsymbol{\rho}) & -\gamma I_{n_{w1}} & 0\\ \mathcal{C}_1^{\mathrm{T}}(\boldsymbol{\rho}) & 0 & -\gamma I_{n_z}\end{bmatrix}\prec 0$$

$$\begin{bmatrix} X(\boldsymbol{\rho}) & I_{n_x}\\ I_{n_x} & Y(\boldsymbol{\rho})\end{bmatrix}\succeq 0$$

where:

$$\hat{\mathcal{A}}(\boldsymbol{\rho}):=\mathcal{A}(\boldsymbol{\rho})-\mathcal{B}_2(\boldsymbol{\rho})\mathcal{C}_{12}(\boldsymbol{\rho});\qquad \tilde{\mathcal{A}}(\boldsymbol{\rho}):=\mathcal{A}(\boldsymbol{\rho})-\mathcal{B}_{12}(\boldsymbol{\rho})\mathcal{C}_2(\boldsymbol{\rho}).$$

The conditions in Theorem 3.3 define a standard infinite-dimensional LMIs problem. As discussed in Section 3.2.2.1, the problem can be converted to a solvable finite-dimensional optimization by projecting the parameter-dependent Lyapunov functions, $X(\boldsymbol{\rho})$ and $Y(\boldsymbol{\rho})$, on a finite set of n_{B} basis functions, as in Theorem 3.1, and by dicretizing the continuous space of variation of the parameters into a finite grid of n_{g} values of $\boldsymbol{\rho} \in \bar{\mathbb{U}}_{\rho}$, as in Proposition 3.1. Thus, by parametrizing the Lyapunov functions through sets of scalar differentiable basis functions, $\{f_i : \mathbb{R}^{n_p} \rightarrow \mathbb{R}\}_{i=1}^{n_{\mathrm{B}}}$ and $\{g_i : \mathbb{R}^{n_p} \rightarrow \mathbb{R}\}_{i=1}^{n_{\mathrm{B}}}$, as:

$$X(\boldsymbol{\rho}) = X_0 + \sum_{i=1}^{n_{\mathrm{B}}} f_i(\boldsymbol{\rho}) X_i; \qquad Y(\boldsymbol{\rho}) = Y_0 + \sum_{i=1}^{n_{\mathrm{B}}} g_i(\boldsymbol{\rho}) Y_i \tag{3.8}$$

where $X_0, X_i \in \mathbb{R}^{n_{x\mathrm{P}} \times n_{x\mathrm{P}}}$ and $Y_0, Y_i \in \mathbb{R}^{n_{x\mathrm{P}} \times n_{x\mathrm{P}}}$, the resulting finite-dimensional control synthesis problem can be formulated as it follows.

Proposition 3.2 ($\mathcal{H}_\infty$ Dynamic Output-Feedback Control Problem)
Given the LPV closed-loop system, Σ_{CL}, in Equation (3.6), *a dynamic output-feedback control problem consists of finding a controller, $K(\boldsymbol{\rho})$, that solves the $\mathcal{H}_\infty$ control problem in Definition 3.9 (guaranteeing robust stability), by satisfying the LMIs conditions derived in Theorem 3.3. According to the formulation in Theorem 3.3, the LPV controller is parameterized as:*

$$K(\boldsymbol{\rho}) : \begin{bmatrix} \dot{\boldsymbol{x}}_K(t) \\ \boldsymbol{u}(t) \end{bmatrix} = \begin{bmatrix} \mathcal{A}_K(\boldsymbol{\rho}) & \mathcal{B}_K(\boldsymbol{\rho}) \\ \mathcal{C}_K(\boldsymbol{\rho}) & \mathcal{D}_K(\boldsymbol{\rho}) \end{bmatrix} \begin{bmatrix} \boldsymbol{x}_K(t) \\ \boldsymbol{y}(t) \end{bmatrix} \tag{3.9}$$

where:

$$\begin{aligned}
\mathcal{A}_K(\boldsymbol{\rho}, \dot{\boldsymbol{\rho}}) &:= \big[\mathcal{A}(\boldsymbol{\rho}) + \gamma^{-1}[Q^{-1}(\boldsymbol{\rho})X(\boldsymbol{\rho})L(\boldsymbol{\rho})\mathcal{B}_{12}^{\mathrm{T}} + \mathcal{B}_1(\boldsymbol{\rho})\mathcal{B}_1^{\mathrm{T}}(\boldsymbol{\rho})]Y^{-1}(\boldsymbol{\rho}) \\
&\qquad + \mathcal{B}_2(\boldsymbol{\rho})F(\boldsymbol{\rho}) + Q^{-1}(\boldsymbol{\rho})X(\boldsymbol{\rho})L(\boldsymbol{\rho})\mathcal{C}_2(\boldsymbol{\rho}) - Q^{-1}(\boldsymbol{\rho})H(\boldsymbol{\rho}, \dot{\boldsymbol{\rho}})\big], \\
\mathcal{B}_K(\boldsymbol{\rho}) &:= -\left[Q^{-1}(\boldsymbol{\rho})X(\boldsymbol{\rho})L(\boldsymbol{\rho})\right], \\
\mathcal{C}_K(\boldsymbol{\rho}) &:= F(\boldsymbol{\rho}),
\end{aligned}$$

and:

$$\begin{aligned}
Q(\boldsymbol{\rho}) &:= \left[X(\boldsymbol{\rho}) - Y(\boldsymbol{\rho})^{-1}\right], \\
F(\boldsymbol{\rho}) &:= -\left[\gamma \mathcal{B}_2^{\mathrm{T}}(\boldsymbol{\rho})Y^{-1}(\boldsymbol{\rho}) + \mathcal{C}_{12}(\boldsymbol{\rho})\right], \\
L(\boldsymbol{\rho}) &:= -\left[\gamma X^{-1}\mathcal{C}_2^{\mathrm{T}}(\boldsymbol{\rho}) + \mathcal{B}_{12}(\boldsymbol{\rho})\right], \\
H(\boldsymbol{\rho}, \dot{\boldsymbol{\rho}}) &:= -\Bigg[\mathcal{A}_F^{\mathrm{T}}(\boldsymbol{\rho})Y^{-1} + Y^{-1}\mathcal{A}_F(\boldsymbol{\rho}) + \sum_i \left(\dot{\boldsymbol{\rho}} \frac{\partial Y^{-1}}{\partial \boldsymbol{\rho}}\right) \\
&\qquad + \gamma^{-1}\mathcal{C}_F^{\mathrm{T}}(\boldsymbol{\rho})\mathcal{C}_F(\boldsymbol{\rho}) + \gamma^{-1}Y^{-1}(\boldsymbol{\rho})\mathcal{B}_1(\boldsymbol{\rho})\mathcal{B}_1^{\mathrm{T}}(\boldsymbol{\rho})Y^{-1}(\boldsymbol{\rho})\Bigg],
\end{aligned}$$

with:

$$\mathcal{A}_F(\boldsymbol{\rho}) := \mathcal{A}(\boldsymbol{\rho}) + \mathcal{B}_2(\boldsymbol{\rho})F(\boldsymbol{\rho}); \qquad \mathcal{C}_F^{\mathrm{T}}(\boldsymbol{\rho}) := \left[\mathcal{C}_{11}^{\mathrm{T}}(\boldsymbol{\rho}) \;\; \mathcal{C}_{12}^{\mathrm{T}}(\boldsymbol{\rho}) + F^{\mathrm{T}}(\boldsymbol{\rho})\right].$$

The solution to the problem consists of a set of n_{g} LTI realizations of the LPV controller in Equation (3.9), evaluated at each selected grid point for frozen values of $\boldsymbol{\rho} \in \bar{\mathbb{U}}_{\rho}$. The implementation of the LPV controller for any intermediate scheduling variables' values relies on the linear interpolation between the LTI set.

3.2.3.3 Polytopic Control Problem Formulation

As previously mentioned in Chapter 2, the control-oriented formulation of an LPV polytopic system is based on an affine model-parameters relation, as in Definition 2.4. In order to respect the affine condition through the formulation of the LMIs controller synthesis problem, the following assumptions have to be imposed.

Assumption 3.1 ((A1) in [AGB95])
The generalized LPV plant must be strictly proper, hence $\mathcal{D}_{22}(\boldsymbol{\rho}) = 0$.

Assumption 3.2 ((A2) in [AGB95])
The input/output matrices, $\mathcal{B}_2(\boldsymbol{\rho})$, $\mathcal{C}_2(\boldsymbol{\rho})$, $\mathcal{D}_{12}(\boldsymbol{\rho})$, $\mathcal{D}_{21}(\boldsymbol{\rho})$, must be parameter-independent.

Based on Assumptions 3.1-3.2, the generalized LPV plant described in Definition 3.7, has to be reformulated as:

$$\Sigma_{\mathrm{P}} : \left[\begin{array}{c} \dot{\boldsymbol{x}}_{\mathrm{P}}(t) \\ \hline \boldsymbol{z}(t) \\ \boldsymbol{y}(t) \end{array}\right] = \left[\begin{array}{c|cc} \mathcal{A}(\rho) & \mathcal{B}_1(\boldsymbol{\rho}) & \mathcal{B}_2 \\ \hline \mathcal{C}_1(\boldsymbol{\rho}) & \mathcal{D}_{11}(\boldsymbol{\rho}) & \mathcal{D}_{12} \\ \mathcal{C}_2 & \mathcal{D}_{21} & 0 \end{array}\right] \left[\begin{array}{c} \boldsymbol{x}_{\mathrm{P}}(t) \\ \hline \boldsymbol{w}(t) \\ \boldsymbol{u}(t) \end{array}\right] \tag{3.10}$$

The following propositions provide the sufficient conditions to ensure the generalized LPV system in Equation (3.10) is quadratically stable in the sense of Definition 3.5. The formulation guarantees the induced L_2-norm performance of the resulting closed-loop system, through the resolution of the optimization problem in Definition 3.9, by employing a polytopic approach. The LMIs conditions have been derived in [SGC97] and reformulated as in [PV08], where additional details and related proofs of the propositions are discussed.

Proposition 3.3 (Feasibility - $\mathcal{H}_\infty$ Polytopic Control Problem)
Consider the LPV closed-loop system, Σ_{CL}, in Equation (3.6), where the generalized open-loop system, Σ_{P}, in Equation (3.10), is formulated as the LPV polytopic system in Equation (2.4). There exists a full-order dynamic output feedback controller, $K(\boldsymbol{\rho})$, that solves the $\mathcal{H}_\infty$ control problem in Definition 3.9 (guaranteeing quadratic stability), if there exist symmetric matrices, $X, Y \in \mathbb{R}^{n_{x\mathrm{P}} \times n_{x\mathrm{P}}}$, and matrices $\tilde{\mathcal{A}}(\boldsymbol{\theta}_i) \in \mathbb{R}^{n_{x\mathrm{P}} \times n_{x\mathrm{P}}}$, $\tilde{\mathcal{B}}(\boldsymbol{\theta}_i) \in \mathbb{R}^{n_{x\mathrm{P}} \times n_y}$, $\tilde{\mathcal{C}}(\boldsymbol{\theta}_i) \in \mathbb{R}^{n_u \times n_{x\mathrm{P}}}$, $\tilde{\mathcal{D}}(\boldsymbol{\theta}_i) \in \mathbb{R}^{n_u \times n_y}$, and a performance level $\gamma > 0 \in \mathbb{R}$, such that:

$$\begin{aligned} &\begin{bmatrix} M_{11} & (\star)^{\mathrm{T}} & (\star)^{\mathrm{T}} & (\star)^{\mathrm{T}} \\ M_{21} & M_{22} & (\star)^{\mathrm{T}} & (\star)^{\mathrm{T}} \\ M_{31} & M_{32} & -\gamma I_{n_w} & (\star)^{\mathrm{T}} \\ M_{41} & M_{42} & M_{43} & -\gamma I_{n_z} \end{bmatrix} \prec 0 \\ &\begin{bmatrix} X & I_{n_{x\mathrm{P}}} \\ I_{n_{x\mathrm{P}}} & Y \end{bmatrix} \succ 0 \end{aligned} \tag{3.11}$$

where:

$$
\begin{aligned}
M_{11} &:= \mathcal{A}(\boldsymbol{\theta}_i)X + X\mathcal{A}^{\mathrm{T}}(\boldsymbol{\theta}_i) + \mathcal{B}_2\tilde{\mathcal{C}}(\boldsymbol{\theta}_i) + \tilde{\mathcal{C}}^{\mathrm{T}}(\boldsymbol{\theta}_i)\mathcal{B}_2^{\mathrm{T}} \\
M_{21} &:= \tilde{\mathcal{A}}(\boldsymbol{\theta}_i) + \mathcal{A}^{\mathrm{T}}(\boldsymbol{\theta}_i) + \mathcal{C}_2^{\mathrm{T}}\tilde{\mathcal{D}}^{\mathrm{T}}(\boldsymbol{\theta}_i)\mathcal{B}_2^{\mathrm{T}} \\
M_{22} &:= Y\mathcal{A}(\boldsymbol{\theta}_i) + \mathcal{A}^{\mathrm{T}}(\boldsymbol{\theta}_i)Y + \tilde{\mathcal{B}}(\boldsymbol{\theta}_i)\mathcal{C}_2 + \mathcal{C}_2^{\mathrm{T}}\tilde{\mathcal{B}}^{\mathrm{T}}(\boldsymbol{\theta}_i) \\
M_{31} &:= \mathcal{B}_1^{\mathrm{T}}(\boldsymbol{\theta}_i) + \mathcal{D}_{21}^{\mathrm{T}}\tilde{\mathcal{D}}^{\mathrm{T}}(\boldsymbol{\theta}_i)\mathcal{B}_2^{\mathrm{T}} \\
M_{32} &:= \mathcal{B}_1^{\mathrm{T}}(\boldsymbol{\theta}_i)Y + \mathcal{D}_{21}^{\mathrm{T}}\tilde{\mathcal{B}}^{\mathrm{T}}(\boldsymbol{\theta}_i) \\
M_{41} &:= \mathcal{C}_1(\boldsymbol{\theta}_i)X + \mathcal{D}_{12}\tilde{\mathcal{C}}(\boldsymbol{\theta}_i) \\
M_{42} &:= \mathcal{C}_1(\boldsymbol{\theta}_i) + \mathcal{D}_{12}\tilde{\mathcal{D}}(\boldsymbol{\theta}_i)\mathcal{C}_2 \\
M_{43} &:= \mathcal{D}_{11}(\boldsymbol{\theta}_i) + \mathcal{D}_{12}\tilde{\mathcal{D}}(\boldsymbol{\theta}_i)\mathcal{D}_{21}
\end{aligned}
$$

hold at each vertex, $\boldsymbol{\theta}_i = [\nu_{i,1}, \ldots, \nu_{i,n_\rho}]$, of the polytope, where $\nu_{i,j}$ is the j^{th} scheduling variables that equals either the upper or the lower bounds, $\overline{\rho_j}$ and $\underline{\rho_j}$, respectively.

Proposition 3.4 (Reconstruction - $\mathcal{H}_\infty$ Polytopic Control Problem)
If the conditions in Proposition 3.3 are fulfilled, then the controller, $K(\boldsymbol{\rho})$ exitsts and can be expressed as:

$$
K(\boldsymbol{\rho}) : \begin{bmatrix} \dot{\boldsymbol{x}}_K(t) \\ \boldsymbol{u}(t) \end{bmatrix} = \begin{bmatrix} \mathcal{A}_K(\boldsymbol{\rho}) & \mathcal{B}_K(\boldsymbol{\rho}) \\ \mathcal{C}_K(\boldsymbol{\rho}) & \mathcal{D}_K(\boldsymbol{\rho}) \end{bmatrix} \begin{bmatrix} \boldsymbol{x}_K(t) \\ \boldsymbol{y}(t) \end{bmatrix} \tag{3.12}
$$

The controller reconstruction is obtained by solving the following system of equations at each vertex, $\boldsymbol{\theta}_i = [\nu_{i,1}, \ldots, \nu_{i,n_\rho}]$, of the polytope, where $\nu_{i,j}$ is the j^{th} scheduling variables that equals either the upper or the lower bounds, $\overline{\rho_j}$ and $\underline{\rho_j}$, respectively:

$$
\begin{aligned}
\mathcal{D}_K(\boldsymbol{\theta}_i) &:= \tilde{\mathcal{D}}(\boldsymbol{\theta}_i) \\
\mathcal{C}_K(\boldsymbol{\theta}_i) &:= \Big(\tilde{\mathcal{C}}(\boldsymbol{\theta}_i) - \mathcal{D}_K(\boldsymbol{\theta}_i)\mathcal{C}_2 X\Big)M^{\text{-T}} \\
\mathcal{B}_K(\boldsymbol{\theta}_i) &:= N^{-1}\Big(\tilde{\mathcal{B}}(\boldsymbol{\theta}_i)) - Y\mathcal{B}_2\mathcal{D}_K(\boldsymbol{\theta}_i)\Big) \\
\mathcal{A}_K(\boldsymbol{\theta}_i) &:= N^{-1}\Big(\tilde{\mathcal{A}}(\boldsymbol{\theta}_i) - Y\mathcal{A}(\boldsymbol{\theta}_i)X - Y\mathcal{B}_2\mathcal{D}_K(\boldsymbol{\theta}_i)\mathcal{C}_2 X \\
&\qquad\qquad\qquad - N\mathcal{B}_K(\boldsymbol{\theta}_i)\mathcal{C}_2 X - Y\mathcal{B}_2\mathcal{C}_K(\boldsymbol{\theta}_i)M^{\mathrm{T}}\Big)M^{\text{-T}}
\end{aligned}
$$

where M and N are defined such that $MN^{\mathrm{T}} = I_{n_{x_{\mathrm{P}}}} - XY$, which are chosen by applying a Singular Value Decomposition (SVD) and a Cholesky factorization.

The solution of the control problem in Proposition 3.4 consists of a set of LTI realizations of the LPV controller in Equation (3.12), evaluated at each vertex of the polytope, $\boldsymbol{\theta}_i \in \Theta$. Since the controllers share the same constant Lyapunov functions, X and Y, quadratic stability properties are ensured across the entire convex subspace described by the polytope. As a drawback, the controller relies on a sub-optimal solution of the LMIs optimization problem in Equation (3.11), solved at each vertex of the polytope, introducing a certain degree of conservatism in the controller synthesis performance.

3.3 Polytopic Controller Design

In this section, the synthesis of the LPV polytopic controller, K_{PY}, is presented. The controller synthesis is based on the approximated LPV polytopic model of the projectile pitch channel dynamics derived in Chapter 2, Section 2.4. The generalized plant architecture is first introduced, defying the core objectives of the design. The controller synthesis addresses the flight envelope represented by the variation of the original scheduling variables: $\alpha \in [0, 16]$ deg, $V \in [160,\ 280]$ m/s, and $h \in [1,\ 15]$ km. However, the actual design polytope, $\hat{\Theta}$, is defined through the corresponding ranges of variation of the identified set of scheduling functions ($\hat{\rho}_1$, $\hat{\rho}_2$, $\hat{\rho}_3$), obtained in Section 2.4, as a result of the approximation process.

Prior to the controller synthesis, the dimensions of the polytope are analyzed in detail and iteratively optimized, in order to minimize the conservatism affecting the optimization problem. Indeed, the polytope mapping process developed in Section 2.4.2 resulted in the identification of a convex space that is larger than the original flight envelope. The iterative computation of the controller design, and the analysis of the resulting performance in time simulations, allows for progressively adjusting the ranges of variation of $\hat{\rho}_1$, $\hat{\rho}_2$, and $\hat{\rho}_3$ that define the polytope, $\hat{\Theta}$. The final results of the design process are investigated in the frequency domain to assess the properties of the closed-loop system in terms of reference tracking and disturbance rejection capabilities.

3.3.1 Polytopic Design Scheme

The design architecture employed for the controller synthesis is presented in Figure 3.1 and complies with the generalized system formulation expressed in Equation (3.10). The second-order actuator model, T_{act}, presented in Equation (1.39) of Chapter 1, is included in the definition of the generalized plant to account for the actuator dynamics, together with the projectile polytopic quasi-LPV model, Σ_{PY}, summarized in Equation (2.42), in the conclusions of Chapter 2. A set of first-order weighting functions, W_e and W_u, imposes the desired closed-loop tracking capability and control effort performances in the frequency domain, by targeting the corresponding tracking error, $e = r - \alpha$, and the derivative of the control deflection input, $\dot{\delta}_{q,\mathrm{cmd}}$. The reference signal, r, consists of an AoA trajectory defined through an LDR optimization law ([Phi08]; [KCL82]). The weighting functions are parametrized as:

$$W_e(s) = \frac{s/M_e + \omega_e}{s + \omega_e \epsilon_e}; \qquad\qquad W_u(s) = \frac{s + \omega_u/M_u}{\epsilon_u s + \omega_u}$$

where the high-frequency gain, $M_e = 2$, the low-frequency gain, $\epsilon_e = 0.01$, and the crossover frequency, $\omega_e = 1$ rad/s, are selected respectively to guarantee 6 dB of module margin for robustness purposes, -40 dB of disturbance attenuation, and a steady-state tracking error $\leq 1\%$ at low frequency. Similarly, $M_u = 5.5$, $\epsilon_u = 0.01$, and $\omega_u = 100$ rad/s provide respectively a maximum 15 dB low-frequency gain, -40 dB of noise attenuation, and an input bandwidth that complies with the actuator operating limitations, aiming to prevent stall regime occurrence.

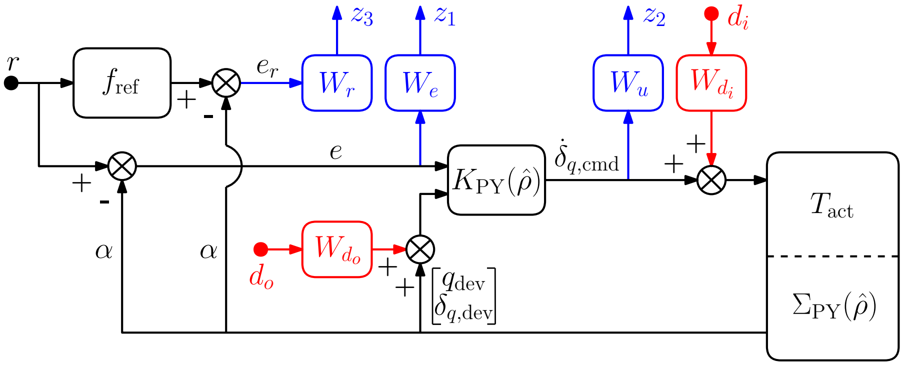

Figure 3.1: Polytopic design scheme architecture.

Since tracking capability and disturbance rejection are demanding properties, the imposition of a single filter cannot simultaneously optimize both. The bandwidth of W_e is dedicated to ensuring a reliable output disturbance rejection to the system, while an additional first-order weighting function, W_r, imposes larger bandwidth requirements to improve the tracking response. The weighting function is applied to the response error, $e_r = f_{\text{ref}} - \alpha$, evaluated as the difference between the tracking response of a desired reference model, f_{ref}, and the tracking response of the projectile dynamics.

A core objective of the reference model selection relies on minimizing the overshoot affecting the system response. Indeed, in a gliding flight scenario, the guidance reference signal is generally engaged at the apogee of the projectile's trajectory, generating sudden and sharp variations in the projectile's attitude. A large overshoot on the AoA might lead to the saturation of the aerodynamic control surfaces, critical for control purposes. As a consequence, the first-order reference model, and the related tracking response weighting function are parametrized respectively as:

$$f_{\text{ref}}(s) = \frac{\omega_f}{s + \omega_f}; \qquad\qquad W_r(s) = \frac{s/M_r + \omega_r}{s + \omega_r \epsilon_r};$$

where the $\omega_f = 10$ rad/s, $M_r = 2$, $\epsilon_r = 0.001$, and $\omega_r = 10$ rad/s, coherently.

Constant weights, $W_{d_i} = 0.6$ and $W_{d_o} = 0.2$, are also applied to the input and output disturbance signals, d_i and d_o respectively, aiming to properly scale the disturbance effects on the model dynamics.

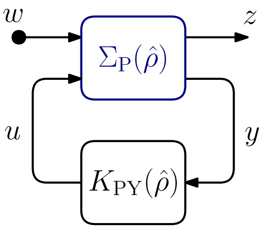

Figure 3.2: General polytopic control scheme configuration.

Remark 3.7
The weighting functions are designed independently of the scheduling functions in $\hat{\rho}(t)$*, meaning that the same performances are imposed at each vertex condition of the polytope, leading to possible conservativeness in the synthesis results.*

The control scheme in Figure 3.1 is then generalized as in Figure 3.2, where the LPV plant, $\Sigma_{\mathrm{P}}(\hat{\rho})$, includes the dynamics of the actuator, the projectile polytopic model, the reference model, and the weighting functions. Thus, according to the generalized polytopic plant formulation in Equation (3.10), the overall generalized state vector is defined as: $\boldsymbol{x}_{\mathrm{P}} = [\boldsymbol{x}^{\mathrm{T}},\, \boldsymbol{x}_{\mathrm{act}}^{\mathrm{T}},\, x_{f_{\mathrm{ref}}},\, x_{W_e},\, x_{W_u},\, x_{W_r}]^{\mathrm{T}} \in \mathbb{R}^9$, with $\boldsymbol{x} = [\alpha,\, q_{\mathrm{dev}},\, \delta_{q,\mathrm{dev}}]^{\mathrm{T}} \in \mathbb{R}^3$. The generalized exogenous input vector, $\boldsymbol{w} = [r,\, d_i,\, d_o]^{\mathrm{T}} \in \mathbb{R}^3$, accounts for the reference guidance signal and the input and output disturbances, while the generated control input, $u \in \mathbb{R}$, corresponds to the commanded virtual pitch deflection rate, $\dot{\delta}_{q,\mathrm{cmd}}$, imposed on the canards. Indeed, the inclusion of the integrator dynamics during the state transformation process resulted in the redefinition of the quasi-LPV model input, σ, as the derivative of δ_q. Finally, the generalized controlled output vector, $\boldsymbol{z} = [z_1,\, z_2,\, z_3]^{\mathrm{T}} \in \mathbb{R}^3$, includes the control optimization objectives, while the set of available measurements, $\boldsymbol{y} = [e,\, q_{\mathrm{dev}},\, \delta_{q,\mathrm{dev}}]^{\mathrm{T}} \in \mathbb{R}^3$, is the controller input.

The generalized plant is then evaluated at each vertex of the polytope, $\hat{\boldsymbol{\theta}}_i \in \hat{\Theta}$ with $i = 1, \ldots, 8$, by substituting the corresponding values of the scheduling functions. The resulting LTI system realizations are employed in the resolution of the set of LMIs that defines the polytopic controller synthesis problem, formulated in Propositions 3.3-3.4.

3.3.2 Polytope Reduction Analysis

The mapping process developed in Chapter 2, Section 2.4.2 allowed defining the polytope's dimensions through the identification of the scheduling functions' variation ranges: $\hat{\rho}_1 \in [0.4,\, 2.9] \times 10^4$, $\hat{\rho}_2 \in [0.05,\, 0.55]$, and $\hat{\rho}_3 \in [-1,\, 4.1]$. As mentioned at the end of Section 2.4.2, the polytope definition is affected by a certain level of conservatism due to the limited accuracy of the flight conditions selection criteria. Consequently, the controller synthesis might account for areas of the flight envelope that are unfeasible for the specific gliding-phase trajectory targeted by the design, over-constraining the optimization problem. In order to optimize the dimensions of the polytope, the variation of each scheduling function, $(\hat{\rho}_1,\, \hat{\rho}_2,\, \hat{\rho}_3)$, is investigated across the original projectile's flight envelope: $\alpha \in [0, 16]$ deg, $V \in [160,\, 280]$ m/s, and $h \in [1,\, 15]$ km. The analysis aims to identify any unfeasible operating conditions, $(\alpha,\, V,\, h)$, generated by the polytope mapping process. Additionally, by iteratively performing the controller synthesis on a progressively optimized convex space, the polytope's dimensions can be properly adjusted to comply with the desired gliding-phase trajectory of the projectile.

Aiming for a clearer understanding of the relation between the original and the newly identified convex spaces, the variation of the scheduling functions is evaluated across the flight domain of each scheduling variable $(\alpha,\, V,\, h)$. The results in Figure 3.3 show the mutual dependence of the scheduling functions on the altitude variation. In particular, both $\hat{\rho}_1$ and $\hat{\rho}_2$ present higher values at lower altitude levels, and vice versa, as observed in Figure 3.3(a).

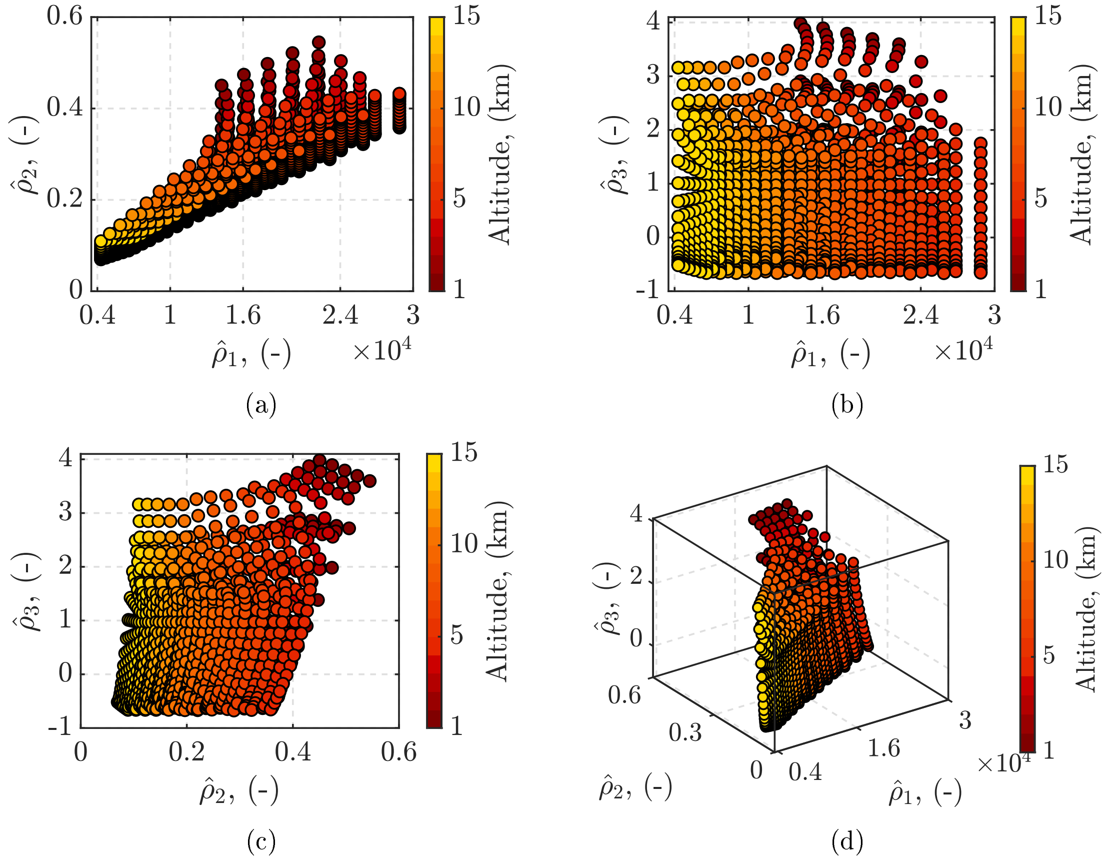

(a) (b) (c) (d)

Figure 3.3: Dependence on the altitude: (a) $\hat{\rho}_1$-$\hat{\rho}_2$; (b) $\hat{\rho}_1$-$\hat{\rho}_3$; (c) $\hat{\rho}_2$-$\hat{\rho}_3$; (d) 3D space.

Differently, Figures 3.3(b)-(c) reveal the nearly independent relation of $\hat{\rho}_3$ to the altitude level. In the following, in order to simplify the analysis of the remaining scheduling variables, α and V, only a subspace of the flight envelope is investigated, belonging to a fixed altitude level: $h = 7$ km. Indeed, the results obtained across the full envelope confirmed that the dependence on the scheduling functions on α and V is not affected by the altitude level.

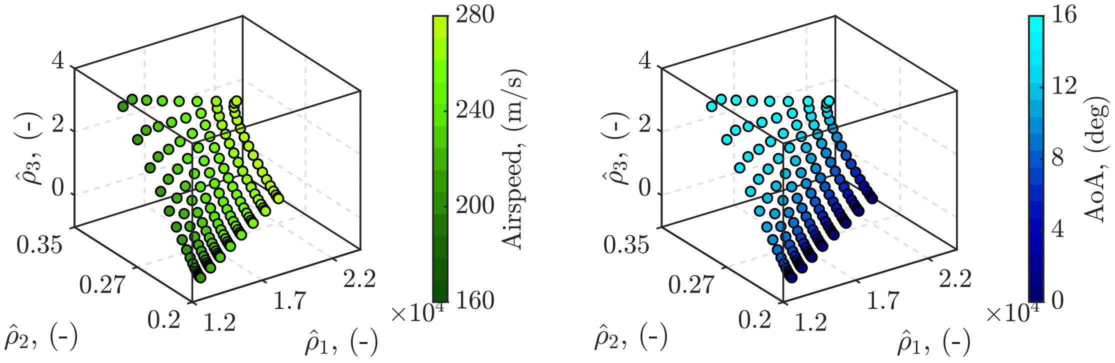

(a) (b)

Figure 3.4: Polytope's 3D dimensions dependence: (a) airspeed; (b) AoA.

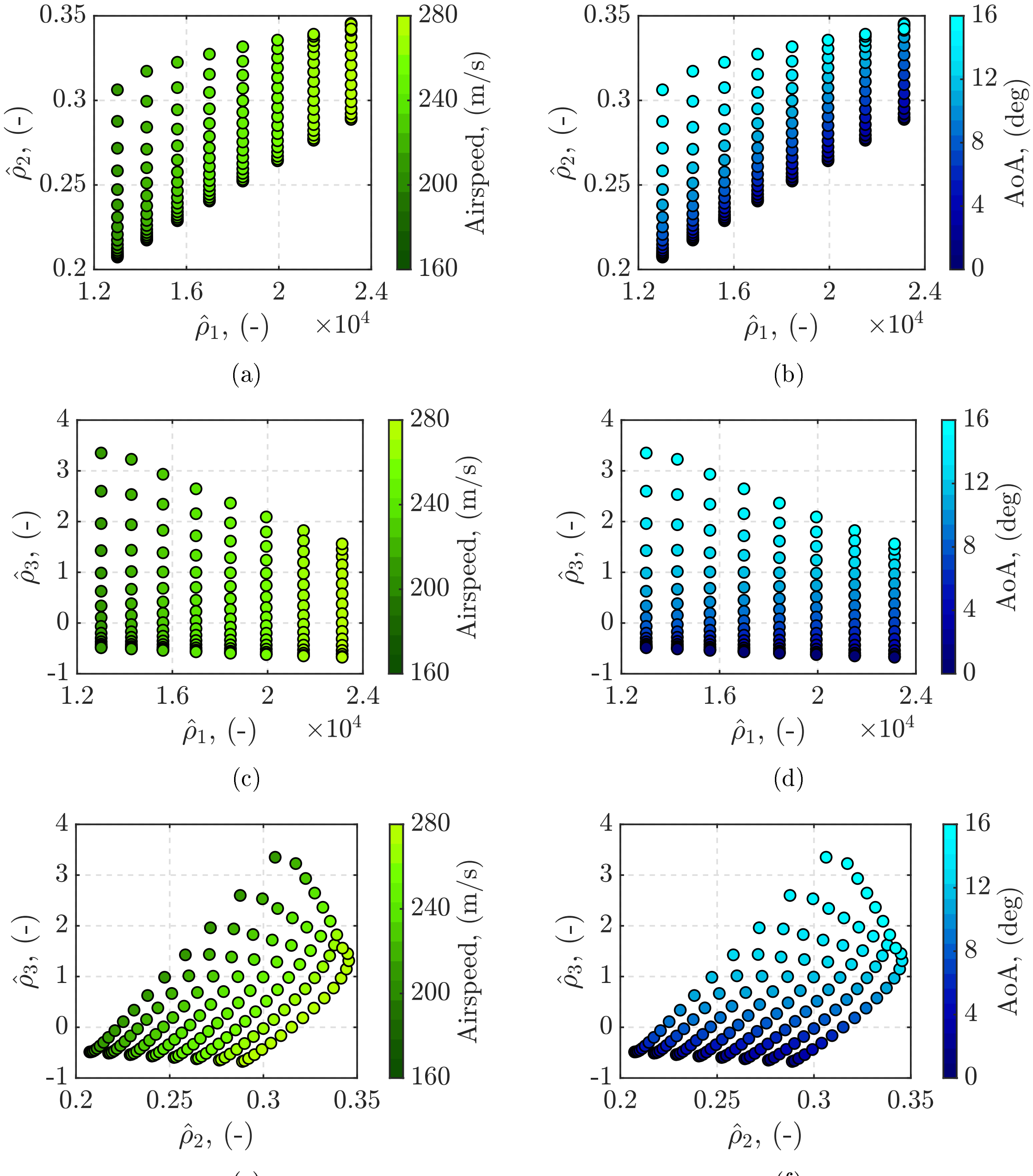

(a) (b)

(c) (d)

(e) (f)

Figure 3.5: Polytope's dimensions dependence on the airspeed and AoA variations: (a)-(b) $\hat{\rho}_1$-$\hat{\rho}_2$, respectively; (c)-(d) $\hat{\rho}_1$-$\hat{\rho}_3$, respectively; (e)-(f) $\hat{\rho}_2$-$\hat{\rho}_3$, respectively.

The results in Figure 3.4 and Figure 3.5 provide a comparison between the mutual dependence of the scheduling functions to the scheduling variables, α and V. As expected, $\hat{\rho}_1$ presents an evident dependence on the airspeed, while it results completely independent of the AoA. Indeed, through the polytopic modeling procedure developed in Chapter 2, $\hat{\rho}_1$ has been defined as the dynamic pressure. On the other hand, the complex parameterizations of the remaining scheduling functions, $\hat{\rho}_2$ and $\hat{\rho}_3$, prevent a straightforward intuition about their variations across the flight envelope. The analyses in Figures 3.5(d)(f) reveal a relevant dependence of $\hat{\rho}_3$ to the AoA variation, while the effect of the airspeed conditions in Figures 3.5(c)(e) appears to be almost negligible. Conversely, the variation of $\hat{\rho}_2$ is characterized by a strong dependence on the airspeed conditions, as in Figures 3.5(a)(e), and a negligible dependence on AoA values. Indeed, the apparent relation shown in Figures 3.5(b)(f) is clarified by the 3D representation in Figure 3.4(b), where the higher values of $\hat{\rho}_2$ only occur for corresponding higher values of $\hat{\rho}_3$ (highly dependent on the AoA).

The observations provided by the different analyses highlighted potential areas of the polytope characterized by unfeasible flight conditions. Indeed, at low altitude levels, $h \leq 3$ km, high values of airspeed are very unlikely to occur, and vice versa, combinations of $h \geq 10$ km and low airspeed regime are not feasible for the projectile's gliding trajectory. The refinement of the variation ranges of $\hat{\rho}_1$, $\hat{\rho}_2$, and $\hat{\rho}_3$, is based on the knowledge acquired through the polytope analyses, and the iterative performance of trajectory simulations of progressively more accurate LPV controllers. As will be shown in the simulation results presented in Chapter 4, the actual area covered by the scheduling functions' trajectories belongs to a bounded subspace of the polytope, $\hat{\Theta}$, identified in Chapter 2. In particular, the limitations imposed on the control effort through the controller design, preventing possible canards saturation, drastically reduced the available AoA variation range and consequently the $\hat{\rho}_3$ boundaries.

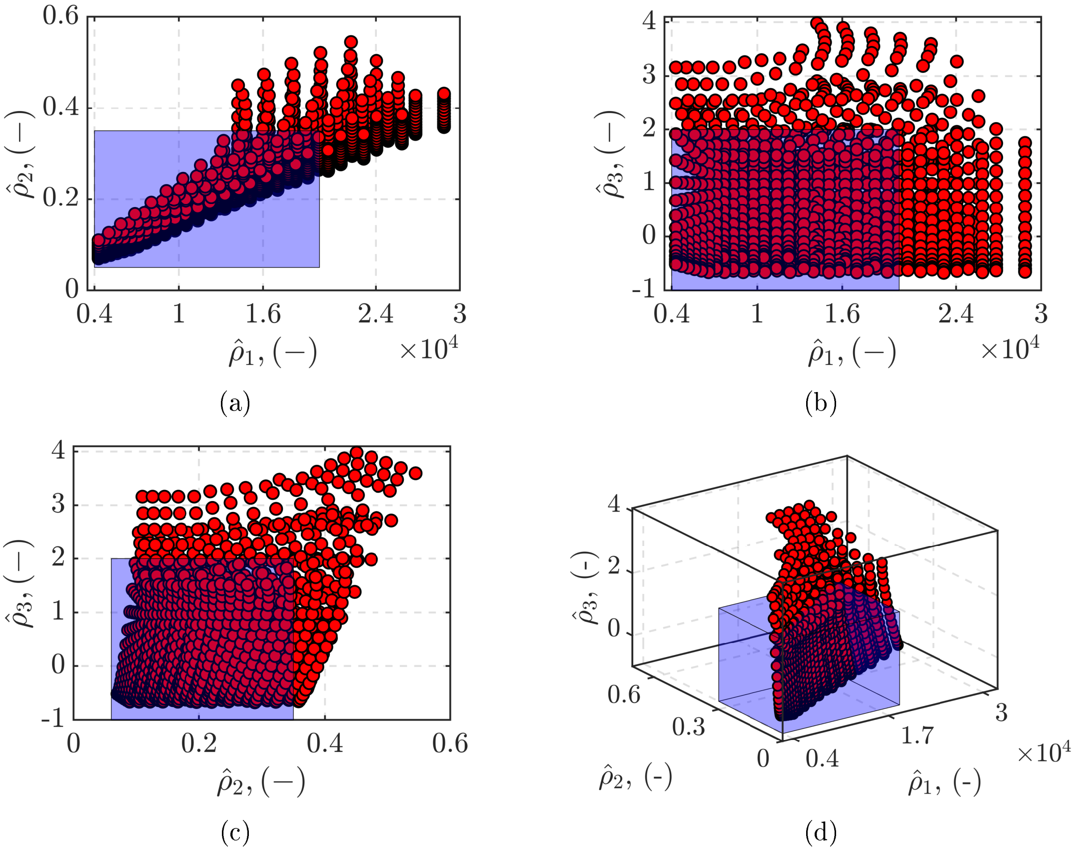

Figure 3.6: Reduced polytope $\hat{\Theta}_R$: (a) $\hat{\rho}_1$-$\hat{\rho}_2$; (b) $\hat{\rho}_1$-$\hat{\rho}_3$; (c) $\hat{\rho}_2$-$\hat{\rho}_3$; (d) 3D space.

By accounting for a certain degree of robustness to handle possible model uncertainties and external disturbances, the reduced dimension polytope, $\hat{\Theta}_{\mathrm{R}}$, is defined by the ranges: $\hat{\rho}_1 \in [0.4, 2] \times 10^4$, $\hat{\rho}_2 \in [0.05, 0.35]$, and $\hat{\rho}_3 \in [-1, 2]$, as in Figure 3.6.

3.3.3 Controller Synthesis Results

The polytopic controller synthesis is formulated as the solution of the optimization problem in Propositions 3.3-3.4, by imposing the closed-loop performances defined in Section 3.3.1 at each vertex of the polytope. The polytope is defined through the reduced scheduling functions' ranges of variation, identified in Section 3.3.2. The control design results, discussed in this section, correspond to the final step of the iterative design process that allowed optimizing the dimensions of the polytope.

Remark 3.8 (Numerical Conditioning)
As discussed in [PV+11], the Feasibility LMIs conditions in Equation (3.11) *are solved to find an optimal performance level, γ^*. In order to improve the numerical conditioning of the optimization, the conditions in Equation* (3.11) *are recomputed a second time, by imposing:*

$$\gamma = \gamma^* \left(1 + \zeta/100\right); \qquad \textit{and} \qquad \begin{bmatrix} X & \varepsilon I_{n_{x\mathrm{P}}} \\ \varepsilon I_{n_{x\mathrm{P}}} & Y \end{bmatrix} \succ 0$$

where $\zeta > 0$ is a tolerance percentage.
Thus, the recomputed optimization relies on the maximization of $\varepsilon > 0$. In this way, the minimal eigenvalues of XY are maximized, avoiding bad conditioning related to the inversion of M and N during the controller Reconstruction in Proposition 3.4.

The LPV/$\mathcal{H}_\infty$ polytopic design, performed by selecting $\zeta = 5$ and imposing a 5% tolerance level, provides an $\mathcal{H}_\infty$ performance level, $\gamma_\infty = 5.8$. The results are investigated in the frequency domain and are shown in Figures 3.7-3.8. Each figure represents a specific closed-loop

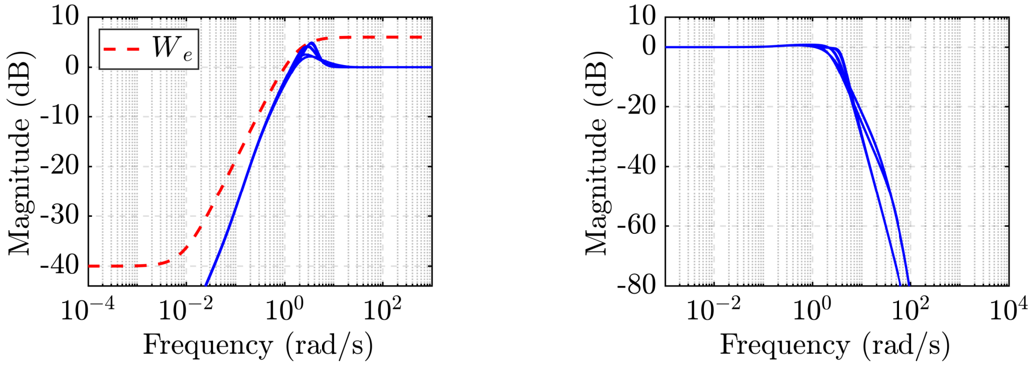

(a) (b)

Figure 3.7: Polytopic design results: (a) Sensitivity functions; (b) Complementary Sensitivity functions.

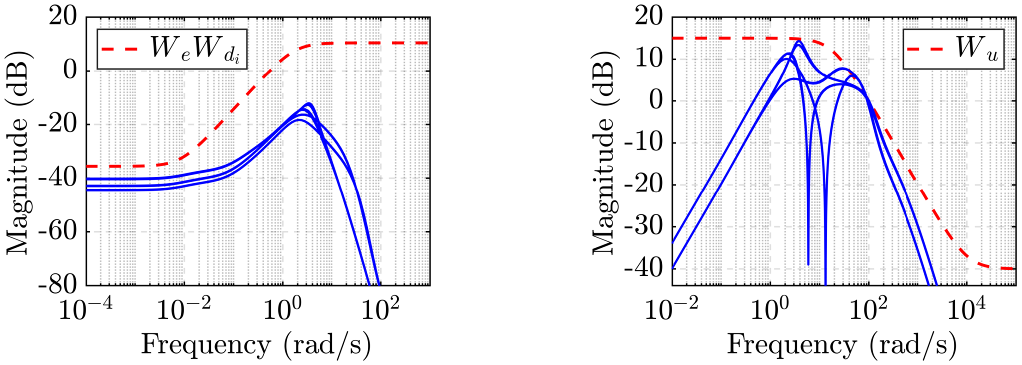

(a) (b)

Figure 3.8: Polytopic design results: (a) Plant Sensitivity functions; (b) Controller Sensitivity functions.

property of the system, evaluated at each of the eight vertex conditions of the polytope (blue lines). As a first observation, Figure 3.7(a) shows how the peaks of the output Sensitivity functions, $S_y = \frac{e}{r}$, remain ≤ 6 dB for each curve, ensuring reliable robustness margins at the vertices of the polytope. The transient dynamics of the system tends to be slightly less responsive due to the LMIs optimization that satisfies simultaneously the frequency requirements at each flight condition. However, the employment of the pair of weighting functions, (W_e, W_r), successfully imposes a reasonable bandwidth to the output Sensitivity functions and considerably improves the low-frequency disturbance rejection capability of the system, as shown through the Plant Sensitive functions, $S_y G = \frac{e}{d_i}$, in Figure 3.8(a). The latter property is fundamental to guaranteeing the controller can handle not only the uncertainties introduced during the modeling and approximation procedures, but especially external disturbances affecting the operating conditions of the projectile (e.g. wind contributions).

Similarly, the polytopic design provides reliable high-frequency noise attenuation to handle possible distortions affecting the measurements, as shown in Figure 3.7(b). Indeed, the peaks of the Complementary Sensitivity functions are maintained at ≤ 1 dB. Concerning the performances imposed on the control effort by the weighting function, W_u, the Controller Sensitivity functions, $KS_y = \frac{\dot{\delta}_{q,\text{cmd}}}{r}$, respect the limitations at all the flight conditions, both in terms of the operating bandwidth and in terms of the low-frequency steady-state amplitude, as shown in Figure 3.8(b). The presence of the reference model increases the effort required by the actuators to provide the desired performance, but the limitations guarantee considerable margins from saturation occurrences.

As discussed in Section 3.2.3.3, the solution of the design corresponds to a set of LTI controllers, $K_{\hat{\theta}_i}$, with $i = 1, \cdots, 8$. In terms of implementation, for any combinations of the scheduling functions' values belonging to the polytope, the LPV polytopic controller, $K_{\text{PY}}(\hat{\boldsymbol{\rho}})$, is obtained through the convex interpolation, $\mu_{\hat{\theta}_i}$, of the set of LTI vertices controllers as:

$$K_{\text{PY}}(\hat{\boldsymbol{\rho}}) = \sum_{i=1}^{8} \mu_{\hat{\theta}_i}(\hat{\boldsymbol{\rho}}) K_{\hat{\theta}_i} \qquad \text{with:} \quad \sum_{i=1}^{8} \mu_{\hat{\theta}_i}(\hat{\boldsymbol{\rho}}) = 1.$$

3.4 Grid-Based Controller Design

This section is dedicated to the synthesis of the grid-based LPV controller, K_{GR}, based on the projectile pitch channel quasi-LPV model derived in Section 2.3.2 of Chapter 2. The design objectives are presented first to derive the generalized scheme employed in the controller synthesis. The synthesis directly addresses the flight envelope defined by the scheduling variables' ranges of variation: $\alpha \in [0, 16]$ deg, $V \in [160, 280]$ m/s, and $h \in [1, 15]$ km.

The grid-based design relies on the resolution of the LMIs optimization, formulated in Theorem 3.3, at each flight point belonging to the selected design grid. The computational complexity affecting the optimization performance tends to exponentially increase with the number of the grid points, n_{g}, and the number of scheduling variables, n_ρ, as $\mathcal{O}(n_{\text{g}}^{n_\rho})$, as discussed in Section 3.2.2.1. Furthermore, no clear guidelines are provided in the selection of the grid points and the density level of the grid to ensure stability in the transient between two flight conditions, as explained in Remark 3.3. As a consequence, the projectile flight envelope is extensively investigated, aiming to identify the most critical flight conditions affecting the stability of the projectile dynamics. The core idea is to reduce the complexity of the optimization problem by restricting the grid points selection to the critical areas of the flight envelope. Additionally, the selection of the basis functions employed in the definition of the LMIs problem is analyzed, trying to accurately characterize the dependence of the projectile stability on each scheduling variable. Indeed, no general criteria are provided either for this latter aspect, as mentioned in Remark 3.2.

Finally, the results of the controller synthesis provide an overview of the corresponding closed-loop frequency properties.

3.4.1 Grid-Based Design Scheme

The overall design scheme is shown in Figure 3.9. Complying with the formulation in Equation (3.7), the generalized plant, Σ_{P}, includes the projectile pitch channel quasi-LPV model, Σ_{GR}, summarized in Equations (2.40)-(2.41) of Chapter 2, and accounting for load factor measurements. Additionally, Σ_{P} includes the second-order actuator model in Equation (1.39), and a set of weighing functions that shapes the $\mathcal{H}_\infty$ frequency properties of the desired closed-loop system. The first-order weighting functions, W_e and W_u, target respectively the system tracking capability and the control effort performances. As for the polytopic case, the core objective consists of the minimization of the tracking error, $e = r - \alpha$, where the reference signal, r, is defined as an optimal AoA trajectory for LDR optimization purposes. The weighting functions are parameterized as follows:

$$W_e(s) = \frac{s/M_e + \omega_e}{s + \omega_e \epsilon_e}; \qquad\qquad W_u(s) = \frac{s + \omega_u/M_u}{\epsilon_u s + \omega_u}$$

where the high-frequency gain, $M_e = 2$, the low-frequency gain, $\epsilon_e = 0.01$, and the crossover frequency, $\omega_e = 1$ rad/s, guarantee 6 dB of module margin, improving the robustness of the

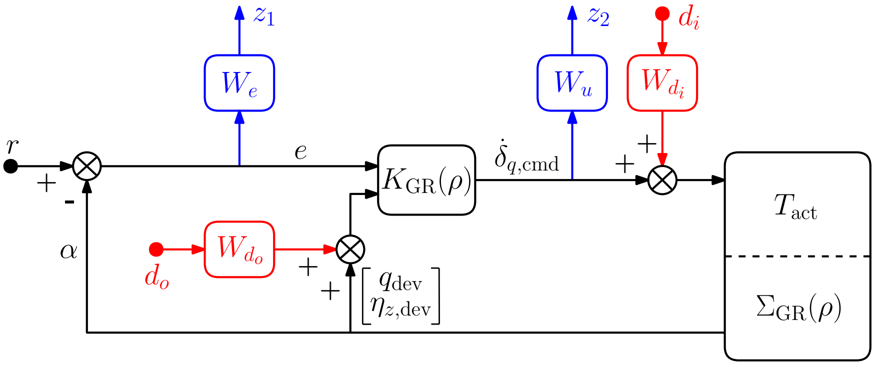

Figure 3.9: Grid-based design scheme architecture.

system, -40 dB of disturbance signals attenuation, and a steady-state tracking error $\leq 1\%$ at low frequency, respectively. Concerning the control signal, $\epsilon_u = 0.01$ and $\omega_u = 100$ rad/s provide an additional -40 dB of high-frequency noise attenuation, and an input bandwidth that complies with the actuator operating limitations. Finally, a low-frequency gain, $M_u = 3$, is imposed on the control signal amplitude.

Differently from the polytopic approach, the grid-based design relies on a parameter-dependent solution of the control problem in Proposition 3.2. At the expense of robust stability guarantees only around the design points instead of broader quadratic stability properties, the optimization can more optimally target each specific flight condition, providing higher computation performance. In this context, the tracking capability and the disturbance rejection of the system can be mutually handled by the single weighting function, W_e, avoiding the employment of an additional reference model/filter. However, the enhancement of the tracking capability may increase the sensitivity of the system to disturbance signals, thus a reliable trade-off has to be achieved avoiding the imposition of an excessive control effort and the consequent occurrence of possible canards stall regime.

Finally, constant weights, $W_{d_i} = 0.6$ and $W_{d_o} = 0.2$, are imposed on the input and output disturbance signals, d_i and d_o, respectively, to improve the controller disturbance rejection, and to satisfy the controller synthesis orthogonality conditions ([Wu95]). The observations discussed in Remark 3.7, concerning the limited performance related to the employment of parameter-independent weighting functions, apply also to the grid-based design.

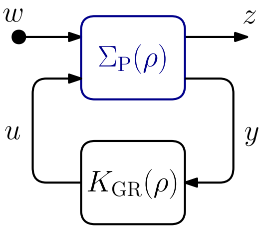

Figure 3.10: General grid-based control scheme configuration.

The generalized control architecture is presented in Figure 3.10, where the generalized state vector, $\boldsymbol{x}_{\mathrm{P}} = [\boldsymbol{x}^{\mathrm{T}}, \boldsymbol{x}_{\mathrm{act}}^{\mathrm{T}}, x_{W_e}, x_{W_u}]^{\mathrm{T}} \in \mathbb{R}^9$, of the open-loop plant, $\Sigma_{\mathrm{P}}(\boldsymbol{\rho})$, defined in Equation (3.7), accounts for the projectile quasi-LPV model, $\boldsymbol{x} = [\alpha, q_{\mathrm{dev}}, \delta_{q,\mathrm{dev}}]^{\mathrm{T}} \in \mathbb{R}^3$, the actuator dynamics, and the weighting functions. The generalized controlled output, $\boldsymbol{z} = [z_1, z_2]^{\mathrm{T}} \in \mathbb{R}^2$, includes the design objectives, while tracking error, off-equilibrium pitch rate, and off-equilibrium load factor, define the available measurements set, $\boldsymbol{y} = [e, q_{\mathrm{dev}}, \eta_{z,\mathrm{dev}}]^{\mathrm{T}} \in \mathbb{R}^3$. Finally, the control input, $u \in \mathbb{R}$, is the derivative of the commanded local pitch deflection, $\dot{\delta}_{q,\mathrm{cmd}}$, while the vector of exogenous input, $\boldsymbol{w} = [r, d_i, d_o]^{\mathrm{T}} \in \mathbb{R}^3$, includes the reference guidance AoA trajectory, and the input/output disturbance signals.

The generalized plant is evaluated at each grid point condition. The obtained set of n_{g} LTI systems is employed for the controller synthesis in the resolution of the LMIs problem formulated in Theorem 3.3.

3.4.2 Grid Design Analysis

The investigated grid-based control design relies on the conversion of an infinite-dimensional LMIs problem into a solvable SDP optimization. As discussed in Section 3.2.2.1, the conversion is based on two relaxation steps:

I. **Projection** of the infinite-dimensional decision variables into a finite set of basis functions, as in Theorem 3.1.

II. **Discretization (gridding)** of the scheduling variables space into a finite set of conditions, as in Proposition 3.1.

As a consequence, the proper formulation of the controller synthesis in Theorem 3.3 is based on the accurate selections of both the set of basis functions and the set of discretized conditions. However, as stated in Remarks 3.2-3.3, no precise general guidelines are provided for any of the selections, requiring the employment of more case-dependent approaches. Additionally, the computational complexity affecting the performance of the optimization tends to increase with the number of grid points, as $\mathcal{O}(n_{\mathrm{g}}^{n_\rho})$. Since the design guarantees robust stability only around the selected grid points, a compromise has to be reached between a reliable dimension of the grid, and the resulting complexity of the overall computation.

In order to improve the performance of the controller synthesis, an exhaustive analysis is developed, investigating the following aspects:

A. **Flight Envelope:** analyze the scheduling variables space to identify the most critical flight conditions affecting the stability properties of the projectile quasi-LPV pitch channel dynamics. The objective is to restrict the area of selection of the design grid points to those characterized by critical stability conditions. Additional considerations about the projectile optimal desired trajectory allow for a more accurate selection.

B. Optimization Performance: estimate the effect of the number of grid points, n_{g}, and basis functions selections on the computational complexity and on the performance of the controller synthesis optimization.

3.4.2.1 A. Flight Envelope Analysis

The identification of the critical areas of the flight envelope relies on the analysis of the pole-zero map of the projectile quasi-LPV model in Equations (2.40)-(2.41). The analysis targets the full ranges of variation of the scheduling variables: $\alpha \in [0, 16]$ deg, $V \in$ [160,

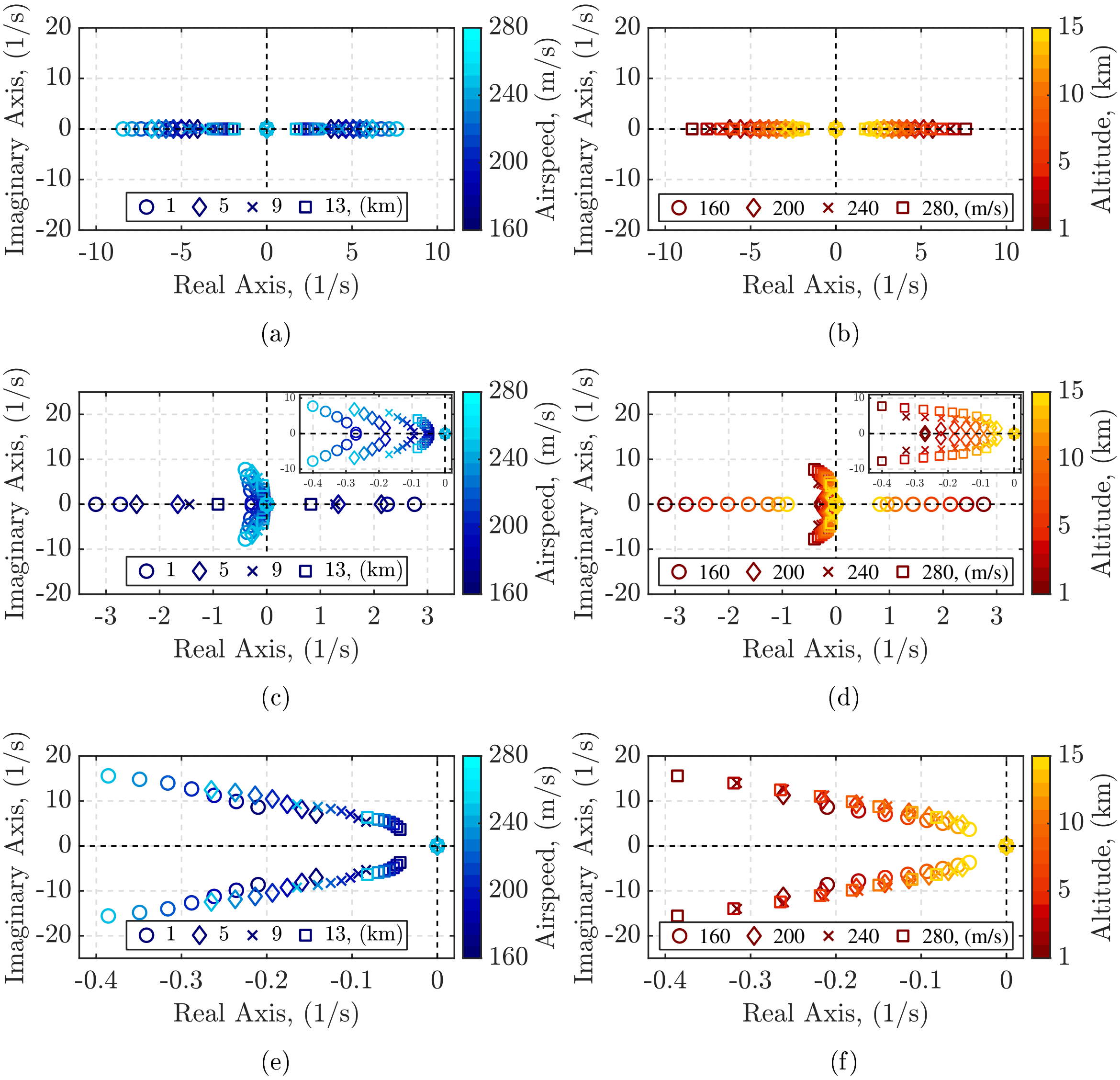

Figure 3.11: Dynamics dependence on the airspeed and altitude variations at: (a)-(b) $\alpha = 5$ deg, respectively; (c)-(d) $\alpha = 9$, respectively; (e)-(f) $\alpha = 13$ deg, respectively.

280] m/s, and $h \in [1,\ 15]$ km, assuming the corresponding discretization steps: $\Delta\alpha = 1$ deg, $\Delta V = 5$ m/s, and $\Delta h = 500$ m, for a total of $n_{\mathrm{g}} = 12750$ grid points. The results in Figure 3.11 provide samples of the complete analysis at selected flight conditions. In particular, Figures 3.11(a)(c)(e) show how the system dynamics varies at certain altitude levels and as a continuous function of the airspeed, respectively, at $\alpha = 5$ deg, at $\alpha = 9$ deg, and $\alpha = 13$ deg. The same results are provided also in Figures 3.11(b)(d)(f), where the attention is focused on the stability dependence on the continuous altitude variation.

The results are employed to derive a 3D stability envelope in the discretized space of the scheduling variables, as shown in Figure 3.12. The stability map targets only a subset of the AoA range, $\alpha \in [5, 10]$ deg, characterized by the transition from unstable to stable dynamics. Indeed, for $\alpha \geq 10$ deg, the system is stable at any $(V,\ h)$ conditions, while for $\alpha \leq 5$ deg, the system is always unstable. As a general result, the system dynamics tends toward a progressively more unstable behavior for decreasing values of the airspeed and altitude levels. As expected, the AoA variation has the most relevant effect on the system stability.

Remark 3.9
The pole-zero stability evaluation relies on the quasi-LPV model of the projectile pitch channel dynamics. Thus, the accuracy of the results in representing the dynamics of the original nonlinear system is limited to the domain of reliability of the quasi-LPV model. However, the dynamics stability transition shown in Figure 3.12 is coherent with the stability considerations discussed in Section 1.3.2.2 of Chapter 1 through the analysis of the aerodynamic pitching moment CFD data.

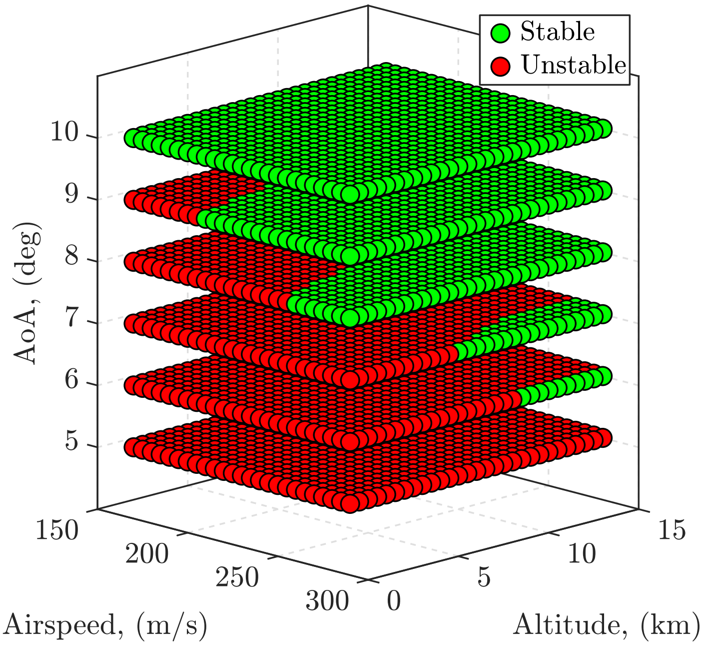

Figure 3.12: 3D discretized system's stability envelope.

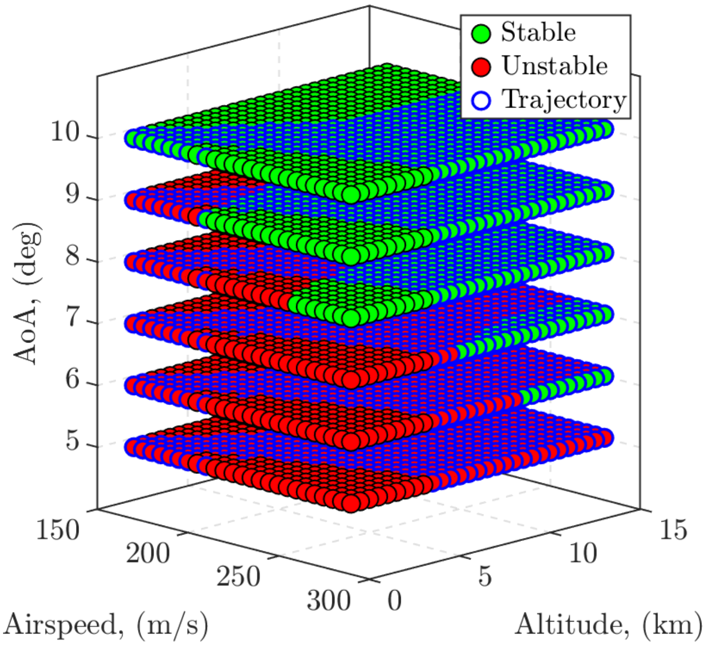

Figure 3.13: Reduced stability envelope based on trajectory considerations.

In order to further restrict the area of selection of the design points, trajectory performance restrictions can be employed. In the polytope mapping procedure developed in Section 2.4.2 of Chapter 2, the **Selection** step consisted of the definition of specific trajectory criteria for the identification of the new convex space. The objective was to restrict the investigated flight envelope to those areas that respect the physical constraints characterizing the scheduling variables across a desired projectile gliding trajectory. By applying the same criteria to the obtained stability results, the critical flight envelope can be reduced, as in Figure 3.13.

3.4.2.2 B. Optimization Performance Analysis

The second part of the analysis aims to estimate the impact of the number of selected grid points, n_g, on the optimization performance and on the computational time, t_eval. Additionally, the analysis investigates the relevance of the basis functions, $f_i(\boldsymbol{\rho})$ and $g_i(\boldsymbol{\rho})$ with $i = [1, \ldots, n_\text{B}]$, selected for each scheduling variable to define the Lyapunov functions, $X(\boldsymbol{\rho})$ and $Y(\boldsymbol{\rho})$, parameterized as in Equation (3.8).

Assumption 3.3
In order to simplify the computation, the same set of basis functions is employed to characterize both $X(\boldsymbol{\rho})$ and $Y(\boldsymbol{\rho})$ parameterizations, thus: $f_i(\boldsymbol{\rho}) = g_i(\boldsymbol{\rho})$ with $i = [1, \ldots, n_\text{B}]$.

The analysis consists of the resolution of the LPV $\mathcal{H}_\infty$ controller synthesis problem in Proposition 3.2, assuming the generalized design scheme defined in Section 3.4.1. The optimization problem is formulated by accounting for one single parameter variation at a time, imposing frozen values for the remaining ones. Thus, three individual analyses are performed, as summarized in Table 3.1.

Table 3.1: Optimization analyses conditions.

Analyzed Variable	$\boldsymbol{\alpha}$ **(deg)**	$\boldsymbol{V}$ **(m/s)**	$\boldsymbol{h}$ **(km)**
$\boldsymbol{\alpha}$	$\in [0, 16]$	230	7
$\boldsymbol{V}$	9	$\in [160, 280]$	7
$\boldsymbol{h}$	9	230	$\in [1, 15]$

For each analyzed variable, the $\mathcal{H}_\infty$ optimization is evaluated by progressively increasing the number of grid points that discretize the corresponding variation range in Table 3.1. At each increment of n_g, the discretized set of grid points is augmented by randomly selecting a new point in the range of variation. The resulting performance level, γ_∞, is employed as a comparison index to estimate the impact of the n_g increment on the quality of the optimization solution. The computation is repeated several times, n_exp, for statistical relevance, accounting for different permutations of the same set of grid points. The average value of each full repetitions set is shown as a global result.

In order to account for the relevance of the basis functions, the full procedure is repeated by employing different sets, $\boldsymbol{f}_\mathrm{B}$, for each scheduling variable, selected based on the mimic principle. The evaluation of the computational time at each iteration of the process provides an index of the optimization complexity increment generated by the grid points and basis functions' selections. The overall procedure is detailed in Algorithm 3.

Algorithm 3 Optimization Performance Analysis

```
For any $\rho \in [\alpha, V, h]$:
    Select the initial analysis range: $\mathrm{R}_\rho = [\rho_\mathrm{min}, \rho_\mathrm{max}]$.
    Select constant values for the remaining variables.

    For $j = [1, \dots, n_\mathrm{exp}]$:

        For $n_\mathrm{g} = [3, \dots, 13]$:
            Select a new random grid point: $\texttt{rand}(\rho_i) \in [\rho_\mathrm{min}, \rho_\mathrm{max}]$.
            Redefine $\mathrm{R}_\rho = [\mathrm{R}_\rho, \texttt{rand}(\rho_i)]$.
            For any set $\boldsymbol{f}_\mathrm{B}$:
                $[t_\mathrm{eval}, \gamma_\infty] = f[\text{Controller Synthesis}](\mathrm{R}_\rho, \boldsymbol{f}_\mathrm{B})$, as in Theorem 3.3.
            end.
        end.
        Reset the initial range: $\mathrm{R}_\rho = [\rho_\mathrm{min}, \rho_\mathrm{max}]$.
    end.
end.
```

The sets of basis functions investigated for each scheduling variable are listed respectively in Tables 3.2-3.3-3.4.

Table 3.2: Basis functions sets: AoA.

Basis Set ($\boldsymbol{\alpha}$)	$\boldsymbol{f}_1$	$\boldsymbol{f}_2$	$\boldsymbol{f}_3$
$\boldsymbol{f}_{\mathrm{B}_1}$	1	α	–
$\boldsymbol{f}_{\mathrm{B}_2}$	1	α	$\sin\alpha$
$\boldsymbol{f}_{\mathrm{B}_3}$	1	α	$\cos\alpha$
$\boldsymbol{f}_{\mathrm{B}_4}$	1	$\sin\alpha$	$\cos\alpha$

Table 3.3: Basis functions sets: airspeed.

Basis Set ($\boldsymbol{V}$)	$\boldsymbol{f}_1$	$\boldsymbol{f}_2$	$\boldsymbol{f}_3$
$\boldsymbol{f}_{\mathrm{B}_1}$	1	V	–
$\boldsymbol{f}_{\mathrm{B}_2}$	1	V	$1/V$
$\boldsymbol{f}_{\mathrm{B}_3}$	1	V	V^2

Table 3.4: Basis functions sets: altitude.

Basis Set ($\boldsymbol{h}$)	$\boldsymbol{f}_1$	$\boldsymbol{f}_2$	$\boldsymbol{f}_3$
$\boldsymbol{f}_{\mathrm{B}_1}$	1	h	–
$\boldsymbol{f}_{\mathrm{B}_2}$	1	h	$1/h$
$\boldsymbol{f}_{\mathrm{B}_3}$	1	h	h^2

The results of the analyses are presented in Figure 3.14. In particular, Figures 3.14(a)(c)(e) show the average γ_∞ performance level obtained across $n_{\mathrm{exp}} = 100$ different optimizations on each basis functions set, $\boldsymbol{f}_{\mathrm{B}_i}$, respectively performed on the α, V, and h variation ranges. The corresponding average computational time curves are shown in Figures 3.14(b)(d)(f). As a first general observation, t_{eval} tends to linearly grow with increasing values of n_{g} in all the optimization scenarios. However, the number, n_{B}, and the complexity of the basis functions set also play a relevant role in terms of performance, since they can easily double the time required to achieve an optimal solution.

AoA Analysis. Concerning the performance level, the employment of the basis functions sets, $\boldsymbol{f}_{\mathrm{B}_3}$ and $\boldsymbol{f}_{\mathrm{B}_4}$ in Table 3.2, provides nearly the same results, as shown in Figure 3.14(a). The γ_∞ values increase when the least complex basis set, $\boldsymbol{f}_{\mathrm{B}_1}$, is considered, while the best optimization results rely on $\boldsymbol{f}_{\mathrm{B}_2}$. Coherently with the expectations, $\boldsymbol{f}_{\mathrm{B}_3}$ and $\boldsymbol{f}_{\mathrm{B}_4}$ show a linear increase of the γ_∞ index w.r.t. n_{g}, since it directly affects the number of LMIs to be solved by the optimization. However, due to the highly nonlinear parameterization, the same dependence is not clearly highlighted by the curves related to $\boldsymbol{f}_{\mathrm{B}_1}$ and $\boldsymbol{f}_{\mathrm{B}_2}$. Thus, a global intuition on the relevance of n_{g} to the optimization problem is not reachable. In terms of computational complexity, the t_{eval} related to $\boldsymbol{f}_{\mathrm{B}_2}$ in Figure 3.14(b) is coherently more than twice larger than the simplest set $\boldsymbol{f}_{\mathrm{B}_1}$, while $\boldsymbol{f}_{\mathrm{B}_3}$ and $\boldsymbol{f}_{\mathrm{B}_4}$ seem to offer a preferable trade-off between performance and computational time.

Airspeed Analysis. The curves in Figure 3.14(c) and Figure 3.14(d) highlight a similar behavior for γ_∞ and t_{eval} compared to the AoA case. Indeed, the simplest set, $\boldsymbol{f}_{\mathrm{B}_1}$ in Table 3.3, is characterized by a linear $\gamma_\infty/n_{\mathrm{g}}$ relation, and a lower computational complexity, respectively. The higher nonlinear parameterization selected for the basis functions sets, $\boldsymbol{f}_{\mathrm{B}_2}$ and $\boldsymbol{f}_{\mathrm{B}_3}$, results in increasingly higher but less predictable performance levels. Accordingly, the computational time necessary to perform the optimization is twice as large as the linear case. As a general observation, γ_∞ achieves the desired objective, $0 < \gamma_\infty < 1$, at almost all the conditions.

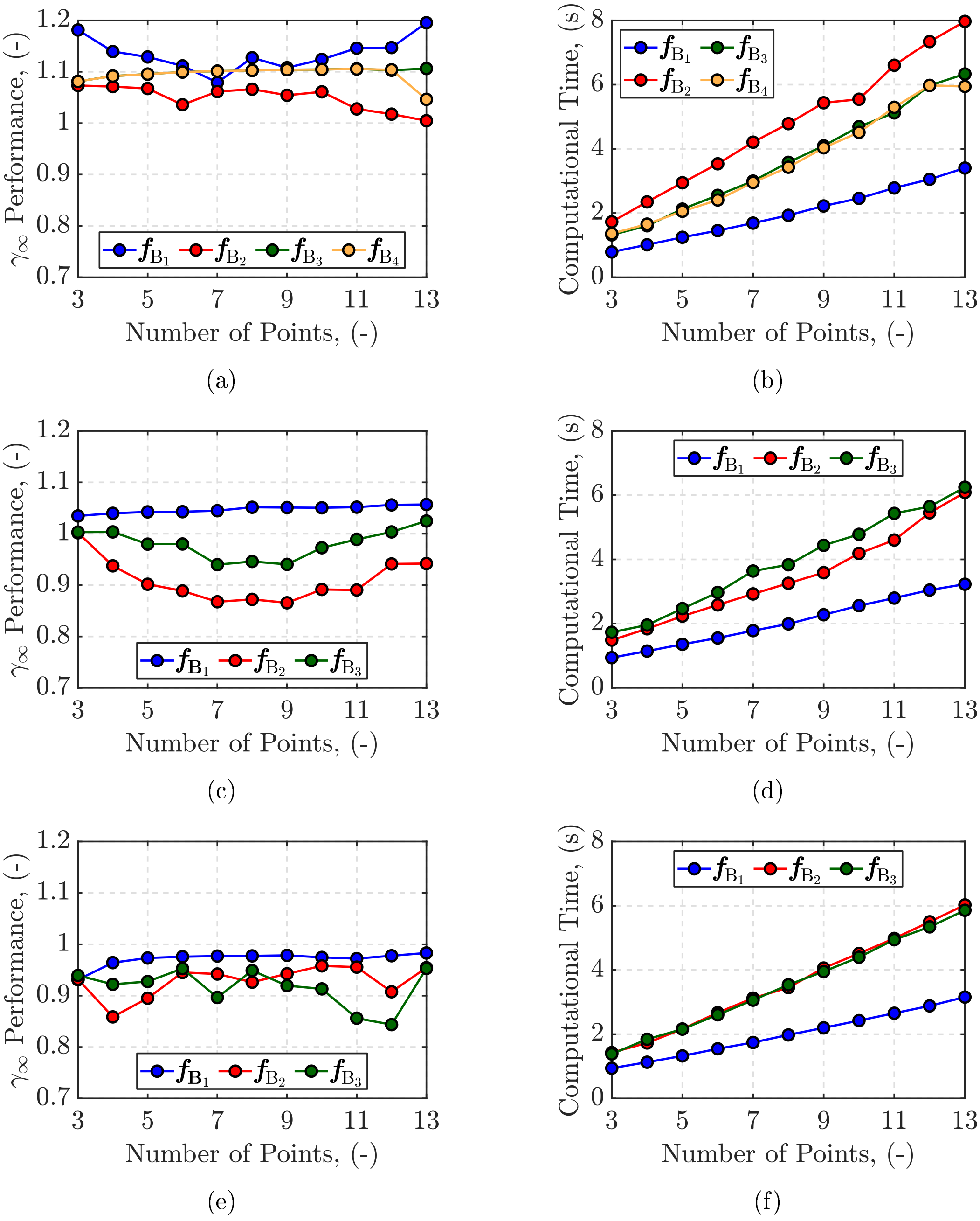

(a) (b) (c) (d) (e) (f)

Figure 3.14: Performance level and computational time dependence on the grid points and basis functions selections: (a)-(b) AoA analysis, respectively; (c)-(d) airspeed analysis, respectively; (e)-(f) altitude analysis, respectively.

Altitude Analysis. The altitude analysis results in Figure 3.14(e) provide the highest optimization performance, ensuring $\gamma_\infty < 0$ for all the sets of basis functions. As for the airspeed case, $\boldsymbol{f}_{\mathrm{B}_1}$ is the only set characterized by a linear performance dependence on the n_{g} increment. Coherently, the computational complexity is minimized only in the linear case.

3.4.3 Controller Synthesis

The grid analysis provides a clearer understanding of the system properties and the relevance of each scheduling variable on the overall controller optimization. The results allow for reducing the computational complexity of the process and improving the performance by focusing the design on a critical subset of the flight envelope.

Considering both the γ_∞ and t_{eval} performances in Figure 3.14, the ranges of each scheduling variable are discretized into following finite sets of flight conditions: $\boldsymbol{\alpha}_{\mathrm{grid}} = [1, 5, 8, 13]$ deg, $\boldsymbol{V}_{\mathrm{grid}} = [180, 200, 240, 270]$ m/s, and $\boldsymbol{h}_{\mathrm{grid}} = [3, 6, 9, 12, 14.5]$ km. Additionally, the grid-based design accounts for the variation rates of the scheduling variables, as mentioned in Remark 3.1. The stricter the conditions imposed to variation rates, the higher the performance of the optimization[1]. The estimation of the scheduling variables max/min variation rates relies on reference gliding phase trajectory simulations: $\dot{\alpha}_{\mathrm{grid}} \in [-30, 30]$ deg/s, $\dot{V}_{\mathrm{grid}} \in [-50, 50]$ m/s^2, and $\dot{h}_{\mathrm{grid}} \in [-100, 100]$ m/s.

The controller synthesis is performed using the LPVTools MATLAB Toolbox ([HSP15]), employing the LMI-Lab optimization solver ([Gah+94]).

Remark 3.10
A relevant functionality limitation of LPVTools concerns the possibility of defining only rectangular grids of discretized scheduling variables. Thus, given two scheduling variables' discretized sets, $\boldsymbol{a} = [a_1, \ldots, a_N]$ and $\boldsymbol{b} = [b_1, \ldots, b_M]$, the corresponding grid is generated as the Cartesian product, $\boldsymbol{a} \times \boldsymbol{b} = \{(a_i, b_j) \mid a_i \in \boldsymbol{a} \text{ and } b_j \in \boldsymbol{b}\}$. As a consequence, the selection and the number of flight conditions are partially limited by the definition of the grid, introducing a certain level of conservatism and unwanted complexity in the controller synthesis.

Based on the results of the grid analyses and accounting for the limitation discussed in Remark 3.10, the Cartesian product between the discretized scheduling variables sets generates a design grid, $\Xi = \boldsymbol{\alpha}_{\mathrm{grid}} \times \boldsymbol{V}_{\mathrm{grid}} \times \boldsymbol{h}_{\mathrm{grid}}$, of $n_{\mathrm{g}} = 80$ flight points, unevenly distributed across the 3D flight domain. The employment of unevenly distributed grid points, targeting the most critical areas of the operating domain, is expected to improve the stability guarantees of the controller synthesis. Concerning the selection of the basis functions, the compromise between performance and complexity leads to the following definition of the parameterized Lyapunov functions in Equation (3.8), accounting for the simplification in Assumption 3.3:

$$X(\boldsymbol{\rho}) = Y(\boldsymbol{\rho}) = X_0 + X_{\alpha,1} \sin\alpha + X_{\alpha,2} \cos\alpha + X_V V + X_h h.$$

---

[1] The polytopic design allows for an infinite variation of each scheduling variables since no limitations are imposed in the LMIs formulation, providing more conservative results but higher stability guarantees.

The selection favored the basis functions' sets that provide a more linear and predictable γ_∞ and t_{eval} dependence w.r.t. the n_{g} increment.

The LPV/$\mathcal{H}_\infty$ grid-based controller optimization provides an overall performance level of $\gamma_\infty = 1.4$, computed in $t_{\text{eval}} \approx 15$ min. The results in the frequency domain are presented in Figure 3.15. Each figure provides a frequency property of the closed-loop system, evaluated at each of the selected n_{g} grid points. The output Sensitivity functions, $S_y = \frac{e}{r}$, in Figure 3.15(a), show reliable tracking performance and robustness margins since the maximum gain of the functions remains always < 6 dB, as desired.

However, the employment of an individual filter, W_e, generates undesired low-frequency peaks > 0 dB of the closed-loop system disturbance rejection properties, as shown in Figure 3.15(c) through the computation of the Plant Sensitivity functions, $S_yG = \frac{e}{d_i}$. The higher responsiveness of the system generates a larger sensitivity to external disturbances and possible overshoots in the system response during time domain simulations. Since the fidelity of the projectile quasi-LPV model is limited to specific ranges of the scheduling variables, an excessive overshoot in the response might bring the system outside the domain of fidelity. In order to

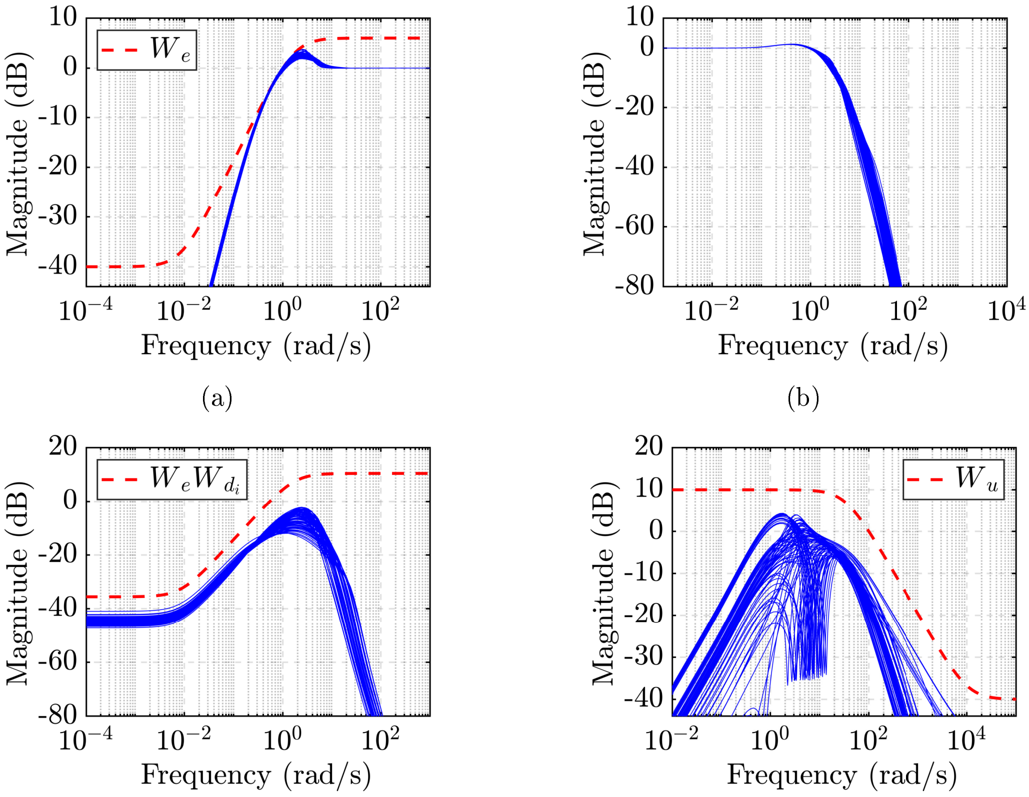

(a) (b) (c) (d)

Figure 3.15: Grid-based design results: (a) Sensitivity functions; (b) Complementary Sensitivity functions; (c) Plant Sensitivity functions; (d) Controller Sensitivity functions.

minimize this effect, the responsiveness of the controller has to be limited. The Controller Sensitivity functions, $KS_y = \frac{\dot{\delta}_{q,\mathrm{cmd}}}{r}$, in Figure 3.15(d) are coherently bounded, both in terms of operating bandwidth and low-frequency gain.

Remark 3.11

The formulation of the grid-based control synthesis in Theorem 3.3 accounts for both scheduling variables' ranges and rates of variation, improving the optimization performance. Thus, the resulting controller in Proposition 3.2 also depends on the variables' rates of variation, $\dot{\boldsymbol{\rho}}$. As a consequence, the LPV controller is evaluated not only across the discretized set of scheduling variables but also across the specified range of variables' variation rates, significantly increasing the resulting number of LTI local controllers to be implemented.

In order to minimize the implementation complexity, a possible solution to Remark 3.11 consists of interpolating the obtained LPV controller across the discretized space of variation of the scheduling variables rate, $\dot{\boldsymbol{\rho}}$. The interpolation on a single grid point (generally the origin, $\dot{\boldsymbol{\rho}} = 0$) eliminates the dependence of the controller formulation on the scheduling variables rates. As a drawback, the stability and performance improvements related to the discretization of $\dot{\boldsymbol{\rho}}$ are neglected. The resulting LPV controller, computed as in Proposition 3.2, is evaluated at each of the n_g scheduling variables' conditions, generating a corresponding set of LTI local realizations to be interpolated online.

3.5 Concluding Remarks

In this chapter, different formulations have been discussed concerning the design of LPV-based controllers for the projectile pitch channel dynamics. The LPV polytopic approach exploits the advantages of the affine model-parameters relation characterizing the system. The controller synthesis is formulated as an LMIs optimization problem where the conditions have to be satisfied only at the vertices of the convex space defined by the ranges of variation of the scheduling functions. The main advantages of the approach rely on the reduced number of conditions to be simultaneously satisfied and on the higher guarantees of quadratic stability across the entire domain covered by the convex polytope. The main drawback is represented by the conservatism that affects the optimization process since the solution is based on a parameter-independent Lyapunov function. In order to improve the optimization performance, a dedicated analysis is developed to optimize the dimensions of the polytope, neglecting any operating conditions that do not belong to the projectile flight envelope. The analysis allowed defining a reduced polytope, $\hat{\Theta}_\mathrm{R}$, by adjusting the ranges of variation of the scheduling functions as: $\hat{\rho}_1 \in [0.4,\, 2] \times 10^4$, $\hat{\rho}_2 \in [0.05,\, 0.35]$, and $\hat{\rho}_3 \in [-1,\, 2]$. The resulting polytopic controller design is based on the $\mathcal{H}_\infty$ approach, aiming to enhance the robustness of the system to internal and external sources of disturbance.

The second approach relies on the discretization (gridding) of the space of variation of the scheduling variables into a finite grid of flight conditions. The LMIs optimization defining the controller synthesis is computed at each of the selected design points. As a consequence, the computational complexity affecting the optimization is highly dependent on the grid definition. However, the solution of the LMIs problem is based on parameter-dependent Lyapunov functions, providing a higher optimization performance. Additionally, the formulation accounts for the variation rate of each scheduling variable, reducing the conservatism affecting the optimization. In order to limit the computational complexity, an exhaustive analysis on the discretized flight envelope targets the stability properties of the system and the desired trajectory performance. The analysis aims at finding an optimal grid dimension as a trade-off between computational complexity and stability guarantees. Additionally, the parameterization of the Lyapunov functions is investigated to properly model the dependence of the functions on each scheduling variable. The results of the analysis provide the following discretized ranges of variations: $\boldsymbol{\alpha}_{\text{grid}} = [1, 5, 8, 13]$ deg, $\boldsymbol{V}_{\text{grid}} = [180, 200, 240, 270]$ m/s, and $\boldsymbol{h}_{\text{grid}} = [3, 6, 9, 12, 14.5]$ km, while the Lyapunov functions have been formulated as:

$$X(\boldsymbol{\rho}) = Y(\boldsymbol{\rho}) = X_0 + X_{\alpha,1} \sin\alpha + X_{\alpha,2} \cos\alpha + X_V V + X_h h.$$

The controller LPV/ $\mathcal{H}_\infty$ design has been computed on the resulting gridded space, Ξ, consisting of $n_{\text{g}} = 80$ flight points. Additionally, the rates of variation of each scheduling variable have been defined as: $\dot{\alpha}_{\text{grid}} \in [-30, 30]$ deg/s, $\dot{V}_{\text{grid}} = [-50, 50]$ m/s^2, and $\dot{h}_{\text{grid}} = [-100, 100]$ m/s.

As a first form of comparison, both the approaches required the development of dedicated processes, aiming to improve the optimization performance. The polytopic design was based on an additional modeling approximation that allowed converting the quasi-LPV projectile pitch channel dynamics into a polytopic model, possibly introducing unwanted sources of uncertainties. However, the polytopic approach guarantees higher robust stability properties across the entire convex space defined by the parameter ranges of variation. Concerning the grid-based design, robust stability guarantees are provided only in the vicinity of the design points. On the other side, the expected higher optimization performances are confirmed both through the γ_∞ results, and by the reduced control effort required to the actuators. From the complexity perspective, the controller synthesis is based on the selection of several tuning parameters (n_{g}, $\boldsymbol{f}_{\text{B}}$), requiring the development of a dedicated time-consuming analysis. Finally, the implementation of the grid-based controller, K_{GR}, relies on the interpolation of 80 LTI local realizations, compared to the reduced 8 LTI local realizations required by the polytopic controller, K_{PY}.

The performance and robustness properties of the two controllers will be tested through time domain simulations in the next chapter, accounting for different sources of external disturbances.

Chapter 4

Controller Performance and Robustness Assessment

Contents

4.1 Introduction

Standard control design procedures target the nominal stability (NS) and performance (NP) properties of the closed-loop system, Σ_{CL}, generated by the interconnection between the plant dynamics and the designed controller. However, several sources of disturbance can deviate the dynamics of the system from its nominal conditions, degrading the capability of the controller to stabilize the resulting perturbed system. Design approaches in the framework of robust control tend to enhance the robustness of the controller in handling disturbance effects up to a certain level. The $\mathcal{H}_\infty$ design presented in Chapter 3 targets this objective by shaping the closed-loop properties of the system. A first qualitative analysis concerning the robustness of the LPV control design has been provided in Sections 3.3.3-3.4.3, respectively for the polytopic and the grid-based controller, through the computation of the sensitivity functions.

The assessment of the system robust stability (RS) and performance (RP), represents a fundamental design step, generally performed a posteriori to validate the controller synthesis. A standard approach relies on the computation of the stability margins related to the nominal loop transfer functions, $L(s)$. The stability margins measure to which extent the gain (GM), and phase (PM) of $L(s)$ can be deviated by input/output perturbation signals, preserving the closed-loop stability. Disk margins analysis (DKM) can additionally account for simultaneous gain/phase perturbations, while multi-loop disk margins consider the simultaneous perturbations affecting the different channels dynamics, when dealing with MIMO systems ([SPG20]). Nevertheless, the stability margins provide only global necessary but not sufficient conditions to assess the robustness of the closed-loop system dynamics, and might fail in the identification of the worst-case operating conditions. System perturbations can be addressed by augmenting the nominal model with structured or unstructured uncertainty dynamics ([SP05]). When the uncertainty ranges associated with specific parameters are known, the μ-sensitivity analysis can be employed to estimate the level of uncertainties the close-loop system can tolerate for each investigated parameter. Differently, unmodeled dynamics fall into the unstructured type of uncertainty, and they are generally clustered into a common uncertain model. The results are generally more conservative compared to the structured case.

This chapter investigates the robust stability (RS) and performance (RP) of the LPV polytopic and grid-based controllers of the projectile pitch channel dynamics. First, a global estimation is provided through a standard stability margins analysis. Then, the design of the uncertain system accounts for the perturbation of a subset of the plant parameters. A μ-sensitivity analysis identifies the relative tolerance of the system to each parameter uncertainty range. Finally, the performances of the controller are tested in trajectory tracking simulation scenarios, where the effects of wind disturbance signals are considered.

The chapter is structured in the following sections:

S4.2: presents a global stability margins analysis targeting the flight conditions at the vertices of the polytope and across the design grid, respectively concerning the polytopic and the grid-based controller. Disk margins and multi-loop analysis are employed to account for both simultaneous GM/PM variations across the different channels dynamics.

S4.3: discusses the robustness properties of the polytopic and the grid-based controller by accounting for structured uncertainties related to selected parameters of the model. A μ-sensitivity analysis is performed to estimate the percentage of uncertainty the closed-loop can tolerate for each parameter before becoming unstable.

S4.4: assesses the performance of the polytopic and the grid-based controller through a set of trajectory tracking simulation scenarios. First, nominal conditions are assumed to verify the NP of the controllers and to estimate the optimal launch conditions. Later, external sources of disturbance are introduced in the simulations in the form of sudden wind contributions (gusts and turbulence). The results presented in this section have been published in [Vin+23b]; [Vin+23c].

4.2 Background on Robustness Analysis

The robustness of a control system is associated with the capability to handle possible deviations from its nominal conditions. As discussed at the beginning of Chapter 1, the model employed for the control design generally consists of an approximation of the real nonlinear system. Thus, multiple sources of uncertainty related to unmodeled dynamics, limited parameters identification accuracy, or perturbations of the operating conditions, may affect the performance of the control system. According to [SP05], the robust stability (RS) of a control system defines the level of uncertainty the system can tolerate ensuring closed-loop stability, while the robust performance (RP) is associated with the performance specifications the system can satisfy in the presence of uncertainties or external disturbance signals.

In the robust control framework, the robustness specifications (RS and RP) are intended to be addressed directly at the design stage. The dynamics of the designed plant is described as the uncertain set, Π, of possible realizations of the perturbed system, $\Sigma_\Delta \in \Pi$, defined as the superposition of the nominal (unperturbed) plant, $\Sigma \in \mathbb{R}^{n \times n}$, and a perturbation term, $\Delta \in \mathbb{R}^{n_\Delta \times n_\Delta}$ (or $\Delta \in \mathbb{C}^{n_\Delta \times n_\Delta}$). Robust control approaches, such as the $\mathcal{H}_\infty$ criterion, aim at satisfying the design specifications for the worst-case realization of the uncertain plant. However, the design results might consist of a non-optimal solution associated to the optimization problem, often over-constraining the performance of the controller. Many applications resolve the control design on the nominal system by enhancing its rejection properties to handle disturbance sources. Then, the robustness assessment is performed a posteriori by introducing a selected level of uncertainty in the designed closed-loop system.

Both the design strategies rely on an a prior accurate selection of the system nominal model, and on the determination of the uncertainties level. The nominal model can be a simplified representation of the original nonlinear dynamics, where the identified nominal parameters are associated with a certain range of inaccuracy. As later discussed, the uncertainties are generally classified as structured or unstructured, depending on their source and the available information. Based on the selected model and class of perturbations, different approaches can be employed to assess the RS and RP of the system. In the following sections, stability margins analyses and parametric μ-sensitivity analyses are proposed as indexes to verify the robustness of the system respectively to unstructured and structured uncertainties.

4.2.1 Model Uncertainty Definition

The nominal model selected for the control design can be affected by several sources of uncertainty. Inaccurate parameters identification, where the uncertainty can be associated with a range of tolerance, generally falls in the class of parametric (structured) uncertainty. Differently, unmodeled or neglected system dynamics, which are more complicated to quantify, belong to the dynamic (unstructured) uncertainty class. Additionally, lumped uncertainties can represent the combined effect of multiple structured and unstructured perturbations.

4.2.1.1 Dynamic (Unstructured) Uncertainty

Since they are not associated with a specific range of tolerance, dynamic uncertainties are defined as a stable global full-block perturbation matrix, $\Delta \in \mathbb{C}^{n_\Delta \times n_\Delta}$, represented in the frequency domain and scaled by means of weighting functions, $W(s)$, s.t. $\|\Delta(s)\|_\infty \leq 1$. Several sources of perturbation can be modeled as a complex unstructured uncertainty such as unmodeled/neglected dynamics (flexible modes), high-frequency modeling inaccuracy, model delays, and system order reduction (approximation).

The perturbations can affect either the input or the output of the nominal model, in different ways. The schemes in Figure 4.1(a) and Figure 4.1(b) show two common unstructured uncertainty explicit representations, namely additive (A) and output multiplicative (O) ([BP02]). The former uncertainty representations can be expressed respectively as follows:

$$\Pi_\mathrm{A}: \ \Sigma_\Delta(s) = \Sigma(s) + W_\mathrm{A}(s)\Delta_\mathrm{A}(s); \qquad \text{with: } \|\Delta_\mathrm{A}(j\omega)\|_\infty \leq 1 \ \forall\omega$$

$$\Pi_\mathrm{O}: \ \Sigma_\Delta(s) = \left(I + W_\mathrm{O}(s)\Delta_\mathrm{O}(s)\right)\Sigma(s); \qquad \text{with: } \|\Delta_\mathrm{O}(j\omega)\|_\infty \leq 1 \ \forall\omega$$

where Δ_A and Δ_O are respectively the additive and the output multiplicative perturbations, while $W_\mathrm{A}(s)$ and $W_\mathrm{O}(s)$ define the corresponding weighting functions.

The weighting functions target the desired perturbation bandwidth and are normally selected as stable minimum-phase scalar-valued transfer functions, or diagonal transfer function matrices when dealing with MIMO systems. In the Nyquist domain, the perturbations can be interpreted as frequency-dependent disc-shaped uncertainty regions of radius $|W(j\omega)|$. Thus, the weighting functions are selected to include all the possible perturbed systems, $\Sigma_\Delta \in \Pi$, s.t. $|W(j\omega)| \geq l(\omega) \ \forall\omega$, where the minimum radius, $l(\omega)$, is defined according to the investigated type of uncertainty as:

$$l_\mathrm{A}(\omega) = \max_{\Sigma_\Delta \in \Pi} \bar{\sigma}\left(\Sigma_\Delta(j\omega) - \Sigma(j\omega)\right); \qquad \text{with: } |W_\mathrm{A}(j\omega)| \geq l_\mathrm{A}(\omega) \ \forall\omega$$

$$l_\mathrm{O}(\omega) = \max_{\Sigma_\Delta \in \Pi} \bar{\sigma}\left(\left(\Sigma_\Delta(j\omega) - \Sigma(j\omega)\right)\Sigma^{-1}(j\omega)\right); \qquad \text{with: } |W_\mathrm{O}(j\omega)| \geq l_\mathrm{O}(\omega) \ \forall\omega$$

respectively, for the additive and the output multiplicative case.

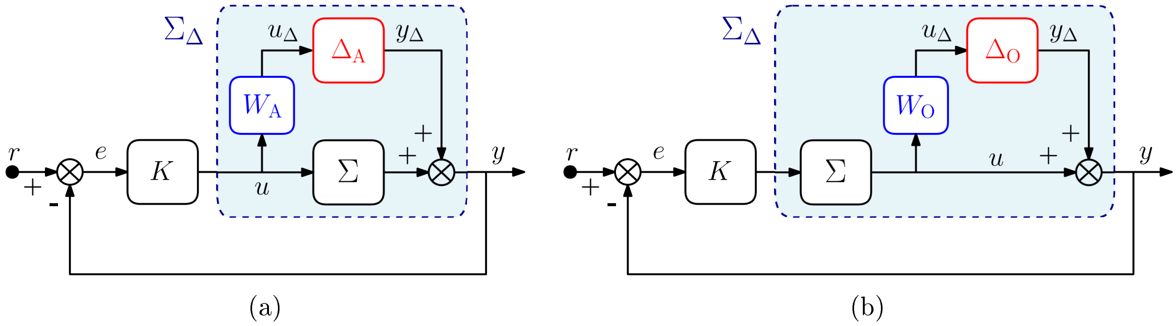

Figure 4.1: Uncertainty representations: (a) additive; (b) output multiplicative.

4.2.1.2 Parametric (Structured) Uncertainty

The uncertainty associated with the limited accuracy of certain model parameters, $\mathrm{p}_\delta \in \mathbb{R}$, can be described by bounding each parameter variation across a selected range of tolerance, $\mathrm{p}_\delta \in [\mathrm{p}_{\min},\ \mathrm{p}_{\max}]$, as:

$$\mathrm{p}_\delta = \bar{\mathrm{p}}\,(1 + r_\delta \delta)\,; \qquad \text{with: } r_\delta = \frac{\mathrm{p}_{\max} - \mathrm{p}_{\min}}{\mathrm{p}_{\max} + \mathrm{p}_{\min}} \tag{4.1}$$

where $\bar{\mathrm{p}} \in \mathbb{R}$ represents the nominal parameter mean value, $r_\delta \in \mathbb{R}$ is the level of relative uncertainty associated with the parameter, and $\delta \in \mathbb{R}$ is any real scalar s.t. $|\delta| \leq 1$.

Remark 4.1
When assessing the robustness of MIMO systems, the parametric uncertainty allows accounting for independent perturbations affecting the transfer functions of different channel dynamics. The employment of global unstructured uncertainties might introduce unrealistic couplings between the channels, resulting in an excessively conservative analysis.

Multiple sources of perturbations can be structured as a single perturbation matrix:

$$\Delta(s) := \mathrm{diag}(\Delta_1(s), \dots, \Delta_q(s), \delta_1 I_{r_1}, \dots, \delta_r I_{r_r}, \epsilon_1 I_{c_1}, \dots, \epsilon_c I_{c_c}) \tag{4.2}$$

including q full block complex transfer matrices, $\Delta_i(s) \in \mathbb{C}^{n_{\Delta,i} \times n_{\Delta,i}}$, r real diagonal blocks consisting of real parametric uncertainties, $\delta_i \in \mathbb{R}$, repeated r_i times, and c complex parametric uncertainties, ϵ_i, repeated c_i times. The uncertainties must be normalized s.t. $\|\Delta_i\|_\infty \leq 1$, $|\delta_i| \leq 1$. As a result, the uncertain model is expressed as the compact upper Linear Fractional Transformation (LFT) form shown in Figure 4.2. The generalized plant, $\Sigma_{\mathrm{P}_\Delta}$ accounts for the generalized nominal plant, Σ_{P}, defined in Chapter 3 during the controller synthesis, augmented with the interconnections with the perturbation matrix.

Remark 4.2
Depending on the number of occurrences (r_i, c_i) of each perturbation in the system (δ_i, ϵ_i), the dimension of the resulting perturbation matrix in the LFT formulation might lead to unfeasible computational complexity and excessively conservative results. The amount of each parameter occurrence is strictly related to the model formulation.

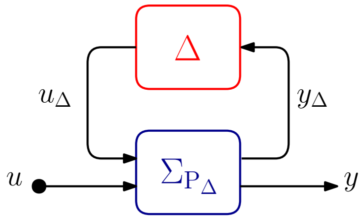

Figure 4.2: LFT uncertain plant representations.

4.2.2 Stability Margins

This section recalls the standard definitions of the stability margins as preliminary necessary but not sufficient conditions to assess the robust stability of a control system. The disk margins formulation is then introduced to compensate for the limitations related to the standard margins, that only account for individual gain or phase perturbations on SISO systems dynamics. Indeed, the disk margins provide more insight into the effect of simultaneous gain and phase perturbations on SISO systems (or MIMO through loop-at-a-time analysis), and of individual gain or phase perturbations across multiple channel dynamics (multi-loop analysis).

4.2.2.1 Standard Margins

In classical SISO systems analysis, the stability margins provide global indexes of robustness to gain and phase perturbations. The computation relies on the frequency properties of the loop transfer function, $L(j\omega)$, obtained by breaking the close-loop system in Figure 4.3(a), where Σ represents the investigated plant dynamics, and K is the designed controller. The robustness can be referred to input or to output disturbance rejection if the closed-loop system is opened in point A or in point B of the scheme in Figure 4.3(a), respectively. For MIMO systems, the input loop transfer function is computed as $L_u = K\Sigma$, while in the output case it corresponds to $L_y = \Sigma K$. The two computations are equivalent referring to SISO systems.

Definition 4.1 (Gain Margin)
The gain margin, GM, *quantifies the range of gain perturbation a nominal closed-loop system can withstand, guaranteeing stability conditions. In the frequency domain, it is defined as the gain values (in dB) of the open-loop function, $L(j\omega)$, corresponding to:*

$$\mathrm{GM} = -20\log|L(j\omega_{180})|$$

where ω_{180} is referred to as the phase crossover frequency at which $\angle L(j\omega_{180}) = -180$ deg.

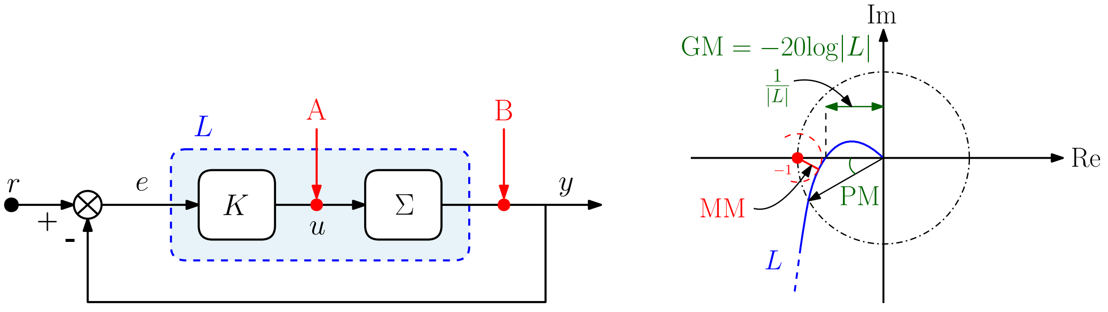

(a) (b)

Figure 4.3: Stability margins analysis: (a) nominal open-loop transfer function; (b) Nyquist domain interpretation.

Definition 4.2 (Phase Margin)
The phase margin, PM, *quantifies the range of phase perturbation a nominal closed-loop system can withstand, guaranteeing stability conditions. In the frequency domain, it is defined as the phase values (in deg) of the open-loop transfer function, $L(j\omega)$, corresponding to:*

$$\mathrm{PM} = 180 + \angle L(j\omega_0)$$

where ω_0 is referred to as the gain crossover frequency at which $|L(j\omega_0)| = 0$ dB.

A more intuitive representation can be provided in the Nyquist domain, through the definition of the system modulus margin.

Definition 4.3 (Modulus Margin)
The modulus margin, MM, consists of the minimum distance between the nominal system open-loop transfer function, $L(j\omega)$, and the critical point $(-1, 0j)$ in the frequency domain ([Fal+15]), evaluated as:

$$\mathrm{MM} = \min_{\omega} |1 + L(j\omega)|$$

for each frequency $\omega \in \mathbb{C}$.

The definition of modulus margin is strictly related to the closed-loop sensitivity properties discussed in Chapter 3. Indeed, by recalling the definition of the Sensitivity function, $S(j\omega)$, the following relation holds:

$$\mathrm{MM} = 1/\mathrm{M}_S; \qquad \text{with: } \mathrm{M}_S = \max_{\omega} |S(j\omega)| = \|S\|_\infty$$

where M_S corresponds to the peak value of the Sensitivity function. A graphical overview of the standard stability margins is shown in Figure 4.3(b).

Remark 4.3 ([SPG20])
The formulation of the standard stability margins is based on the assumption of individual gain or phase perturbations on single-channel dynamics (SISO systems). Simultaneous variations of gain and phase margins can destabilize the system even when large GM and PM are guaranteed. Similarly, simultaneous perturbations affecting multiple MIMO systems channel dynamics can be critical for closed-loop stability.

4.2.2.2 Disk Margins

A more complete assessment of the closed-loop system robustness to perturbation sources is provided through the evaluation of the disk margin (DKM) index. The disk margin relies on the identification of the minimal complex multiplicative uncertainty, $f_{\min}$, that destabilizes the system within a collection of simultaneous gain and phase variations. The collection of perturbations is parameterized in the complex plane as a disk, $\mathbb{D}(\xi, \sigma) \in \mathbb{C}$, of size ξ and skew σ. In particular, the parameter ξ quantifies the amount of simultaneous gain and phase variations generated by a gain-bounded dynamic uncertainty, δ, while σ consists of a balancing coefficient representing the relative gain increase/decrease caused by the perturbations. Balanced disk margins are computed for $\sigma = 0$, meaning that the gain increases and decreases symmetrically.

Definition 4.4 (Disk Margin)
Given a collection of simultaneous gain and phase perturbations, $f \in \mathbb{D}(\xi, \sigma)$, such that:

$$\mathbb{D}(\xi, \sigma) = \left\{ \frac{1 + \left(\frac{1-\sigma}{2}\right)\delta}{1 - \left(\frac{1+\sigma}{2}\right)\delta} : \delta \in \mathbb{C} \text{ with } |\delta| < \xi \right\}$$

the disk margin for a fixed skew value, σ, is defined as the largest disk size, $\xi_{\max}$, such that the closed-loop system is stable for all perturbation $f \in \mathbb{D}(\xi_{\max}, \sigma)$.

Theorem 4.1 ([SPG20])
Given a skew parameter, σ, defining the disk margin, and assuming a stable closed-loop system described by the nominal SISO loop transfer function, $L(j\omega)$, the disk margin is computed as:

$$\xi_{\max} = \frac{1}{\|S + \frac{\sigma-1}{2}\|_\infty}$$

where $S(j\omega) = (I + L(j\omega))^{-1}$ represents the closed-loop Sensitivity function.

When balanced conditions $\sigma = 0$ are assumed, the expression in Theorem 4.1, can be simplified as the symmetric $S - T$ disk margin ([BP02]):

$$\xi_{\max} = \frac{1}{\|\frac{S-T}{2}\|_\infty}. \tag{4.3}$$

The notation of the disk margin in Definition 4.4 can be associated with the standard gain and phase margins in Definition 4.1 and Defintion 4.2, respectively. As discussed in [SPG20], by geometrical considerations, and assuming the balanced conditions, $\sigma = 0$, the following disk gain and phase margin expressions can be recovered:

$$\pm\text{DGM} = \frac{2 \pm \xi_{\max}}{2 \mp \xi_{\max}}; \qquad \text{DPM} = \arccos\left(\frac{1 + (-\text{DGM})(+\text{DGM})}{(-\text{DGM}) + (+\text{DGM})}\right). \tag{4.4}$$

The above expressions provide a robustness index for gain-only or phase-only system perturbations at specific σ conditions. However, the same geometrical considerations allow quantifying the effect of combined gain and phase variations which can be represented as a stable region of mutual perturbations.

In order to extend the margins analysis to a broader class of MIMO systems, the computation can involve individual channels of the system at a time (‘loop-at-a-time margins’) or the simultaneous perturbations affecting the different channels (‘multi-loop margins’).

Loop-at-a-time margins. The computation consists of applying a complex perturbation, $f \in \mathbb{D}(\xi, \sigma)$, to a selected channel dynamics, while keeping the remaining ones at nominal conditions. Assuming to analyze the system robustness to input disturbances (as explained in Figure 4.3(a)), the loop is opened only along the investigated channel, as shown in Figure 4.4. The perturbation is then applied to the resulting SISO open-loop transfer function. This procedure can be repeated for each channel and allows the computation of the different disk stability margins in the sense of Definitions 4.1-4.3.

Multi-loop margins. Account for the simultaneous perturbation of multiple channel dynamics, providing a more global and reliable estimation of MIMO systems robustness properties. The multi-loop disk margin, ξ_{MM}, consists of the largest disk that includes all the perturbations applied on the different channels. This approach can be employed to investigate the robustness of both input and output perturbations, such as multi-loop input disk margin, multi-loop output disk margin, or global multi-loop input/output disk margin.

The computation of the MIMO system multi-loop disk margin relies on the definition of the structured singular value function, $\mu : \mathbb{C}^{n_\Delta \times n_\Delta} \to [0, \infty)$, first proposed in [Saf82]. As detailed later in Section 4.2.3.2, the structured singular value was contemporarily introduced in [Doy82] as a more general tool for the assessment of MIMO system RS and RP, accounting for structured uncertainty. Assume a set of $n_\Delta \in \mathbb{R}$ complex perturbations, $f_1, \ldots, f_{n_\Delta} \in \mathbb{D}(\xi, \sigma)$, structured as the diagonal perturbation matrix, Δ, in Equation (4.2), for a given skew value, σ, s.t. $\|\Delta\| := \max_{i=1,\ldots,n_\Delta} |\delta_i| < \xi$. Since the RS condition for the closed-loop system is equivalently formulated through the stability of the standard $M\Delta$ structure, shown in Figure 4.5(c), the MIMO system multi-loop disk margin, ξ_{MM}, can be computed as follows.

Theorem 4.2 ([SPG20])
Given a skew parameter σ defining the disk margin, and assuming a stable closed-loop $M\Delta$ representation, the multi-loop disk margin is computed as:

$$\xi_{\mathrm{MM}} = \left\| \mu\left(S + \frac{\sigma - 1}{2I_{n_\Delta}} \right) \right\|_\infty := \max_{\omega \in \mathbb{R} \cup \{+\infty\}} \mu(M(j\omega)).$$

A proper formulation of the structured singular value function, μ, is provided in Definition 4.5. The DGM and DPM associated with the computed 'multi-loop' disk margin can be evaluated through the expression defined in Equation (4.4).

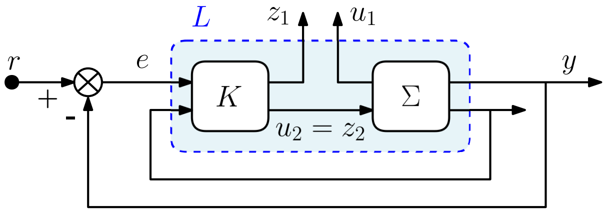

Figure 4.4: Loop-at-a-time disk margins computation scheme.

4.2.3 Robust Stability and Performance

The formulation of the robustness analysis problem relies on the generalized control configuration scheme presented in Figure 4.5(a), where K is the nominal controller, Δ is the diagonal perturbation matrix (structured or unstructured), and $\Sigma_{\mathrm{P}_\Delta}$ is the generalized plant introduced in Figure 4.2. In particular, by defining the nominal closed-loop system, N, generated by the lower LFT of the generalized plant w.r.t. the designed controller, as:

$$N := \mathcal{F}_l\left(\Sigma_{\mathrm{P}_\Delta}, K\right) = \begin{bmatrix} N_{11} & N_{12} \\ N_{21} & N_{22} \end{bmatrix}$$

the system RS and RP conditions can be equivalently formulated w.r.t. the standard $N\Delta$ structure, as shown in Figure 4.5(b).

The corresponding uncertain closed-loop transfer function from the exogenous input vector, $\boldsymbol{w}$, to the controlled output, $\boldsymbol{z}$, is obtained as the upper LFT of N w.r.t. Δ, as it follows:

$$\mathcal{F}_u\left(N, \Delta\right) := N_{22} + N_{21}\Delta(I - N_{11}\Delta)^{-1}N_{12}. \tag{4.5}$$

In order to analyze the system robust stability properties, the $N\Delta$ structure is further rearranged as the $M\Delta$ formulation presented in Figure 4.5(c), where $M = N_{11}$. Indeed, by assuming the stability of both the nominal closed-loop, N, and the perturbation matrix, Δ, instability of the closed-loop in Equation (4.5) may arise only through the term $(I - N_{11}\Delta)$.

If the robustness analysis accounts for unstructured uncertainties, Δ is modeled as a full complex perturbation matrix, s.t. $\|\Delta\|_\infty \leq 1$, as discussed in Section 4.2.1.1. The analysis provides only a global sufficient condition through the computation of the maximal admissible norm for Δ. Differently, when the perturbation matrix is structured as in Equation (4.2), the analysis is performed for each block diagonal element of Δ, by means of the structured singular value computation.

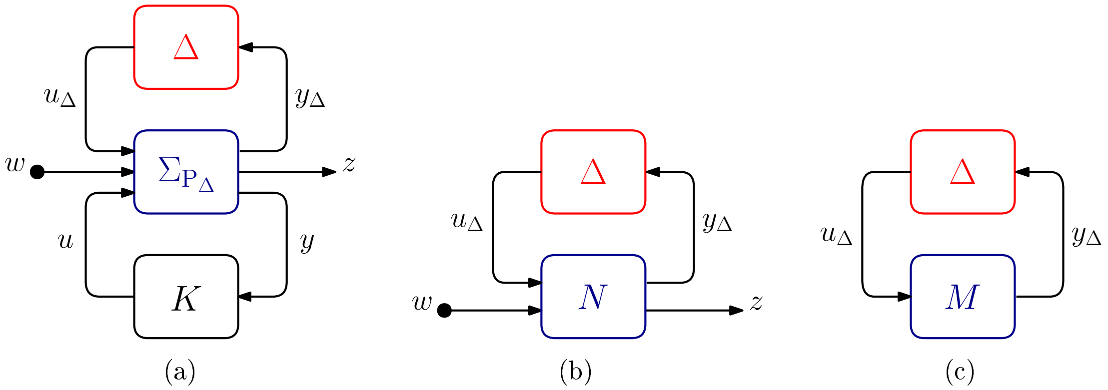

Figure 4.5: Robustness analysis schemes: (a) generalized uncertain control configuration; (b) standard $N\Delta$ structure; (b) standard $M\Delta$ closed-loop structure.

4.2.3.1 Unstructured Uncertainty: RS and RP

The robust stability conditions of the $M\Delta$ closed-loop system in Figure 4.5(c), when Δ is defined as a full unstructured perturbation matrix, can be derived through the application of the Small Gain Theorem, as it follows.

Theorem 4.3 (Small Gain Theorem)
Given a stable system, $M(j\omega)$, the closed-loop $M\Delta$ structure is well-posed and internally stable for all stable perturbations, $\Delta(j\omega)$, s.t.:

$$\|\Delta(j\omega)\|_\infty \leq 1,\ \forall\omega \in \mathbb{R} \quad \Longleftrightarrow \quad \|M(j\omega)\|_\infty \leq 1,\ \forall\omega \in \mathbb{R}. \tag{4.6}$$

The same results can be obtained through the Determinant Stability Condition Theorem defined in [SP05], as an extension of the generalized Nyquist Theorem. Indeed, when robust stability is investigated for SISO systems, the analysis can be simply assessed by verifying that the loop transfer function of the $M\Delta$ structure does not encircle the critical point, $(-1, 0j)$, in the Nyquist plot, for any stable matrix $\Delta(j\omega)$.

The definition of the robust performance conditions can be derived by applying the Small Gain Theorem on the augmented $N\hat{\Delta}$ closed-loop structure presented in Figure 4.6. The additional perturbation term, Δ_f, consists of a fictitious full matrix that represents the $\mathcal{H}_\infty$ performance imposed through the robustness analysis.

Theorem 4.4 (Robust Performance)
Given a stable nominal closed-loop system, N, the robust performance of the related $N\hat{\Delta}$ structure is guaranteed if and only if:

$$\|\mathcal{F}_u(N, \Delta)\|_\infty < 1, \quad \forall\ \|\Delta\|_\infty \leq 1. \tag{4.7}$$

Remark 4.4
The performance selected to assess the robustness of a control system is generally more relaxed compared to the criteria imposed during the nominal control design through the weighting functions, as discussed in Chapter 3.

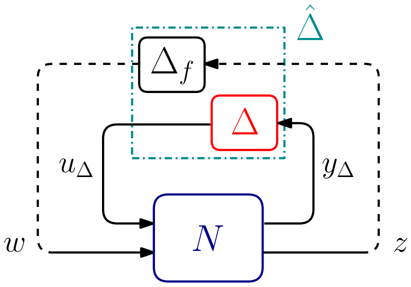

Figure 4.6: Augmented $N\hat{\Delta}$ structure for RP assessment.

4.2.3.2 Structured Uncertainty: RS and RP

When the perturbation respects the block diagonal structure in Equation (4.2), the RS condition defined in Theorem 4.3 becomes only sufficient but not necessary, as for the unstructured case. In order to exploit the advantages provided by the structured formulation, the RS problem relies on the identification of the smallest structured perturbation, $\Delta(s) \in \underline{\Delta}(s)$, s.t. $\det(I - M\Delta) = 0$, where $\underline{\Delta}(s) \in \mathbb{C}^{n_\Delta \times n_\Delta}$ refers to the common block diagonal structure in Equation (4.2).

Definition 4.5 (Structured Singular Value)
Given a complex matrix, $M(s) \in \mathbb{C}^{m\times m}$, and a set of complex structured matrices, $\Delta(s) \in \underline{\Delta}$, the structured singular value, $\mu(M)$, is the real non-negative function defined as:

$$\mu(M) := \frac{1}{\min\{\bar{\sigma}(\Delta) : \Delta \in \underline{\Delta} \mid \det(I - M\Delta) = 0\}}$$

Theorem 4.5 (Structured Small Gain Theorem)
Given a MIMO LTI stable system, $M(j\omega)$, and a stable perturbation matrix, $\Delta(j\omega)$, the resulting $M\Delta$ structure is stable for all $\Delta \in \underline{\Delta}$, with $\bar{\sigma}(\Delta) \leq 1$, if and only if:

$$\mu(M(j\omega)) < 1,\ \forall\omega \in \mathbb{R}; \qquad \text{with} : M(j\omega) := N_{11}(j\omega)$$

The structured singular value in Definition 4.5 can be also employed for the assessment of the system RP. Indeed, the condition imposed in Theorem 4.4 can be equivalently expressed through the computation of μ on the augmented $N\hat{\Delta}$ structure in Figure 4.6.

Proposition 4.1 (Robust Performance)
Given a stable nominal closed-loop system, N, the robust performance of the related $N\hat{\Delta}$ structure is guaranteed if and only if:

$$\mu_{\hat{\Delta}}(N(j\omega)) < 1,\ \forall\omega \in \mathbb{R}; \qquad \text{with} : \hat{\Delta} = \begin{bmatrix} \Delta_f & 0 \\ 0 & \Delta \end{bmatrix}$$

where the full complex perturbation, Δ_f, has the dimensions of $\mathcal{F}_u\left(N,\Delta\right)^{\mathrm{T}}$.

The complexity associated with the evaluation of μ is characterized by a non-polynomial hard growth w.r.t. the dimension and the type of perturbations investigated, possibly resulting in an unfeasible computation ([TO95]). A standard approach relies on the computation of an upper and lower bound of μ. In particular, the upper bound provides a sufficient stability/performance condition w.r.t. the selected perturbations, while the lower bound provides a sufficient condition for the system instability. A tight evaluation of upper and lower bounds allows for minimizing the conservatism introduced by the computation process. Depending on the selected perturbations, several efficient algorithms have been proposed to provide a reliable estimation of μ.

4.3 Controllers Robustness Analysis

This section provides a preliminary and non-exhaustive robustness analysis performed on the LPV polytopic and grid-based controllers, (K_{PY} and K_{GR}), designed in Chapter 3. The analysis is based on a first global evaluation of the controllers RS through the computation of the disk margins across the polytope vertices, for the polytopic controller, and at the design points, concerning the grid-based controller. Later, a more precise RS and RP estimation is performed through the definition of a structured set of uncertain parameters (parametric uncertainty), and the computation of the corresponding structured singular values (μ-analysis).

Remark 4.5 (Analysis Limitations)
It is important to emphasize that the robustness analysis applies standard LTI approaches to LPV control systems. Indeed, LPV control design techniques provide higher theoretical guarantees of stability across the designed operating envelope, compared to classical LTI approaches, as discussed in Chapter 3. On the other side, standard LTI control design targets a single or a set of operating conditions individually, resulting in higher optimization performances compared to the LPV design approaches. Hence, higher robustness properties can be imposed at the design stage in terms of disturbance rejection and noise attenuation. Finally, a complete robustness analysis should account for several forms of uncertainties, including time-varying perturbations applied to the scheduling variables, which is not the purpose of the present work.

4.3.1 Stability Margins Computation

The robust stability of the LPV controllers is investigated in the frequency domain through the computation of the stability margins. The analysis is performed at each vertex of the reduced polytope, $\hat{\Theta}_{\mathrm{R}}$, and at each grid point of the grid, Ξ, selected in Chapter 3, through the computation of the DKM associated with both input and output disturbance. Since the quasi-LPV projectile pitch channel model, Σ_{GR}, in Equations (2.40)-(2.41) and the polytopic model, Σ_{PY}, in Equation (2.42) consist of SIMO systems, the computation of 'loop-at-a-time' DKM and 'multi-loop' DKM are preferred. As discussed in Section 4.2.2.2, the 'loop-at-a-time' DKM accounts for simultaneous variations of GM and PM on a single channel, while 'multi-loop' DKM investigates individual GM or PM perturbations on multiple channels.

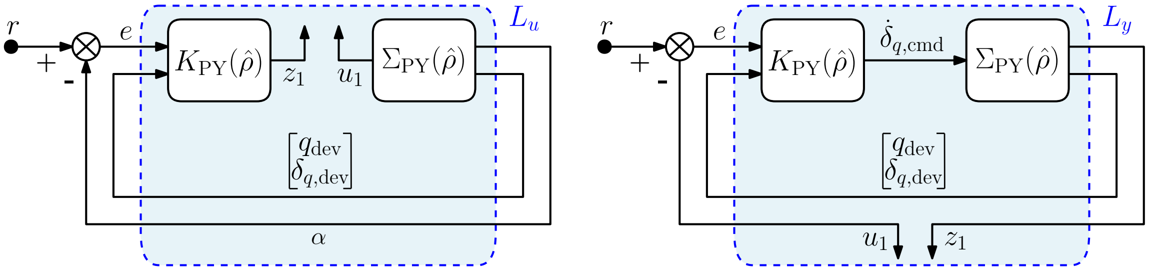

(a) (b)

Figure 4.7: Analysis schemes: (a) input disturbance; (b) output disturbance.

The input and output DKM computation schemes related to the polytopic controller are shown in Figures 4.7(a)-(b), respectively. The same schemes are employed for the grid-based controller analysis. In particular, the input loop transfer, L_u shown in Figure 4.7(a), consists of a SISO system that can be directly analyzed through the DKM computation introduced in Equation (4.3), assuming the balanced case ($\sigma = 0$). Differently, 'loop-at-a-time' output DKM are computed for each channel dynamics through the output loop transfer, L_y, as shown in Figure 4.7(b). The evaluation of the 'multi-loop' output DKM provides an additional global insight into the robustness of the controllers. All the margins are computed through the MATLAB `diskmargin` function.

A graphical interpretation of the results is provided through the representation of the worst-case Nyquist exclusion region across all the vertices of the polytope, and all the grid-points of the design grid. The Nyquist exclusion region consists of the area of the complex plane around the critical point, $(-1, 0j)$, never crossed by the loop transfer function. The intercepts of the exclusion region with the real axis correspond to the DGM of the system, subjected to gain-only perturbations, while the intercepts with the unit circle define the DPM of the system, subjected to phase-only perturbations, computed as in Equation (4.4). Additionally,

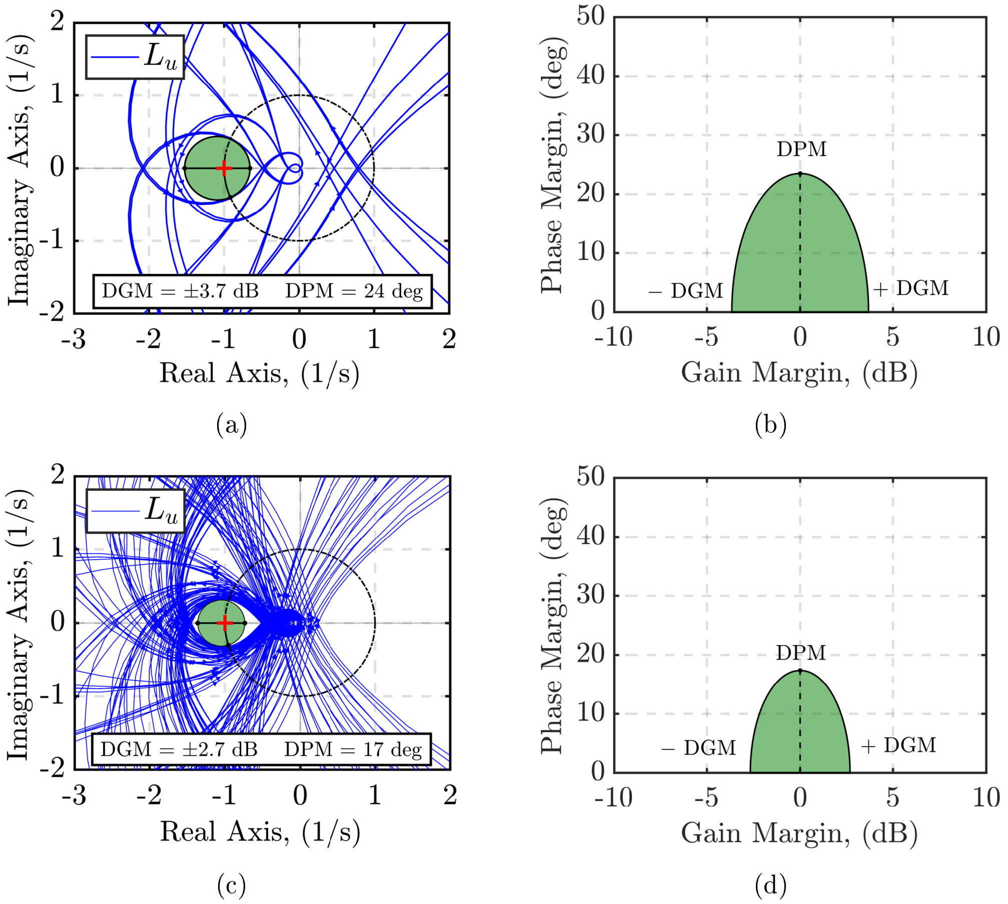

(a) (b)

(c) (d)

Figure 4.8: Input DKM: (a)-(c) polytopic/ grid-based Nyquist exclusion region, respectively; (b)-(d) polytopic/grid-based mutual GM/PM variation, respectively.

the corresponding worst-case DGM and DPM mutual variation are evaluated to account for the effect of simultaneous gain and phase perturbations.

Concerning the input DKM analysis, the worst-case Nyquist exclusion regions related to the polytopic and the grid-based controller are represented in Figure 4.8(a) and Figure 4.8(c), respectively, while Figure 4.8(b) and Figure 4.8(d) show the corresponding worst-case DGM and DPM mutual variations. The results reveal limited margins for input gain and phase variations, especially concerning the grid-based controller. The limited input disturbance rejection properties of the controllers could depend on the performance requirements imposed at the control design stage. Indeed, a simple scaling factor was imposed to model the input disturbance effect on the system. The imposition of a higher-order weighting function might enhance the rejection performance of the controller, at the expense of possibly lower tracking capability and maneuverability. The results are summarized in Table 4.1.

The same approach is employed to represent the 'loop-at-a-time' output DKM. The worst-case Nyquist exclusion regions related to the polytopic output channels, (α, q_{dev}, $\delta_{q,\text{dev}}$), are presented in Figures 4.9(a)(c)(e), respectively. The corresponding worst-case DGM and DPM mutual variations are proposed in Figures 4.9(b)(d)(f). The results related to the grid-based output channels, (α, q_{dev}, $\eta_{z,\text{dev}}$), are equivalently presented in Figure 4.10. The results concerning the α and the $\delta_{q,\text{dev}}$ (or $\eta_{z,\text{dev}}$) channels reveal relevant margins, both in terms of gain/phase-only perturbations (DGM and DPM), and when mutual gain/phase variations are considered. However, weaker margins characterize the q_{dev} channel of both the polytopic and grid-based systems. As pointed out during the input DKM analysis, the limited performance of the q_{dev} channel could be caused by the absence of strict disturbance rejection requirements imposed at the control design stage. Indeed, as shown by the control configuration schemes in Figure 3.1 and Figure 3.9, weighting functions were imposed only to shape the disturbance rejection/tracking performance of the controlled output (α). Further development of the design schemes, accounting for all the output channels, might provide more balanced performance, especially for the grid-based controller case where the margins related to the $\eta_{z,\text{dev}}$ channel are much larger compared to the remaining ones. The results of the 'loop-at-a-time' output DKM are summarized in Table 4.3.

Table 4.1: Input DKM results.

	Input		
	DGM	DPM	$\xi_{\max}$
PY	3.7 dB	24 deg	0.4
GR	2.7 dB	17 deg	0.3

Table 4.2: 'Multi-loop' output DKM results.

	Multi-loop Output		
	DGM	DPM	ξ_{MM}
PY	2 dB	12 deg	0.2
GR	2.3 dB	14 deg	0.2

Table 4.3: 'Loop-at-a-time' output DKM results.

	Output: α			**Output: q_{dev}**			**Output: $\delta_{q,\text{dev}}/\eta_{z,\text{dev}}$**		
	DGM	DPM	$\xi_{\max}$	DGM	DPM	$\xi_{\max}$	DGM	DPM	$\xi_{\max}$
PY	7.1 dB	42 deg	0.8	2.9 dB	19 deg	0.3	6.2 dB	38 deg	0.7
GR	7.7 dB	45 deg	0.8	2.5 dB	17 deg	0.3	25 dB	80 deg	1.8

Finally, a global evaluation of the output DKM is computed through the 'multi-loop' approach, defined in Theorem 4.2. The worst-case results related to the polytopic and the grid-based controller are presented in Table 4.2. As expected, the DKM results are influenced

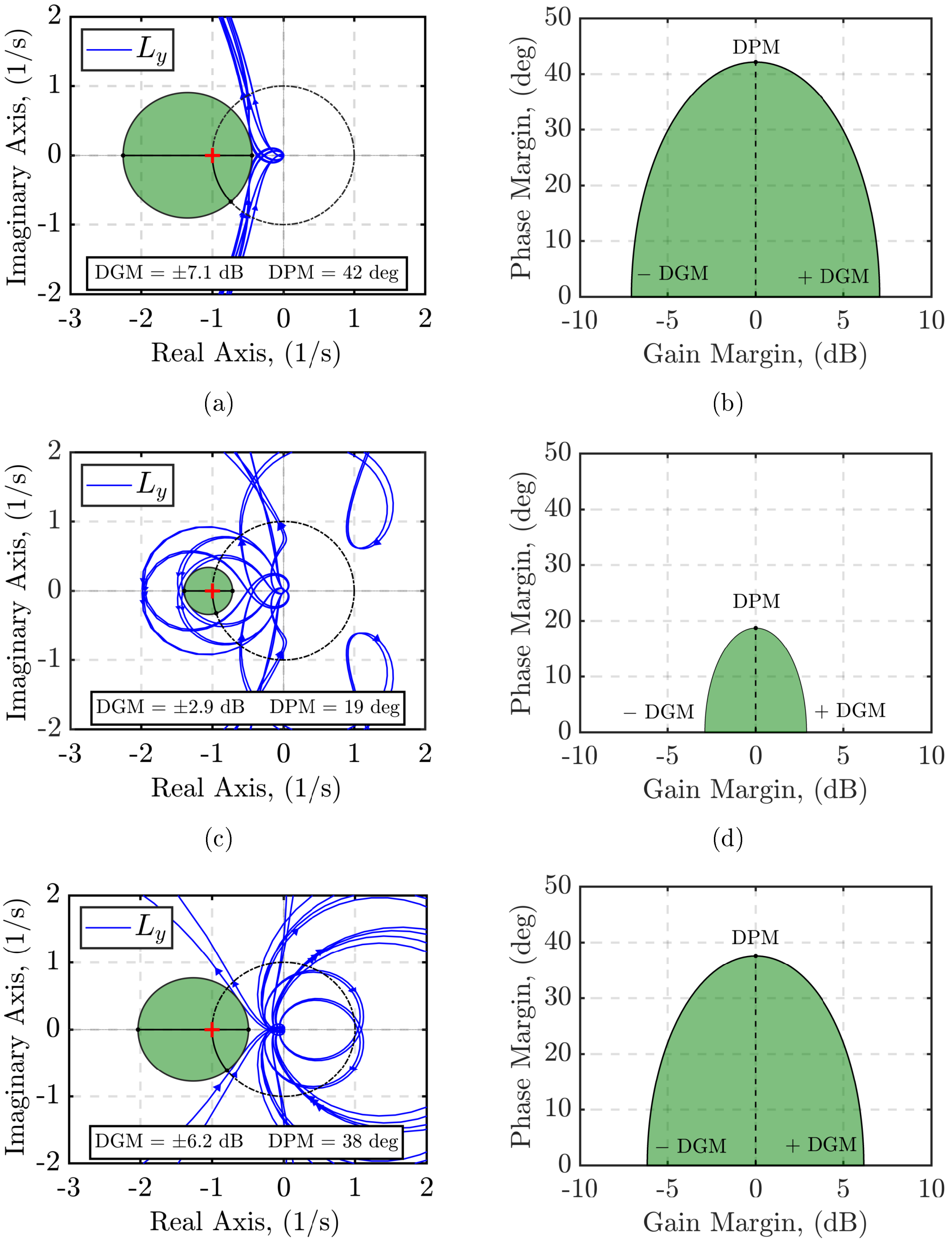

(a) (b)

(c) (d)

(e) (f)

Figure 4.9: Polytopic output DKM Nyquist exclusion region and mutual GM/PM variation related to the: (a)-(b) α channel, respectively; (c)-(d) q_{dev} channel, respectively; (e)-(f) $\delta_{q,\text{dev}}$ channel, respectively.

by the limited performance observed on the q_{dev} output channel. Additionally, the evaluation of the 'multi-loop' DKM can be affected by a relevant level of conservatism. An accurate model of the system uncertainty might provide a more reliable estimation of the system robustness.

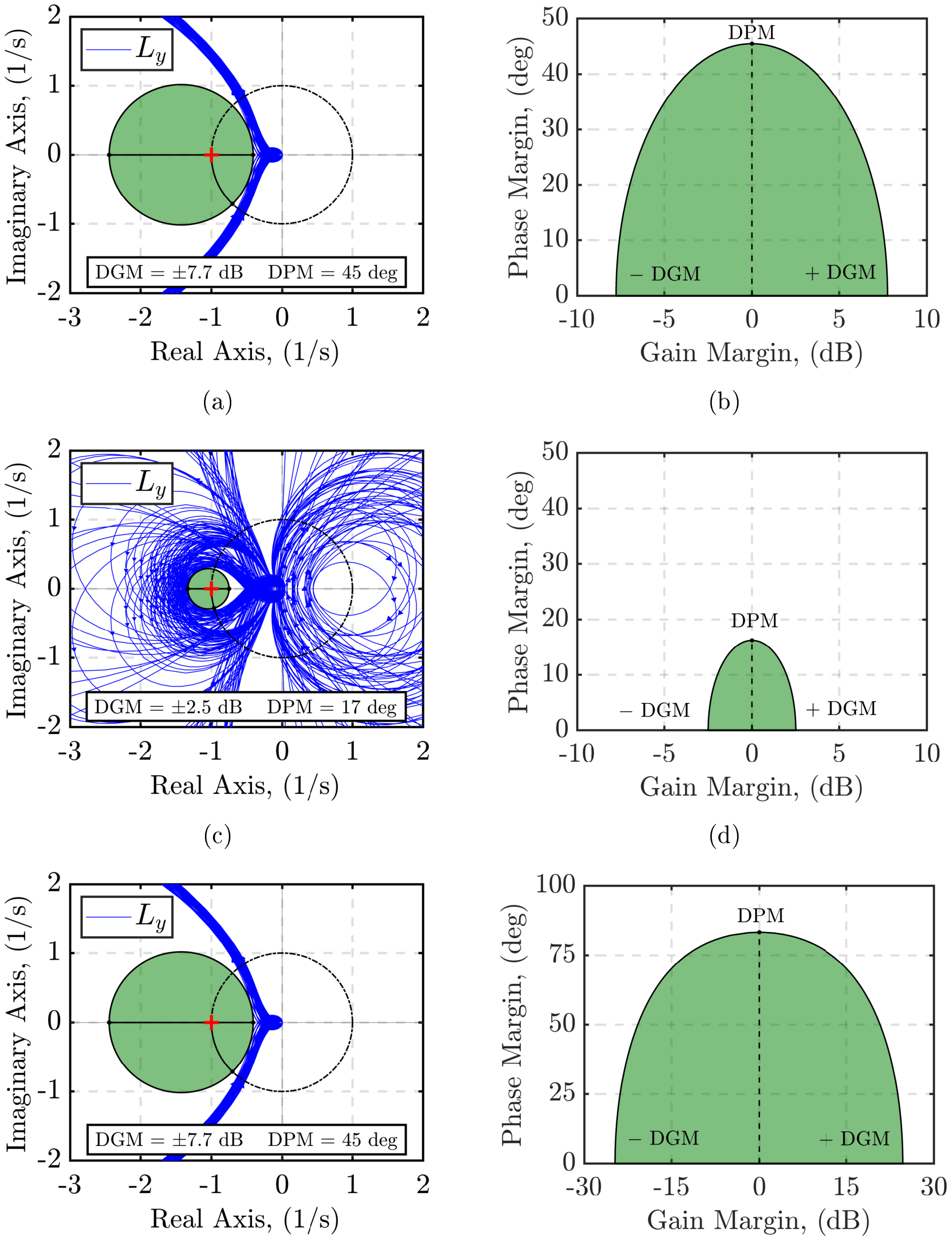

(a) (b)

(c) (d)

(e) (f)

Figure 4.10: Grid-based output DKM Nyquist exclusion region and mutual GM/PM variation related to the: (a)-(b) α channel, respectively; (c)-(d) q_{dev} channel, respectively; (e)-(f) $\eta_{z,\mathrm{dev}}$ channel, respectively.

4.3.2 μ-Analysis: Robust Stability and Performance

A further assessment of the RS and RP related to the polytopic and the grid-based controllers relies on the μ-analysis described in Section 4.2.3.2. The analysis targets the robustness of the closed-loop systems to the effect of real parametric uncertainties, structured as the diagonal matrix, Δ, defined in Equation (4.2). As for the stability margins analysis, the μ-analysis is computed across all the vertices of the reduced polytope, $\hat{\Theta}_{\mathrm{R}}$, and all the grid points of the design grid, Ξ. The scheme shown in Figure 4.11 represents the $M\Delta$ structure employed for the robust stability assessment, related to the polytopic closed-loop. In particular, $\Sigma_{\mathrm{PY}_{\Delta}}$ includes the nominal LPV polytopic model, Σ_{PY}, in Equation (2.42), employed during the control design stage, and the interconnection with the perturbation matrix. The same scheme is also used during the grid-based RS analysis by imposing the dedicated nominal model, $\Sigma_{\mathrm{GR}_{\Delta}}$, and nominal controller, K_{GR}. Concerning the RP, the related $N\hat{\Delta}$ structure is obtained by including the set of exogenous signals, $\boldsymbol{w}$, the controlled output, $\boldsymbol{z}$, and the weighting functions imposed at the control design stage, in the $M\Delta$ scheme in Figure 4.11.

The analysis intends to target the uncertainty associated with a set of selected parameters: the dynamic pressure, $\bar{q}$, the aerodynamic pitching coefficient, $C_{m_{\mathrm{S}}}$, and the aerodynamic virtual pitch force and pitching moment control coefficients, $C_{Z_{\delta_q}}$ and $C_{m_{\delta_q}}$, respectively. The dynamic pressure has a strong impact on the projectile dynamics since it models both the effect of altitude and airspeed variations. Additionally, it represents one of the scheduling functions, $\hat{\rho}_1$, defining the polytopic model. The aerodynamic pitching moment coefficient is strictly related to the static stability conditions of the projectile dynamics, as discussed in Section 1.3.2.2. Finally, the control coefficients have been first modeled through the regression on the CFD acquisition presented in Section 1.3.3.4, and then approximated during the quasi-LPV modeling process developed in Section 2.3.2.1. Thus, they could be affected by a relevant uncertainty level. However, due to the complex formulation of the projectile quasi-LPV and polytopic models, an excessively large number of occurrences characterizes most of the parameters, leading to an unfeasible computational complexity, as mentioned in Remark 4.2. A straightforward solution consists of the representation of the parametric uncertainties as a set of global real uncertainties, directly affecting the entries of the LPV state space models, Σ_{PY} and Σ_{GR}. The uncertain matrix entries are modeled as in Equation 4.1, where the

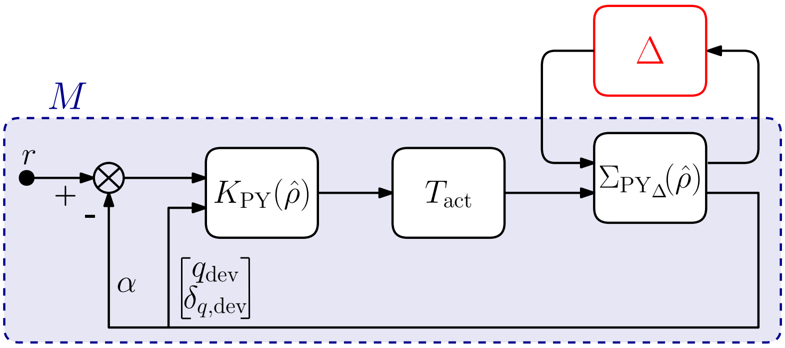

Figure 4.11: Polytopic closed-loop $M\Delta$ structure.

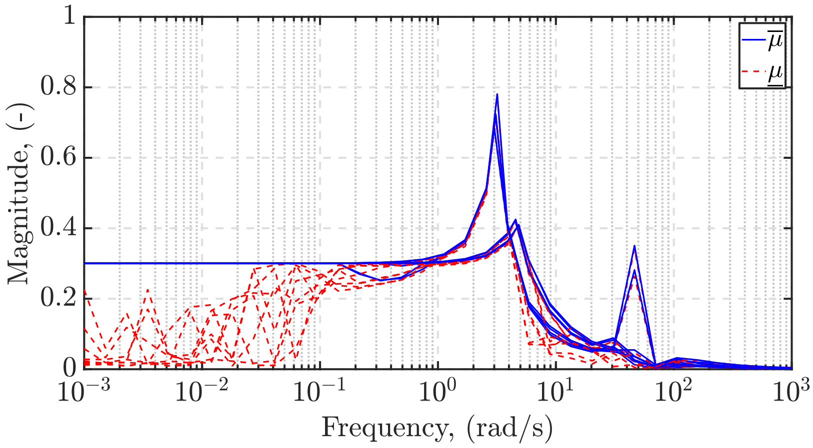

Figure 4.12: Polytopic system RS analysis results.

nominal values are associated with a selected interval of tolerance, defined through a level of relative uncertainty, r_δ (as a percentage), and a real scalar, $\delta \in [-1, 1]$. The selection of the level of relative uncertainty for each matrix entry depends on the number of occurrences of each original uncertain parameter. The selected set of percentages is provided in Table 4.4.

Table 4.4: Sets of relative uncertainty levels.

	$\mathcal{A}_{12}$	$\mathcal{A}_{13}$	$\mathcal{A}_{22}$	$\mathcal{A}_{23}$	$\mathcal{A}_{32}$	$\mathcal{A}_{33}$	$\mathcal{C}_{32}$	$\mathcal{C}_{33}$
PY	20%	30%	30%	30%	30%	30%	–	–
GR	20%	20%	20%	30%	30%	30%	20%	20%

The results of the RS and RP analyses are computed through the MATLAB `robstab` and `robgain` functions, and provided in the form of upper and lower bounds of the structured singular value, defined respectively as $\overline{\mu}$ and $\underline{\mu}$. The curves in Figure 4.12 and Figure 4.13, show the μ-analysis RS results related to the polytopic and the grid-based systems, respec-

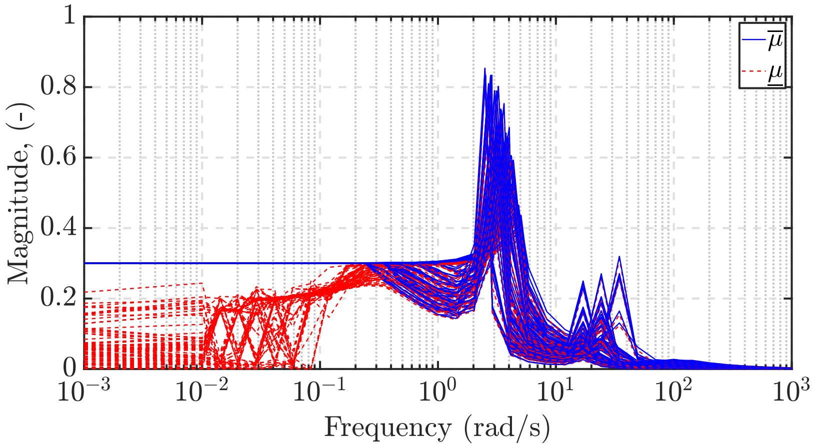

Figure 4.13: Grid-based system RS analysis results.

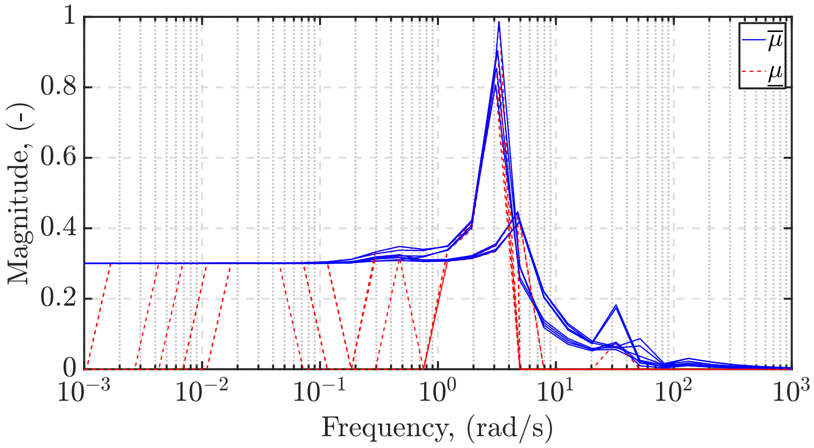

Figure 4.14: Polytopic system RP analysis results.

tively. The upper and lower bounds are tight at higher frequencies, confirming the accuracy of the evaluation, while a certain level of conservatism might affect the computation at lower frequency. However, in both analyses, the $\overline{\mu}$ peak corresponding to the worst-case RS conditions, remains far below the critical level 1, as imposed by Theorem 4.5. In particular, a peak of $\overline{\mu} = 0.79$ provides a 160% tolerance of the polytopic closed-loop system to the modeled uncertainty. Similarly, a peak of $\overline{\mu} = 0.83$ confirms the robust stability of the grid-based closed-loop system, with a tolerance of 130% to the modeled uncertainty.

The results related to the RP analyses on the polytopic and grid-based systems are presented in Figure 4.14 and Figure 4.15, respectively. As mentioned in Remark 4.4, the RP imposed by the analysis is generally more relaxed compared to the nominal case. Thus, a relaxation coefficient, r_γ, is applied to the $\mathcal{H}_\infty$ performance level, γ_∞, obtained during the controller design. The polytopic closed-loop RP is achieved, as in Proposition 4.1, by relaxing the design performance, $\gamma_\infty = 5.8$, with a ratio $r_\gamma = 2.5$. Similarly, the RP of the grid-based system is guaranteed by imposing a $r_\gamma = 4$ relaxation to the design performance $\gamma_\infty = 1.4$.

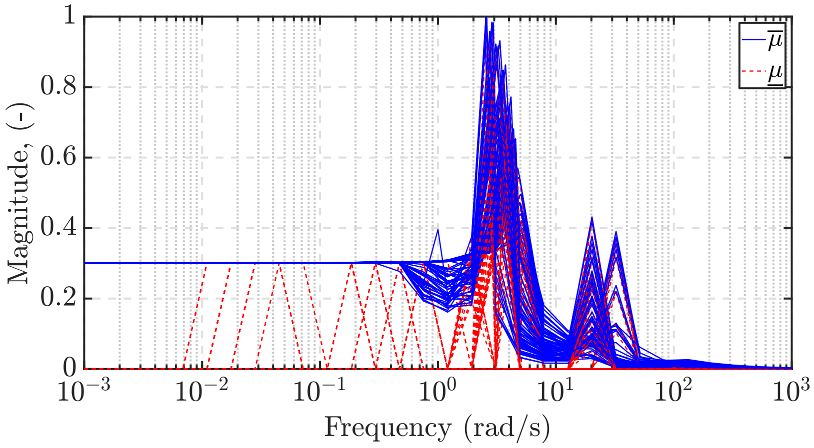

Figure 4.15: Grid-based system RP analysis results.

4.4 Tracking Performance Simulations

This section investigates the trajectory tracking performance of the polytopic and the grid-based controllers (K_{PY} and K_{GR}) in the nonlinear 6-DoF simulator introduced at the end of Chapter 1. The equivalent controllers implementation scheme is proposed in Figure 4.16, where the *Projectile Airframe* block includes the projectile 6-DoF nonlinear dynamics in Equations (1.43)-(1.46), while T_{act} consists of the actuator dynamics defined in Equation (1.39). To comply with the LPV controller formulations, the *Output Deviation* block includes the computation of the off-equilibrium state variables, q_{dev} and $\delta_{q,\mathrm{dev}}$, and output variable, $\eta_{z,\mathrm{dev}}$, as defined in Equation 2.13. The computation implies the online evaluation of the corresponding equilibrium functions, formulated in Equation (2.28) and Equation (2.32), respectively. Additionally, the *Output Deviation* block addresses the online computation of the scheduling functions, ($\hat{\rho}_1$, $\hat{\rho}_2$, $\hat{\rho}_3$), defined through the development of the polytopic model in Section 2.4.

The simulations consist of trajectory tracking scenarios, where the reference signal corresponds to an optimal AoA trajectory. The reference trajectory is generated online through the Lift-to-Drag Ratio (LDR) optimization guidance law described in Equations (1.37)-(1.38). The core objective relies on the maximization of the projectile operating range capability. A first set of baseline simulations is performed to assess the range performance of the polytopic and the grid-based controllers at nominal flight conditions. The simulations are repeated by varying the firing parameters in order to find the optimal conditions for the range enhancement. These conditions are later employed for a comparison between the performance of each controller at nominal conditions and when wind disturbance signals are considered.

4.4.1 Controllers Implementation

As discussed in Sections 3.3.3-3.4.3, the designed LPV controllers are evaluated, respectively, at each scheduling functions condition, ($\hat{\rho}_1$, $\hat{\rho}_2$, $\hat{\rho}_3$), corresponding to a vertex of the polytope, $\hat{\Theta}_{\mathrm{R}}$, and at each scheduling variables combination, (α, V, h), belonging to a point of the design grid, Ξ. As a result, a set of 8 local LTI realizations of K_{PY}, and a set of 80 local LTI realizations of K_{GR} are stored for the implementation of the online controller interpolation.

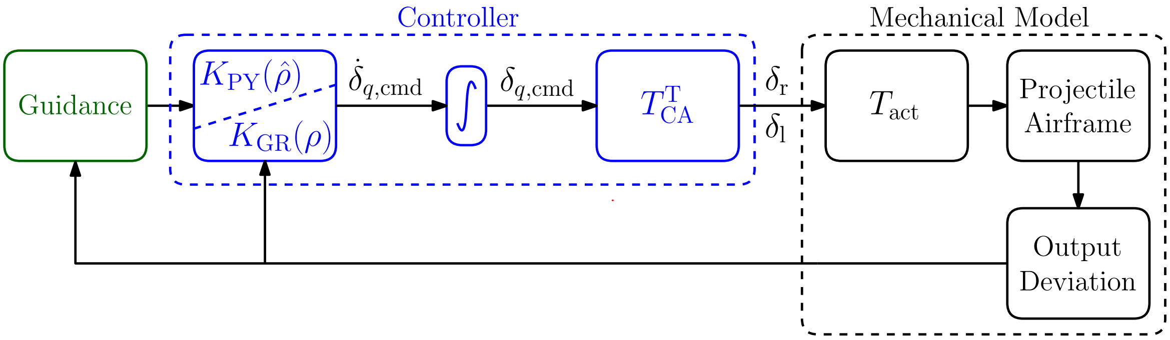

Figure 4.16: Nonlinear simulation implementation scheme.

Since the polytope has been defined as a 3D cuboid, the interpolation of K_{PY} can be achieved through the online implementation of the interpolation function, $\mu_{\hat{\theta}}$, defined as in Equation (2.5). As discussed in [Dub18], the interpolation relies on a binary representation of the polytope vertices, thus improving the computation efficiency. The interpolation of K_{GR} is implemented through a dedicated function, `LPVBlock`, provided by the LPVTools MATLAB Toolbox ([HSP15]). As mentioned in Remark 3.11, before the online implementation, a first interpolation has been performed to eliminate the dependence of the controller K_{GR} to the parameter variation rates. This operation halves the number of LTI local controllers obtained during the synthesis process from 160 to 80, simplifying the implementation.

Finally, at the output of each controller in the 6-DoF simulator of Figure 4.16, an integrator is imposed to convert the generated controller command, $\dot{\delta}_{q,\mathrm{cmd}}$, into the corresponding pitch deflection, $\delta_{q,\mathrm{cmd}}$. Indeed, due to the input integration included during the LPV modeling process in Section 2.3.2.2, the input of the quasi-LPV/polytopic projectile models employed during the control design depends on the pitch deflection rate. The obtained pitch deflection command is then converted into a set of real canard deflections, (δ_{r}, δ_{l}), to be performed by the actuators, through the allocator function defined as the transpose of the transformation matrix, T_{CA}, in Equation (1.25).

4.4.2 Baseline Simulations

The first set of simulations aims to test the range performance of the controllers at different firing conditions. A fixed initial firing velocity of $u_0 = 939$ m/s (zone 6) is assumed across all the simulations to maximize the projectile range capability. The effect of the variation of the initial elevation angle, θ_{e}, is investigated according to the set of values listed in Table 4.5. The analysis allows for identifying the set of optimal firing conditions, ($u_{0,\mathrm{opt}}$, $\theta_{\mathrm{e,opt}}$), that maximize the trajectory range of the projectile.

Table 4.5: Set of initial elevation angles.

	Test 1	**Test 2**	**Test 3**	**Test 4**
$\boldsymbol{\theta}_{\mathbf{e}}$	50 deg	55 deg	60 deg	65 deg

The trajectory results presented in Figure 4.17 show the range performance of the projectile related to the set of increasing initial firing angles in Table 4.5. The same trajectories are obtained when K_{PY} or K_{GR} are implemented. As highlighted by the results, the range capability tends to increase with the firing angle up to $\theta_{\mathrm{e}} = 60$ deg. The reasons behind this behavior rely mainly on two consequential considerations. First, as shown in Figure 4.17, at larger firing angles the apogee point tends to occur at higher altitude levels. Since the air density diminishes with the altitude increment, the Lift force generated by the interaction between the projectile and the air mass reduces accordingly. As a consequence, the projectile performs a sharp fall in the first part of the gliding trajectory before the increment in the air density provides enough Lift. Thus, after a certain level, the projectile cannot exploit the altitude increment at the apogee.

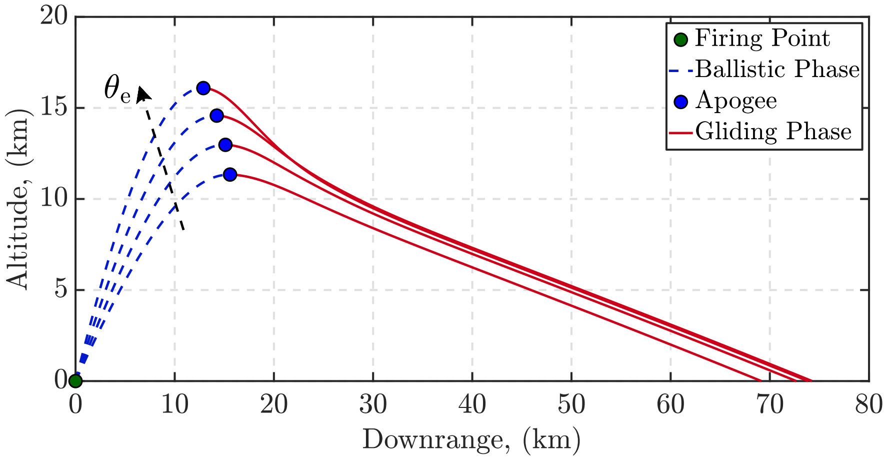

Figure 4.17: K_{PY} and K_{GR} baseline simulations: trajectory performance comparison.

A direct consequence of the altitude increment is additionally highlighted in Figures 4.18(a)-(b), concerning the V-h trajectory relation obtained through the employment of K_{PY} and K_{GR}, respectively. Indeed, the relation between the airspeed and the altitude trajectories reveals how increasing firing angle values push the apogee point towards higher altitude and lower airspeed conditions. The lower airspeed experienced by the projectile at higher altitude levels further reduces the generated Lift force. The results suggest how the apogee V-h conditions achieved with a $\theta_{\mathrm{e}} = 60$ deg angle provide the best compromise in terms of range performance.

The AoA trajectories are presented in Figures 4.18(c)-(d), respectively for K_{PY} and K_{GR}. The results show how the peak of the AoA increases with the value of the firing angle. In particular, for $\theta_{\mathrm{e}} > 60$ deg the AoA peak increases over the range covered by the CFD data acquisitions ($\alpha \in [0, 16]$ deg), reducing the reliability of the projectile dynamics model. Additionally, the AoA trajectories in Figure 4.18(b), associated with lower θ_{e} values, are affected by a larger initial oscillation immediately after the apogee. Indeed, when the apogee is reached and the guidance law is engaged, the initialization value of the reference trajectory is different from the AoA value of the projectile. The mismatch between the two values tends to increase for lower values of θ_{e}, generating a sharp AoA variation rate. While the polytopic control design accounts for worst-case infinite variations of the scheduling variables, the grid-based design allows for specifying the expected variation rate range for each variable. Since a range of $\dot{\alpha} \in [-30, 30]$ deg/s has been selected in Section 3.4.3, the sharp variation experienced at the engagement of the guidance low might affect the performance of the controller.

Similar observations can be made concerning the canards total pitch deflection trajectories, a_{CAN}, in Figures 4.18(e)-(f). The total pitch deflection corresponds to the overall deflection angle perceived by the canards, expressed as the linear superposition between the local pitch deflection commanded by the controller, and the AoA characterizing the trajectory of the projectile, as $a_{\mathrm{CAN}} = \alpha + \delta_q$. Higher values of the firing angle generate higher peaks of canard deflection, possibly leading to stall regime. In particular, for $\theta_{\mathrm{e}} > 60$ deg, the a_{CAN} peak exceeds the canard deflection range characterized by a linear aerodynamic response,

$\delta_r, \delta_l \in [-20, 20]$ deg, identified during the modeling process in Section 1.3.3.4. As for the AoA, deflection values that exceed the range of modeling fidelity might reduce the accuracy of the projectile model. Indeed, the linearity conditions imposed through the Aerodynamic Superposition Assumption 1.7 are not satisfied.

Additional results are provided in Figure 4.19 concerning the trajectories of the scheduling

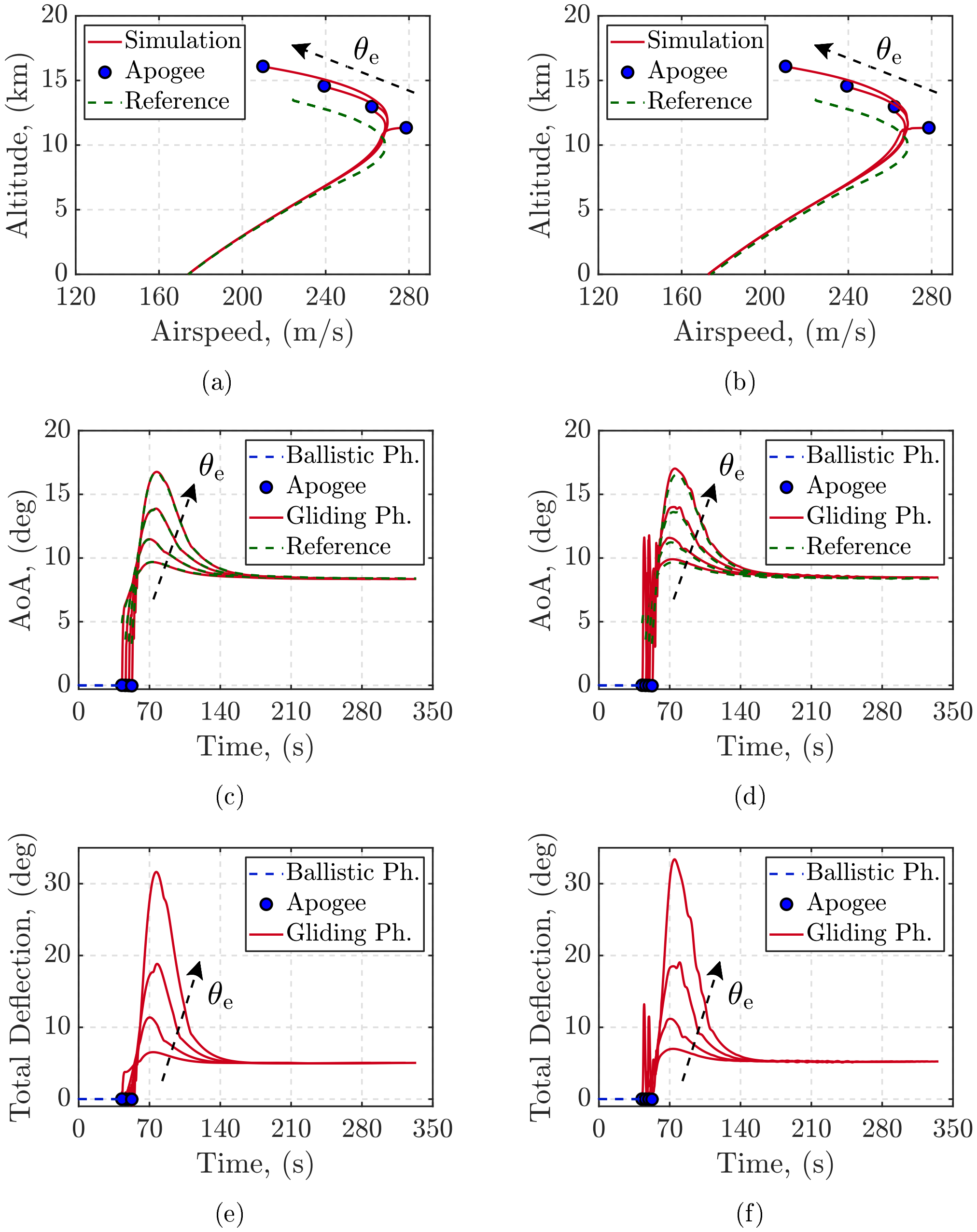

(a) (b)

(c) (d)

(e) (f)

Figure 4.18: K_{PY} and K_{GR} baseline simulations: (a)-(b) V-h relation trajectories, respectively; (c)-(d) AoA trajectories, respectively; (e)-(f) canards total pitch deflection trajectories, respectively.

functions, ($\hat{\rho}_1$, $\hat{\rho}_2$, $\hat{\rho}_3$), employed in the design of K_{PY}. Increasing values of the firing angle tend to push the scheduling functions trajectories at the borders of the designed polytope. However, even at $\theta_{\mathrm{e}} > 65$ deg, where the trajectories partially cross the polytope borders, the controller succeeds in stabilizing the system, proving reliable robustness properties to possible variations of the flight conditions. The overall evolution of the scheduling functions is provided in Figure 4.19(d), where the relative variations of $\hat{\rho}_1$, $\hat{\rho}_2$, and $\hat{\rho}_3$ are represented in the 3D space defined by the reduced polytope, $\hat{\Theta}_{\mathrm{R}}$.

Finally, Figure 4.20 shows the evolution of the original scheduling variables, (α, V, h), across the design point selected for the synthesis of the K_{GR}, in the parameterized 3D flight envelope, Ξ. The projection of the trajectories on the different planes recovers the results discussed above in terms of the V-h relation. In particular, assuming $\theta_{\mathrm{e}} = 65$ deg as firing angle, the trajectory leaves the cluster of grid points where the set of local controllers is defined, leading to a possibly less efficient controller interpolation. Nevertheless, the interpolation guarantees the stability of the closed-loop at any flight conditions, confirming the robustness of the design.

A more exhaustive overview concerning the results of the simulations is provided in the next

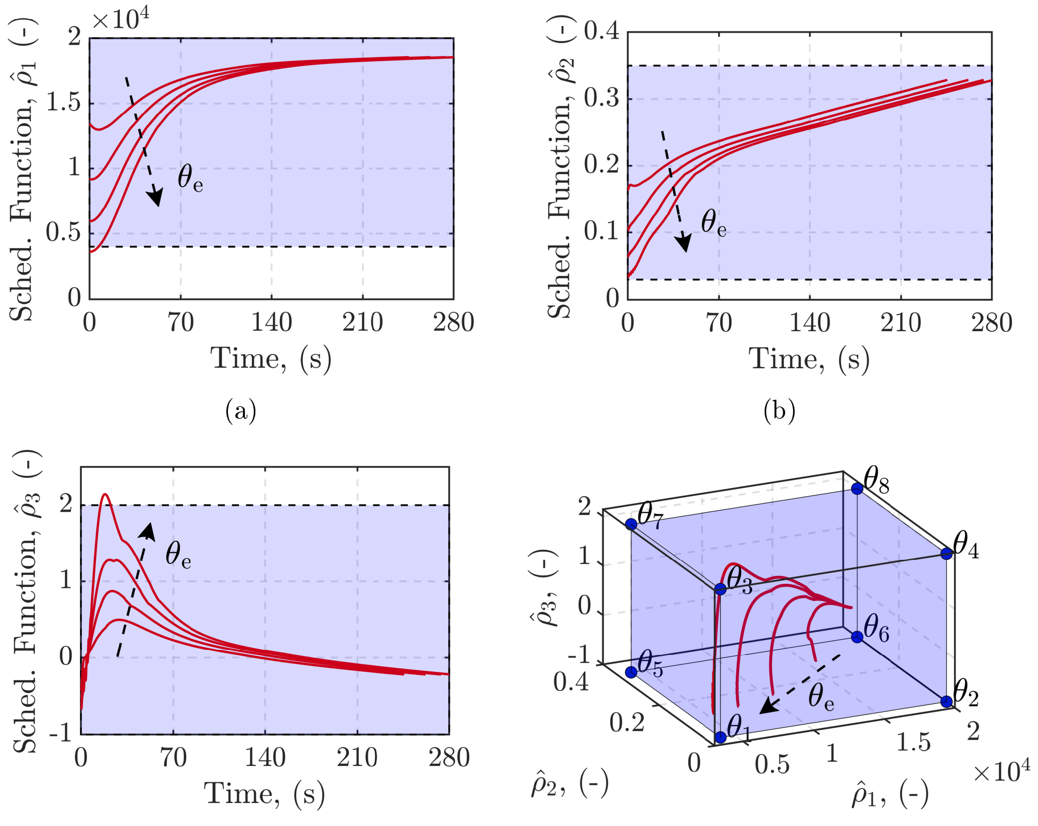

(a) (b)

(c) (d)

Figure 4.19: K_{PY} baseline simulations: (a) $\hat{\rho}_1$ trajectories; (b) $\hat{\rho}_2$ trajectories; (c) $\hat{\rho}_3$ trajectories; (d) 3D scheduling functions trajectories.

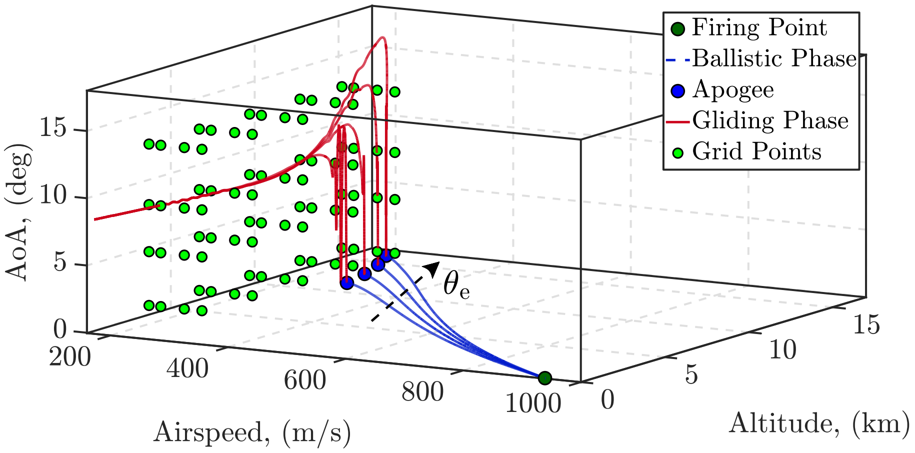

Figure 4.20: K_{GR} baseline simulations: 3D scheduling variables trajectories.

section through a comparison between the performance of K_{PY} and K_{GR} at nominal flight conditions and when wind contributions are considered. In particular, the effects of wind turbulence and sudden wind gusts will be investigated. The results of the above simulations at multiple firing conditions suggest the selection of an initial elevation angle, $\theta_{\mathrm{e}} = 60$ deg, for range optimization purposes. As a consequence, this optimal firing angle will be employed in the next round of simulations to further assess the performance of the controllers.

4.4.3 Wind-based Disturbance Simulations

In order to further assess the tracking and stabilization performance of the LPV polytopic and grid-based controllers, an additional round of simulations addresses the effects of external time-varying disturbances. The disturbance signals correspond to wind contributions in the form of turbulence and sudden gusts, affecting the vertical and longitudinal components of the relative wind velocity, $\boldsymbol{v}_E^A$. As discussed in Chapter 1 through the Zero Wind Assumption 1.3, the nominal modeling conditions account for zero relative motion between the air frame, A, and the Earth frame, E. The wind disturbances are simulated during the gliding phase of the trajectory after the apogee is reached and the canards are deployed.

A realization of the longitudinal and the vertical wind profiles is presented in Figures 4.21(a)-(b), respectively. The profile is obtained as the superposition between a continuous turbulence perturbation and a discrete wind gust. The band-limited white noise turbulence signal relies on the Von Kármán spectral representation implemented in the dedicated MATLAB/Simulink `Aerospace Blockset` ([MF97]; [Gag03]), imposing the parameters listed in Table 4.6. In particular, v_{low} defines the wind speed at low altitude, n_{T}, stands for the noise sample time, L_{high} sets the scale length that determines the power spectral density asymptote and gust load, and [u_{T}, v_{T}, w_{T}, p_{T}] is the vector of noise seeds used to generate the random signals. Since the simulation targets the pitch channel of the projectile dynamics, the lateral and the roll signals, v_{T} and p_{T}, are set to zero.

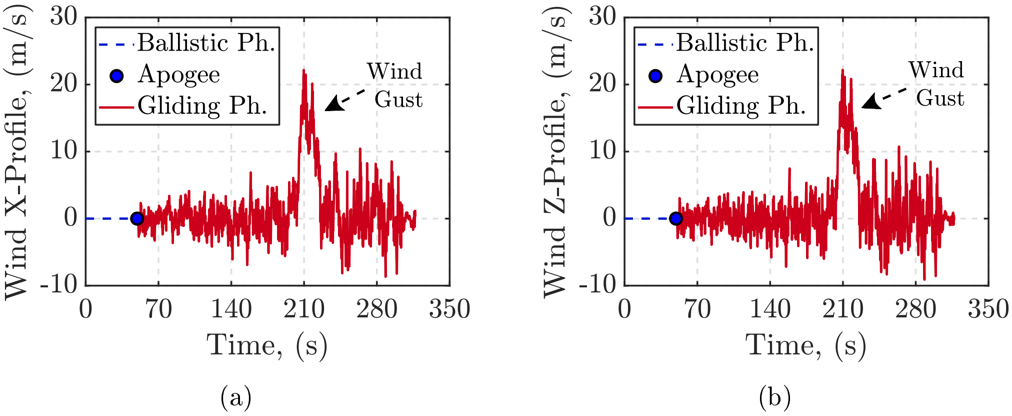

Figure 4.21: Wind velocity profile: (a) longitudinal; (b) vertical.

Similarly, a standard '1-cosine' shape wind gust is obtained through the discrete model provided in the `Aerospace Blockset` ([MF80]). A set of sequential ascending and descending gusts (Gust_A and Gust_D) models the sudden variation of the wind profile as a global gust occurring during the gliding phase of the trajectory, in the time interval, $t_\text{G} \in [200, 220]$ s. The parameters selected to define the gust shapes are presented in Table 4.7. The gust length coefficients, d_{x_G} and d_{z_G}, define the extension of the gusts along the longitudinal and vertical axes, respectively, while the amplitude coefficients, u_G and w_G, set the magnitude of the corresponding wind velocity signals along each axis.

Table 4.6: Wind turbulence parameters.

v_low (m/s)	L_high (m)	n_T (s)	u_T (−)	w_T (−)
5	200	0.1	1000	1000

Table 4.7: Wind gusts parameters.

	d_{x_G} (km)	d_{z_G} (km)	u_G (m/s)	w_G (m/s)	t_G (s)
Gust$_\text{A}$	2	2	+15	+15	200
Gust$_\text{D}$	2	2	−15	−15	220

The performance related to the polytopic and the grid-based controllers, investigated at both nominal and wind-perturbed flight conditions, are individually compared in the following dedicated sections.

4.4.3.1 Polytopic Controller Simulations

The performances of the polytopic controller are compared through the same trajectory tracking scenario simulated both at nominal conditions and in the presence of wind contributions, modeled as the velocity profiles in Figures 4.21(a)-(b). The optimal firing conditions identified in Section 4.4.2 are assumed in both scenarios. The trajectories in Figure 4.22 show the effect of the wind disturbance on the projectile operating range capability. The curves are perfectly superposed until the occurrence of the wind gust, suggesting how the controller manages to stabilize the system and limit the oscillation generated by the continuous turbulence signal. Even though the large amplitude imposed on the wind gust does not destabilize the projectile dynamics, the longitudinal contribution of the gust signal reduces the range capability.

These considerations are confirmed by the AoA trajectory in Figure 4.23(b) where the turbulence generates a very contained oscillation of the AoA signal around the nominal curve shown in Figure 4.23(a). The occurrence of the wind gusts on the vertical axis results in a mild peak of AoA, which is recovered immediately after the gusts contributions have vanished. As an important remark, the reference AoA trajectory does not aim at maintaining a constant value but rather at finding the optimal condition that maximizes the Lift-to-Drag Ratio at each flight point. Thus, if the inclusion of a wind contribution increases the AoA of the projectile, the guidance algorithm eventuates the new optimal AoA reference based on the current conditions. Concerning the pitch rate trajectory, the large oscillation observed in Figure 4.23(d) derives only from the turbulence effect since no contributions are generated through the application of the gusts.

The curves in Figures 4.23(e)-(f) and Figures 4.24(a)-(b) represent respectively the results related to the pitch angle and Mach number trajectories. In both cases, a very contained oscillation is observed in the interval of occurrence of the wind gusts. The effect related to the turbulence signal seems almost negligible. Concerning the V-h trajectories relation in Figures 4.24(c)-(d), the signal oscillates around the reference nominal trajectory and rapidly recovers from the perturbation generated by the wind gusts that mainly reduces the projectile airspeed. A fundamental confirmation regarding the performance of the polytopic controller relies on the canards' total deflection angle trajectories in Figures 4.24(e)-(f). Indeed, despite the large amplitude of the gust perturbation affecting the trajectory, the canards deflection remains in the safe range of linear aerodynamic response assumed for the CFD data acquisition and regression procedure. Additionally, the deflection angle peak value is maintained far below the

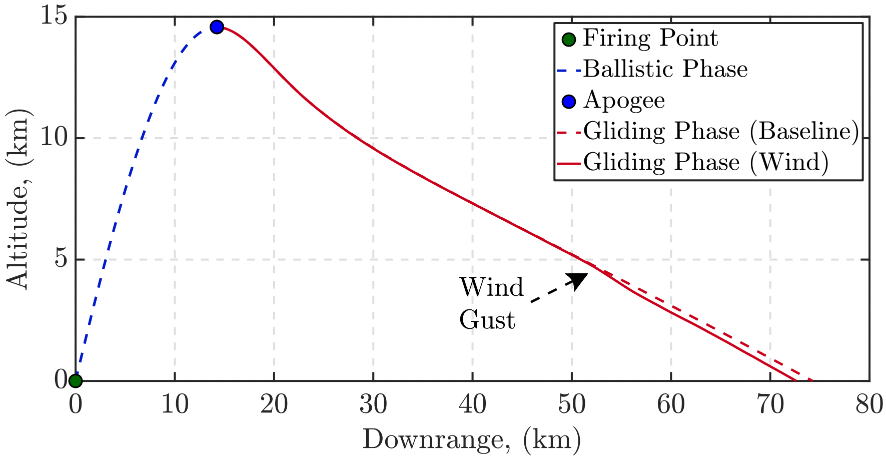

Figure 4.22: Polytopic simulations: trajectory performance.

limit of saturation of the canards. As observed for the AoA trajectory, the turbulence signal generates a contained oscillation around the nominal curve shown in Figure 4.24(e).

The results presented in Figure 4.25 show the effect of the wind disturbance on the set of scheduling functions ($\hat{\rho}_1$, $\hat{\rho}_2$, $\hat{\rho}_3$). Despite the introduction of the turbulence and the wind gusts, all the scheduling functions vary inside the convex subspace (blue box) defined by

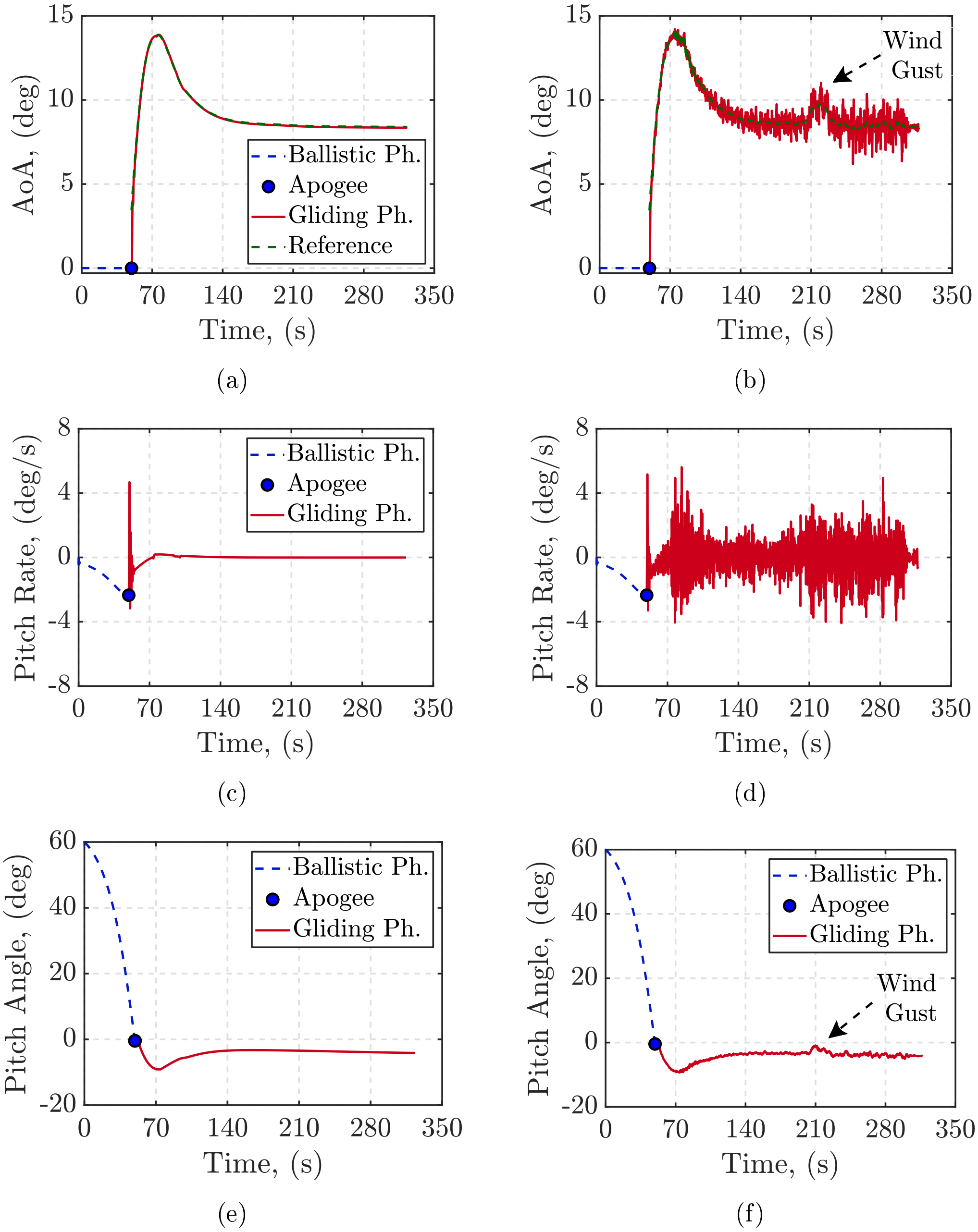

(a) (b)

(c) (d)

(e) (f)

Figure 4.23: Polytopic simulations: (a)-(b) AoA nominal and perturbed trajectories, respectively; (c)-(d) pitch rate nominal and perturbed trajectories, respectively; (e)-(f) pitch angle nominal and perturbed trajectories, respectively.

the polytope, $\hat{\Theta}_{\mathrm{R}}$, as observed in Figures 4.26(a)-(b). The comparison between the nominal curves and the trajectories affected by the wind disturbance reveals once again a contained oscillation and a limited peak in response to the gust contributions. A direct consequence related to the oscillation of the scheduling functions can be observed in Figures 4.27(a)-(b) through the interpolation trajectories associated with each of the LTI local controllers designed

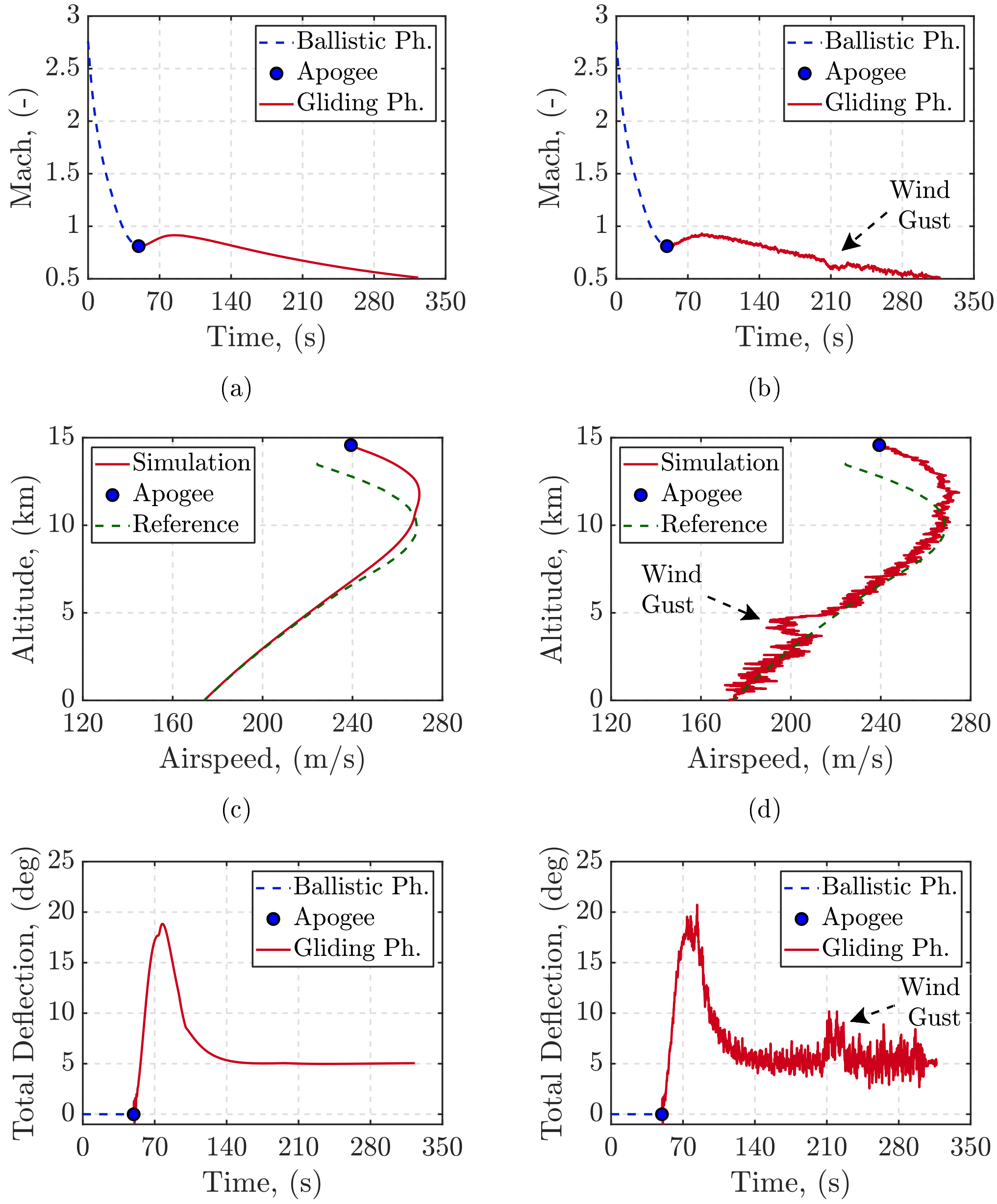

(a) (b)

(c) (d)

(e) (f)

Figure 4.24: Polytopic simulations: (a)-(b) Mach nominal and perturbed trajectories, respectively; (c)-(d) V-h relation nominal and perturbed trajectories, respectively; (e)-(f) canards total pitch deflection nominal and perturbed trajectories, respectively.

at the vertices of the polytope. The nominal case dataset in Table 4.8 provides an overview of the relevance of each local controller (at the $\hat{\boldsymbol{\theta}}_i$ vertex, with $i = 1, \cdots, 8$) on the overall interpolation process, across the entire trajectory of the projectile. As expected, $K_{\hat{\theta}_1}$ and $K_{\hat{\theta}_3}$ show a prevalent percentage in the controller interpolation at the beginning of the simulation, while the influence of $K_{\hat{\theta}_6}$ and $K_{\hat{\theta}_8}$ increases along with the trajectory and provides on average

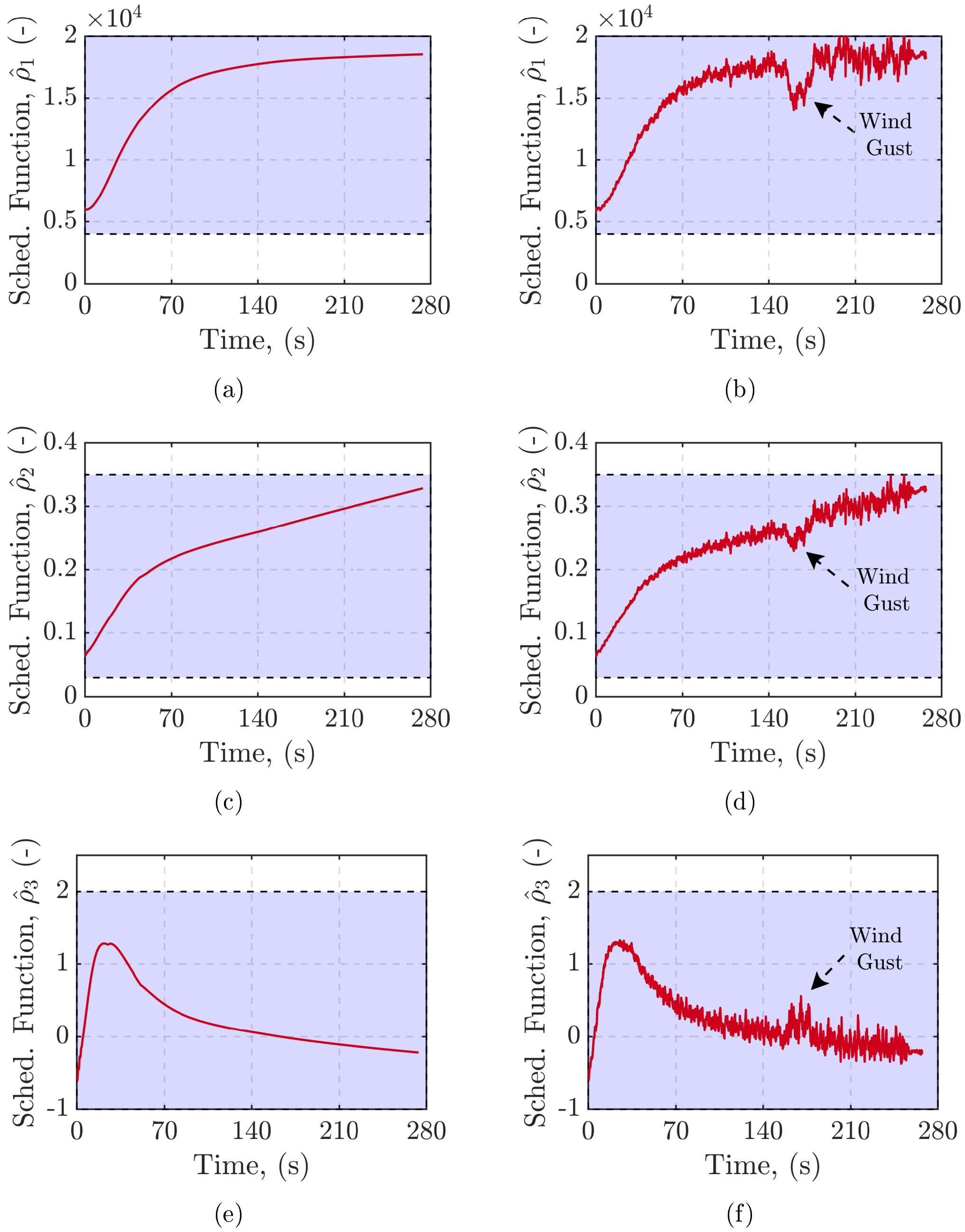

Figure 4.25: Polytopic simulations: (a)-(b) $\hat{\rho}_1$ nominal and perturbed trajectories, respectively; (c)-(d) $\hat{\rho}_2$ nominal and perturbed trajectories, respectively; (e)-(f) $\hat{\rho}_3$ nominal and perturbed trajectories, respectively.

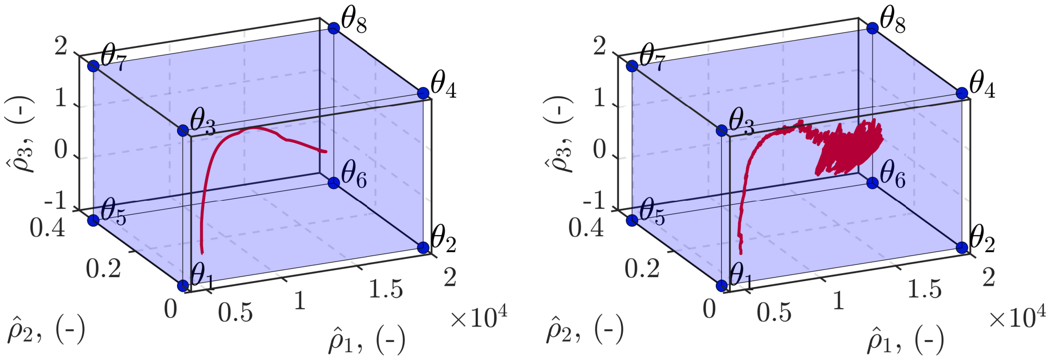

(a) (b)

Figure 4.26: Polytopic simulations: (a) 3D nominal scheduling functions trajectories; (b) 3D perturbed scheduling functions trajectories.

Table 4.8: Controller interpolation functions analysis.

Interp.	**Controllers**	$\hat{\boldsymbol{\rho}}_1$	$\hat{\boldsymbol{\rho}}_2$	$\hat{\boldsymbol{\rho}}_3$	**max %**	**min %**	**Average %**
$\mu_{\hat{\theta}_1}$	$K_{\hat{\theta}_1}$	$0.4 \cdot 10^4$	0.05	-1	68	0.4	13
$\mu_{\hat{\theta}_2}$	$K_{\hat{\theta}_2}$	$2 \cdot 10^4$	0.05	-1	9	5	7
$\mu_{\hat{\theta}_3}$	$K_{\hat{\theta}_3}$	$0.4 \cdot 10^4$	0.05	2	41	0.1	9
$\mu_{\hat{\theta}_4}$	$K_{\hat{\theta}_4}$	$2 \cdot 10^4$	0.05	2	17	2	6
$\mu_{\hat{\theta}_5}$	$K_{\hat{\theta}_5}$	$0.4 \cdot 10^4$	0.35	-1	17	0.5	11
$\mu_{\hat{\theta}_6}$	$K_{\hat{\theta}_6}$	$2 \cdot 10^4$	0.35	-1	63	0.1	28
$\mu_{\hat{\theta}_7}$	$K_{\hat{\theta}_7}$	$0.4 \cdot 10^4$	0.35	2	20	1	9
$\mu_{\hat{\theta}_8}$	$K_{\hat{\theta}_8}$	$2 \cdot 10^4$	0.35	2	22	0.1	16

the most relevant contributions. Despite the fact that the 3D trajectory of the scheduling functions in Figure 4.26(a) seems to be quite independent of the local controllers $K_{\hat{\theta}_4}$, $K_{\hat{\theta}_5}$,

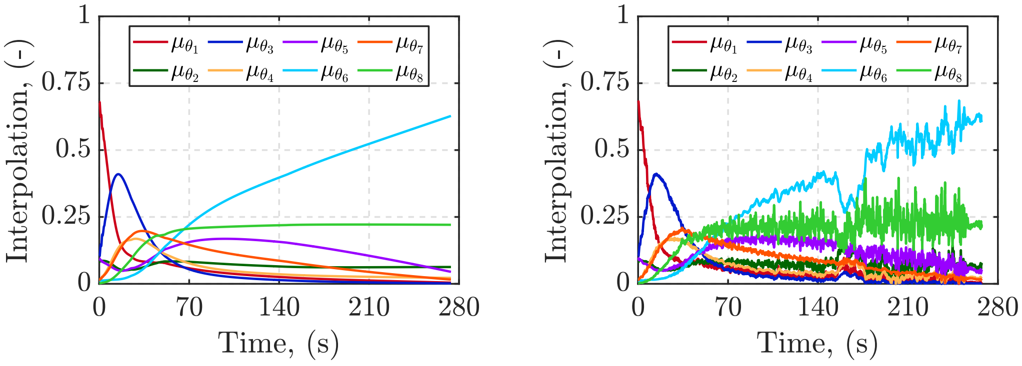

(a) (b)

Figure 4.27: Polytopic simulations: (a) 3D nominal interpolation functions trajectories; (b) 3D perturbed interpolation functions trajectories.

and $K_{\hat{\theta}_7}$, the results in Table 4.8 show their non-negligible role in the interpolation. On the contrary, the last controller, $K_{\hat{\theta}_2}$, appears to be generally of marginal importance. The restricted subspace covered by the 3D trajectory in Figure 4.26(a) suggests how a redefinition of the polytope's shape might further improve the optimization of the controller design. The presence of the wind contributions in Figure 4.27(b) generates an evident oscillation of the interpolation functions around their nominal values. Nevertheless, the interpolation conditions expressed in Equation (2.5) are satisfied at each flight point across the trajectory.

4.4.3.2 Grid-Based Controller Simulations

The same simulations comparison is proposed to assess the performance of the grid-based controller when the nominal conditions are affected by the wind velocity profiles in Figures 4.21(a)-(b). As in the polytopic case, the operating range performance shown by the trajectories in Figure 4.28 is slightly reduced by the effect of the longitudinal wind gusts, while the turbulence signal does not seem to have an impact on the trajectory. However, the controller successfully preserves the projectile dynamics stability at any flight conditions.

The impact of the disturbance signal is more evident through the AoA and pitch rate trajectories comparison presented in Figures 4.29(a)-(b) and Figures 4.29(c)-(d), respectively. Indeed, signal oscillations larger than in the polytopic case characterize the curves of the perturbed simulations. However, even when wind gusts occur, the stability of the closed-loop dynamics is guaranteed. The expected larger oscillations are coherent with the lower stability guarantees provided by the grid-based design compared to the polytopic one. Additionally, the lower initial oscillation observed in the nominal AoA trajectory in Figure 4.29(a) depends on the smaller gap between the AoA curve and the reference signal. The improvement is obtained by selecting $\theta_\mathrm{e} = 60$ deg as the initial firing angle. Similar results can be observed also in the pitch angle trajectories in Figures 4.29(e)-(f). The wind disturbance deviates the curve from its nominal value before properly re-converging at the impact point.

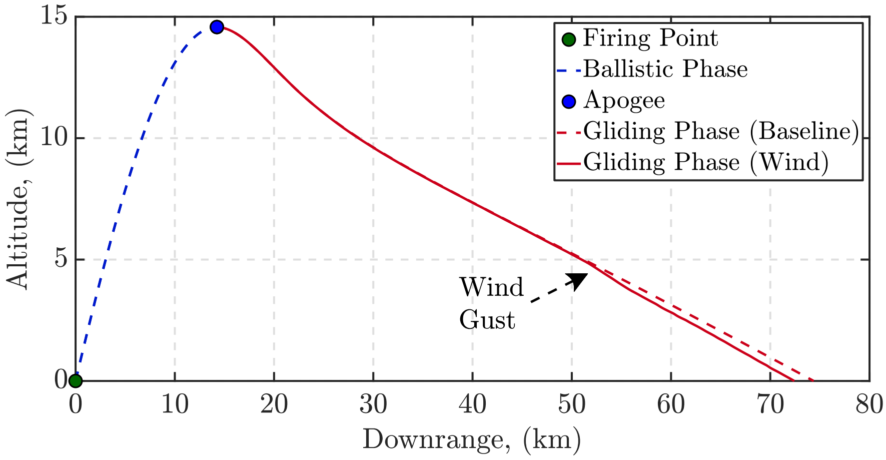

Figure 4.28: Grid-based simulations: trajectory performance.

While a mild oscillation affects the Mach trajectories in Figures 4.30(a)-(b), the impact of the wind gusts modifies the V-h relation which converges to the reference nominal value once the gusts vanish, as in Figures 4.30(c)-(d). A relevant oscillation characterizes also the canards total pitch deflection trajectories. As presented in Figures 4.30(e)-(f) the occurrence of the gusts combined with the continuous turbulence disturbance pushes the canards' deflection

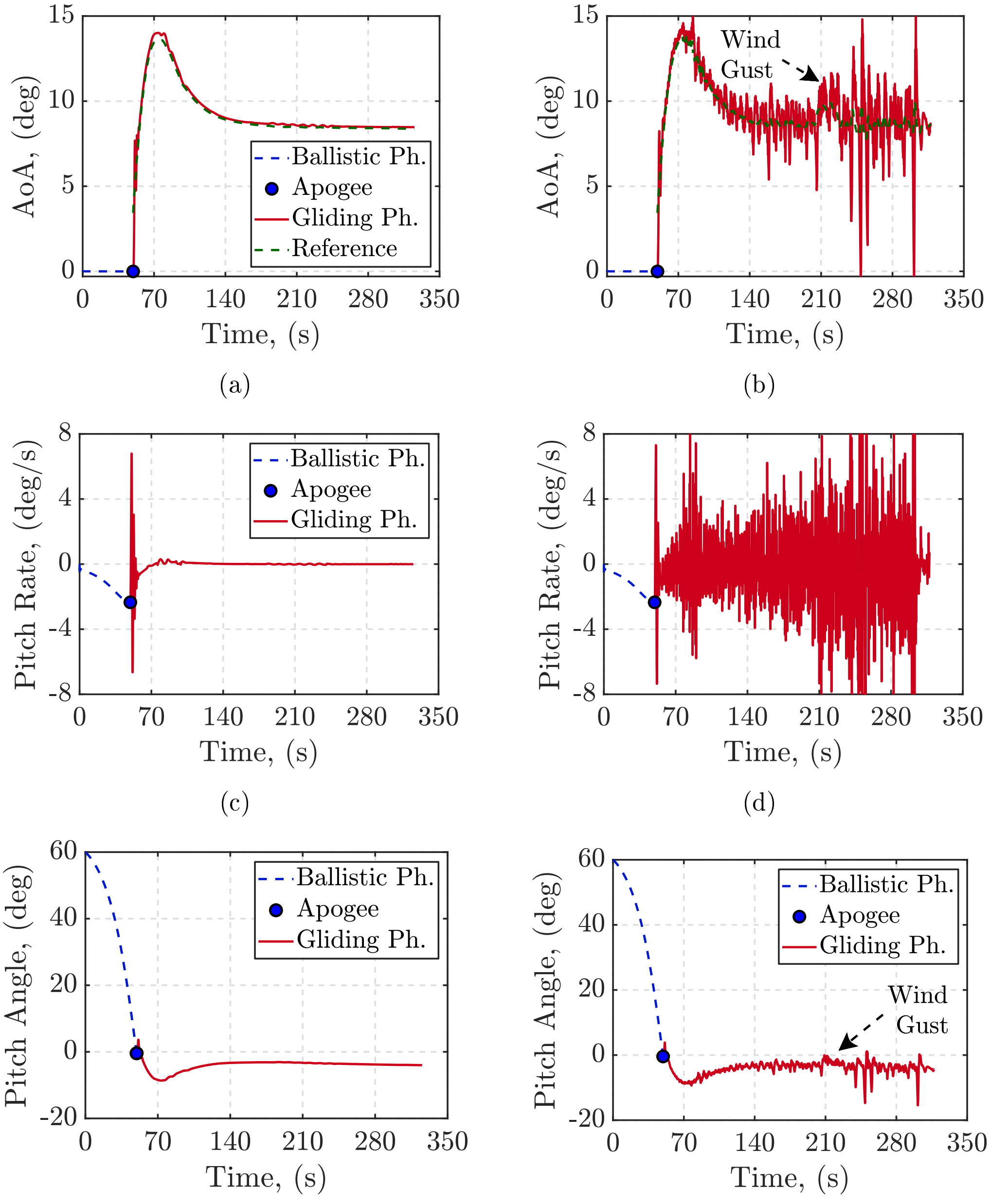

(a) (b)

(c) (d)

(e) (f)

Figure 4.29: Grid-based simulations: (a)-(b) AoA nominal and perturbed trajectories, respectively; (c)-(d) pitch rate nominal and perturbed trajectories, respectively; (e)-(f) pitch angle nominal and perturbed trajectories, respectively.

close to the identified limits of linear aerodynamic response. However, large margins are maintained from any stall regime conditions.

As discussed in Section 3.4, the grid-based control design approach allows for the definition of the specific rate of variation range of each of the investigated scheduling variables. At the

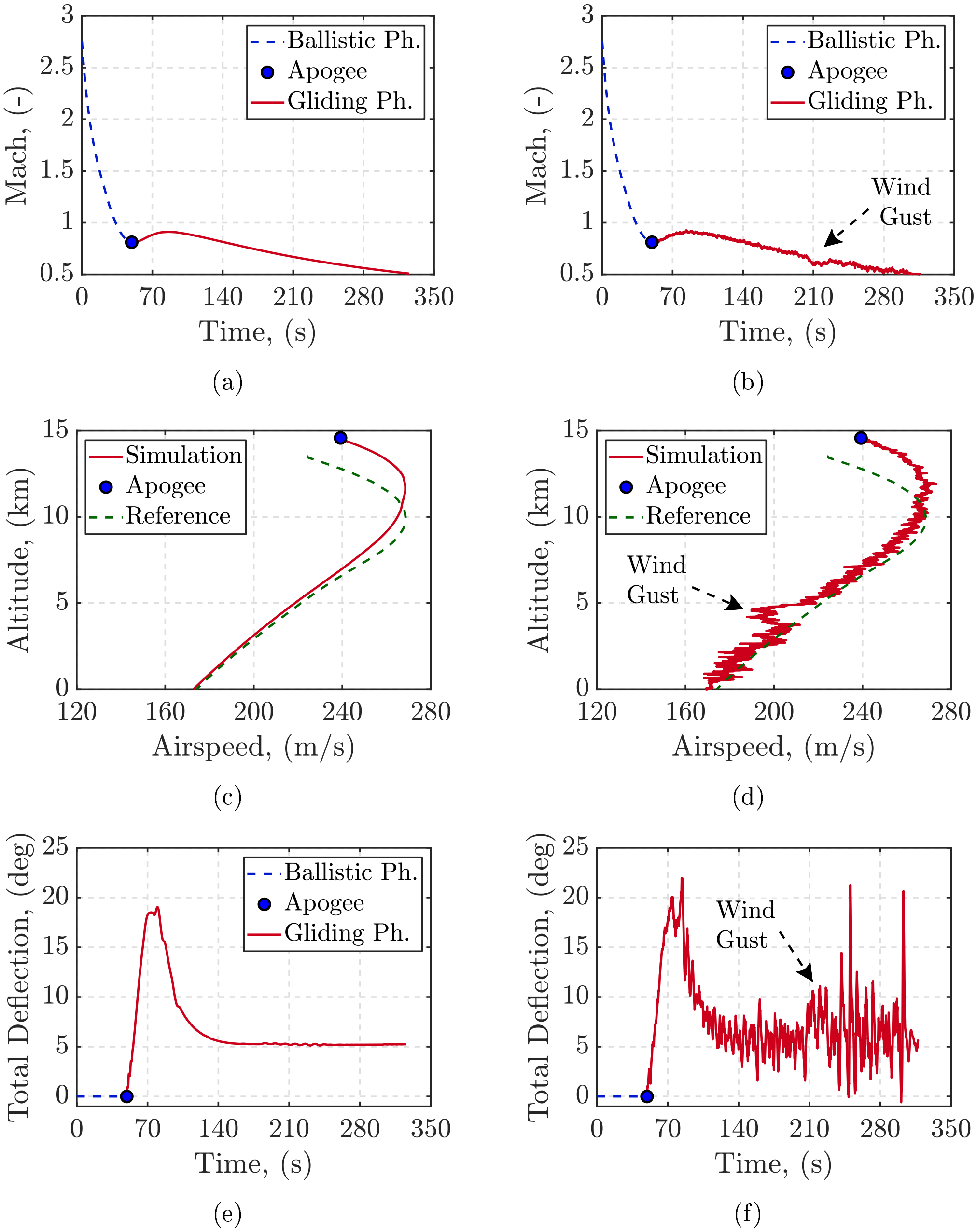

Figure 4.30: Grid-based simulations: (a)-(b) Mach nominal and perturbed trajectories, respectively; (c)-(d) V-h relation nominal and perturbed trajectories, respectively; (e)-(f) canards total pitch deflection nominal and perturbed trajectories, respectively.

design stage, the following ranges have been selected: $\dot{\alpha}_{\text{grid}} \in [-30, 30]$ deg/s, $\dot{V}_{\text{grid}} = [-50, 50]$ m/s^2, and $\dot{h}_{\text{grid}} = [-100, 100]$ m/s. In order to guarantee that the closed-loop stability properties are preserved, the scheduling variables rates should remain within the limits imposed by the design ranges across the entire trajectory. As shown in Figures 4.31(a)(c)(e), the scheduling variables rates largely respect the boundaries imposed during the control design. The only

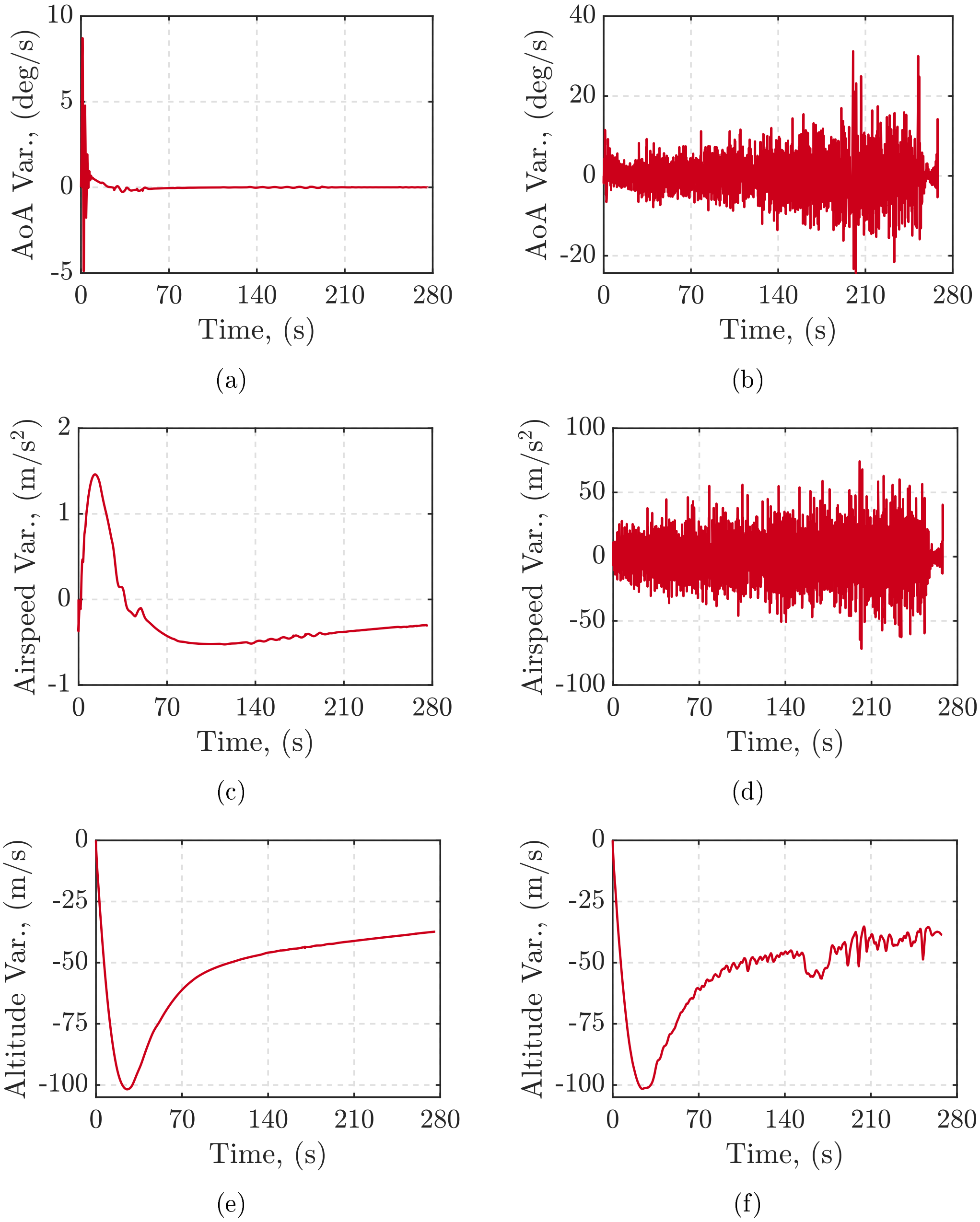

Figure 4.31: Grid-based simulations: (a)-(b) AoA variation rate nominal and perturbed trajectories, respectively; (c)-(d) airspeed variation rate nominal and perturbed trajectories, respectively; (e)-(f) altitude variation rate nominal and perturbed trajectories, respectively.

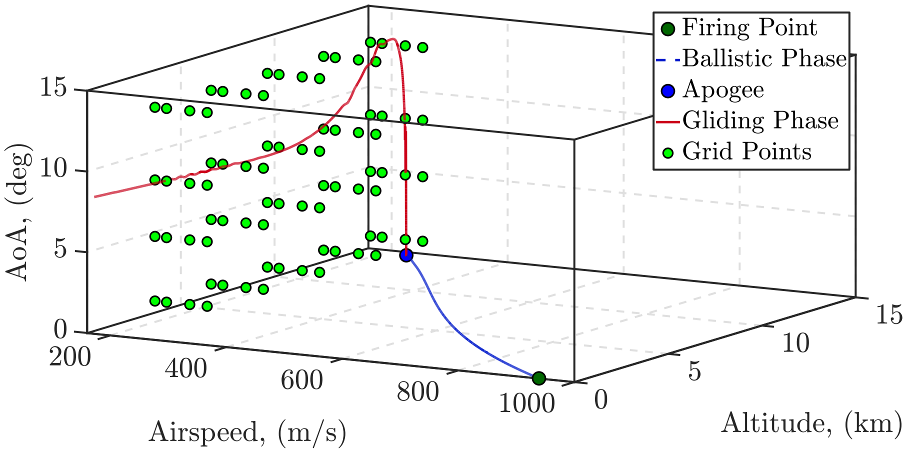

Figure 4.32: Grid-based nominal simulation: 3D scheduling variables trajectory.

exception consists of the altitude trajectory in Figure 4.31(e), where the peak value reaches the lower bound of the rate of variation range. However, the results of the nominal simulation confirm the capability of the controller to stabilize the system across the entire trajectory. Concerning the effect of the wind disturbance, the curves in Figures 4.31(b)(d) are affected by a large oscillation mainly generated by the high-frequency turbulence signal. The AoA variation rate peak reaches the upper bound of the design range without exceeding it, while the airspeed rate trajectory crosses several times both the upper and the lower variation rate boundaries. Nevertheless, the controller manages to stabilize the projectile dynamics even in the extreme case of scheduling variables sudden variations.

Finally, a global overview regarding the evolution of the scheduling variables trajectory across the design grid-points is provided in Figure 4.32, relative to the nominal conditions, and in Figure 4.33, accounting for the effects of the wind disturbance.

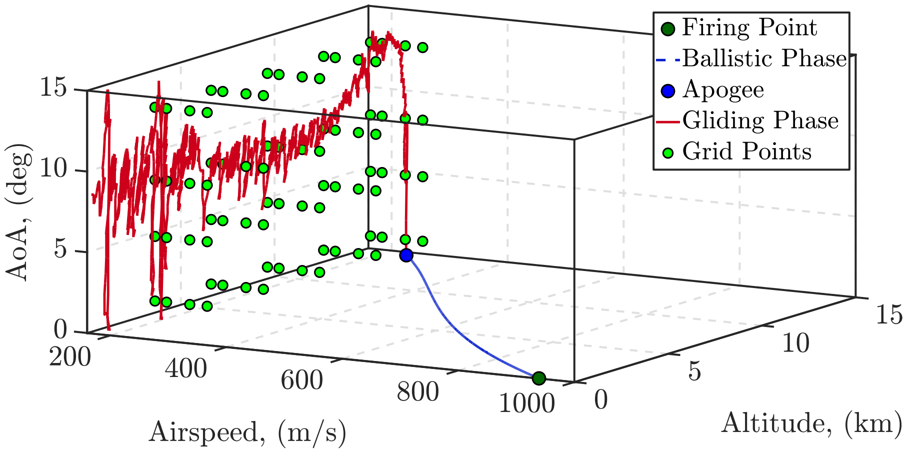

Figure 4.33: Grid-based perturbed simulation: 3D scheduling variables trajectory.

4.5 Concluding Remarks

In this chapter, the performances of the polytopic and the grid-based controllers have been investigated w.r.t. several forms of system disturbance. A first robustness analysis relies on the evaluation of the stability margins of the input/output loop transfer functions related to each system. Since both the quasi-LPV and the polytopic models consist of SIMO systems, the computation of the disk margins is preferred to the standard definitions of SISO gain and phase margins. The results obtained through the analysis of both systems reveal large output disk margins relative to the first and the third channel dynamics. Nevertheless, possible robustness weaknesses are highlighted through the evaluation of the input disk margin and the output disk margins related to the second channel dynamics.

The stability margins provide only necessary but not sufficient conditions to assess the system robust stability and might result in a very conservative investigation. Thus, the performances of the controllers have been further tested through a μ-sensitivity analysis, targeting the robustness w.r.t. structured system parametric uncertainties. A set of parameters was selected based on the effect of their variation on the system dynamics stability. The uncertain set includes the parameters: $\bar{q}$, $C_{Z_{\delta_q}}$, $C_{m_{\delta_q}}$, and $C_{m_{\mathrm{S}}}$, each associated with an estimated range of tolerance (expressed as a percentage of uncertainty). However, due to the excessive complexity of the numerical formulation, the individual parametric uncertainties are modeled as global perturbation affecting each entry of the systems' state space representation. The μ-analysis performed on the dedicated set of uncertainties reveals satisfactory robust stability and robust performance properties of both the polytopic and the grid-based closed-loop systems to parametric uncertainties. In particular, the percentage of system uncertainty the polytopic controller can handle is higher compared to the corresponding grid-based performance. These results are coherent with the stronger stability theoretical guarantees provided by the polytopic controller synthesis.

Finally, the performances of the controllers have been tested w.r.t. the effect of time-varying disturbance signals. A first set of nominal trajectory tracking simulations is performed by implementing the controllers in the 6-DoF nonlinear simulator environment. The simulations allow identifying the optimal firing velocity and elevation angle (939 m/s, 60 deg). In the second stage, wind disturbances are included in the simulation scenarios in the form of continuous turbulence and discrete wind gusts velocity profiles. The results confirm the robustness of the polytopic controller in handling the large signal oscillations generated by the wind contributions. Indeed, the perturbed scheduling functions' trajectories lie in the convex space employed during the controller synthesis, thus ensuring the stability of the closed-loop system even in the presence of large disturbance signals. The grid-based controller also succeeded in preserving the stability of the projectile across the entire trajectory, even though the obtained flight parameters are generally affected by much larger oscillations around their nominal values, compared to their polytopic counterpart.

Conclusion and Perspectives

General Conclusions

The purpose of the thesis consists of the investigation of linear parameter-varying (LPV) techniques for the modeling and control design of a new concept of Long-Range Guided Projectile (LRGP). The development of a range-extended munition aims to target the technological gap between standard gun-launched ballistic/guided projectiles and the more sophisticated rocket-propelled missile applications. The LPV framework represents a relevant novelty in the design of projectile applications, offering several advantages in terms of model fidelity and control guarantees compared to standard approaches. However, the lack of a rich literature background poses several open challenges:

- **I:** The highly nonlinear flight dynamics/aerodynamics governing the projectile behavior increases significantly the complexity of the LPV modeling process. The process has to account for a large number of varying parameters with a non-negligible impact on the system stability and performance.
- **II:** The case-dependent nature of the LPV model formulation, based on the projectile nonlinear dynamics, requires an exhaustive investigation of the dynamics of the system. Depending on the objectives of the design, several control-oriented modeling approaches can be employed to obtain an accurate LPV model.
- **III:** The projectile ballistic trajectory covers a significant envelope of flight conditions. The LPV-based control design targets the synthesis of a controller (or a set of controllers) able to guarantee stability at any operating conditions. The formulation of the controller synthesis relies on an LMIs-based optimization problem whose numerical complexity is strictly dependent on the number of conditions accounted for in the design.

Chapter 1: A major contribution presented in this work consists of the proposition of a complete modeling and control design process of the projectile concept. Indeed, Chapter 1 has been dedicated to the development of a reliable 6-DoF flight dynamics model of the projectile, based on standard flight mechanics considerations and on an ad-hoc designed aerodynamic model. The modeling challenge relies on the need to find an accurate aerodynamic regression model that properly fits a large set of CFD data and is suitable for the subsequent LPV control-oriented reformulation. To this end, two regression models have been proposed. A first control-oriented polynomial model was derived on a limited set of CFD data, accounting for the dynamic decoupling between the pitch and the roll-yaw channels. A second multivariable regression was performed on the entire CFD dataset obtaining a general aerodynamic model to be employed in the validating simulations. The models' domain of fidelity is strictly related to the specific framework developed for the CFD data acquisition. The assumption of multiple aerodynamic contributions superposition holds only under limited conditions that have to be accounted for at both the LPV modeling and control design stages. The full model characterization has been validated in a dedicated nonlinear simulator environment through preliminary ballistic trajectory simulations.

Chapter 2: The control-oriented LPV modeling relies on the accurate selection of the varying parameters. Since the projectile dynamics depends on several flight parameters, the selection implies an exhaustive analysis of the performance of the systems, with special attention dedicated to the stability conditions. The reformulation of nonlinear system dynamics into an LPV model represents a delicate process, which strongly depends on the investigated application. Few approaches have been proposed in the literature as a general solution to this task, yet accounting for relevant assumptions and limitations. The employment of the state transformation technique is restricted to a certain class of nonlinear systems, namely output nonlinear (or output dependent). Despite the fact that the projectile dynamics falls into this category, ad-hoc adjustments were necessary to fully comply with the formulation requirements. The presentation of the complete modeling process from the nonlinear to the LVP formulation, including all the considerations related to the conversion, provides an interesting study case, often not detailed in many standard applications. Furthermore, the reformulation of the projectile quasi-LPV model as a polytopic system added a layer of complexity through the approximation analysis. The identification of a new set of scheduling functions relied on an accurate mapping process, aiming to minimize the conservatism introduced by the formulation. The definition of a 3D convex space poses a significant design challenge in reason of the consequent complexity.

Chapter 3: The complexity concerning the synthesis of an LPV autopilot for guided munitions consists of the large variation characterizing most of the flight parameters during the trajectory. Indeed, the controller optimization has to satisfy the constraints imposed at several flight conditions, often resulting in very conservative solutions. The polytopic design ensures stronger stability guarantees at the expense of more conservative optimization results. The formulation requires a dedicated modeling process which adds a layer of complexity and approximation to the resulting design accuracy. The polytope dimension optimization allows for reducing the conservativeness affecting the design by neglecting areas of the convex space never covered by the projectile trajectory. The reduction consists of an intrinsically case-dependent approach that targets a specific projectile optimal trajectory. However, due to the model convexity requirements, unfeasible flight conditions were still included in the definition of the polytope. A further improvement would require the employment of a more sophisticated interpolation approach, allowing for more complicated polytope shapes that better fit the actual trajectories of the scheduling variables.

Regarding the grid-based design, the complexity consists of the lack of general guidelines in the selection of the operating grid points and in the definition of the parameter-dependent Lyapunov functions. The higher optimization performances are associated with lower stability guarantees at the controller interpolation stage, highlighting the relevance of the grid-points selection. In the presented study, a dedicated analysis targets these aspects through the identification of the most critical areas of the projectile flight envelope. An interesting contribution relies on the challenge posed by the selection of a 3D grid of conditions, which increases exponentially the numerical complexity of both the controller synthesis and the implementation burden. Further considerations concerning the computational times and the model-parameters dependence allow for the definition of an appropriate trade-off between design complexity and controller performance. However, only partial guarantees of stability are provided, requiring a proper stability assessment through dedicated simulations.

Chapter 4: The polytopic design proved relevant advantages through the simulation performance and robustness analysis, both in terms of system stabilization and implementation ease. Indeed, the stronger stability guarantees implied by the polytopic controller synthesis were confirmed w.r.t. structured uncertainties through the μ-sensitivity analysis, and to time-varying wind disturbance in the trajectory tracking scenario. Additionally, the complexity of the modeling design process is compensated by the implementation ease, represented by a limited amount of controllers to be interpolated online. Possible design weaknesses were highlighted by the stability margins related to input/output disturbance, suggesting the need for stricter design requirements. On the other side, even though the grid-based controller succeeded in stabilizing the projectile dynamics across the entire flight trajectory, larger sensitivity to wind disturbance has been observed through the simulations. The controller synthesis guarantees higher local performance and robustness properties, as shown by the analysis. Nevertheless, the milder certainties provided at the controller interpolation stage suggest the need for a denser set of design points around the desired projectile trajectory. A reformulation of the LMIs optimization problem could allow for precisely targeting the critical areas of the flight envelope, limiting the increment of computational and implementation complexity.

Future Perspectives

The limitations observed during the nonlinear and the LPV modeling processes have raised several points of improvement:

- **Aerodynamic Regression:** The aerodynamic model could be further developed by exploiting the dependence of the aerodynamic coefficients w.r.t. the Mach variation. Despite the unavoidable increase in the formulation complexity, this solution could improve the accuracy of the resulting projectile LPV model.
- **Reference Variables:** The selection of the aerodynamic angle-of-attack (AoA) as a scheduling and reference tracking variable represents a quite unusual choice. Indeed, accurate AoA measurements require dedicated instrumentation, often not provided on munition technologies. Additionally, both direct measurements and parameter estimations are particularly sensitive to wind disturbance. The reformulation of the projectile flight model in terms of the acceleration dynamics could simplify the implementation process. Accordingly, acceleration reference trajectories are generally employed in the mid-course guidance phase, due to the measurements availability.

- **LPV Modeling Approach:** Alternative modeling techniques could be considered to relax the constraints imposed by the state transformation approach. Recent studies investigate the LPV system formulation as the superposition of a structured model, based on standard inertial mechanics considerations, and a parameter-varying correction term. The latter can be directly fitted from real measurements by means of sophisticated identification techniques (such as neural networks).

The results obtained through the LPV-based control design approaches suggested possible improvements according to the following aspects:

- **Polytope Definition:** The polytopic design provides appealing advantages in terms of theoretical guaranteed properties and implementation ease. However, the resolution of the corresponding optimization problem is generally affected by a significant level of conservativeness. In the presented study, the simulated scheduling functions trajectories reveal areas of the designed polytope that are never covered, possibly representing unfeasible flight conditions. A reformulation of the polytope shape, and the employment of more sophisticated controller interpolation functions, might further improve the performance of the control design. The reformulation could be achieved by means of a change of variables, defining the polytope around the trajectory that the projectile is expected to perform. This solution would allow for a more optimal case-dependent formulation of the controller synthesis, significantly reducing the conservativeness affecting the computation, and preserving the guarantees provided by the polytopic design.
- **Grid Selection:** A fundamental aspect of the grid-based design concerns the identification of the necessary flight points to guarantee projectile stability across the entire trajectory. The employment of the LPVTools MATLAB functions imposes the definition of a rectangular/cubic grid, based on each scheduling variable range of variation. As a consequence, several unwanted flight conditions are targeted by the design, increasing both the conservativeness of the results and the numerical complexity of the computation. A proper reformulation of the LMIs optimization problem might allow for relaxing the shape constraints imposed by LPVTools. Since the robust stability properties guaranteed by the grid-based design do not account for any convexity limitations in the definition of the design grid, the grid points could be clustered around the desired projectile trajectory, optimizing the number of controllers to be implemented and interpolated online. Additionally, by minimizing the number of LTI controllers, the interpolation could be extended to include the controllers obtained by gridding the subspace of the scheduling variables rates of variations, improving the overall performance.
- **Lateral Controller:** The LPV modeling a control design could be extended to account for the roll-yaw channel dynamics of the projectile. A preliminary study suggested how through the decoupling between pitch and roll-yaw dynamics, and employing mild approximations, a reliable roll-yaw dynamics quasi-LPV model can be easily derived. Polytopic and grid-based design techniques would allow the design of an LPV controller that implements a full Bank-To-Turn flight strategy in combination with the already presented pitch channel autopilot.

Appendix A

Aerodynamic Analysis

This appendix provides complementary information concerning the aerodynamic modeling process discussed in Chapter 1. In particular, Section A.1 presents the complete set of Computational Fluid Dynamics (CFD) acquisitions related to the static aerodynamic coefficients. The full derivation of the multivariable aerodynamic regression model is detailed in Section A.2, concerning both the formulation of the aerodynamic static forces and moments coefficients (Section A.2.1-A.2.2). Finally, Section A.2.1 provides the complete set of regression model comparison results based on the accuracy analysis explained in Section 1.3.3.3.

A.1 Static Coefficients CFD Acquisitions

The full set of aerodynamic coefficients introduced in Section 1.3.2.1 is presented hereafter.

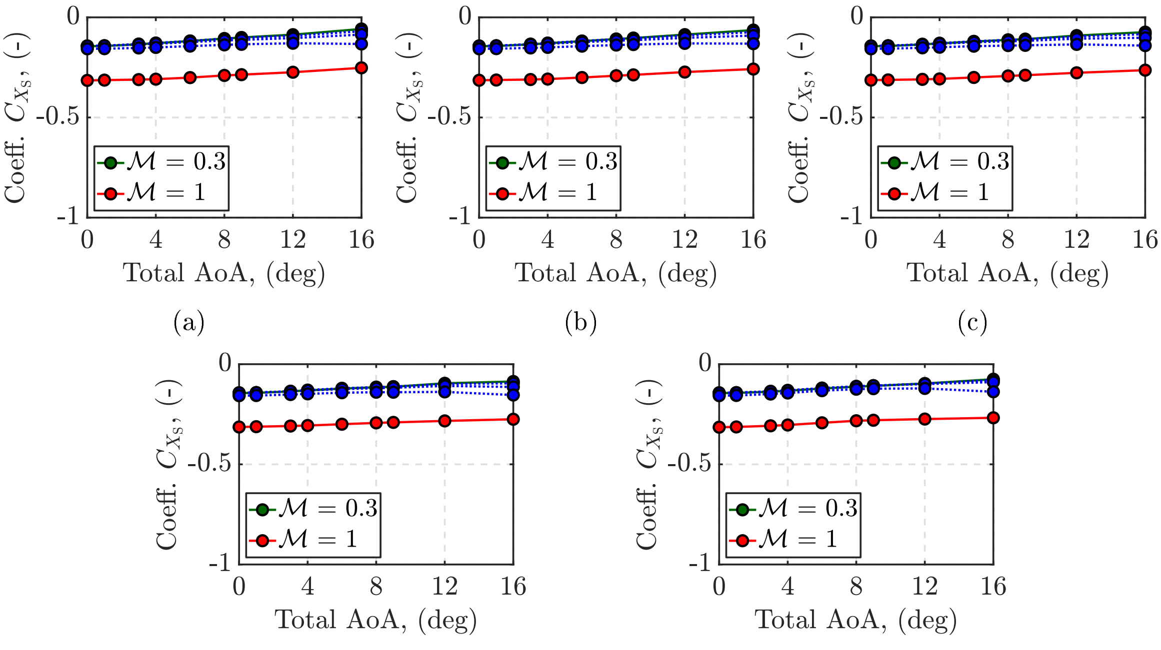

(a) (b) (c)

(d) (e)

Figure A.1: CFD static longitudinal coefficient dataset, C_{X_S}: (a) $\phi' = 0$ deg; (b) $\phi' = 15$ deg; (c) $\phi' = 30$ deg; (d) $\phi' = 45$ deg; (e) $\phi' = 90$ deg.

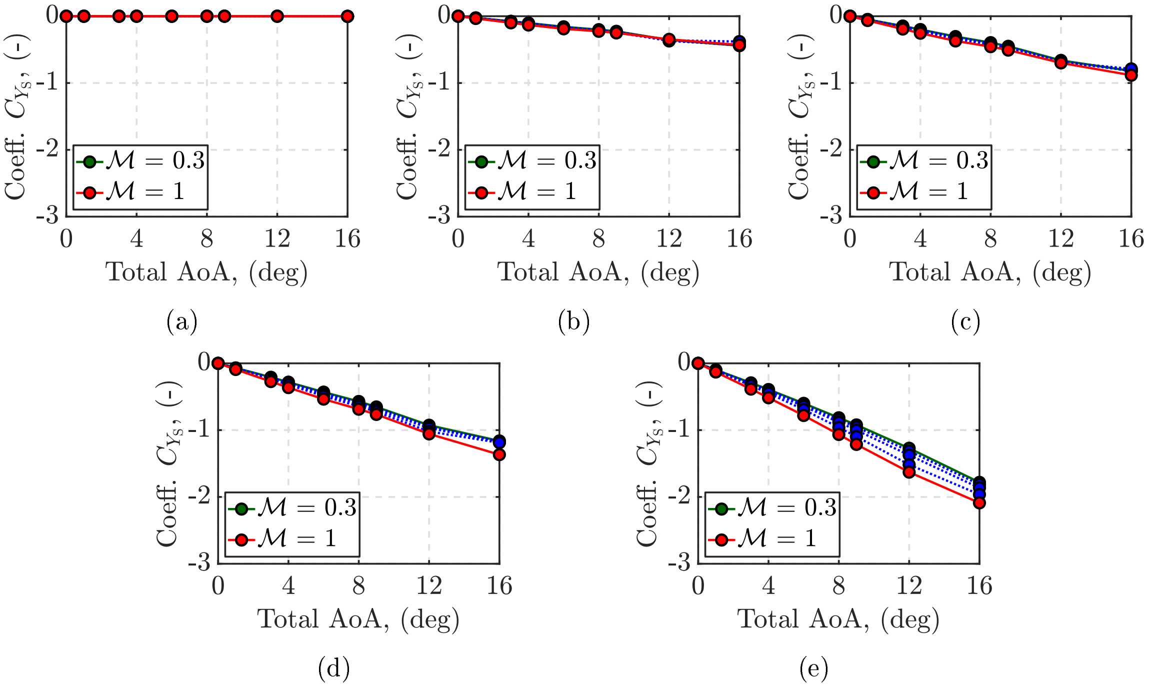

Figure A.2: CFD static lateral coefficient dataset, C_{Y_S}: (a) $\phi' = 0$ deg; (b) $\phi' = 15$ deg; (c) $\phi' = 30$ deg; (d) $\phi' = 45$ deg; (e) $\phi' = 90$ deg.

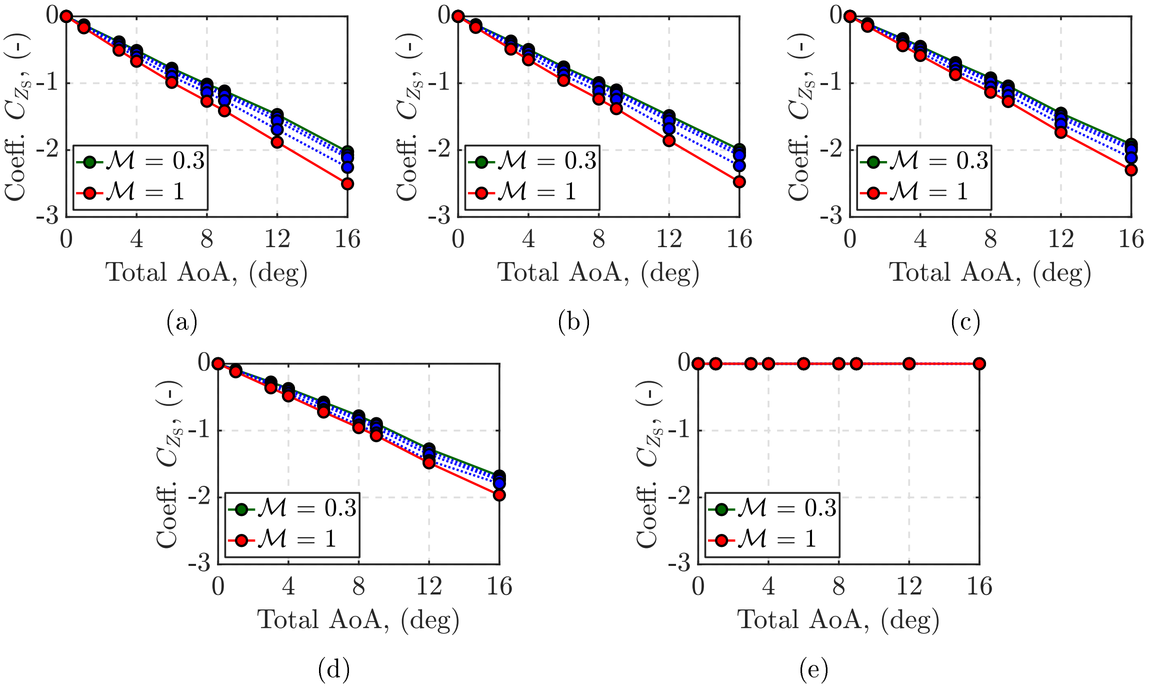

Figure A.3: CFD static vertical coefficient dataset, C_{Z_S}: (a) $\phi' = 0$ deg; (b) $\phi' = 15$ deg; (c) $\phi' = 30$ deg; (d) $\phi' = 45$ deg; (e) $\phi' = 90$ deg.

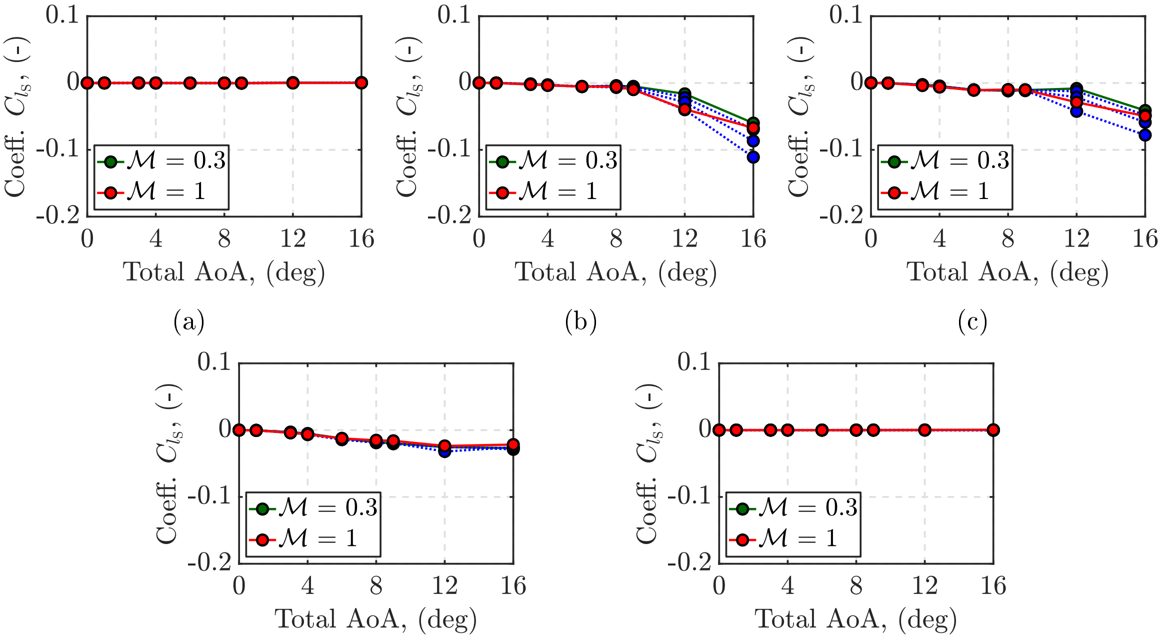

(a)

(b)

(c)

(d)

(e)

Figure A.4: CFD static rolling coefficient dataset, C_{l_S}: (a) $\phi' = 0$ deg; (b) $\phi' = 15$ deg; (c) $\phi' = 30$ deg; (d) $\phi' = 45$ deg; (e) $\phi' = 90$ deg.

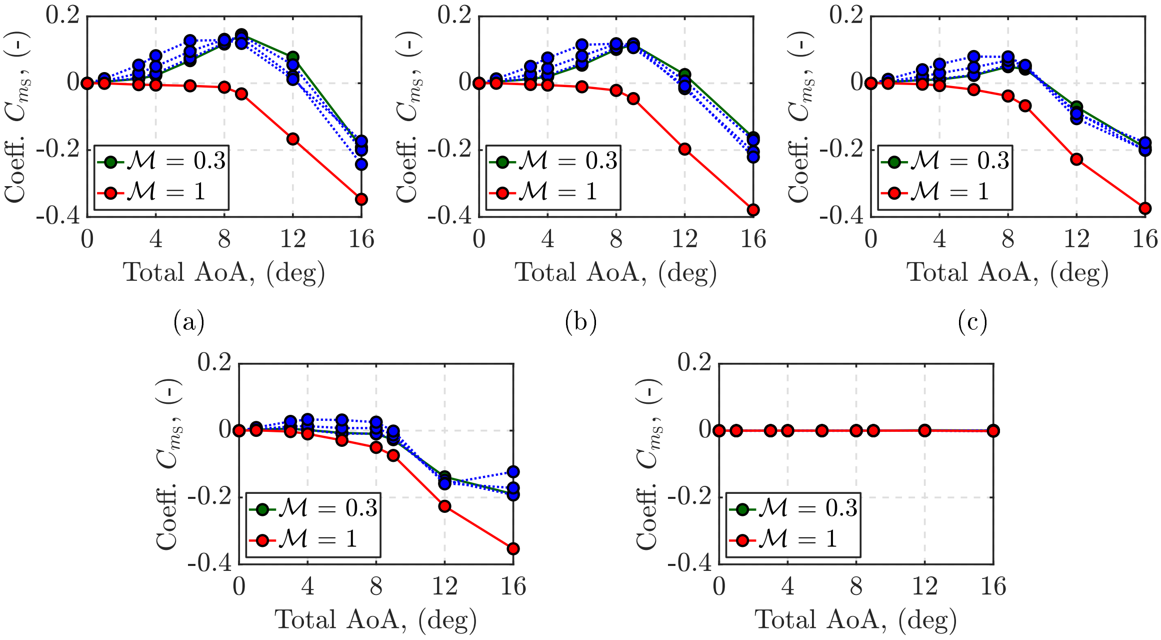

(a)

(b)

(c)

(d)

(e)

Figure A.5: CFD static pitching coefficient dataset, C_{m_S}: (a) $\phi' = 0$ deg; (b) $\phi' = 15$ deg; (c) $\phi' = 30$ deg; (d) $\phi' = 45$ deg; (e) $\phi' = 90$ deg.

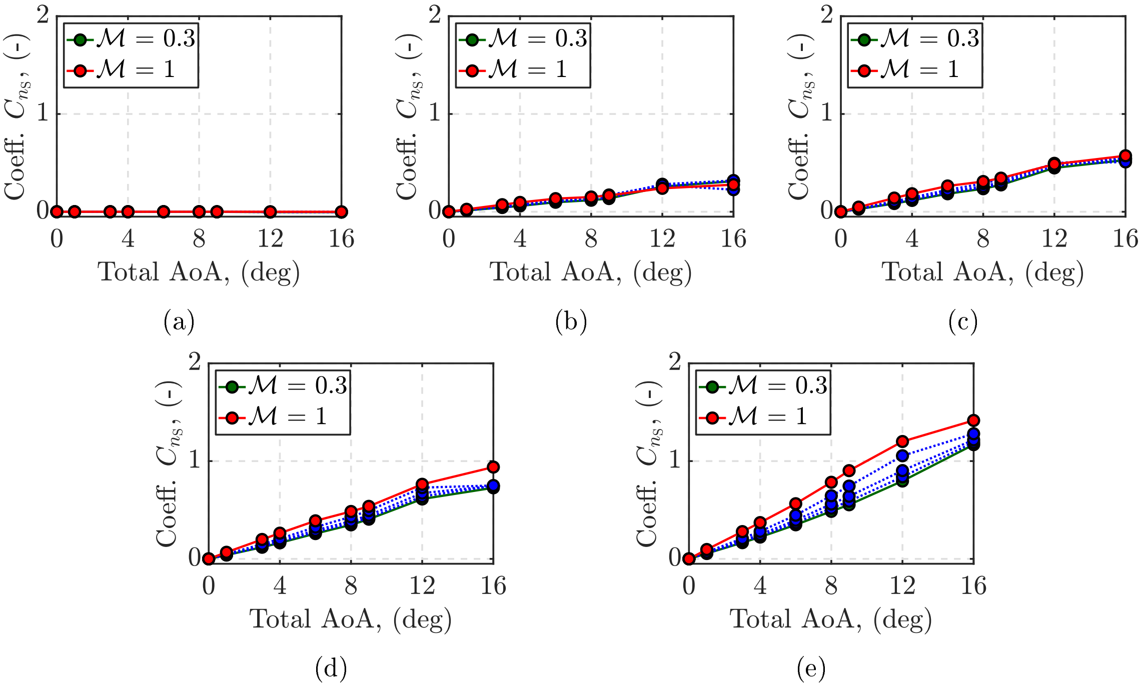

Figure A.6: CFD static yawing coefficient dataset, C_{ns}: (a) $\phi' = 0$ deg; (b) $\phi' = 15$ deg; (c) $\phi' = 30$ deg; (d) $\phi' = 45$ deg; (e) $\phi' = 90$ deg.

A.2 Multivariable Regression Model Derivation

The expressions of the static aerodynamic forces and moments employed for the multivariable regression analysis described in Section 1.3.3.2 rely on the formulation provided in [McC99]. The aerodynamic forces expressed in the body coordinates, $]^B$, are derived as projections of the aerodynamic Drag and Lift contributions, D and L, respectively. Similarly, the aerodynamic moments are generated by the normal component of the obtained aerodynamic forces. The expressions are first formulated in tensor notation and then projected w.r.t. the appropriate coordinate systems.

A.2.1 Regression Models: Force Coefficients

According to the air frame (A) and body frame (B) definitions, provided in Section 1.2.2 of Chapter 1, the Drag and Lift aerodynamic forces can be expressed in their tensor forms as follows:

$$\boldsymbol{D}_B = -\bar{q}SC_D\boldsymbol{a}_1; \qquad \boldsymbol{L}_B = \bar{q}SC_{L_\alpha}[\boldsymbol{a}_1 \times (\boldsymbol{b}_1 \times \boldsymbol{a}_1)] \tag{A.1}$$

where $\bar{q}$ represents the dynamic pressure, S is the projectile reference surface, C_D and C_{L_α} stand for the Drag and Lift aerodynamic coefficients, respectively, whereas $\boldsymbol{a}_1$ and $\boldsymbol{b}_1$ correspond to the longitudinal base vectors defining the air (A) and the body (B) frames, respectively. In particular, $\boldsymbol{a}_1$ is aligned with the relative wind direction, $\boldsymbol{v}_B^A$, while $\boldsymbol{b}_1$ points towards the nose of the projectile, as detailed in Section 1.2.2.

The aerodynamic forces expressions in Equation (A.1) can be projected along the corresponding preferred wind coordinate system, assuming the polar aeroballistic angles notation, $]^A$. Indeed, the aeroballistic coordinate system is aligned with the projectile load factor plane (LF), where the Drag and Lift forces are generated. The resulting projections are formulated as:

$$[\boldsymbol{D}_B]^A = -\bar{q}SC_D \begin{bmatrix} 1 \\ 0 \\ 0 \end{bmatrix}; \qquad [\boldsymbol{L}_B]^A = \bar{q}SC_{L_\alpha} \begin{bmatrix} 0 \\ 0 \\ -\sin\alpha' \end{bmatrix} \tag{A.2}$$

where α' corresponds to the aerodynamic total angle-of-attack.

Applying the wind-to-body coordinates transformation matrix defined in Equation (1.8), the Drag and Lift force projections in Equation (A.2) can be expressed w.r.t. the body coordinates, complying with the general aerodynamic model formulation proposed in Section 1.3. The resulting Drag and Lift force projections in the body coordinate system are expressed as follows:

$$[\boldsymbol{D}_B]^B = -\bar{q}SC_D \begin{bmatrix} \cos\alpha' \\ \sin\alpha'\sin\phi' \\ \sin\alpha'\cos\phi' \end{bmatrix}; \qquad [\boldsymbol{L}_B]^B = \bar{q}SC_{L_\alpha} \begin{bmatrix} \sin^2\alpha' \\ -\cos\alpha'\sin\alpha'\sin\phi' \\ cos\alpha'\sin\alpha'\cos\phi' \end{bmatrix} \tag{A.3}$$

where ϕ' represents the aerodynamic roll angle.

Finally, through the relations formulated in Equation (1.28), the aerodynamic Drag and Lift forces in Equation (A.3) projected in the body frame, can be expressed as a function of the Cartesian aerodynamic AoA and AoS, α and β, respectively as:

$$[\boldsymbol{D}_B]^B = -\bar{q}SC_D \begin{bmatrix} \cos\alpha\cos\beta \\ \sin\beta \\ \sin\alpha\cos\beta \end{bmatrix}; \qquad [\boldsymbol{L}_B]^B = \bar{q}SC_{L_\alpha} \begin{bmatrix} \sin^2\alpha + \cos^2\alpha\sin^2\beta \\ -\cos\alpha\sin\beta\cos\beta \\ -\sin\alpha\cos\alpha\cos^2\beta \end{bmatrix}. \tag{A.4}$$

The superposition of the Drag and Lift force projections in Equation (A.4) generates the static contributions of the projectile aerodynamics forces, ($f_{\mathrm{a}_1,\mathrm{s}}$, $f_{\mathrm{a}_2,\mathrm{s}}$, $f_{\mathrm{a}_3,\mathrm{s}}$), expressed w.r.t. the body coordinate system, as introduced in Equation (1.24). These contributions are parameterized as a function of the Drag and Lift aerodynamic force coefficients, and of the aerodynamic AoA and AoS, as:

$$\begin{aligned} [\boldsymbol{f}_{\mathrm{a,s}}]^B = \begin{bmatrix} f_{\mathrm{a}_1,\mathrm{s}} \\ f_{\mathrm{a}_2,\mathrm{s}} \\ f_{\mathrm{a}_3,\mathrm{s}} \end{bmatrix} &= \bar{q}S \begin{bmatrix} C_{X_\mathrm{S}} \\ C_{Y_\mathrm{S}} \\ C_{Z_\mathrm{S}} \end{bmatrix} \\ &= \bar{q}S \begin{bmatrix} -C_D\cos\alpha\cos\beta + C_{L_\alpha}\left(\sin^2\alpha + \cos^2\alpha\sin^2\beta\right) \\ -C_D\sin\beta - C_{L_\alpha}\cos\alpha\sin\beta\cos\beta \\ -C_D\sin\alpha\cos\beta - C_{L_\alpha}\sin\alpha\cos\alpha\cos^2\beta \end{bmatrix}. \end{aligned} \tag{A.5}$$

According to the general aerodynamic coefficients formulation, imposed through the CFD data acquisition and defined in Equation (1.27), C_{X_S}, C_{Y_S}, and C_{Z_S} correspond to the static components of the aerodynamic coefficients along the body coordinate system.

Thus, by addressing the Drag and Lift coefficients, C_D and C_{L_α} as regression parameters, the expressions in Equation (A.5) can be employed as fitting models during the multivariable regression analysis on the Computational Fluid Dynamics (CFD) acquisitions performed in Section 1.3.3.2:

$$\begin{aligned} C_{X_\mathrm{S}} &= C_{X_2}\cos\alpha\cos\beta + C_{X_3}\left(\sin^2\alpha + \cos^2\alpha\sin^2\beta\right), \\ C_{Y_\mathrm{S}} &= C_{Y_1}\sin\beta + C_{Y_3}\cos\alpha\sin\beta\cos\beta, \\ C_{Z_\mathrm{S}} &= C_{Z_2}\sin\alpha\cos\beta + C_{Z_3}\sin\alpha\cos\alpha\cos^2\beta. \end{aligned} \tag{A.6}$$

Accounting for simple trigonometric manipulations, the coefficient derivative C_{X_3} can be equivalently split into a static derivative, C_{X_0}, and a higher-order derivative, C_{X_4}. Additionally, the higher-order derivative, C_{Z_3}, is not considered in the regression model in reason of the already high accuracy provided by the first-order derivative. The employment of these considerations on the parameterized model in Equation (A.6) leads to the final expressions of the aerodynamic coefficients multivariable regression model presented in Equation (1.31):

$$\begin{aligned} C_{X_\mathrm{S}}(\mathcal{M},\alpha,\beta) &= C_{X_0}(\mathcal{M}) + C_{X_2}(\mathcal{M})\cos\alpha\cos\beta + C_{X_4}(\mathcal{M})\cos^2\alpha\cos^2\beta, \\ C_{Y_\mathrm{S}}(\mathcal{M},\alpha,\beta) &= C_{Y_1}(\mathcal{M})\sin\beta + C_{Y_3}(\mathcal{M})\cos\alpha\sin\beta\cos\beta, \\ C_{Z_\mathrm{S}}(\mathcal{M},\alpha,\beta) &= C_{Z_2}(\mathcal{M})\sin\alpha\cos\beta. \end{aligned}$$

Since the CFD data have been acquired at different flight regimes, the regression models intrinsically depend on the Mach number variation, $\mathcal{M}$. The regression analysis is performed by iteratively selecting a specific Mach value. Each set of identified regression coefficients is stored in dedicated lookup tables and interpolated online during the simulations.

A.2.2 Regression Models: Moment Coefficients

The static (pitching) component of the aerodynamic moments can be derived from the Drag and Lift forces projection, as done for the aerodynamic forces in Section A.2.1. In particular, the static aerodynamic moments are generated by the normal force, $\boldsymbol{N}_B$, expressed in tensor form as detailed in [McC99]:

$$\boldsymbol{N}_B = \bar{q}SC_{N_\alpha}[\boldsymbol{b}_1 \times (\boldsymbol{b}_1 \times \boldsymbol{a}_1)] \tag{A.7}$$

where C_{N_α} represents the normal force coefficient derivative, defined as:

$$C_{N_\alpha} = C_D + C_{L_\alpha}\cos\alpha\cos\beta.$$

By projecting the tensor expression in Equation (A.7) in the wind aeroballistic coordinates and applying the transformations from the polar aeroballistic to the body coordinate system, the resulting normal force corresponds to the superposition of Drag and Lift forces along the 2^B and the 3^B coordinate axes, expressed in Equation (A.5):

$$[\boldsymbol{N}_B]^B = \bar{q} S C_{N_\alpha} \begin{bmatrix} 0 \\ -\sin\beta \\ -\sin\alpha\cos\beta \end{bmatrix} = \bar{q} S \begin{bmatrix} 0 \\ -C_D \sin\beta - C_{L_\alpha} \cos\alpha \sin\beta \cos\beta \\ -C_D \sin\alpha\cos\beta - C_{L_\alpha} \sin\alpha\cos\alpha\cos^2\beta \end{bmatrix}. \tag{A.8}$$

The corresponding aerodynamic static (pitching) moments, generated by the normal force, are expressed in tensor form as follows:

$$\boldsymbol{m}_{B,\mathrm{S}} = \boldsymbol{s}_{\text{CM-CP}} \times \boldsymbol{N}_B; \qquad \text{with: } \boldsymbol{s}_{\text{CM-CP}} = d_{\text{CM-CP}} \boldsymbol{b}_1 \tag{A.9}$$

where $d_{\text{CM-CP}}$ represents the distance between the center of mass (CM) and the center of pressure (CP) of the projectile.

The projections of the aerodynamic moments in Equation (A.9) w.r.t. the body coordinates can be inferred from the normal force expression in Equation (A.8) as:

$$\begin{aligned} [\boldsymbol{m}_{B,\mathrm{S}}]^B = \begin{bmatrix} m_{B_1,\mathrm{S}} \\ m_{B_2,\mathrm{S}} \\ m_{B_3,\mathrm{S}} \end{bmatrix} = \bar{q} S d \begin{bmatrix} 0 \\ C_{m_\mathrm{S}} \\ C_{n_\mathrm{S}} \end{bmatrix} &= \bar{q} S d C_{m_\alpha} \begin{bmatrix} 0 \\ \sin\alpha\cos\beta \\ -\sin\beta \end{bmatrix} \\ &= \bar{q} S d \begin{bmatrix} 0 \\ -C_D \sin\alpha\cos\beta - C_{L_\alpha} \sin\alpha\cos\alpha\cos^2\beta \\ -C_D \sin\beta - C_{L_\alpha} \cos\alpha\sin\beta\cos\beta \end{bmatrix} \end{aligned} \tag{A.10}$$

where $C_{m_\alpha} = \left(\frac{d_{\text{CM-CP}}}{d}\right) C_{N_\alpha}$ corresponds to the pitching moment coefficient derivative, while d is the projectile reference caliber.

Assuming the Drag and Lift force coefficients, C_D and C_{L_α}, as the regression parameters to be identified through regression analysis on the CFD data, the formulations in Equation (A.10) can be employed as fitting models. The aerodynamic static moments model presented in Equation (1.31) are then recovered, including the implicit dependence on the Mach regime:

$$\begin{aligned} C_{m_\mathrm{S}}(\mathcal{M},\alpha,\beta) &= C_{m_2}(\mathcal{M}) \sin\alpha\cos\beta + C_{m_4}(\mathcal{M}) \sin\alpha\cos\alpha\cos^2\beta, \\ C_{n_\mathrm{S}}(\mathcal{M},\alpha,\beta) &= C_{n_1}(\mathcal{M}) \sin\beta + C_{n_3}(\mathcal{M}) \cos\alpha\sin\beta\cos\beta. \end{aligned}$$

A.3 Regression Models: Accuracy Comparison Results

This section presents the complete set of results related to the accuracy comparison between the *Polynomial Regression* and *Multivariable Regression* models, PR and MR respectively. The analysis is based on the Algorithm 1 introduced in Section 1.3.3.3. The results are provided in terms of the root mean square error (RMSE) of the difference between each regression model and the corresponding CFD data. The error is then normalized (NRMSE) through the Min-Max values of the CFD acquisitions at each investigated flight condition.

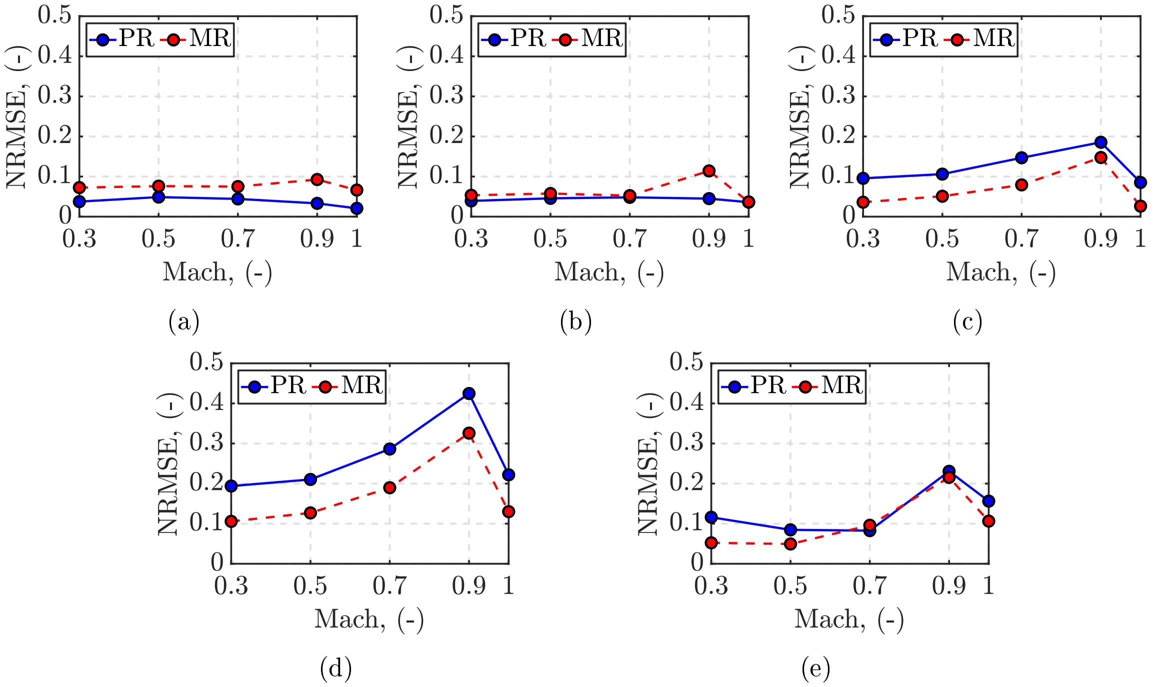

(a) (b) (c)

(d) (e)

Figure A.7: C_{X_S} interpolation NRMSE comparison at different flight conditions: (a) $\phi' = 0$ deg; (b) $\phi' = 15$ deg; (c) $\phi' = 30$ deg; (d) $\phi' = 45$ deg; (e) $\phi' = 90$ deg.

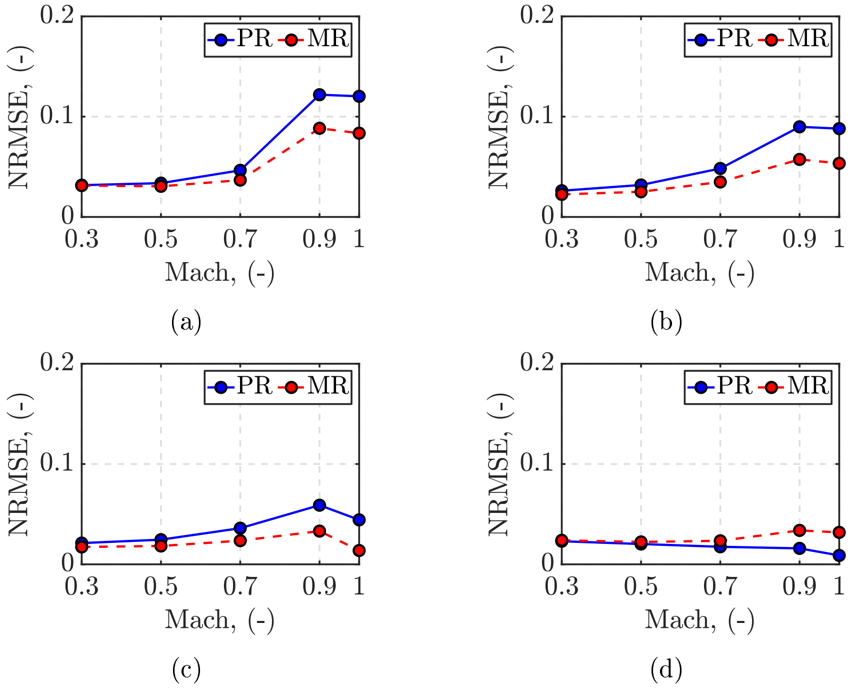

(a) (b)

(c) (d)

Figure A.8: C_{Y_S} interpolation NRMSE comparison at different flight conditions: (a) $\phi' = 15$ deg; (b) $\phi' = 30$ deg; (c) $\phi' = 45$ deg; (d) $\phi' = 90$ deg.

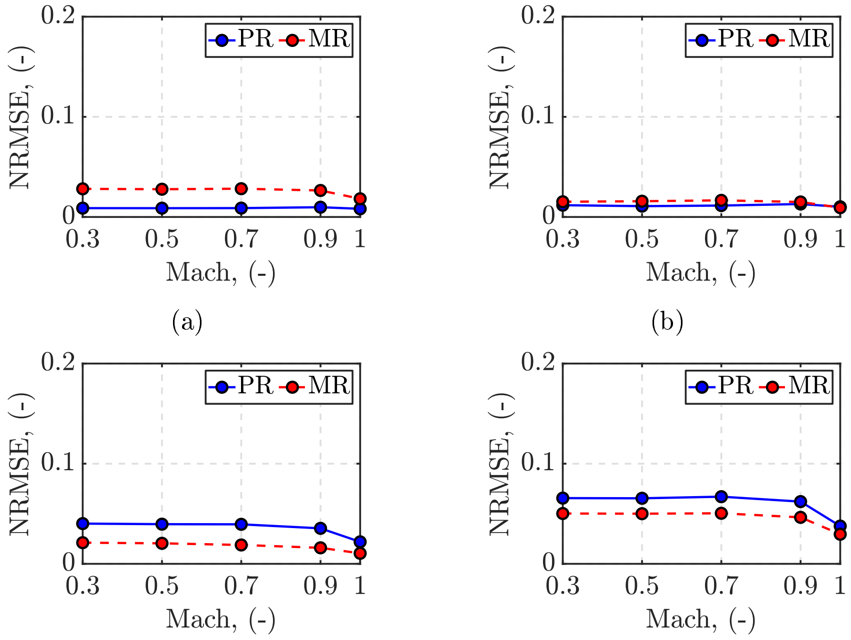

(a) (b) (c) (d)

Figure A.9: C_{Z_S} interpolation NRMSE comparison at different flight conditions: (a) $\phi' = 0$ deg; (b) $\phi' = 15$ deg; (c) $\phi' = 30$ deg; (d) $\phi' = 45$ deg.

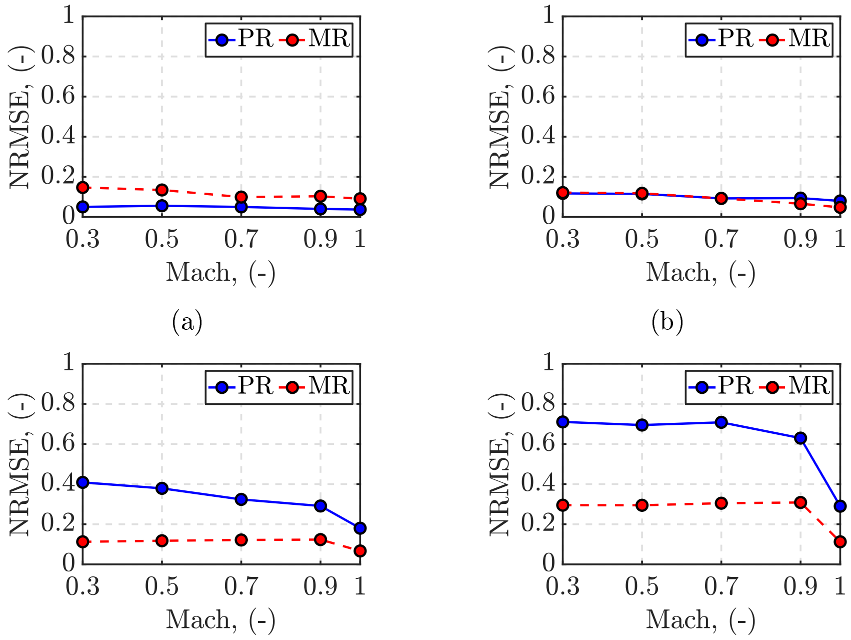

(a) (b) (c) (d)

Figure A.10: C_{m_S} interpolation NRMSE comparison at different flight conditions: (a) $\phi' = 0$ deg; (b) $\phi' = 15$ deg; (c) $\phi' = 30$ deg; (d) $\phi' = 45$ deg.

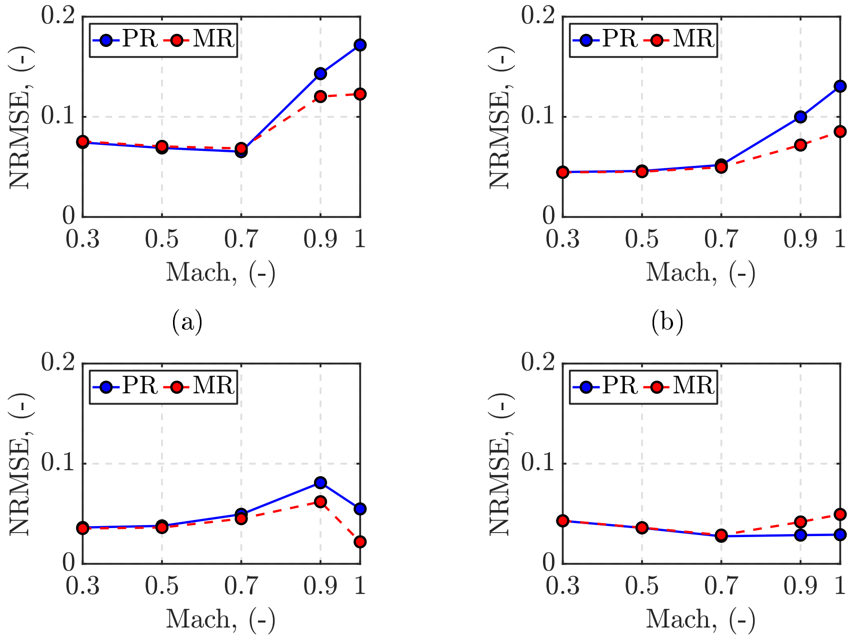

(a) (b) (c) (d)

Figure A.11: C_{n_S} interpolation NRMSE comparison at different flight conditions: (a) $\phi' = 15$ deg; (b) $\phi' = 30$ deg; (c) $\phi' = 45$ deg; (d) $\phi' = 90$ deg.

In particular, the results in Figure A.9 and Figure A.10, related to the vertical force and pitching moment aerodynamic coefficients, do not account for the comparison at $\phi' = 90$ deg. As detailed in Section 1.3.2.1, at those flight conditions the aerodynamic contributions depend exclusively on the angle-of-sideslip (AoS). Since the vertical force and pitching moment are generated by the angle-of-attack (AoA) variation, the CFD data acquired at $\phi' = 90$ deg consist mainly of noise signals related to the limited numerical precision. For the same reason, the results in Figure A.8 and Figure A.11, related to the lateral force and the yawing moment aerodynamic coefficients, do not include the comparison at $\phi' = 0$ deg where the aerodynamic contributions depend exclusively on the AoA.

Appendix B

State Transformation Conditions

The existence of the equilibrium functions expressed in Equation (2.28) at any flight conditions relies on the conditions imposed by the resolution of the system in Equation (2.27). The conditions are expressed as follows:

$$\begin{cases} 2C_{m_{\delta_q}}V^2 m + \bar{q}Sd(C_{m_{\delta_q}}C_{Z_q} - C_{m_q}C_{Z_{\delta_q}})\cos\alpha \neq 0 & \text{(a)} \\ 2V^2 m + \bar{q}SdC_{Z_q}\cos\alpha \neq 0 & \text{(b)} \\ S \neq 0 & \text{(c)} \\ d \neq 0 & \text{(d)} \\ \bar{q} \neq 0 & \text{(e)} \end{cases} \tag{B.1}$$

By definition, the reference surface, S, the reference caliber, d, the projectile mass, m, and the dynamic pressure, $\bar{q}$, are always positive values. Hence, conditions (c)-(d)-(e) are satisfied at any flight conditions. In particular, the dynamic pressure is defined as a function of the airspeed, V, and the altitude-dependent air density, ρ, as $\bar{q} = \rho(h)V^2/2$. As a consequence, the only exception to condition (e) occurs at the projectile impact point, where $V = 0$ m/s.

The conditions (a)-(b) in Equation (B.1) can be reformulated in terms of the dynamic pressure, respectively as:

$$\begin{cases} \bar{q} \neq \frac{2C_{m_{\delta_q}}V^2 m}{Sd(C_{m_q}C_{Z_{\delta_q}} - C_{m_{\delta_q}}C_{Z_q})\cos\alpha} & \text{(a)} \\ \bar{q} \neq -\frac{2V^2 m}{SdC_{Z_q}\cos\alpha} & \text{(b)} \end{cases} \tag{B.2}$$

In particular, the aerodynamic control and damping vertical coefficients, $C_{Z_{\delta_q}}$ and C_{Z_q}, assume always negative values, while the corresponding aerodynamic control and damping pitching moment coefficients, $C_{m_{\delta_q}}$ and C_{m_q}, are defined positive at any flight conditions. Additionally, since the inequality $C_{m_q}C_{Z_{\delta_q}} > C_{m_{\delta_q}}C_{Z_q}$ has been verified across the entire projectile flight envelope[1], the right-hand side terms of conditions (a)-(b) in Equation (B.2) represent always positive quantities, coherently with the definition of $\bar{q}$.

However, a mismatch of several orders of magnitude has been observed between the admissible range of dynamic pressure variation, $\bar{q} \in [0, 30000]$ kg/(ms^2), and the values imposed by the right-hand side terms of conditions (a)-(b) in Equation (B.2). As a consequence, the full set of conditions in Equation (B.1) is satisfied, proving the existence of the equilibrium functions at any flight conditions.

---

[1] The coefficients' values cannot be disclosed in reason of confidentiality.

Bibliography

[AA98] Pierre Apkarian and Richard J. Adams. "Advanced Gain-Scheduling Techniques for Uncertain Systems". In: *IEEE Transactions on Control Systems Technology* 6.1 (1998), pp. 21–32 (cit. on p. 105).

[ABG95] Pierre Apkarian, Jean-Marc Biannic, and Pascal Gahinet. "Self-scheduled H_∞ control of missile via linear matrix inequalities". In: *Journal of Guidance, Control, and Dynamics* 18.3 (1995), pp. 532–538 (cit. on p. 9).

[Afa98] Igor Afanasyev. "The legacy of the V-2: The First Soviet ballistic missiles". In: *The Journal of Slavic Military Studies* 11.4 (1998), pp. 164–174 (cit. on p. 1).

[AG95] Pierre Apkarian and Pascal Gahinet. "A Convex Characterization of Gain-Scheduled h/sub/spl infin//Controllers". In: *IEEE Transactions on Automatic Control* 40.5 (1995), pp. 853–864 (cit. on p. 65).

[AGB95] Pierre Apkarian, Pascal Gahinet, and Greg Becker. "Self-Scheduled H_∞ Control of Linear Parameter-Varying Systems: a Design Example". In: *Automatica* 31.9 (1995), pp. 1251–1261 (cit. on pp. 9, 65, 100, 112).

[ATB01] Pierre Apkarian, Hoang Duong Tuan, and Jacques Bernussou. "Continuous-Time Analysis, Eigenstructure Assignment, and H/sub 2/Synthesis with Enhanced Linear Matrix Inequalities (LMI) Characterizations". In: *IEEE Transactions on Automatic Control* 46.12 (2001), pp. 1941–1946 (cit. on p. 107).

[Atm] *Standard Atmosphere.* Standard. ISO 2533:1975. International Organization for Standardization, May 1975 (cit. on p. 54).

[AZF06] Jamshaid Ali, Changyun Zhang, and Jiancheng Fang. "An algorithm for astro-inertial navigation using CCD star sensors". In: *Aerospace Science and Technology* 10.5 (2006), pp. 449–454 (cit. on p. 5).

[Bal02] Gary J. Balas. "Linear, Parameter-Varying Control and its Application to Aerospace Systems". In: *Proceedings of the 23rd International Congress of Aeronautical Sciences.* ICAS. Toronto, Canada, 2002 (cit. on p. 72).

[Bal+97] Gary J. Balas et al. "On the design of LPV controllers for the F-14 aircraft lateral-directional axis during powered approach". In: *Proceedings of the 1997 American Control Conference.* Vol. 1. IEEE. Albuquerque, NM, US, 1997, pp. 123–127 (cit. on p. 8).

[BG22] Joshua Bryson and Benjamin C. Gruenwald. "Linear Parameter Varying Model Predictive Control of a High-Speed Projectile". In: *AIAA SCITECH 2022 Forum.* American Institute of Aeronautics and Astronautics (AIAA). San Diego, CA, US, 2022, p. 1585 (cit. on p. 9).

[BGL22] Joshua T. Bryson, Benjamin C. Gruenwald, and US Army Combat Capabilities Development Command Army Research Laboratory. *Automated Gain-Scheduling Approach for Three-Loop Autopilot.* Tech. rep. Tech. Rep. ARL-TR-9564, DEVCOM Army Research Laboratory, 2022 (cit. on p. 7).

[Bla91] John H. Blakelock. *Automatic control of aircraft and missiles.* John Wiley & Sons, 1991 (cit. on pp. 4, 31).

[BLM22] Simon Bagy, Michel Libsig, and Bastien Martinez. "Design and optimization of long-range guided ammunition". In: *56th 3AF International Conference on Applied Aerodynamics.* 2022 (cit. on p. 33).

[Boy+94] Stephen Boyd et al. *Linear Matrix Inequalities in System and Control Theory.* Society for Industrial and Applied Mathematics (SIAM), 1994, p. 193 (cit. on pp. 68, 101, 109).

[BP02] Declan Bates and Ian Postlethwaite. *Robust Multivariable Control of Aerospace systems.* Vol. 8. IOS Press, 2002 (cit. on pp. 138, 142).

[BP94] Greg Becker and Andy Packard. "Robust Performance of Linear Parametrically Varying Systems using Parametrically-Dependent Linear Feedback". In: *Systems & Control Letters* 23.3 (1994), pp. 205–215 (cit. on p. 109).

[BPC02] Bradley Burchett, Allen Peterson, and Mark Costello. "Prediction of swerving motion of a dual-spin projectile with lateral pulse jets in atmospheric flight". In: *Mathematical and computer modelling* 35.7-8 (2002), pp. 821–834 (cit. on p. 3).

[Bra+13] Robert Braun et al. "Advances in Inertial Guidance Technology for Aerospace Systems". In: *AIAA Guidance, Navigation, and Control (GNC) Conference.* Boston, MA,US, 2013, p. 5123 (cit. on p. 5).

[Bri14] Corentin Briat. *Linear Parameter-Varying and Time-Delay Systems.* 1st. Springer Berlin, Heidelberg, 2014, p. 394 (cit. on pp. 101, 103, 104).

[Bug23] Shannon Bugos. "Russia Suspends New START". In: *Arms Control Today* 53.2 (2023), pp. 24–25 (cit. on p. 2).

[CA00] Mark Costello and Raditya Agarwalla. "Improved dispersion of a fin-stabilized projectile using a passive movable nose". In: *Journal of Guidance, Control, and Dynamics* 23.5 (2000), pp. 900–903 (cit. on p. 3).

[CA91] Ian Clark and David Angell. "Britain, the United States and the control of nuclear weapons: The diplomacy of the Thor deployment 1956–58". In: *Diplomacy and Statecraft* 2.3 (1991), pp. 153–177 (cit. on p. 1).

[Cam07] Benjabin Campion. "SPACIDO 1D Course Correction Fuze". In: *51ft Annual Fuze Conference Annual Guns & Missiles Symposium.* Nashville, US, 2007 (cit. on p. 3).

[CFC12] Gene Cooper, Frank Fresconi, and Mark Costello. "Flight stability of an asymmetric projectile with activating canards". In: *Journal of Spacecraft and Rockets* 49.1 (2012), pp. 130–135 (cit. on pp. 3, 4, 29, 32).

[Cha+17] Dominique Chargelegue et al. *Full-caliber, spin-stabilized guided projectile with long range.* US Patent App. 15/334,818. 2017 (cit. on p. 4).

[CL08] Francesco Casella and Marco Lovera. "LPV/LFT Modelling and Identification: Overview, Synergies and a Case Study". In: *2008 IEEE International Conference on Computer-Aided Control Systems.* IEEE. San Antonio, TX, US, 2008, pp. 852–857 (cit. on p. 65).

[Cor+20] Matteo Corno et al. “An LPV Approach to Autonomous Vehicle Path Tracking in the Presence of Steering Actuation Nonlinearities”. In: *IEEE Transactions on Control Systems Technology* 29.4 (2020), pp. 1766–1774 (cit. on pp. 66, 100).

[CS96] Lance H. Carter and Jeff S. Shamma. “Gain-scheduled bank-to-turn autopilot design using linear parameter varying transformations”. In: *Journal of guidance, control, and dynamics* 19.5 (1996), pp. 1056–1063 (cit. on pp. 8, 62, 70, 72).

[CWB11] Daniel Corriveau, Pierre Wey, and Claude Berner. “Thrusters pairing guidelines for trajectory corrections of projectiles”. In: *Journal of Guidance, Control, and Dynamics* 34.4 (2011), pp. 1120–1128 (cit. on p. 3).

[DM08] O Douglas and C Mark. “Model predictive control of a direct fire projectile equipped with canards”. In: *Journal of Dynamic Systems, Measurement, and Control* 130.6 (2008), 061010 (11) (cit. on p. 3).

[DOBG99] Maurício C. De Oliveira, Jacques Bernussou, and José C. Geromel. “A New Discrete-Time Robust Stability Condition”. In: *Systems & control letters* 37.4 (1999), pp. 261–265 (cit. on p. 107).

[DOGH99] MC De Oliveira, JC Geromel, and Liu Hsu. “LMI Characterization of Structural and Robust Stability: the Discrete-Time Case”. In: *Linear Algebra and its applications* 296.1-3 (1999), pp. 27–38 (cit. on p. 107).

[Dor63] Walter R. Dornberger. “The German V-2”. In: *Technology and Culture* 4.4 (1963), pp. 393–409 (cit. on p. 1).

[Doy82] John Doyle. “Analysis of Feedback Systems with Structured Uncertainties”. In: *IEE Proceedings D Control Theory and Applications.* Vol. 129. 6. Institution of Electrical Engineers (IEE). 1982, pp. 242–250 (cit. on p. 143).

[Dub18] Donatien Dubuc. “Observation and Diagnosis for Trucks”. PhD thesis. Université Grenoble Alpes, 2018 (cit. on pp. 66, 156).

[Fal+15] Alexandre Falcoz et al. “Systematic Design Methods of Robust and Structured Controllers for Satellites: Application to the Refinement of Rosetta’s Orbit Controller”. In: *CEAS Space Journal* 7.3 (2015), pp. 319–334 (cit. on p. 141).

[FC06] Geoffrey Frost and Mark Costello. “Control authority of a projectile equipped with an internal unbalanced part”. In: *Journal of Dynamic Systems, Measurement, and Control* 128.4 (2006), pp. 1005–1012 (cit. on p. 3).

[Fre11] Frank Fresconi. “Guidance and control of a projectile with reduced sensor and actuator requirements”. In: *Journal of Guidance, Control, and Dynamics* 34.6 (2011), pp. 1757–1766 (cit. on pp. 3, 4, 29).

[GA13] Pascal Gahinet and Pierre Apkarian. “Automated tuning of gain-scheduled control systems”. In: *52nd IEEE Conference on Decision and Control.* IEEE. Firenze, Italy, 2013, pp. 2740–2745 (cit. on p. 7).

[Gag03] Stacey Gage. “Creating a Unified Graphical Wind Turbulence Model from Multiple Specifications”. In: *AIAA Modeling and simulation technologies conference and exhibit.* Austin, Texas, 2003, p. 5529 (cit. on p. 160).

[Gah+94] Pascal Gahinet et al. “The LMI Control Toolbox”. In: *Proceedings of 1994 33rd IEEE conference on decision and control*. Vol. 3. IEEE. 1994, pp. 2038–2041 (cit. on p. 131).

[Gal76] Pierre M. Gallois. “French Defense Planning—The Future in the Past”. In: *International Security* 1.2 (1976), pp. 15–31 (cit. on p. 1).

[GB08] Michael Grant and Stephen Boyd. “Graph Implementations for Nonsmooth Convex Programs”. In: *Recent Advances in Learning and Control*. Ed. by V. Blondel, S. Boyd, and H. Kimura. Lecture Notes in Control and Information Sciences. `http://stanford.edu/~boyd/graph_dcp.html`. Springer-Verlag Limited, 2008, pp. 95–110 (cit. on p. 102).

[GB22] Benjamin C Gruenwald and Joshua Bryson. “A gain-scheduled approach for the control of a high-speed guided projectile”. In: *AIAA SCITECH 2022 Forum*. San Diego, CA ,US: American Institute of Aeronautics and Astronautics (AIAA), 2022, p. 0612 (cit. on p. 7).

[GC02] Bernard J. Guidos and Gene R. Cooper. “Linearized motion of a fin-stabilized projectile subjected to a lateral impulse”. In: *Journal of spacecraft and rockets* 39.3 (2002), pp. 384–391 (cit. on p. 3).

[Gena] *Flight Test Report Atlas Missile 17E*. Tech. rep. San Diego, CA, US: GENERAL DYNAMICS/ASTRONAUTICS SAN DIEGO, 1961 (cit. on p. 1).

[Genb] *Flight Test Report Atlas Missile 71D*. Tech. rep. San Diego, CA, US: GENERAL DYNAMICS/ASTRONAUTICS SAN DIEGO, 1960 (cit. on p. 1).

[Gil44] Cedric Giles. “The V-1 Robot Bomb: Details of the German Air Torpedo”. In: *Astronautics* 14.59 (1944), pp. 4–5 (cit. on p. 1).

[GL08] Eric Gagnon and Marc Lauzon. “Course correction fuze concept analysis for in-service 155 mm spin-stabilized gunnery projectiles”. In: *AIAA guidance, navigation and control conference and exhibit*. American Institute of Aeronautics and Astronautics (AIAA), 2008, p. 6997 (cit. on p. 3).

[GL09] Eric Gagnon and Marc Lauzon. *Low cost guidance and control solution for in-service unguided 155 mm artillery shell*. Tech. rep. 2009 (cit. on p. 3).

[Gol80] Joe P. Golden. “Terrain Contour Matching (TERCOM): A Cruise Missile Guidance Aid”. In: *24th Annual Technical Symposium, Image Processing for Missile Guidance*. Vol. 0238. International Society for Optics and Photonics. San Diego, US: Society of Photo-Optical Instrumentation Engineers (SPIE), 1980, pp. 10–18 (cit. on pp. 2, 5).

[Gra05] Lester W. Grau. “The High-precision Tulip: Development and Combat Employment of the Soviet Laser-Guided Mortar Round”. In: *Journal of Slavic Military Studies* 18.4 (2005), pp. 717–722 (cit. on p. 4).

[Gro17] Woolf Gross. “An Orphan Weapon System: One Battalion’s Saga of Operationalizing the Lance Missile in US Army Europe”. In: *On Point* 22.3 (2017), pp. 36–43 (cit. on p. 1).

[Gue71] Mauricio Guelman. “A qualitative study of proportional navigation”. In: *IEEE Transactions on Aerospace and Electronic Systems* AES-7.4 (1971), pp. 637–643 (cit. on p. 5).

[GWT13] Vincen Gassman, Phillip Wernert, and Spilios Theodoulis. *A Matlab/Simulink simulator for the perfromance anlysis of guided projectiles.* Tech. rep. Saint Louis, France: ISL, 2013 (cit. on p. 52).

[Hee12] Gretchen Heefner. *The Missile Next Door: The Minuteman in the American Heartland*. Harvard University Press, 2012 (cit. on p. 1).

[Her17] Teguh Herlambang. “Design of a navigation and guidance system of missile with trajectory estimation using ensemble Kalman Filter square root (EnKF-SR)”. In: *2017 4th International Conference on Computer Applications and Information Processing Technology (CAIPT).* Kuta Bali, Indonesia, 2017, pp. 1–7 (cit. on p. 5).

[HG93] Rick A Hyde and Keith Glover. “The application of scheduled H/sub infinity/controllers to a VSTOL aircraft”. In: *IEEE Transactions on Automatic Control* 38.7 (1993), pp. 1021–1039 (cit. on p. 7).

[HJ89] Albert E Hodapp Jr. “Passive means for stabilizing projectiles with partially restrained internal members”. In: *Journal of Guidance, Control, and Dynamics* 12.2 (1989), pp. 135–139 (cit. on p. 3).

[HSB14] Arnar Hjartarson, Peter Seiler, and Gary J. Balas. “LPV Analysis of a Gain Scheduled Control for an Aeroelastic Aircraft”. In: *2014 American Control Conference.* IEEE. Portland, OR, US, 2014, pp. 3778–3783 (cit. on p. 8).

[HSP15] Arnar Hjartarson, Peter Seiler, and Andrew Packard. “LPVTools: A toolbox for Modeling, Analysis, and Synthesis of Parameter Varying Control Systems”. In: *1st IFAC Workshop on Linear Parameter Varying Systems LPVS 2015.* Vol. 48. 26. IFAC-PapersOnLine. Grenoble,France: Elsevier, 2015, pp. 139–145 (cit. on pp. 131, 156).

[HW15] Christian Hoffmann and Herbert Werner. “A Survey of Linear Parameter-Varying Control Applications Validated by Experiments or High-Fidelity Simulations”. In: *IEEE Transactions on Control Systems Technology* 23.2 (2015), pp. 416–433 (cit. on pp. 66, 100).

[JC01] Thanat Jitpraphai and Mark Costello. “Dispersion reduction of a direct fire rocket using lateral pulse jets”. In: *Journal of Spacecraft and Rockets* 38.6 (2001), pp. 929–936 (cit. on p. 3).

[Jin+18] XianJian Jin et al. “Robust Gain-Scheduled Output Feedback Yaw Stability Control for In-Wheel-Motor-Driven Electric Vehicles with External Yaw-Moment”. In: *Journal of the Franklin Institute* 355.18 (2018), pp. 9271–9297 (cit. on pp. 66, 100).

[Kap+22] Dimitrios Kapsalis et al. “A Reduced LPV Polytopic Look-Ahead Steering Controller for Autonomous Vehicles”. In: *Control Engineering Practice* 129 (2022), p. 105360 (cit. on pp. 66, 100).

[KCL82] H. J. Kelley, E. M. Cliff, and F. H. Lutze. “Boost–glide range-optimal guidance”. In: *Optimal Control Applications and Methods* 3.3 (1982), pp. 293–298 (cit. on pp. 53, 114).

[Kha02] Hassan K. Khalil. *Nonlinear Systems*. Pearson Education. Prentice Hall, 2002 (cit. on p. 103).

[KK91] Hassan K. Khalil and Petar V. Kokotovic. “On stability properties of nonlinear systems with slowly varying inputs”. In: *IEEE Transactions on Automatic Control* 36.2 (1991), p. 229 (cit. on p. 8).

[Kno93] Jeffrey W. Knopf. “Beyond two-level games: domestic–international interaction in the intermediate-range nuclear forces negotiations”. In: *International Organization* 47.4 (1993), pp. 599–628 (cit. on p. 2).

[Kop05] Carlo Kopp. *Tomahawk Cruise Missile Variants/BGM/RGM/AGM-109 Tomahawk/TASM/TLAM/GCLM/MRASM*. Tech. rep. Air Power Australia, 2005 (cit. on p. 2).

[KPT13] Tae-Hun Kim, Bong-Gyun Park, and Min-Jea Tahk. “Bias-Shaping Method for Biased Proportional Navigation with Terminal-Angle Constraint”. In: *Journal of Guidance, Control, and Dynamics* 36.6 (2013), pp. 1810–1816 (cit. on p. 5).

[KW08] A. Kwiatkowski and H. Werner. “PCA-Based Parameter Set Mappings for LPV Models With Fewer Parameters and Less Overbounding”. In: *IEEE Transactions on Control Systems Technology* 16.4 (2008), pp. 781–788 (cit. on pp. 66, 100).

[LB79] KH Lloyd and DP Brown. “Instability of spinning projectiles during terminal guidance”. In: *Journal of Guidance and Control* 2.1 (1979), pp. 65–70 (cit. on p. 3).

[Lib+19] Michel Libsig et al. *CS 2019 - long range guided projectile (LRGP)*. Tech. rep. Saint Louis, France: ISL, DGA, 2019 (cit. on pp. 9, 18, 29).

[Lib+20] Michel Libsig et al. *CS 2020 - long range guided projectile (LRGP)*. Tech. rep. Saint Louis, France: ISL, DGA, 2020 (cit. on pp. 9, 18, 29).

[Lib+21] Michel Libsig et al. *CS 2021 - long range guided projectile (LRGP)*. Tech. rep. Saint Louis, France: ISL, DGA, 2021 (cit. on pp. 9, 18, 29).

[LL00] Douglas J. Leith and William E. Leithead. “Survey of gain-scheduling analysis and design”. In: *International journal of control* 73.11 (2000), pp. 1001–1025 (cit. on pp. 7, 70, 72).

[LL98] Douglas J. Leith and William E. Leithead. “Gain-scheduled and nonlinear systems: dynamic analysis by velocity-based linearization families”. In: *International Journal of Control* 70.2 (1998), pp. 289–317 (cit. on pp. 8, 62, 69).

[Lof04] Johan Lofberg. “YALMIP: A Toolbox for Modeling and Optimization in MATLAB”. In: *2004 IEEE international conference on robotics and automation (IEEE Cat. No. 04CH37508)*. IEEE. Taipei, Taiwan, 2004, pp. 284–289 (cit. on p. 102).

[LR90] Douglas A. Lawrence and Wilson J. Rugh. “On a stability theorem for nonlinear systems with slowly varying inputs”. In: *IEEE Transactions on Automatic Control* 35.7 (1990), pp. 860–864 (cit. on p. 8).

[LSZ14] Hugo Lhachemi, David Saussie, and Guchuan Zhu. “A robust and self-scheduled longitudinal flight control system: a multi-model and structured h-infinity approach”. In: *AIAA guidance, navigation, and control conference*. National Harbor, MD, US: American Institute of Aeronautics and Astronautics (AIAA), 2014, p. 0601 (cit. on p. 7).

[LSZ16] Hugo Lhachemi, David Saussié, and Guchuan Zhu. “Gain-scheduling control design in the presence of hidden coupling terms”. In: *Journal of guidance, control, and dynamics* 39.8 (2016), pp. 1871–1879 (cit. on p. 7).

[Lya92] Aleksandr Mikhailovich Lyapunov. “The General Problem of the Stability of Motion”. In: *International journal of control* 55.3 (1992), pp. 531–534 (cit. on p. 103).

[MA77] Phillip H. Morrison and David S. Amberntson. “Guidance and Control of a Cannon-Launched Guided Projectile”. In: *Journal of Spacecraft and Rockets* 14.6 (1977), pp. 328–334 (cit. on p. 4).

[Mac87] Donald MacKenzie. “Missile accuracy: A case study in the social processes of technological change”. In: *The social construction of technological systems: New directions in the sociology and history of technology* (1987), pp. 195–222 (cit. on p. 2).

[Mal+08] Gregory Malejko et al. “Jet interaction effect on the precision guided mortar munition (PGMM)”. In: *26th Proceedings of the Army Sciences Conference, Orlando, FL*. ARMY ARMAMENT RESEARCH DEVELOPMENT and ENGINEERING CENTER PICATINNY ARSENAL NJ. Porto, Portugal, 2008 (cit. on p. 4).

[Mar+15] Andres Marcos et al. “LPV Modeling and LFT Uncertainty Identification for Robust Analysis: Application to the VEGA Launcher during Atmospheric Phase.” In: *IFAC-PapersOnLine* 48.26 (2015). 1st IFAC Workshop on Linear Parameter Varying Systems LPVS 2015, pp. 115–120 (cit. on p. 65).

[Mar+18] Bastien Martinez et al. *Concept study of Long Range Projetile - Long Range Guided Projectile (LRGP project)*. Tech. rep. Saint Louis, France: ISL, DGA, 2018 (cit. on pp. 9, 18, 29).

[MB04] Andrés Marcos and Gary J. Balas. “Development of linear-parameter-varying models for aircraft”. In: *Journal of Guidance, Control, and Dynamics* 27.2 (2004), pp. 218–228 (cit. on pp. 8, 62, 69, 70).

[MC65] Sidney Harry Miller and RAND CORP SANTA MONICA CALIF. *The Minuteman Missile System*. Rand Corporation, 1965 (cit. on p. 1).

[McC99] Robert McCoy. *Modern Exterior Ballistics: The Launch and Flight Dynamics of Symmetric Projectiles*. Schiffer Publishing, 1999 (cit. on pp. 32, 39, 42, 180, 182).

[MF80] US Military Specification MIL-F. *U.S. Military Specification MIL-F-8785C*. Tech. rep. Washington, DC, 1980 (cit. on p. 161).

[MF97] US Military Specification MIL-F. *U.S. Military Handbook MIL-HDBK-1797*. Tech. rep. Washington, DC, 1997 (cit. on p. 160).

[MS12] Javad Mohammadpour and Carsten W. Scherer. *Control of Linear Parameter Varying Systems with Applications.* 1st. Springer Science & Business Media, 2012 (cit. on pp. 63, 65, 101).

[Mur78] Charles H Murphy. "Influence of moving internal parts on angular motion of spinning projectiles". In: *Journal of Guidance and Control* 1.2 (1978), pp. 117–122 (cit. on p. 3).

[NPM79] Robert A. Nulk, Harold L. Pastricky, and Phillip A. Morrison. "Copperhead Semiactive Laser Guidance System Development". In: *Journal of Guidance and Control* 2.5 (1979), pp. 374–381 (cit. on p. 4).

[NRR93] Robert A Nichols, Robert T Reichert, and Wilson J Rugh. "Gain scheduling for H-infinity controllers: A flight control example". In: *IEEE Transactions on Control systems technology* 1.2 (1993), pp. 69–79 (cit. on p. 7).

[OFS98] R.S. Ornedo, K.A. Farnsworth, and G.S. Sandhoo. "GPS and radar aided inertial navigation system for missile system applications". In: *IEEE 1998 Position Location and Navigation Symposium.* Palm Springs, CA, US, 1998, pp. 614–621 (cit. on p. 5).

[Ohl+97] Ernest Ohlmeyer et al. "GPS-aided navigation system requirements for smart munitions and guided missiles". In: *Guidance, Navigation, and Control Conference.* New Orleans,LA,US, 1997, p. 3683 (cit. on p. 5).

[OPB96] Douglas W. Owens, Gregory S. Parnell, and Robert L. Bivins. "Strategic arms reduction treaty (START) drawdown analyses". In: *Operations research* 44.3 (1996), pp. 425–434 (cit. on p. 2).

[Ost12] Eva Ostertagová. "Modelling using polynomial regression". In: *Procedia Engineering* 48 (2012), pp. 500–506 (cit. on p. 39).

[Ozg94] Deborah A. Ozga. "A chronology of the missile technology control regime". In: *The Nonproliferation Review* 1.2 (1994), pp. 66–93 (cit. on p. 1).

[Pac+91] Andy Packard et al. "A Collection of Rrobust Control Problems Leading to LMIs". In: *[1991] Proceedings of the 30th IEEE Conference on Decision and Control.* IEEE. Brighton, UK, 1991, pp. 1245–1250 (cit. on p. 65).

[Pad82] Fletcher C. Paddison. "The Talos control system". In: *Johns Hopkins APL Technical Digest* 3.2 (1982), pp. 154–156 (cit. on p. 7).

[Pan+21] Li Panshuo et al. "Polytopic LPV Approaches for Intelligent Automotive Systems: State of the Art and Future Challenges". In: *Mechanical Systems and Signal Processing* 161 (2021), p. 107931 (cit. on pp. 66, 100).

[PBC07] Thomas Pettersson, Richard Buretta, and David Cook. "Aerodynamics and flight stability for a course corrected artillery round". In: *23rd Int. Symp. on Ballistics, Tarragona, Spain.* 2007 (cit. on p. 3).

[PDP05] Luca Palladino, Gilles Duc, and Richard Pothin. "LPV Control for μ-split Braking Assistance of a Road Vehicle". In: *Proceedings of the 44th IEEE Conference on Decision and Control.* IEEE. Seville, Spain, 2005, pp. 2664–2669 (cit. on pp. 66, 100).

[Per11] Max Perrin. “Course Correction Fuzes Integration Technologies”. In: *Proceedings of the 55th Annual Fuze Conference*. Salt Lake City, UT, US, 2011, pp. 24–26 (cit. on p. 3).

[Pfi12] Harald Pfifer. “Quasi-LPV model of a NDI-controlled missile based on function substitution”. In: *Proceedings of the AIAA Guidance, Navigation, and Control Conference*. Minneapolis, MN, US, 2012, p. 4970 (cit. on pp. 6, 62, 69).

[PH10] Harald Pfifer and Simon Hecker. “LPV Controller Synthesis for a Generic Missile Model”. In: *2010 IEEE International Conference on Control Applications*. IEEE. Yokohama, Japan, 2010, pp. 1838–1843 (cit. on p. 68).

[PH11] Harald Pfifer and Simon Hecker. “Generation of Optimal Linear Parametric Models for LFT-Based Robust Stability Analysis and Control Design”. In: *IEEE Transactions on Control Systems Technology* 19.1 (2011), pp. 118–131 (cit. on pp. 8, 65).

[Phi08] Craig A. Phillips. “Guidance Algorithm for Range Maximization and Time-of-Flight Control of a Guided Projectile”. In: *Journal of Guidance, Control, and Dynamics* 31.5 (2008), pp. 1447–1455 (cit. on p. 114).

[Pin+22] Sofiane Pineau et al. “Autopilot Design for Dual-Spin Projectiles using Incremental Nonlinear Dynamic Inversion”. In: *Proceedings of the 2022 30th Mediterranean Conference on Control and Automation (MED)*. Vouliagmeni, Greece: IEEE, 2022, pp. 444–449 (cit. on pp. 3, 6).

[Pin+23] Sofiane Pineau et al. “L1 Adaptive Augmentation of an Incremental Nonlinear Dynamic Inversion Autopilot for Dual-Spin Guided Projectiles”. In: *AIAA Scitech 2023 Forum*. National Harbor, MD, US: American Institute of Aeronautics and Astronautics (AIAA), 2023, p. 1998 (cit. on p. 6).

[PP97] Albert Piccirillo and Albert Piccirillo. “The origins of the anti-ship guided missile”. In: *1997 World Aviation Congress*. Anaheim, CA, US, 1997, p. 5652 (cit. on p. 3).

[PPV01] Emmanuel Prempain, Ian Postlethwaite, and Dave Vorley. “A Gain Scheduled Autopilot Design for a Bank-to-Turn Missile”. In: *Proceedings of the 2001 European Control Conference (ECC)*. IEEE. Porto, Portugal, 2001, pp. 2052–2057 (cit. on pp. 8, 61, 70).

[Pra89] John Prados. “China’s “new thinking” on nuclear arms”. In: *Bulletin of the Atomic Scientists* 45.5 (1989), pp. 32–35 (cit. on p. 1).

[PS90] William C. Potter and Adam Stulberg. “The Soviet Union and the spread of ballistic missiles”. In: *Survival* 32.6 (1990), pp. 543–557 (cit. on p. 1).

[PV08] Charles Poussot-Vassal. “Robust LPV Multivariable Automotive Global Chassis Control”. PhD thesis. Institut National Polytechnique de Grenoble-INPG, 2008 (cit. on p. 112).

[PV+11] Charles Poussot-Vassal et al. “Attitude and Handling Improvements Through Gain-Scheduled Suspensions and Brakes Control”. In: *Control Engineering Practice* 19.3 (2011). Special Section: IFAC World Congress Application Paper Prize Papers, pp. 252–263 (cit. on p. 120).

[PVR12] Charles Poussot-Vassal and Clement Roos. “Generation of a Reduced-Order LPV/LFT Model from a Set of Large-Scale MIMO LTI Flexible Aircraft Models”. In: *Control Engineering Practice* 20.9 (2012), pp. 919–930 (cit. on pp. 8, 65).

[Qua+15] Wei Quan et al. *INS/CNS/GNSS integrated navigation technology*. Springer, 2015 (cit. on p. 5).

[RC08] Jonathan Rogers and Mark Costello. “Control authority of a projectile equipped with a controllable internal translating mass”. In: *Journal of Guidance, Control, and Dynamics* 31.5 (2008), pp. 1323–1333 (cit. on p. 3).

[RS00] Wilson J. Rugh and Jeff S. Shamma. “Research on gain scheduling”. In: *Automatica* 36.10 (2000), pp. 1401–1425 (cit. on pp. 7, 70, 99).

[Rug90] Wilson J. Rugh. “Analytical framework for gain scheduling”. In: *1990 American Control Conference*. IEEE. San Diego, CA, US, 1990, pp. 1688–1694 (cit. on p. 7).

[SA90] Jeff S Shamma and Michael Athans. “Analysis of gain scheduled control for nonlinear plants”. In: *IEEE Transactions on Automatic Control* 35.8 (1990), pp. 898–907 (cit. on pp. 7, 8).

[SA92] Jeff S. Shamma and Michael Athans. “Gain scheduling: Potential Hazards and Possible Remedies”. In: *IEEE Control Systems Magazine* 12.3 (1992), pp. 101–107 (cit. on pp. 8, 70, 99).

[Saf82] Michael G. Safonov. “Stability Margins of Diagonally Perturbed Multivariable Feedback Systems”. In: *IEE Proceedings D (Control Theory and Applications)*. Vol. 129. 6. IET. 1982, pp. 251–256 (cit. on p. 143).

[SBK02] Jong-Yeob Shin, Gary J. Balas, and M. Alpay Kaya. “Blending Methodology of Linear Parameter Varying Control Synthesis of F-16 Aircraft System”. In: *Journal of Guidance, Control, and Dynamics* 25.6 (2002), pp. 1040–1048 (cit. on p. 69).

[SC10] Mishah Uzziél Salman and Borchin Chang. “Active coning compensation for control of spinning flying vehicles”. In: *2010 IEEE International Conference on Control Applications*. IEEE. 2010, pp. 1832–1837 (cit. on p. 3).

[SC93] Jeff S. Shamma and James R. Cloutier. “Gain-scheduled missile autopilot design using linear parameter varying transformations”. In: *Journal of Guidance, Control, and Dynamics* 16.2 (1993), pp. 256–263 (cit. on pp. 8, 62, 70, 72).

[Sèv+14] Florian Sève et al. “Pitch/yaw channels control design for a 155mm projectile with rotating canards, using a H_∞ loop-shaping design procedure”. In: *AIAA Guidance, Navigation, and Control Conference*. American Institute of Aeronautics and Astronautics (AIAA). National Harbor, MD, US, 2014, p. 1474 (cit. on pp. 7, 9, 68).

[Sev+17] Florian Seve et al. “Flight dynamics modeling of dual-spin guided projectiles”. In: *IEEE Transactions on Aerospace and Electronic Systems* 53.4 (2017), pp. 1625–1641 (cit. on p. 3).

[SGB13] Olivier Sename, Peter Gaspar, and József Bokor. *Robust Control and Linear Parameter Varying Approaches: Application to Vehicle Dynamics.* 1st. Vol. 437. Springer, 2013 (cit. on pp. 63, 101).

[SGC97] Carsten Scherer, Pascal Gahinet, and Mahmoud Chilali. “Multiobjective Output-Feedback Control via LMI Optimization”. In: *IEEE Transactions on automatic control* 42.7 (1997), pp. 896–911 (cit. on pp. 100, 112).

[Sma70] Ian Smart. “The Strategic Arms Limitation Talks”. In: *The World Today* 26.7 (1970), pp. 296–305 (cit. on p. 2).

[Sor60] H.W. Sorenson. *Range and Guidance Accuracy Capability of the Atlas Missile System.* Tech. rep. San Diego, CA, US: GENERAL DYNAMICS/ASTRONAUTICS SAN DIEGO, 1960 (cit. on p. 1).

[SP05] Sigurd Skogestad and Ian Postlethwaite. *Multivariable Feedback Control: Analysis and Design.* 2nd. john Wiley & sons, 2005 (cit. on pp. 136, 137, 145).

[SPG20] Peter Seiler, Andrew Packard, and Pascal Gahinet. “An Introduction to Disk Margins”. In: *IEEE Control Systems Magazine* 40.5 (2020), pp. 78–95 (cit. on pp. 136, 141–143).

[ST19] Florian Sève and Spilios Theodoulis. “Design of an H_∞ Gain-Scheduled Guidance Scheme for a Guided Projectile”. In: *Journal of Guidance, Control, and Dynamics* 42.11 (2019), pp. 2399–2417 (cit. on pp. 7, 9).

[Sto08] Doug Storsved. “PGK and the impact of affordable precision on the fires mission”. In: *43rd Annual Guns & Missiles Symposium.* 2008, pp. 21–24 (cit. on p. 3).

[Str+15] Guillaume Strub et al. “Pitch axis control for a guided projectile in a wind tunnel hardware-in-the-loop setup”. In: *Journal of Spacecraft and Rockets* 52.6 (2015), pp. 1614–1626 (cit. on p. 68).

[Str+18] Guillaume Strub et al. “Gain-scheduled autopilot design and validation for an experimental guided projectile prototype”. In: *Journal of Guidance, Control, and Dynamics* 41.2 (2018), pp. 461–475 (cit. on pp. 7, 9).

[Stu00] David K Stumpf. *Titan Ii (c).* University of Arkansas Press, 2000 (cit. on p. 1).

[Sè+17] Florian Sève et al. “Gain-scheduled H_∞ loop-shaping autopilot design for spin-stabilized canard-guided projectiles”. In: *Aerospace Lab* 13 (2017), pp. 1–24 (cit. on p. 7).

[TD09] Spilios Theodoulis and Gilles Duc. “Missile Autopilot Design: Gain-Scheduling and the Gap Metric”. In: *Journal of Guidance, Control, and Dynamics* 32.3 (2009), pp. 986–996 (cit. on p. 7).

[Tha+19] Sovanna Thai et al. “Robust design for the roll-channel autopilot of a canard-guided dual-spin projectile”. In: *IFAC-PapersOnLine* 52.12 (2019), pp. 232–237 (cit. on p. 3).

[Tha+20] Sovanna Thai et al. "Gain-Scheduled Autopilot Design with Anti-Windup Compensator for a Dual-Spin Canard-Guided Projectile". In: *Proceedings of the 2020 IEEE Conference on Control Technology and Applications (CCTA)*. Montreal, QC, Canada: IEEE, 2020, pp. 156–161 (cit. on pp. 7, 68).

[Tha+23] Sovanna Thai et al. "Robust gain-scheduled autopilot design with anti-windup compensation for a guided projectile". In: *CEAS Aeronautical Journal* 14 (2023), 765–786 (cit. on p. 7).

[The+10] Spilios Theodoulis et al. "LPV modeling of guided projectiles for terminal guidance". In: *18th Mediterranean Conference on Control and Automation, MED'10*. IEEE. Marrakech, Morocco, 2010, pp. 1455–1460 (cit. on pp. 9, 61, 68, 70).

[The+13] Spilios Theodoulis et al. "Guidance and Control Design for a Class of Spin-Stabilized Fin-Controlled Projectiles". In: *Journal of Guidance, Control, and Dynamics* 36.2 (2013), pp. 517–531 (cit. on p. 9).

[Tip+20] Steven Tipán et al. "Nonlinear Dynamic Inversion Autopilot Design for Dual-Spin Guided Projectiles". In: *IFAC-PapersOnLine* 53.2 (Jan. 2020), pp. 14827–14832 (cit. on pp. 3, 6).

[Tit+04] David Titterton et al. *Strapdown Inertial Navigation Technology*. IEE Radar Series. Institution of Engineering and Technology, 2004 (cit. on p. 5).

[TMW11] Spilios Theodoulis, Yannick Morel, and Philippe Wernert. "Modelling and stability analysis of the 155 mm spin-stabilised projectile equipped with steering fins". In: *International Journal of Modelling, Identification and Control* 14.3 (2011), pp. 189–204 (cit. on p. 3).

[TO95] Onur Toker and Hitay Ozbay. "On the/spl Nscr//spl Pscr/-Hardness of the Purely Complex/spl mu/Computation, Analysis/Synthesis, and some Related Problems in Multidimensional Systems". In: *Proceedings of 1995 American Control Conference-ACC'95*. Vol. 1. IEEE. 1995, pp. 447–451 (cit. on p. 146).

[Tót10] Roland Tóth. *Modeling and Identification of Linear Parameter-Varying Systems*. 1st. Vol. 403. Springer, 2010, p. 325 (cit. on p. 68).

[TP21] Spilios Theodoulis and Michael Proff. "Robust Flight Control Tuning for Highly Agile Missiles". In: *AIAA Scitech 2021 Forum*. Virtual event, 2021, p. 1568 (cit. on p. 7).

[TPB00] Weehong Tan, Andrew K. Packard, and Gary J. Balas. "Quasi-LPV Modeling and LPV Control of a Generic Missile". In: *Proceedings of the 2000 American Control Conference. ACC (IEEE Cat. No. 00CH36334)*. Vol. 5. IEEE. Chicago, IL, US, 2000, pp. 3692–3696 (cit. on pp. 8, 69).

[TSW15] Spilios Theodoulis, Florian Sève, and Philippe Wernert. "Robust gain-scheduled autopilot design for spin-stabilized projectiles with a course-correction fuze". In: *Aerospace Science and Technology* 42 (2015), pp. 477–489 (cit. on pp. 3, 7, 9).

[TW11] Spilios Theodoulis and Philippe Wernert. “Flight control for a class of 155 mm spin-stabilized projectiles with course correction fuse (CCF)”. In: *Proceedings of the 2011 AIAA Guidance, Navigation, and Control Conference*. Portland, OR, USA, 2011, p. 6247 (cit. on p. 3).

[Vas+20] Joseph D. Vasile et al. “A Multi-Disciplinary Approach to Design Long Range Guided Projectiles”. In: *AIAA Scitech 2020 Forum*. Orlando, FL, US: American Institute of Aeronautics and Astronautics (AIAA), 2020, p. 1993 (cit. on p. 4).

[Vina] “Flight Dynamics Modeling and Simulator Design for a New Class of Long-Range Guided Projectiles”. In: *Proceedings of the 2022 CEAS EuroGNC conference*. CEAS-GNC-2022-034. Berlin, Germany, 2022, p. 034 (cit. on p. 62).

[Vinb] “Quasi-LPV Modeling of Guided Projectile Pitch Dynamics through State Transformation Technique”. In: vol. 55. 35. 5th IFAC Workshop on Linear Parameter Varying Systems LPVS 2022. Montreal, Canada: Elsevier, 2022, pp. 43–48 (cit. on p. 18).

[Vin+23a] Gian Marco Vinco et al. “Linear Parameter Varying Pitch Autopilot Design for a class of Long Range Guided Projectiles”. In: *AIAA SCITECH 2023 Forum*. National Harbor, MD, US & Online: American Institute of Aeronautics and Astronautics (AIAA), 2023, p. 2498 (cit. on p. 100).

[Vin+23b] Gian Marco Vinco et al. “LPV Modeling and Control Design for Guided Projectiles through Reduced Polytopic Representation”. In: *Journal of Guidance, Control, and Dynamics* (2023) (cit. on pp. 100, 136).

[Vin+23c] Gian Marco Vinco et al. “Uneven Grid-based Linear Parameter-Varying Controller Design for Guided Projectiles”. In: *22nd IFAC World Congress 2023*. Vol. 56. 2. Yokohama, Japan: Elsevier, 2023, pp. 4496–4501 (cit. on pp. 100, 136).

[VM82] Paul L. Vergez and James R. McClendon. “Optimal control and estimation for strapdown seeker guidance of tactical missiles”. In: *Journal of Guidance, Control, and Dynamics* 5.3 (1982), pp. 225–226 (cit. on p. 5).

[Wal02] J. Waldmann. “Line-of-sight rate estimation and linearizing control of an imaging seeker in a tactical missile guided by proportional navigation”. In: *IEEE Transactions on Control Systems Technology* 10.4 (2002), pp. 556–567 (cit. on p. 5).

[Wel00] Lawrence L. Wells. “The projectile GRAM SAASM for ERGM and Excalibur”. In: *IEEE 2000. Position Location and Navigation Symposium (Cat. No.00CH37062)*. San Diego, CA, US: IEEE, 2000, pp. 106–111 (cit. on p. 4).

[Wer07] Phillip Wernert. *Simulations de trajectoires de projectiles à 6 degrés de liberté dans le cadre de la mécanique du vol avion. Partie 3 : Utilisation de repères non liés au projectile*. Tech. rep. Saint Louis, France: ISL, 2007 (cit. on p. 52).

[WFAT03] Amy F. Woolf, Defense Foreign Affairs, and Division Trade. “Nuclear Arms Control: The Strategic Offensive Reductions Treaty”. In: Congressional Research Service, Library of Congress. 2003 (cit. on p. 2).

[WPB95] Fen Wu, Andy Packard, and Gary Balas. “LPV control design for pitch-axis missile autopilots”. In: *Proceedings of 1995 34th IEEE Conference on Decision and Control*. Vol. 1. IEEE. New Orleans, LA, US, 1995, pp. 188–193 (cit. on pp. 9, 100).

[Wr98] Kevin A. Wise and David J. B. roy. “Agile Missile Dynamics and Control”. In: *Journal of Guidance, Control, and Dynamics* 21.3 (1998), pp. 441–449 (cit. on p. 3).

[Wu95] Fen Wu. *Control of linear parameter varying systems*. Ph.D. dissertation. University of California, Berkeley, 1995 (cit. on p. 123).

[Wu+96] Fen Wu et al. “Induced L2-Norm Control for LPV Systems with Bounded Parameter Variation Rates”. In: *International Journal of Robust and Nonlinear Control* 6.9-10 (1996), pp. 983–998 (cit. on pp. 9, 100, 110).

[YWA13] Ting Yue, Lixin Wang, and Junqiang Ai. “Gain self-scheduled H_∞ control for morphing aircraft in the wing transition process based on an LPV model”. In: *Chinese journal of aeronautics* 26.4 (2013), pp. 909–917 (cit. on p. 8).

[Zal11] Steven J. Zaloga. *V-1 Flying Bomb 1942–52: Hitler's infamous “doodlebug”*. Bloomsbury Publishing, 2011 (cit. on p. 1).

[Zal13] Steven J. Zaloga. *V-2 Ballistic Missile 1942–52*. Bloomsbury Publishing, 2013 (cit. on p. 1).

[Zip14] Peter H. Zipfel. *Modeling and Simulation of Aerospace Vehicle Dynamics*. 3rd. American Institute of Aeronautics and Astronautics, Inc., 2014 (cit. on pp. 18, 21, 25, 39, 52).

[Zip19] P. H. Zipfel. *Introduction to Tensor Flight Dynamics: A Paradigm Shift*. Modeling and Simulation Technologies, Jan. 2019 (cit. on p. 25).

[Zip76] Peter H. Zipfel. “Aerodynamic Symmetry of Aircraft and Guided Missiles”. In: *Journal of Aircraft* 13.7 (1976), pp. 470–475 (cit. on p. 27).

[ZZW14] Hui Zhang, Xinjie Zhang, and Junmin Wang. “Robust Gain-Scheduling Energy-to-Peak Control of Vehicle Lateral Dynamics Stabilisation”. In: *Vehicle System Dynamics* 52.3 (2014), pp. 309–340 (cit. on pp. 66, 100).

Résumé — L'avènement de technologies de guidage avancées au cours des dernières décennies a ravivé l'intérêt pour l'emploi de munitions d'artillerie guidées lancées par canon dans les opérations stratégiques. L'amélioration de la portée des munitions, tout en évitant de modifier le canon, implique l'étude de configurations aérodynamiques innovantes. Une solution prometteuse pourrait être identifiée dans une nouvelle architecture stabilisée par des ailerons, visant à améliorer la capacité de portée par un vol plané dirigé. L'utilisation d'un concept non gyrostabilisé réduit la dynamique hautement non linéaire générée par les termes de couplage aérodynamique. La conception axée sur la commande des applications aérospatiales repose généralement sur des techniques standard de séquencement de gains basées sur la linéarisation, où des approximations locales de la dynamique non linéaire permettent de concevoir un ensemble de contrôleurs linéaires à temps invariants (LTI) à des points de vol sélectionnés. Les contrôleurs sont ensuite interpolés en ligne pour couvrir toutes les conditions appartenant à l'enveloppe de vol du système. Malgré un large éventail d'applications réussies, séquencement de gains s'est avéré présenter d'importantes limitations théoriques et pratiques, à la fois en termes de précision de la modélisation et de stabilité garantie de l'interpolation des contrôleurs. Récemment, les techniques linéaires à paramètres variables (LPV) ont suscité une attention croissante dans la modélisation et la commande d'un large éventail d'applications de missiles et d'aéronefs. En particulier, les modèles LPV/quasi-LPV peuvent prendre en compte les variations temporelles d'un ensemble sélectionné de paramètres, ce qui permet de mieux saisir la dynamique non linéaire complexe qui caractérise les systèmes aérospatiaux. En conséquence, la conception vise la synthèse d'un contrôleur qui fournit des propriétés de stabilité globale sur l'ensemble de l'enveloppe décrite par la variation des paramètres. Dans ce contexte, le projet vise à étudier la modélisation et la conception du la commande d'une nouvelle classe de projectiles guidés stabilisés par des ailerons dans le cadre du LPV. Une analyse de régression sur des données issues de simulations numériques de dynamique des fluides permet de caractériser l'aérodynamique du projectile et de définir le modèle de dynamique de vol non linéaire correspondant. La dynamique non linéaire est ensuite formulée comme un modèle quasi-LPV pour une conception axée sur la commande grâce à une sélection précise des paramètres variables étudiés. La synthèse de l'autopilote est réalisée par l'utilisation d'approches LPV/$\mathcal{H}_\infty$ standard : polytopique et basée sur une grille. L'objectif principal consiste à suivre un signal de guidage de référence augmentant la portée, tout en assurant la stabilité du projectile sur l'ensemble de la trajectoire de vol plané. L'approche polytopique repose sur la définition d'un espace convexe de variation linéaire des paramètres, offrant des garanties de stabilité plus solides. L'approche basée sur une grille effectue la conception du contrôleur à travers une grille de conditions de vol sélectionnées, assurant une meilleure optimisation de la synthèse du contrôleur. La robustesse et les performances de suivi des contrôleurs sont testées dans un environnement de simulateur non linéaire, en tenant compte des sources externes de perturbation telles que le vent et des incertitudes paramétriques possibles du modèle.

Mots clés : Systèmes Linéaires à Paramètres Variables (LPV), Commande de vol, Commande Robuste, Dynamique de vol, Commande $\mathcal{H}_\infty$.

Abstract — The advent of advanced guidance technologies in the last decades has renewed the interest in the employment of gun-launched artillery-guided munitions in strategic operations. The enhancement of munitions range performance, under the avoidance of any modifications to the firing gun, implies the investigation of innovative aerodynamic configurations. A promising solution could be identified in a novel fin-stabilized architecture, aiming to improve the range capability through a gliding steered flight. The employment of a non-spinning concept reduces the highly nonlinear dynamics generated by the aerodynamic coupling terms. The control design of aerospace applications generally relies on standard linearization-based gain-scheduling techniques, where local approximations of the nonlinear dynamics allows for the design of a set of Linear-Time Invariant controllers (LTI) at selected flight points. The controllers are then interpolated online to cover all the conditions belonging to the system flight envelope. Despite a broad range of successful applications, gain-scheduling design has been proven to present important theoretical and practical limitations, both in terms of modeling accuracy and guaranteed stability of the controller interpolation. Recently, the Linear Parameter-Varying (LPV) framework has attracted increasing attention in the modeling and control of a wide range of missile and aircraft applications. In particular, LPV/quasi-LPV models can account for the time variation of a selected set of parameters, which results in a higher capability in capturing the complex nonlinear dynamics characterizing aerospace systems. Accordingly, the design targets the synthesis of a controller that provides global stability properties across the entire envelope described by the variation of the parameters. In this context, the project aims to investigate the modeling and control design of a new class of fin-stabilized guided projectiles in the LPV framework. An exhaustive regression analysis on Computational Fluid Dynamics (CFD) simulation results allows for characterizing the aerodynamics of the projectile and defining the corresponding nonlinear flight dynamics model. The nonlinear dynamics is then formulated as a quasi-LPV model for control design purposes through an accurate selection of the investigated varying parameters. The synthesis of the autopilot is achieved through standard LPV/$\mathcal{H}_\infty$ approaches: polytopic and grid-based. The core objective consists of the tracking of a reference range-enhancement guidance signal while ensuring the stability of the projectile across the entire gliding trajectory. The polytopic approach relies on the definition of a convex space of linear variation of the parameters, providing stronger stability guarantees. The grid-based approach performs the design of the controller across a grid of selected flight conditions, ensuring higher controller synthesis optimization. The robustness and the tracking performance of the controllers are tested in a nonlinear simulator environment, addressing external sources of disturbance such as wind gusts, and accounting for possible model parametric uncertainties.

Keywords: Linear Parameter-Varying (LPV), Flight Control, Robust Control, Flight Dynamics, $\mathcal{H}_\infty$ Control.

GIPSA-lab, 11 Rue des Mathématiques, Saint-Martin-d'Hères
Grenoble, France

French-German Research Institute of Saint-Louis (ISL), 5 rue du Général Cassagnou
Saint-Louis, France